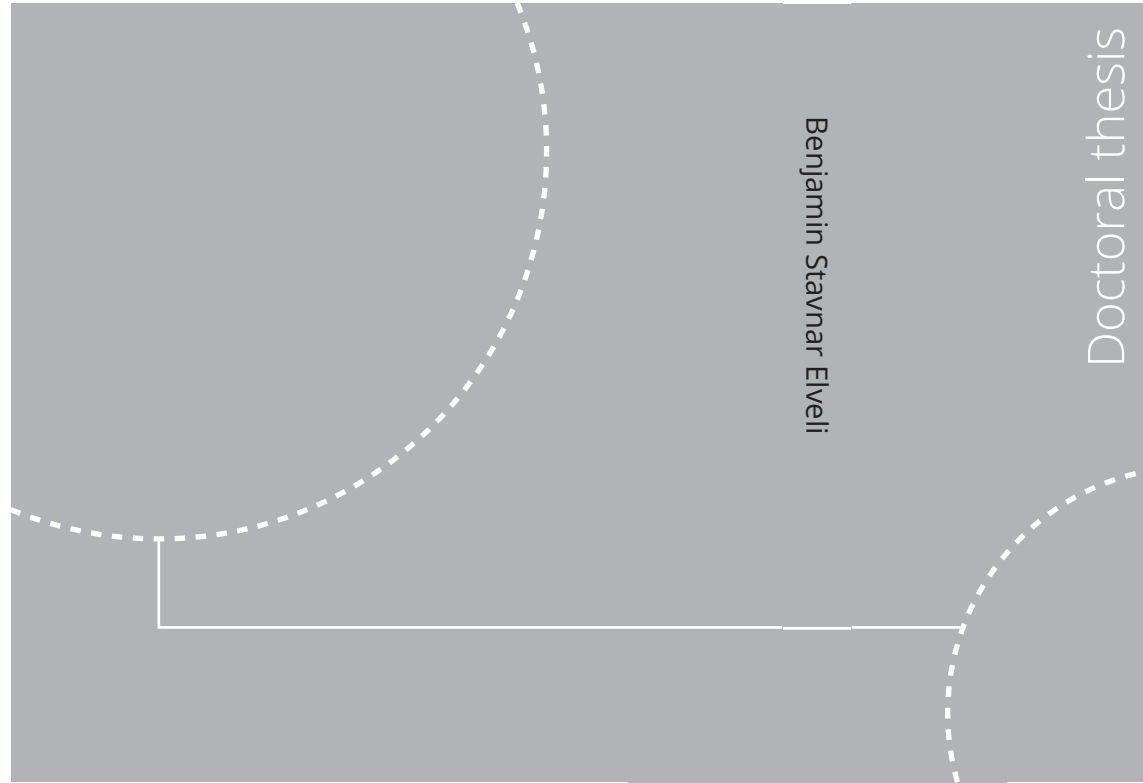


ISBN 978-82-326-5179-5 (printed ver.)
ISBN 978-82-326-5383-6 (electronic ver.)
ISSN 1503-8181 (printed ver.)
ISSN 2703-8084 (electronic ver.)



Doctoral theses at NTNU, 2022:392

Benjamin Stavnar Elveli

Behaviour, modelling and
simulation of thin steel plates
subjected to combined blast
and impact loading

Doctoral theses at NTNU, 2022:392

NTNU
Norwegian University of
Science and Technology
Thesis for the degree of
Philosophiae Doctor
Faculty of Engineering
Department of Structural Engineering

 **NTNU**
Norwegian University of
Science and Technology

 NTNU

 **NTNU**
Norwegian University of
Science and Technology

Benjamin Stavnar Elveli

Behaviour, modelling and simulation of thin steel plates subjected to combined blast and impact loading

Thesis for the degree of Philosophiae Doctor

Trondheim, December 2022

Norwegian University of Science and Technology
Faculty of Engineering
Department of Structural Engineering



Norwegian University of
Science and Technology

NTNU

Norwegian University of Science and Technology

Thesis for the degree of Philosophiae Doctor

Faculty of Engineering
Department of Structural Engineering

© Benjamin Stavnar Elveli

ISBN 978-82-326-5179-5 (printed ver.)
ISBN 978-82-326-5383-6 (electronic ver.)
ISSN 1503-8181 (printed ver.)
ISSN 2703-8084 (electronic ver.)

Doctoral theses at NTNU, 2022:392



Printed by Skipnes Kommunikasjon AS

Preface

This thesis is submitted in partial fulfilment of the requirements for the degree of Philosophiae Doctor in Structural Engineering at the Norwegian University of Science and Technology (NTNU). All work has been conducted at the Structural Impact Laboratory (SIMLab) at the Department of Structural Engineering, NTNU, and at an indoor testing facility operated by The Norwegian Estate Defence Agency (NDEA). The funding of this thesis was provided by the Faculty of Engineering and the Centre for Advanced Structural Analysis (CASA), appointed by the Research Council of Norway as a Centre for Research-based Innovation (CRI).

The work was supervised by Associate Professor Vegard Aune as the main supervisor, and by Professor Tore Børvik as the co-supervisor. The thesis consists of five parts, represented as an article collection. Part 1 is published in an international peer-reviewed journal, while Part 2 and Part 3 are published in international conference proceedings. Part 4 and Part 5 are both submitted for possible publication in international peer-reviewed journals. The synopsis motivates and binds together each of the five contributions in this thesis. The first author has performed all experiments, numerical work, and prepared the manuscripts with guidance of the supervisors and the co-authors. The experiments presented in Part 5 were performed together with Knut Ove Hauge and Ole Vestrum at NDEA.

Benjamin Stavnar Elveli
Trondheim, Norway
November 21, 2022

Abstract

This thesis studies the effects of combined fragment impact and blast loading on thin steel plates. It is here assumed that the fragments strike before the arrival of the blast wave. The fragments are represented through pre-cut defects of idealized geometries and by ballistic impact holes in the target plates before the exposure to blast loading.

The effects of strength versus ductility on the dynamic response and fracture resistance of thin steel plates were investigated by studying plates with and without pre-formed defects exposed to blast-like loading conditions in a shock tube facility. Several geometries of the pre-formed defects were tested and compared using three different plate materials of target plates, i.e., two dual-phase steels and one martensitic steel. The three materials had different work hardening, an incremental increase in yield strength and a corresponding decrease in elongation to failure. The material with the highest strength and lowest elongation to fracture consistently resulted in the largest resistance to plastic deformation and lowest resistance to fracture.

Fragment impact in thin steel plates typically results in perforation with surrounding plastic deformations and damage to the material. To investigate the effect of more realistic pre-formed defects, target plates exposed to high-velocity impact were compared to target plates containing pre-cut circular holes during blast loading. To establish a controllable and measurable test environment, the ballistic impact was conducted using small-arms projectiles fired from a fixed rifle. The blast load was applied separately in a shock tube facility. Even though the pre-cut holes and the ballistic impact holes were both circular with similar diameters, the ballistic impact holes introduced small petalling cracks and plastic deformations to the material around the perforation hole. As expected, crack propagation during blast loading initiated at these petalling cracks. The target plates exposed to ballistic impact showed reduced fracture resistance compared to the target plates with pre-cut circular holes. An interesting observation was that this became more pronounced with increased material strength.

To increase the complexity of the blast environment, the target plates were exposed to partially confined detonations of C-4. This study was limited to only one plate material, where the target plates contained either pre-cut circular holes or holes from ballistic impact. Compared to the loading conditions from the shock tube, the partially confined detonations

resulted in a much higher peak reflected pressure and a significant reduction of the positive duration phase. The corresponding pressure fields showed large time-dependent variations on the blast-exposed area of the target plates. Despite the changes in blast environment, no additional differences between the two plate configurations were observed. All blast tests were successfully measured both in terms of plate response and the corresponding pressure measurements. The global plastic deformations of the target plates showed a final deformed shape of a global dome with a superimposed local dome.

The extensive dataset collected from the blast tests was used for the validation of various numerical techniques for modelling and simulation of blast loaded plates. The simulations with the best agreement to the experimental findings, were the shock tube experiments. That is, in the case where the numerical simulations were defined as purely Lagrangian analyses with the blast load applied as prescribed pressure histories. As the complexity of the blast environments increased for the partially confined detonations, both Arbitrary Lagrangian-Eulerian (ALE) and particle-based simulations had to be applied to describe the fluid-structure interaction (FSI) between the explosive, the confinement and the target plate. Considerable deviations between the two numerical approaches were observed. Compared to the experimental findings, the ALE simulations and the particle-based simulations underestimated and overestimated the loading conditions with approximately 10 %, respectively.

This work provides insight into the behaviour, modelling and simulation of thin steel plates subjected to blast loading. Parameters influencing the dynamic response have been identified and investigated. The experimental dataset is therefore well suited to evaluate more numerical methods and develop new computational methods in future studies.

This work also confirms the trade-off between CPU time and accuracy in the numerical modelling and simulation of combined fragment impact and blast loading. That is, simulations of fragment impact require a very fine discretization of the target plate to obtain reliable predictions, while simulations of the blast response have to use a coarser mesh to run within a reasonable CPU times. This is challenging when modelling the combined effect of fragment impact and blast loading of plated structures, especially if a realistic fracture mode from the ballistic impact and a feasible CPU cost during the blast loading phase of the simulation are important.

The main finding of this work is that fragment impacts prior to blast loading can significantly reduce the blast resistance of thin steel plates. Particularly in the case of high-strength, martensitic steel plates.

Acknowledgements

Throughout the four years I have spent on my thesis, my supervisors Vegard Aune and Tore Børvik have always provided me with great guidance and support. Whenever I have stopped by your offices asking for help, you have taken the time to discuss whatever I have been struggling with, even when you have been busy with other things. This would never have been possible without your patience with me and your passion and involvement in this project, and for that, I would like to express my deepest gratitude to the both of you.

The experimental campaigns were carried out with the help of Trond Auestad, Ole Vestrum, and Knut Ove Hauge. Your expertise in experimental testing have been essential and are greatly appreciated. I also thank Mads Iddberg for your efforts during our first round of experimental work. The funding for the project was provided by the Faculty of Engineering and the Centre for Advanced Structural Analysis (CASA), appointed by the Research Council of Norway as a Centre for Research-based Innovation (CRI).

The unique working environment and expertise available at the SIMLab group must also be mentioned. I think I speak for every PhD student at the department by saying that the willingness of the post-docs, researchers, and professors to share knowledge among us PhD students has been a key factor for our progress. A special thanks goes to Dr. Torodd Berstad for being a total legend in LS-DYNA, and for always being helpful with numerical issues. My four years at SIMLab would not have been the same without all of my colleagues and our many discussions and arguments. An extra shout-out goes to Kristoffer Brekken, Sindre Olufsen, Øystein Jacobsen, Ruben Sælen, Jonas Rudshaug, Victor Andrè, Sigurd Aune, Vetle Espeseth, and Martin Kristoffersen. You are probably all tired of me knocking on your door whenever I am stuck with something or just want to socialize.

For me, it has also been very important to stay active and have fun outside of work hours to remain productive at work. My flatmates have done an excellent job of always being up for some boarding, climbing, or just having dinner and socializing. The support from friends and family has also been important, and helped me to stay motivated. Lastly, I have to thank to my girlfriend, Katalin, for always being positive, kind, and loving. I have often felt stressed, tired, or just moody during the work on this thesis, but somehow Kat has always responded by being understanding and supportive.

Contents

Preface	i
Abstract	iv
Acknowledgements	v
Synopsis	1
1 Introduction	1
2 Objectives and scope	7
2.1 Objectives	7
2.2 Scope	8
3 Research methods	9
4 Summary	11
4.1 Part 1	11
4.2 Part 2	12
4.3 Part 3	12
4.4 Part 4	13
4.5 Part 5	14
4.6 Conference contributions	15
5 Conclusions	17
6 Suggested further work	21
References	23

Articles	27
Part 1	
On the strength–ductility trade-off in thin blast-loaded steel plates with and without initial defects — An experimental study	27
Part 2	
Influence of material properties on the performance of blast-loaded steel plates with pre-cut defects	53
Part 3	
Blast-load response of thin steel plates after ballistic impact from small-arms projectiles	61
Part 4	
Performance of thin blast-loaded steel plates after ballistic impact from small-arms projectiles	73
Part 5	
Thin steel plates exposed to combined ballistic impact and partially confined airblast loading	109

Synopsis

1 Introduction

Explosions can occur in a variety of environments, either created by accidents or intentionally. The rapid release of energy during an explosion and the following blast wave propagation may accelerate objects within the blast's vicinity to high velocities, as shown in Figure 1.1. Such objects could be parts initially contained within the explosive device (such as fragments from a ruptured casing, ball bearings, etc.) or they can originate from external objects (e.g., gravel, rocks, or debris from surrounding structures). This makes structures located in the vicinity of the point of detonation prone to the combined effect of fragment impact and blast loading. The accelerated objects can impact the structure before, during, or after the arrival of the blast wave, depending on the distance to the explosive charge [1], as illustrated in Figure 1.3. In fact, the combined effects of fragment impact and blast loading have been shown to be more severe than one of the two loading cases acting alone [1–4]. In scenarios where fragments impact the structure before the arrival of the shock wave, the fragments may reduce the structural integrity. This means that the blast loading could act on a pre-damaged structure containing weak points for initiation of fracture. Therefore, the cases where the fragment impact occurs before the blast wave are assumed to give the highest damage potential [5].

Historically, the scope of blast resistant design has been focused on massive military structures and government buildings [6]. Therefore, concrete structures have been the preferred choice for blast protection, where concrete slabs exposed to combined fragment impact and blast loading have been the subject of many studies in the past few decades (see e.g., [7–11]). However, civilian engineering structures are often architectural, lightweight, and flexible, and studies on thin-walled metallic components are therefore of interest (see e.g. [12, 13]). Compared to massive concrete structures, lightweight and flexible components can undergo large plastic deformations without experiencing material fracture. The energy absorbing mechanisms and the structural response during blast loading of such structures typically depend upon the design and properties of the specific structure under consideration. As a consequence, it is difficult to establish universal guidelines for protective design of flexible and lightweight structures in today's design codes. By



Figure 1.1: Detonation of a vehicle borne improvised explosive device, illustrating accelerated fragments moving together with the shock wave. The propagation of the shock wave is indicated with the white arrows. Courtesy of The Norwegian Defence Estate Agency (Forsvarsbygg).

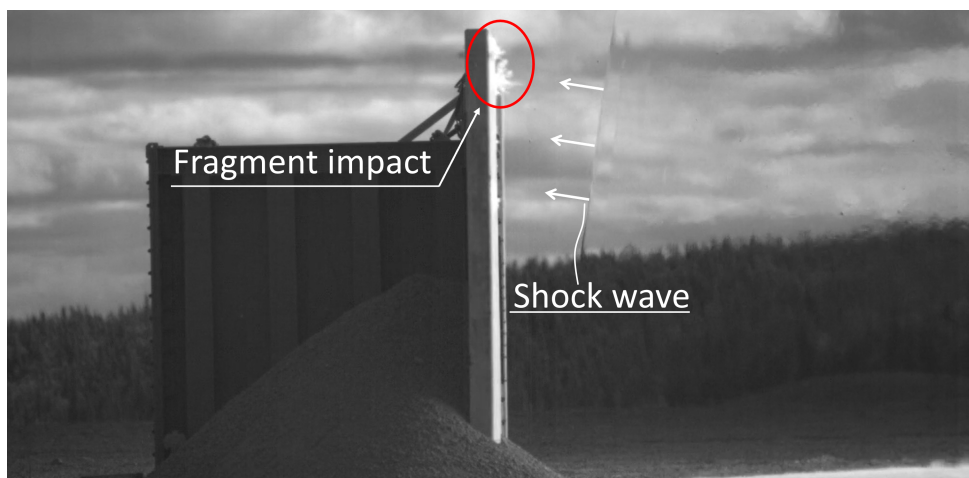


Figure 1.2: Detonation of a cased explosive, illustrating fragment impact before the arrival of the shock wave. The propagation of the shock wave is indicated with the white arrows, and the fragment impact with a red circle. Courtesy of The Norwegian Defence Estate Agency (Forsvarsbygg).

assuming the fragments to strike before the arrival of the blast wave, the loading scenario may be decomposed into two sequential loading events. With this assumption, the combined loading effect can be studied by evaluating the dynamic response of structures with pre-cut defects, representing the reduced structural integrity from the fragment impact [13–17]. Such studies avoid all uncertainties related to the fragment impact itself, and impose well defined geometries to be studied under the exposure to blast loads. It has

been shown that the size, shape, number, and distribution of the pre-cut defects strongly affect the fracture resistance during blast loading. However, the loading conditions from combined fragment impact and blast loading consist of three main contributors [1, 2]:

1. The pressure history from the blast wave, activating a global response of the structure.
2. The momentum transferred from the fragments, activating a global response of the structure.
3. Local damage to the structure in the vicinity of each fragment impact, reducing the global load carrying capacity of the structure.

It is emphasized that the studies on target plates with pre-cut defects represent idealized geometries with no surrounding material damage or plastic deformations, as one would expect from a real fragment impact. The transferred impulse from the fragments is also neglected, and the simplified approach could lead to non-conservative approximations of the combined loading effect. However, there are cases where the fragment impulse may be neglected, based on the ratio between the blast and the fragment impulse [1, 5]. In cases where only a few fragments impact the structure, their impulse contribution typically becomes negligible, and only the local damage created by the fragments needs to be considered.

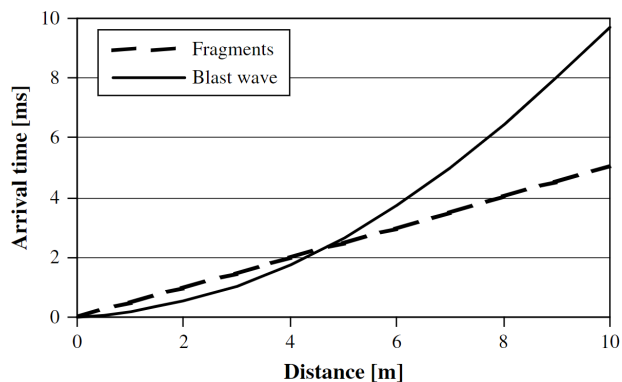


Figure 1.3: Time of arrival for the blast wave and fragments plotted as functions of the stand-off distance for a 250 kg GP-bomb, taken from [2].

For thin-walled metallic structures, blast loading and high-velocity fragment impact result in two distinctly different deformation responses. The pressure history from a blast load may last for several milliseconds [18], acting over a large area, resulting in a global

deformation response of the structure. On the contrary, a high velocity fragment impact event generally has a much shorter duration, and activates mostly local deformations in the impact zone. Consequently, this leads to large local strains and high strain rates under adiabatic conditions in the case of fragment impact, whereas a blast load gives more moderate strains and strain rates. The different nature of a high velocity fragment impact and a blast load may result in different requirements of the desired material properties for a protective structure. For metallic components, both ballistic impact and blast loading evaluated separately have been described successfully using an elastic-thermoviscoplastic constitutive relation and a ductile fracture criterion [19, 20].

The expected failure mechanisms during a high velocity fragment impact is very similar to that of a ballistic impact event. Børvik et al. [21] showed that the ballistic perforation resistance of steel plates increases almost linearly with the yield stress of the target material. In a recent study on blast-loaded aluminium plates, Granum et al. [14] showed that both material strength, work hardening, and ductility strongly affected the blast resistance. From a protective point of view, a common understanding for metallic components is that higher strength leads to better protection. High strength is generally accompanied by low ductility, and the trade-off between strength and ductility has been a long-standing dilemma in materials science [22]. Thus, it is not given that higher strength leads to increased protection against combined fragment impact and blast loading.

To fully understand the various effects of combined fragment impact and blast loading, experimental studies are ideal, as they represent the actual physics of the problem. Furthermore, theoretical and numerical methods must be validated against experimental data to ensure that they provide reliable predictions. Testing on full-scale prototype structures is normally considered too expensive, time-consuming, and infeasible. Hence, controlled small-scale experiments on plated structures have significant potential to improve our fundamental understanding of the combined effect of fragment impact and blast loading.

Detonating cased explosives is probably the most obvious way to produce a loading scenario consisting of high-velocity fragments and a blast wave. The shape and distribution of the fragments are dependent upon the fracture process of the casing. Moreover, the resulting pressure history of the blast wave is reduced to create and accelerate the fragments [23]. Because of the potentially dense cloud of flying fragments, it is also challenging to position pressure sensors and cameras close to the blast-loaded structure without destroying the measuring equipment. In other words, detonation of cased explosives can often result in non-repeatable experiments that are difficult to monitor.

Researchers and practitioners have therefore tried to establish controlled, robust and reliable experimental setups to study the combined effects of fragment impact and blast loading. Cai et al. [24] detonated cylindrical charges with pre-fabricated square fragments attached to the bottom face of the explosive. A similar approach was explored by Del Linz et al. [9], where several ball bearings were applied instead of pre-fabricated square fragments. Using high-speed cameras, the ball bearing velocities were measured right before impact, and the location of each impact was determined by visual inspection after the combined loading event. Langdon et al. [25] developed a novel experimental technique where one single ball bearing was placed at the bottom centre of a cylindrical explosive charge. The impulse from the ball bearing and the blast wave was successfully decomposed into two separate contributions from the experiments. A similar setup was established by Atoui et al. [26], where a solid explosive with an embedded steel sphere was detonated at the entrance of an explosive driven shock tube. The objective of the setup was to control the time interval between the arrival of the steel sphere and the shock wave at the blast-loaded target. The experimental setup succeeded in creating repeatable loading conditions, where the spatiotemporal evolution of both the shock and the sphere were recorded using an optical measurement technique. A recent study by Li et al. [12] suggested an experimental technique to replicate the scenario of combined blast and impact loading without the use of actual blast experiments. A composite projectile consisting of an aluminium foam cylinder with a hollow mid-section filled with a blunt steel projectile was fired against thin steel plates using a gas gun facility. The impact of the outer aluminium foam resulted in a uniformly distributed pressure across the thin steel plate, while the blunt projectile represented the impact from one single fragment. The difference in the arrival times for the projectile and the aluminium foam was adjusted by changing the depth of the hollow mid-section. The experimental results suggested that the composite projectile was able to generate a global deformation response (similar to what is expected from a blast wave) and a projectile perforation.

The simplification of evaluating the fragment impact using one single object motivates further development towards more controlled and repeatable experimental studies. By further assuming the global impulse transfer from the fragment impact to be negligible compared to the impulse of the blast pressure, the two loading events could be evaluated separately. This enables more detailed studies on the effect of the material damage surrounding a fragment impact hole on the blast resistance.

From a numerical point of view, establishing computationally efficient and accurate models describing both a fragment impact and a blast load are generally a challenging task. As a fragment impact represents a localized phenomenon with large plastic strains and

strain rates, a fine discretization is required for an accurate description of the perforation event [27, 28]. For the perforation of thin-walled structures with high-velocity fragments, the full loading event has a short duration, which gives a reasonable CPU time, even for a fine discretization. The blast load needs to be evaluated over a much larger time-span due to a slower global dynamic response. Combining a sufficiently fine discretization for a fragment impact event with the required run time for a blast load could lead to excessive CPU costs, and a trade-off between accuracy and efficiency must be considered.

Another challenge in blast-loaded and flexible structures is to obtain accurate measurements of the actual pressure load acting on the deformable structure [29]. The pressure history typically depends upon the location, size and type of the explosive material, as well as geometrical surroundings. Additionally, the deformation history of the blast-loaded structure has also been shown to affect the loading [30, 31]. Perforations may also serve as venting holes, affecting the pressure build-up of the blast-loaded structure [17, 32]. With respect to the geometrical surroundings, it has been shown both numerically and experimentally that internal blast loads impose amplified pressure histories [32–34] and significantly increased damage potentials compared to free field detonations [35]. To capture fluid-structure interaction (FSI) effects from a potential confinement or by the structural deformation itself, more advanced modelling and simulations are required. Hence, the need for experimental validation becomes even more important for increased numerical complexity [36]. In turn, validated numerical models can be a helpful tool for improving existing experimental setups and to identify "worst-case" scenarios. This motivates predictable and well-defined experimental and numerical studies on the combined fragment impact and blast loading in various blast environments.

2 Objectives and scope

2.1 Objectives

The main objective of this PhD project was to gain new knowledge and a better understanding of combined fragment impact and blast loading of thin steel plates. Special emphasis will be placed on designing controlled and reliable experiments to study such loading events and to validate state-of-the-art numerical methods. Validated numerical models are helpful for both evaluating and improving the experimental setups, as well as gaining a better understanding of the complex loading events.

The overall research objectives are:

- Conduct a critical and thorough review of the literature in testing, behaviour, modelling and simulation of combined fragment impact and blast loading events.
- Generate an experimental dataset covering combined fragment impact and blast loading through controlled and repeatable tests in laboratory environments. The fragment impacts will be represented by traditional small-arms projectiles and by manufacturing pre-formed defects in thin steel plates prior to the blast loading.
- Use the experimental dataset as basis of comparison to evaluate the predictive capabilities of the computational methods typically used in blast-resistant design.
- Study the influence of material behaviour (strength, work hardening and ductility) in loading scenarios covering fragment impact prior to the blast loading. Three different materials were considered, i.e., two dual-phase steels (Docol 600DL and Docol 1000DP) and one martensitic steel (Docol 1400M).
- Perform experimental and numerical investigations on the effect of fragment impact prior to blast loading during more complex blast loading conditions than those generated in a shock tube facility. This was obtained by exposing the target plates to blast loading from explosive charges of Composition C-4 inside a steel tube. The target plates were clamped to one of the tube flanges, whereas the other end was kept open in an attempt to obtain partially confined loading conditions.

2.2 Scope

Due to the wide range of topics related to the testing, behaviour, modelling and simulation of plated structures subjected to combined fragment impact and blast loading, it was necessary to impose some limitations on the proposed work:

- The test setups were limited to thin steel plates in controlled and repeatable laboratory environments. The majority of the experiments were performed at SIMLab, Department of Structural Engineering, NTNU. All ballistic tests were conducted in the SIMLab Gas Gun Facility (SGGF), while the blast loading was generated using the SIMLab Shock Tube Facility (SSTF). In addition, some blast tests were conducted using live explosives in an indoor testing facility owned by the Research and Development Section of the Norwegian Defence Estate Agency (NDEA).
- The material modelling of the steel plates was limited to an isotropic and elastic-thermoviscoplastic behavior with an uncoupled, ductile fracture model. The material parameters governing the quasi-static behavior of the steel materials were determined from material tests. The dynamic behaviour of the materials was determined from previous works available in the open literature.
- The numerical framework for the blast simulations mainly consists of two different models. First, a model describing the SSTF experiments, and second, a model including the detonation of high explosives. The modelling of the shock tube experiments was defined through purely Lagrangian simulations where the blast loading was applied as pressure histories obtained from previous experiments. The detonation of high explosives was represented as an Arbitrary Eulerian-Lagrangian (ALE) model, with a multi-material description of the fluid domain. All material parameters for the high explosive and air were taken from validated models in the open literature.
- All numerical techniques were limited to those available in the commercial finite element software. Simplifications were introduced when necessary to ensure computational efficiency.

3 Research methods

A schematic overview of the research methods used in this thesis is given in Figure 3.1. The methodology was based on the research infrastructure already available at SIMLab, Department of Structural Engineering, NTNU, and an indoor testing facility operated by the Norwegian Defence Estate Agency (NDEA). The objectives presented in Section 2.1 were studied by the following steps:

1. An extensive dataset of experiments was established by performing blast tests in the SSTF on target plates containing pre-cut defects of different idealized geometries. In addition, the effect of changes in material strength, work hardening and ductility was investigated by conducting quasi-static material tests for all tested plate geometries.
2. More realistic perforations were introduced in the steel plates by firing small-arms projectiles in SIMLab's ballistic range prior to the blast loading in the shock tube. The effect of more realistic perforations was evaluated by comparing the response of target plates containing an initial ballistic impact hole to target plates with a pre-cut circular hole. This was done in an attempt to isolate the effect of material damage around the ballistic impact holes, compared to pre-cut holes with an idealized, circular geometry.
3. The influence of a more complex loading environment was studied by exposing the target plates to blast loading from an explosive charge of Composition C-4 inside a steel tube. The target plates were clamped to one of the tube flanges, whereas the other end was kept open. The effect of the loading environment was then evaluated on the target plates with initial ballistic impact holes and pre-cut circular holes.
4. All blast tests were monitored using several pressure sensors synchronized with two high-speed cameras in a stereovision setup. Three-dimensional digital image correlation (3D-DIC) was used to determine the dynamic response of the target plates.
5. All numerical models and simulations were validated against the experimental observations, focusing on both the predictive capabilities and the limitations of the methods under consideration.

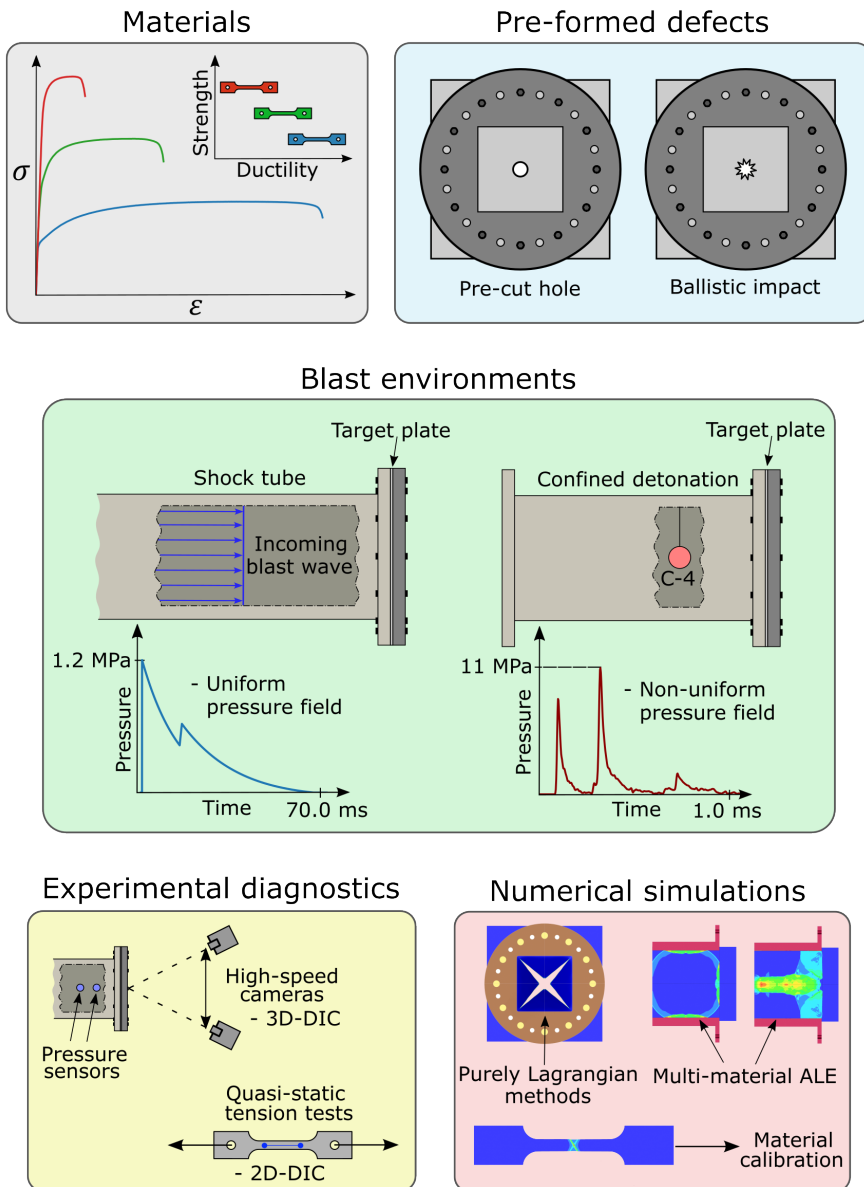


Figure 3.1: An overview of the research methods and work done in this PhD thesis.

4 Summary

This thesis is based on a collection of five papers, i.e., three journal articles and two conference papers. One journal article is already published in an international peer-reviewed journal, while the two others are prepared and submitted for possible journal publication. Two conference papers were published in international conference proceedings. A brief summary of each article is given in this section.

4.1 Part 1

- [1] B. S. Elveli, M. B. Iddberg, T. Børvik and V. Aune (2022). *On the strength-ductility trade-off in thin blast-loaded steel plates with and without initial defects - An experimental study*. Thin-Walled Structures 171, 108787.

Increased material strength is commonly associated with better protection in blast-resistant design. However, higher material strength comes at the cost of reduced ductility, and it is still not clear how this trade-off affects the load carrying capacity of blast-loaded structures. This work presents an experimental investigation of the strength-ductility trade-off on the dynamic response of thin steel plates subjected to blast-like loading conditions. Two different plate materials were applied for this purpose; one dual-phase, medium-strength, high-hardening steel, and one martensitic, high-strength, low-hardening steel. Seven plate geometries with various pre-formed defects were tested for both materials, triggering distinctly different deformation and fracture modes in the plates. In total, six different blast intensities were applied, and all tests were recorded using two high-speed cameras synchronized with pressure measurements. 3D-DIC measurements were used to track the mid-point displacement and deformation profile of the target plates until fracture.

For plates without defects, the high-strength, low-hardening steel resulted in the smallest deflections for a given load. However, for plates with pre-formed defects, the medium-strength, high-hardening steel showed a superior resistance to fracture. The geometry of the pre-formed defects was found to significantly influence the global deformation, the resistance against crack propagation, and the fracture mode.

4.2 Part 2

- [2] B. S. Elveli, T. Børvik and V. Aune (2021). *Influence of material properties on the performance of blast-loaded steel plates with pre-cut defects*. In: Proceedings of DYMAT 2021 - 13th International Conference on the Mechanical and Physical Behaviour of Materials under Dynamic Loading, 02028. September 20-24, Madrid, Spain

Experimental and numerical investigations are carried out to determine how thin steel plates with pre-cut defects behave under blast loading. The defects considered in this study are represented by four square holes, symmetrically distributed around the centre of the target plates. The target plates were manufactured from two types of steel, i.e., a dual-phase medium strength steel and a high-strength martensitic steel. A shock tube facility was used to expose the plates to blast-like loading conditions.

The experiments showed that both the blast resistance and the corresponding fracture mode changed with material properties. Numerical simulations were performed using the finite element code LS-DYNA, where the numerical results were found to be in good agreement with the experimental data in predicting the ductile fracture during the blast-structure interaction. The numerical simulations confirmed that significant work hardening will distribute the plasticity throughout the plate material during deformation, while limited work hardening tends to localize the plasticity that results in earlier fracture.

4.3 Part 3

- [3] B. S. Elveli, T. Børvik and V. Aune (2019). *Blast-load response of thin steel plates after ballistic impact from small-arms projectiles*. In: proceedings of Light-Weight Armour Group for Defence and Security (2019), 166-175. October 8-9, Roubaix, France

This paper investigates the dynamic response of 0.8 mm thick steel plates exposed to a combination of ballistic impact and blast loading. Two different materials, i.e., a medium-strength (Docol 600DL) steel and a high-strength (Docol 1400M) steel, were studied, and special focus was placed on the influence of material strength, work hardening and ductility. Docol 600DL has a yield stress of 325 MPa and exhibits significant work hardening and ductility, while Docol 1400M has a much higher strength with a yield

stress of 1200 MPa, but less work hardening and ductility. The loading of the plates was applied in two stages. First, ballistic impact tests using a smoothbore 7.62 Mauser rifle and APM2 bullets were conducted to perforate the plates at selected points. Second, the impacted plates were tested against blast loading in a shock tube. Both tests were recorded using high-speed cameras. For the blast-loading event, the high-speed cameras were used together with 3D-DIC for a detailed representation of the dynamic response of the plates. In addition, numerical results obtained from Abaqus/Explicit were compared and discussed against the experimental findings. Special focus was given to the pre-damage caused by the bullet impact and its effect on the cracking of the plate during the subsequent blast-loading tests.

It was found that the crack initiation and the direction of the crack propagation during blast loading were strongly dependent on the initial cracks and damage from the ballistic impact tests. Further, the plates with the highest strength and lowest ductility (Docol 1400M) showed less resistance against the subsequent blast load compared to the medium-strength (Docol 600DL) plates with higher ductility. The numerical simulations were found to be in good agreement with the experimental findings.

4.4 Part 4

- [4] B. S. Elveli, T. Berstad, T. Børvik and V. Aune. (2022). *Performance of thin blast-loaded steel plates after ballistic impact from small-arms projectiles*. Submitted for possible publication to International Journal of Impact Engineering.

It is known from real blast-load events that the combined effect of fragment impact and blast loading is more severe than the effect of the blast loading alone. The present study investigates this effect by comparing the blast response of thin steel plates pre-damaged by either ballistic impacts or idealized pre-cut circular holes under similar blast loading conditions. The ballistic impacts were performed with a rifle, firing 7.62 mm APM2 projectiles, and the subsequent blast loading was applied in a shock tube facility. During the blast tests, pressure measurements and two high-speed cameras were used to record the dynamic response of the target plates and allowed for a reliable experimental procedure. To investigate the strength-ductility trade-off dilemma of the material during extreme loading, three different steels with different levels of strength and ductility were used in the tests. Numerical simulations were conducted in an attempt to obtain more insight into the fracture characteristics of the plates.

For similar loading conditions and material, the target plates exposed to ballistic impact showed a reduced resistance to fracture during blast loading compared with target plates containing pre-formed circular holes. As for the effect of material strength and ductility, the global deformation decreased, while the localization of plasticity increased, with an increased material strength. The fracture resistance was also observed to decrease with increased material strength. The numerical models were able to capture the main trends observed in the physical tests, i.e., a decrease in fracture resistance with initial ballistic impact, and a reduction in fracture resistance with increased material strength. The numerically predicted crack paths also showed a strong dependence upon the initial cracks caused by the petals from the ballistic impacts.

4.5 Part 5

- [5] B. S. Elveli, O. Vestrum, K. O. Hauge, T. Berstad, T. Børvik and V. Aune. (2022). *Thin steel plates exposed to combined ballistic impact and partially confined airblast loading*. Submitted for possible publication to Engineering Failure Analysis.

Pre-formed defects created by high-velocity impact have the potential to reduce the structural integrity of lightweight, flexible structures. This study evaluates the effect of realistic pre-formed defects in thin steel plates exposed to partially confined detonations. Target plates containing pre-cut circular holes with a diameter of 8.0 mm are compared to target plates exposed to an initial ballistic impact from 7.62 mm APM2 projectiles. The target plates were exposed to blast loading generated from detonating C-4 inside a steel tube. The stand-off distance was fixed and set equal to the tube radius, where the rear end of the tube was kept open. All blast tests were recorded with several pressure sensors, synchronized with two high-speed cameras monitoring the dynamic response of the target plates. This allowed for a reliable experimental procedure, serving as a benchmark for different numerical methods. For similar loading conditions, the target plates containing initial ballistic impact showed a reduced fracture resistance during blast loading compared to the target plates with pre-cut circular holes. Two different numerical approaches were tested and compared, i.e., a purely Lagrangian particle-based approach and a fully coupled simulation using an ALE description of the blast domain. The ALE simulations were found to underestimate the structural response, while the particle-based approach overestimated the structural response.

4.6 Conference contributions

The work with this thesis has also resulted in the following presentations at international conferences:

- [6] B. S. Elveli, T. Børvik, V. Aune (2019). *Blast-load response of thin steel plates after ballistic impact from small-arms projectiles*. Presented at the Light-Weight Armour Group for Defence and Security, LWAG, October 8-9, Roubaix, France.
- [7] B. S. Elveli, T. Børvik, V. Aune (2021). *Influence of material properties on the performance of blast-loaded steel plates with pre-cut defects*. Presented at DYMAT 2021 - 13th International Conference on the Mechanical and Physical Behaviour of Materials under Dynamic Loading, Online attendance, September 20-24.
- [8] B. S. Elveli, T. Børvik, V. Aune (2022). *Blast resistance of pre-damaged steel plates*. Presented at ICILSM 2022 - 3rd International Conference on Impact Loading of Structures and Materials, June 13-17, Trondheim, Norway.

5 Conclusions

The effect of combined fragment impact and blast loading on thin steel plates has been investigated through an extensive experimental campaign and numerical simulations. The main findings and conclusions are summarized below.

- Experimental and computational frameworks are successfully established, enabling controlled and reliable studies on combined fragment impact and blast loading on plated structures. These frameworks have been used to perform both experimental and numerical studies on thin steel plates, where the experimental data has served as a basis for evaluation of the numerical simulations. The experiments and simulations provide valuable insight into the behaviour, modelling, and simulation of plated structures exposed to combined loading effects. Parameters influencing the dynamic response of the plates have been investigated and identified.
- As expected, pre-cut square holes and slits with idealized geometries resulted in larger global deformations and significantly reduced fracture resistance during blast loading compared to target plates without defects.
- The target plates with ballistic impact holes consistently experienced fracture at lower blast intensities than the plates with pre-cut circular holes. The failure modes were also affected by the material damage in the vicinity of the ballistic holes, where the petalling cracks initiated the crack propagation during blast loading. When fracture did not occur, the global deformations of the target plates with pre-cut circular holes and ballistic impact holes were similar to those without pre-formed defects.
- In the case of pre-formed defects, the blast resistance decreased with increasing material strength. The plate material with the lowest yield strength showed the highest level of work hardening, the lowest hardening rate and the largest engineering and true plastic fracture strains. As work hardening distributes plastic deformations over a larger area, this reduces localization of plasticity leading to an increased engineering failure strain. However, this work does not contain sufficient evidence to conclude whether it is the work hardening or the true plastic fracture strain of the material that is the most prominent factor for the fracture resistance.

- The partially confined detonations succeeded in creating a more complex loading environment. Compared to shock tube tests, the overall trend was that these explosive detonations provided an increase in peak pressure by a factor of approximately 10 and a reduction in the duration of the loading event by a factor of 70. The partially confined detonations also resulted in highly non-uniform pressure distributions across the blast-exposed area of the target plates.
- Despite the significant changes in the blast loading environment, the trend in global deformation and fracture resistance were the same as when evaluating the target plates with idealized pre-cut circular holes, ballistic impact holes, and plates without defects. That is, the change in loading environment did not change the overall conclusions from the shock tube tests in terms of plate response. Thus, the target plates with ballistic impact holes failed at lower blast intensities than the plates with idealized pre-cut circular holes. Moreover, the petalling cracks initiated the crack propagation during blast loading.
- For all simulations of the shock tube tests, the predictions generally coincides well with the experimental findings by the use of purely Lagrangian analyses. Provided that fracture did not occur, it was observed a slight increase in magnitude of permanent deformation (approximately 10%) in the simulations compared to the experimental observations. This was expected because the simulations neglect fluid-structure interaction (FSI) effects, and the applied pressure histories are obtained in separate tests on rigid target plates.
- As the complexity of the blast environment was increased from shock tube tests to performing partially confined detonations of C-4, the purely Lagrangian analyses were replaced by arbitrary Lagrangian-Eulerian (ALE) simulations and a Lagrangian particle-based approach. This resulted in larger deviations from the experimental findings. The structural response during blast loading was underestimated by approximately 10% with the ALE simulations, and overestimated by approximately 10% with the particle simulations.
- The numerical simulations did not provide accurate predictions of the fracture mode caused by the ballistic impact using the Cockcroft-Latham (CL) failure criterion in combination with a temperature criterion for coarse mesh sizes. To capture the experimentally observed petalling cracks during ballistic impact, a strain-based failure criterion was included in addition to the CL criterion to erode elements at low triaxialities.

- The findings in this work confirm the trade-off between computational (CPU) time and accuracy in the numerical modelling and simulation of combined ballistic impact and blast loading. That is, simulations of ballistic impact require a very fine discretization of the target plate to obtain reliable predictions, while blast simulations need to use a much coarser mesh to run within a reasonable computational time. This is challenging when modelling the combined effect of fragment impact and blast loading on plated structures, especially if a realistic fracture mode from the ballistic impact and a feasible CPU cost during the blast loading phase of the simulation are important.
- Hence, the extensive experimental dataset presented herein enables and motivates the validation and development of computational methods on the combined effects of fragment impact and blast loading.

6 Suggested further work

Based on the work and findings presented in this thesis, the following is suggested as further work:

- Conduct more detailed numerical simulations of the experiments in Part 1 of this thesis (see Ref. [16]). Special emphasis should be placed on the influence of FSI effects on the failure of the plates with pre-formed holes and pre-formed slits.
- Extend the experimental study to also include high-velocity impact from more realistic fragments. The small-arms projectiles used in this thesis represent an ideal geometry for perforation and more irregularly shaped fragments could result in significantly different crack patterns around the perforation holes. More complex crack patterns may lead to an increased loss of structural integrity.
- Thicker target plates will tend to avoid the numerical discretization issues encountered through the work in this thesis. For instance, by changing to aluminium plates with slightly larger thickness, the deformation mode and magnitude may still be comparable to the thinner steel plates. This may also prove beneficial to the numerical work in Part 5, where an increased thickness of the target plates could reduce the leakage issues in the ALE methods.
- Use numerical simulations to optimize the position of the pressure sensors for experimental testing of confined detonations.
- Extend the numerical framework to explore recently implemented finite volume solvers in the description of detonating high explosives. Such solvers are now available in LS-DYNA through the Dual CESE module.
- Define studies to identify the effect of the saturated impulse on the dynamic response of the blast loaded plates. The deformation response in blast loaded thin metallic plates tends to depend upon a saturated portion of the impulse from the blast load. This effect was not considered in detail in this thesis, but may be explored in an attempt to reduce the CPU cost during the blast loading phase.

- Other constitutive relations and failure criteria should be considered, in an attempt to better predict ductile fracture at low triaxialities during the ballistic impact.
- This work also motivates studies on the performance of damage- or plasticity-based adaptive mesh refinement (AMR) in an attempt to overcome the trade-off between computational (CPU) time and accuracy in the numerical modelling and simulation of combined ballistic impact and blast loading.
- Use anisotropic metals or even more advanced materials to study the influence of heterogeneity in material parameters on the blast resistance of plated structures subjected to combined fragment impact and blast loading.
- Further development of experimental techniques for more detailed studies on the effect of combined fragment impact and blast loading. This may be achieved using new experimental facilities allowing for the fragment and blast wave to impact simultaneously; dynamic fragmentation of steel casing during a confined explosion and the subsequent response of steel plates during such loading scenarios; developing new experimental techniques to obtain more information from optical measurements (e.g., flow visualization or reconstruction of pressure fields based on 3D-DIC measurements).

References

- [1] Grisaro, H. Y. and Dancygier, A. N. “Characteristics of combined blast and fragments loading”. *International Journal of Impact Engineering* 116 (2018), pp. 51–64.
- [2] Nystrøm, U. and Gylltoft, K. “Numerical studies of the combined effects of blast and fragment loading”. *International Journal of Impact Engineering* 36 (2009), pp. 995–1005.
- [3] Marchand, K. A., Vargas, M. M., and Nixon, J. D. *The Synergistic Effects of Combined Blast and Fragment Loadings*. Tech. rep. San Antonio Texas, 1992.
- [4] Hyde, D. W., Station, U. A. E. W. E., and Engineers, U. S. A. C. of. *User’s Guide for Microcomputer Programs ConWep and FunPro, Applications of TM 5-855-1, ”Fundamentals of Protective Design for Conventional Weapons”*. Instruction report. U.S. Army Engineer Waterways Experiment Station, 1988.
- [5] Grisaro, H. Y. and Dancygier, A. N. “Representation of damage caused by fragmentation impact in design and analysis of reinforced concrete barriers”. *Engineering Structures* 197 (2019), p. 109387. ISSN: 0141-0296.
- [6] Wilkinson, W., Cormie, D., and Arkinstall, M. “Calculation of blast loads for design against terrorism.” *Proceedings of the Institution of Civil Engineers - Engineering and Computational Mechanics* 166 (2013), pp. 132–139.
- [7] Leppänen, J. “Experiments and numerical analyses of blast and fragment impacts on concrete”. *International Journal of Impact Engineering* 31.7 (2005), pp. 843–860.
- [8] Grisaro, H. Y. and Dancygier, A. N. “Dynamic response of RC elements subjected to combined loading of blast and fragments.” *Journal of Structural Engineering* 147 (2020), p. 04020315.
- [9] Linz, P. D., Fan, S. C., and Lee, C. K. “Modeling of Combined Impact and Blast Loading on Reinforced Concrete Slabs”. *Latin American Journal of Solids and Structures* 13 (Dec. 2016), pp. 2266–2282.
- [10] Linz, P. D., Fung, T. C., Lee, C. K., and Riedel, W. “Response mechanisms of reinforced concrete panels to the combined effect of close-in blast and fragments: An integrated experimental and numerical analysis”. *International Journal of Protective Structures* 12.1 (2021), pp. 49–72.

- [11] Goswami, A., Ganesh, T., and Adhikary, S. D. “RC structures subjected to combined blast and fragment impact loading: A state-of-the-art review on the present and the future outlook”. *International Journal of Impact Engineering* 170 (2022), p. 104355. ISSN: 0734-743X.
- [12] Li, L., Zhang, Q.-C., Zhang, R., Wang, X., Zhao, Z.-Y., He, S.-Y., Han, B., and Lu, T. J. “A laboratory experimental technique for simulating combined blast and impact loading.” *International Journal of Impact Engineering* 134 (2019), p. 103382.
- [13] Li, W., Wang, P., Feng, G., Lu, Y., Yue, J., and Li, H. “The deformation and failure mechanism of cylindrical shell and square plate with pre-formed holes under blast loading.” *Defence Technology* 17.4 (2021), pp. 1143–1159. ISSN: 2214-9147.
- [14] Granum, H., Aune, V., Børvik, T., and Hopperstad, O. S. “Effect of heat-treatment on the structural response of blast-loaded aluminium plates with pre-cut slits”. *International Journal of Impact Engineering* 132 (2019), p. 103306.
- [15] Li, Y., Wu, W., Zhu, H., Wua, Z., and Dub, Z. “The influence of different pre-formed holes on the dynamic response of square plates under air-blast loading”. *Engineering Failure Analysis* 78 (2017), pp. 122–133.
- [16] Elveli, B. S., Iddberg, M. B., Børvik, T., and Aune, V. “On the strength–ductility trade-off in thin blast-loaded steel plates with and without initial defects — An experimental study”. *Thin-Walled Structures* 171 (2022), p. 108787. ISSN: 0263-8231.
- [17] Zhang, C., Tan, P., and Yuan, Y. “Confined blast loading of steel plates with and without pre-formed holes”. *International Journal of Impact Engineering* 163 (2022), p. 104183.
- [18] Kingery, C. and Bulmash, G. “Airblast parameters from TNT spherical air burst and hemispherical surface burst.” (1984).
- [19] Børvik, T., Hopperstad, O. S., Berstad, T., and Langseth, M. “A computational model of viscoplasticity and ductile damage for impact and penetration”. *The European Journal of Mechanics A/Solids* 20 (2001), pp. 685–712.
- [20] Aune, V., Valsamos, G., Casadei, F., Langseth, M., and Børvik, T. “On the dynamic response of blast-loaded steel plates with and without pre-formed holes”. *International Journal of Impact Engineering* 108 (2017), pp. 27–46.
- [21] Børvik, T., Dey, S., and Clausen, A. H. “Perforation resistance of five different high-strength steel plates subjected to small-arms projectiles”. *International Journal of Impact Engineering* 36 (2009), pp. 948–964.

- [22] Wei, Y., Li, Y., Zhu, L., Liu, Y., Lei, X., Wang, G., Wu, Y., Mi, Z., Liu, J., Wang, H., and Gao, H. “Evading the strength–ductility trade-off dilemma in steel through gradient hierarchical nanotwins”. *Nature communications* 5 (Apr. 2014), p. 3580.
- [23] Hutchinson, M. D. “The escape of blast from fragmenting munitions casings”. *International Journal of Impact Engineering* 36.2 (2009), pp. 185–192. ISSN: 0734-743X.
- [24] Cai, S., Liu, J., Zhang, P., Li, C., Cheng, Y., and Chen, C. “Experimental study on failure mechanisms of sandwich panels with multi-layered aluminum foam/UHMWPE laminate core under combined blast and fragments loading”. *Thin-Walled Structures* 159 (2021), p. 107227. ISSN: 0263-8231.
- [25] Qi, R., Langdon, G. S., Cloete, T. J., and Yuen, C. K. “Behaviour of a blast-driven ball bearing embedded in rear detonated cylindrical explosive”. *International Journal of Impact Engineering* 146 (2020), p. 103698.
- [26] Atoui, O., Kechagiadakis, G., Moumen, A., Maazoun, A., Belkassem, B., Pyl, L., and Lecomte, D. “An Explosive Driven Shock Tube-Based Laboratory Scale Test for Combined Blast and Fragment Impact Loading”. *Applied Sciences* 12.14 (2022). ISSN: 2076-3417.
- [27] Børvik, T., Hopperstad, O. S., Berstad, T., and Langseth, M. “Numerical simulation of plugging failure in ballistic penetration”. *International Journal of Solids and Structures* 38 (2001), pp. 6241–6264.
- [28] Dey, S., Børvik, T., Hopperstad, O. S., Leinum, J. R., and Langseth, M. “The effect of target strength on the perforation of steel plates using three different projectile nose shapes”. *International Journal of Impact Engineering* 30 (2004), pp. 1005–1038.
- [29] Kaufmann, R., Olufsen, S., Fagerholt, E., and Aune, V. “Reconstruction of surface pressures on flat plates impacted by blast waves using the Virtual Fields Method”. *International Journal of Impact Engineering* 171 (2023), p. 104369.
- [30] Aune, V., Valsamos, G., Casadei, F., Langseth, M., and Børvik, T. “Fluid-structure interaction effects during the dynamic response of clamped thin steel plates exposed to blast loading”. *International Journal of Mechanical Sciences* 195 (2021), p. 106263. ISSN: 0020-7403.
- [31] Subramaniam, K. V., Nian, W., and Andreopoulos, Y. “Blast response simulation of an elastic structure: Evaluation of the fluid–structure interaction effect”. *International Journal of Impact Engineering* 36.7 (2009), pp. 965–974. ISSN: 0734-743X.

- [32] Langdon, G., Kriek, S., and Nurick, G. “Influence of venting on the response of scaled aircraft luggage containers subjected to internal blast loading”. *International Journal of Impact Engineering* 141 (2020), p. 103567. ISSN: 0734-743X.
- [33] Silvestrini, M., Genova, B., and Leon Trujillo, F. “Energy concentration factor. A simple concept for the prediction of blast propagation in partially confined geometries”. *Journal of Loss Prevention in the Process Industries* 22.4 (2009), pp. 449–454. ISSN: 0950-4230.
- [34] Yao, S., Zhang, D., Lu, Z., Lin, Y., and Lu, F. “Experimental and numerical investigation on the dynamic response of steel chamber under internal blast”. *Engineering Structures* 168 (2018), pp. 877–888. ISSN: 0141-0296.
- [35] Geretto, C., Yuen, S., and Nurick, G. “An experimental study of the effects of degrees of confinement on the response of square mild steel plates subjected to blast loading”. *International Journal of Impact Engineering* 79 (2015). Recent development of experimental techniques under impact loading- IUTAM Symposium, Xian, 2013, pp. 32–44. ISSN: 0734-743X.
- [36] Børvik, T., Hanssen, A., Langseth, M., and Olovsson, L. “Response of structures to planar blast loads – A finite element engineering approach”. *Computers & Structures* 87.9 (2009), pp. 507–520. ISSN: 0045-7949.

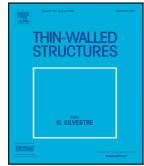
PART 1

Benjamin Stavnar Elveli, Mads Bakken Iddberg, Tore Børvik, Vegard Aune

On the strength–ductility trade-off in thin blast-loaded steel plates with and without initial defects — An experimental study

Thin-Walled Structures 171 (2022) 108787.

<https://doi.org/10.1016/j.tws.2021.108787>



Full length article

On the strength–ductility trade-off in thin blast-loaded steel plates with and without initial defects — An experimental study



Benjamin S. Elveli ^{a,b,*}, Mads B. Iddberg ^c, Tore Børvik ^{a,b}, Vegard Aune ^{a,b}

^a Structural Impact Laboratory (SIMLab), Department of Structural Engineering, NTNU – Norwegian University of Science and Technology, Trondheim, Norway

^b Centre for Advanced Structural Analysis (CASA), NTNU, Trondheim, Norway

^c SINTEF Manufacturing AS, Raufoss, Norway

ARTICLE INFO

Keywords:

Airblast loading
Perforated plates
Ductile fracture
Dual phase steel
Martensitic steel

ABSTRACT

An increase in material strength is commonly associated with better protection in blast-resistant design. However, higher material strength comes at the cost of reduced ductility, and it is still not clear how this trade-off affects the load carrying capacity of blast-loaded structures. This work presents an experimental investigation of the strength–ductility trade-off on the dynamic response of thin steel plates subjected to blast-like loading conditions. Two different plate materials were applied for this purpose; one dual-phase, medium-strength, high-hardening steel, and one martensitic, high-strength, low-hardening steel. Seven plate geometries with various pre-formed defects were tested for both materials, triggering distinctly different deformation and fracture modes in the plates. In total, six different blast intensities were applied, and all tests were recorded using two high-speed cameras synchronized with pressure measurements. 3D-DIC measurements were used to track the mid-point displacement and deformation profile of the target plates until fracture. For plates without defects, the high-strength, low-hardening steel resulted in the smallest deflections for a given load. However, for plates with pre-formed defects, the medium-strength, high-hardening steel showed a superior resistance to fracture. The geometry of the pre-formed defects was found to significantly influence the global deformation, the resistance against crack propagation, and the fracture mode.

1. Introduction

The protection of vital infrastructure against blast or impact loading is still an active field of research (see e.g., [1–5]). In an urban environment, industrial accidents and terrorist attacks both impose threats of explosions in the proximity of civil engineering structures. Such explosions may further result in a combined blast and impact loading, consisting of a blast wave accompanied by fragments [6,7]. Depending on the distance between the point of detonation and the structure, the fragments may impact before, simultaneously, or after the arrival of the blast wave [8]. If the structure is impacted by fragments prior to the blast loading, these fragments may introduce initial damage and perforations, reducing the structural integrity. It has been shown that the combination of these two loads is more critical than the effect of the blast or impact loading alone [9,10]. Despite these observations, such combined loading scenarios are not covered by design codes and few studies are available in the open literature.

Historically, the scope of blast-resistant design has been on massive military structures and government buildings [11]. Concrete structures have therefore been the preferred choice for blast protection,

where concrete slabs exposed to combined blast and fragment loading have been a subject of several studies over the last few decades (see e.g., [12–15]). Leppänen [12] studied concrete blocks exposed to the combination of blast and fragment loading both experimentally and numerically. Bearing balls were glued to explosive charges, and the fragment velocities were measured using an accelerometer and an impact sensor. Grisaro and Dancygier [13] conducted numerical investigations on the dynamic response of a one-way reinforced concrete element exposed to the combination of blast and fragment loading, where the numerical results were validated against experimental and analytical results. Motivated by the potential amplification of damage caused by the interaction between fragment impacts and blast waves, Linz et al. [14] first studied concrete slabs exposed to the combination of a cylindrical explosive charge and ball bearings as fragments before examining the effect of cased explosives on reinforced concrete components for protective structures [15]. It was found that the damage from the combined loading was more severe than for the two cases evaluated separately, which is in good agreement with the findings by Nyström and Gylloft [10].

* Corresponding author at: Structural Impact Laboratory (SIMLab), Department of Structural Engineering, NTNU – Norwegian University of Science and Technology, Trondheim, Norway.

E-mail address: benjamin.s.elveli@ntnu.no (B.S. Elveli).

<https://doi.org/10.1016/j.tws.2021.108787>

Received 13 July 2021; Received in revised form 2 November 2021; Accepted 2 December 2021

Available online 20 December 2021

0263-8231/© 2021 The Author(s). Published by Elsevier Ltd. This is an open access article under the CC BY license (<http://creativecommons.org/licenses/by/4.0/>).

In contrast, civilian structures are often lightweight and flexible, and the response of thin-walled metallic components are therefore of interest (see e.g., [16–18]). Assuming that the fragments strike before the arrival of the blast wave, Rakvåg et al. [16] investigated the effect of different pre-cut defects in thin square Docol 600DL steel plates subjected to a fast transient pressure loading. The defect shapes were squares, diamonds, slits, and circular holes. All plates had four equal defects symmetrically distributed around the centre, and it was found that the defect shape and area had a significant influence on the maximum deflection. It is however important to notice that the test setup used in Ref. [16] did not result in a blast wave impacting the target plates, but a rapid change in pressure on the two sides of the target plate.

Inspired by the work of Rakvåg et al. [16], the response of Q345 steel plates with different pre-cut holes exposed to a blast load caused by detonating a charge of TNT was studied by Li et al. [19]. The explosive charge was placed at a fixed stand-off distance, while varying the amount of TNT to control the blast intensity. The pre-formed defects were included to imitate the effect of fragment impact prior to the blast loading. Plates with square, circular, and diamond-shaped defects were tested. For the plates with square and circular defects, no fracture was observed for any of the applied blast intensities. On the contrary, all plates with the diamond-shaped defect fractured during testing, and it was concluded that the shape of the defect altered the capacity to fracture.

Aune et al. [20] studied the dynamic response of thin Docol 600DL steel plates subjected to blast loading. The study was conducted using a compressed gas-driven shock tube to generate a controlled and repeatable blast environment [21]. Thin steel plates with and without pre-formed defects were tested. Special focus was placed on the influence of the pre-formed holes on the dynamic response and on the fracture modes of the plates. The study indicated an increase in global displacement for plates with pre-formed holes compared to plates without pre-formed defects under similar loading conditions.

In protective design, a common understanding is that an increased material strength leads to better protection (see e.g., [22,23]). Børvik et al. [24] showed both experimentally and numerically that the ballistic perforation resistance increases almost linearly with the yield stress of the target material, while the dominant indicator for blast resistance of ductile plates is less pronounced in the literature. Both Langdon et al. [25] and McDonald et al. [26] suggested that the specific energy to tensile fracture could serve as an indicator for the fracture resistance, whereas McDonald et al. [26] further showed that high-strength steels could outperform more ductile steels under blast loading.

Increased material strength is typically accompanied by reduced ductility, and this strength–ductility trade-off has been a long-standing dilemma in materials science [27]. Geometrical defects like sharp notches and holes introduced by impacting fragments typically involve stress concentrations and large local plastic deformations upon loading. The presence of these local plastic deformations questions whether ductility could be critical for the protection against combined blast and impact loading. A recent study by Holmen et al. [28] on the perforation resistance of high-strength aluminium plates indicates that even though strength was observed to be the most important parameter for perforation resistance, work hardening and ductility became increasingly important in predicting the fragmentation of the target plate material. Granum et al. [29] carried out experiments and numerical simulations on the blast performance of 1.5 mm thick aluminium plates with four different pre-formed defects. Three different tempers were used to vary the material properties with respect to strength, work hardening, and ductility. It was found that both the fracture mode and the blast performance were sensitive to changes in the number, spatial distribution, and orientation of the pre-formed defects, as well as changes in material properties. These results indicated that the ductility and work hardening were more important for the blast resistance than the strength.

Steel is often preferred in protective structures due to its combination of high strength, high ductility and good formability, resulting in an effective load carrying capability at a relatively low cost compared to many other materials. The mechanical properties of steel result from a combination of chemical composition, heat treatment and manufacturing process. Generally, dual-phase steels are characterized by a microstructure consisting of hard martensitic islands, surrounded by a softer ferrite matrix. The soft ferrite matrix provides high ductility, while the hard martensite contributes to increased strength [30]. An increased proportion of martensite therefore results in a strength–ductility trade-off, leading to an increase in strength while decreasing the ductility of the material.

Motivated by the observed trade-off between material strength and ductility in recent studies [25,28,29], this study provides an unique experimental dataset giving further insight on the strength–ductility trade-off in thin, blast-exposed steel plates. A comprehensive experimental campaign enabled detailed studies on the influence of material strength and ductility on the performance of plates with different initial defects (shape, number and spatial distribution). Two different steel alloys being Docol 600DL and Docol 1400M were chosen to represent medium- and high-strength steels, respectively. The main objectives of this study are: (1) to provide new insight into the importance of the material strength and ductility on the blast performance of thin, plated structures with and without pre-formed defects; and (2) to establish a comprehensive experimental dataset allowing for validation and further development of computational methods in forthcoming studies.

2. Materials

2.1. Materials description

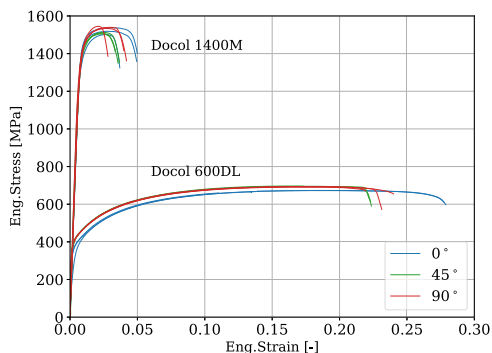
The materials investigated in this study were Docol 600DL and Docol 1400M steels, produced by the Swedish manufacturer SSAB [31]. Both alloys are cold-rolled and available in a thickness range from 0.5 mm to 2.1 mm. Docol 600DL is a dual-phase, medium-strength, high-hardening steel, while Docol 1400M is a martensitic, high-strength, low-hardening steel. These materials are mainly developed for use in the automotive industry. The pure martensitic Docol 1400M material has a yield strength roughly 5 times higher than the dual-phase Docol 600DL (see Table 2), whereas Docol 600DL has about 5 times larger elongation to fracture. The chemical composition and nominal material parameters for both steels are given in Tables 1 and 2, respectively.

2.2. Material testing

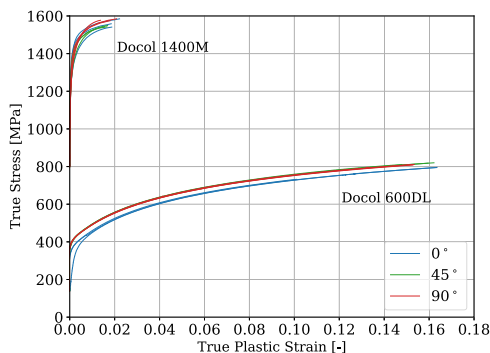
Quasi-static tension tests were performed to characterize the mechanical response of the materials at large deformations. For the Docol 600DL material, the test results from Aune et al. [20] were adopted. Quasi-static tension tests of the Docol 1400M material were carried out using an Instron 5982 testing machine at a constant deformation rate of 2.1 mm/min, using the same experimental setup as presented in Ref. [20]. A uniaxial test specimen with a gauge area of 70 mm × 12.5 mm was used (see e.g., Gruben et al. [32] for the specimen geometry), giving an initial strain rate in the material of $\dot{\epsilon}_0 = 5 \cdot 10^{-4} \text{ s}^{-1}$. To investigate the material anisotropy, tensile specimens were extracted at 0°, 45° and 90° relative to the rolling direction of the plates. A speckle pattern was applied to the surface of the tensile specimens using an airbrush, enabling two-dimensional (2D) digital image correlation (DIC) to obtain the displacement field on the surface of the specimens during the post-processing of the images [33]. Global strains were calculated from the displacement field using a virtual extensometer with an initial length of 60 mm. The force was measured by the load cell of the testing machine and synchronized with images of the specimen surface captured at a sampling rate of 4 Hz.

Table 1
Chemical composition of Docol 600DL and Docol 1400M (in wt.%). The data is taken from [31].

Material	C (max %)	Si (max %)	Mn (max %)	P (max %)	S (max %)	Al (min %)	Nb+Ti (max %)
Docol 600DL	0.10	0.40	1.50	0.010	0.002	0.040	–
Docol 1400M	0.20	0.40	1.60	0.020	0.010	0.015	0.10



(a)



(b)

Fig. 1. Stress–strain curves obtained from tension tests of the two materials: (a) engineering stress–strain curves and (b) true stress–plastic strain curve until diffuse necking. Source: The curves for Docol 600DL are taken from [20].

Table 2

Nominal material parameters for the two materials under consideration as given by SSAB [31]. Here, E is the elastic modulus, ν is the Poisson's ratio, ρ is the density, σ_y is the initial yield stress, σ_{uts} is the ultimate tensile strength, and ϵ_{fail} is the elongation to fracture.

Material	E [GPa]	ν [-]	ρ [kg/m ³]	σ_y [MPa]	σ_{uts} [MPa]	ϵ_{fail} [%]
Docol 600DL	210.0	0.33	7850	280–360	600–700	20
Docol 1400M	210.0	0.33	7850	1150–	1400–1600	3

Fig. 1(a) presents a comparison of the engineering stress–strain curves until fracture, while Fig. 1(b) provides the true stress–plastic strain curves for Docol 600DL and Docol 1400M up to diffuse necking. As expected, significant differences in both strength, work hardening and ductility are observed between the two steels. Docol 600DL yields at about 350 MPa, whereas Docol 1400M yields at roughly 1200 MPa. Furthermore, it is seen that Docol 600DL has approximately 5 times larger elongation to fracture than Docol 1400M when considering the engineering strains. Fig. 1(b) shows that the true stress for Docol 600DL is increased from around 350 MPa at initial yield to just above 800 MPa at the onset of diffuse necking. This corresponds to an increase of about 130% relative to the initial yield stress. Docol 1400M shows an increase in true stress less than 30% from initial yield to diffuse necking. From the true stress–plastic strain curves, it is evident that Docol 600DL undertakes a significantly larger amount of work hardening than Docol 1400M. All observed differences in behaviour for the two materials are in good agreement with the mechanical properties described in Section 2.1.

Fig. 1 reveals variations in both flow stress and elongation to fracture for both materials. The degree of deviation between tests appears to depend on the orientation of the tensile specimen relative to the rolling direction of the plate. Tests on specimens oriented 45° relative to the rolling direction showed the least variation both with respect to the stress level and elongation to fracture. The results from tests on specimens in the 0° and 90° orientations appear to experience larger variations. It should finally be noted that the observed variations in the tension tests for this batch of Docol 1400M were comparable to the variations found in tests on similar materials, see e.g., [20,32,34].

3. Experimental study

3.1. Experimental setup

The experiments were performed in the SIMLab Shock Tube Facility (SSTF) at NTNU. A detailed presentation of the SSTF and its performance in generating blast-like loading conditions is given by Aune et al. [21], and will therefore only be presented briefly in this section. The SSTF is designed to create pressure waves in air with similar characteristics as a real blast wave. The facility is equipped with two synchronized high-speed cameras (Phantom v2511) pointed at the target plate as well as pressure sensors located at different locations within the SSTF, allowing for detailed studies of the dynamic response of plated structures. The experimental setup used in this study is shown in Fig. 2.

The propagation of the blast wave is initiated at the driver side of the shock tube and impacts the target plate just inside the tank at the right end of the tube. In this study, all experiments were performed with a driver length of 0.77 m and compressed air was used to pressurize the driver section.

The target plates were mounted to the shock tube by using a clamping assembly. The dimensions of the clamping assembly are given in Fig. 3. All target plates had dimensions of 625 mm \times 625 mm \times 0.8 mm and a blast-exposed area of 300 mm \times 300 mm.

Both the incoming and reflected overpressure were sampled with a frequency of 500 kHz at Sensor 1, see Figs. 2 and 3. Sensor 1 is located 245 mm upstream of the target plates and serves as the best available estimate for the pressure acting on the surface of the target plates. Hence, all pressure histories presented in this study are measured at Sensor 1 and represent the overpressure relative to atmospheric conditions.

Two high-speed cameras were positioned in a stereoscopic setup and used to capture images at a sampling rate of 37 kHz. Prior to each test, the target plates were spray-painted with a black and white speckle pattern, allowing the displacement field to be obtained during post-processing of the image pairs by using the in-house 3D-DIC software eCorr [35]. A common time axis was used for the post-processing, where the time $t = 0$ was set to the time when the incoming pressure wave reached Sensor 1 (see Fig. 3).

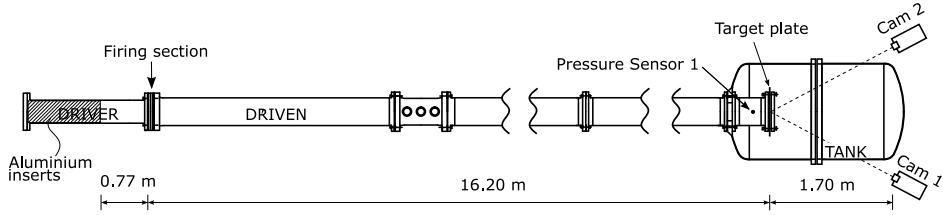


Fig. 2. Illustration of the SIMLab Shock Tube Facility (SSTF), where the pressure sensor used in this study (Sensor 1) is located 245 mm upstream the target plate.

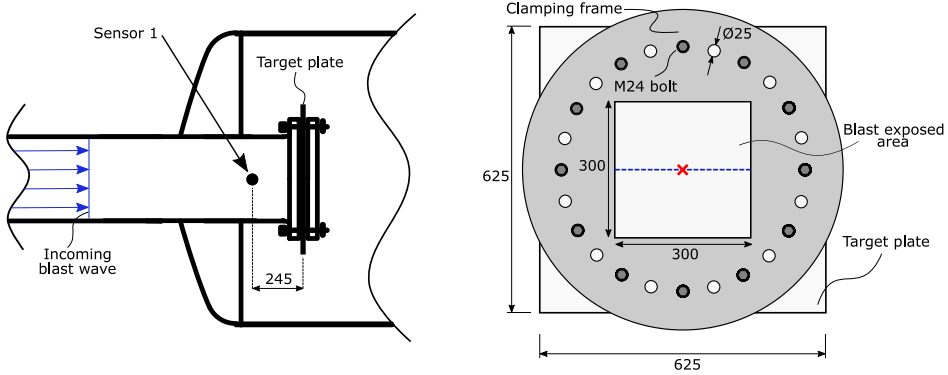


Fig. 3. Clamping assembly in the SSTF: The downstream end of the SSTF (left), where the clamping assembly and pressure sensor (Sensor 1) are located, and a detailed sketch of the clamping assembly including the target plate (right). The red cross at the centre of the blast-exposed surface indicates the sampling point for mid-point displacements, and the blue horizontal line shows the position for the sampling of deformation profiles. (For interpretation of the references to colour in this figure legend, the reader is referred to the web version of this article.)

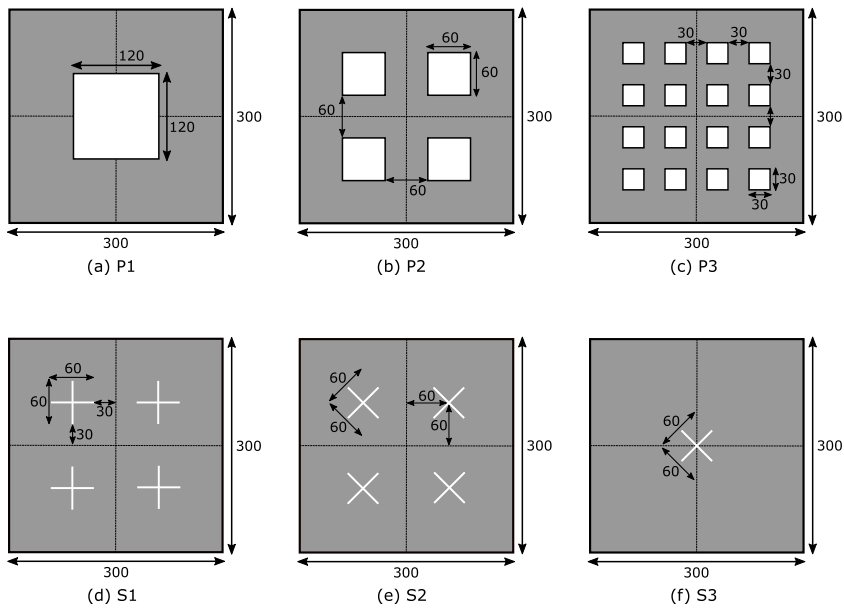


Fig. 4. Geometry of the target plates with pre-formed holes in (a)–(c), named P1, P2, and P3, respectively, and pre-formed slits in (d)–(f), named S1, S2, and S3, respectively.

Table 3
Experimental programme.

Firing pressure	FP	P1	P2	P3	S1	S2	S3
5 bar	D6_FP_05 D14_FP_05	D6_P1_05 D14_P1_05	D6_P2_05 D14_P2_05	-	D6_S1_05 D14_S1_05	-	-
10 bar	-	D6_P1_10 D14_P1_10	-	-	D6_S1_10 D14_S1_10	D6_S2_10 D14_S2_10	- D14_S3_10
15 bar	D6_FP_15 D14_FP_15	D6_P1_15 D14_P1_15	D6_P2_15 D14_P2_15	D6_P3_15 D14_P3_15	D6_S1_15 D14_S1_15	D6_S2_15 D14_S2_15	- D14_S3_15
25 bar	D6_FP_25 D14_FP_25	D6_P1_25	D6_P2_25 D14_P2_25	D6_P3_25 D14_P3_25	-	D6_S2_25 D14_S2_25	D6_S3_25 D14_S3_25
35 bar	D6_FP_35 D14_FP_35	-	D6_P2_35 D14_P2_35	D6_P3_35 D14_P3_35	-	-	D6_S3_35
60 bar	D6_FP_60 D14_FP_60	-	-	-	-	-	-

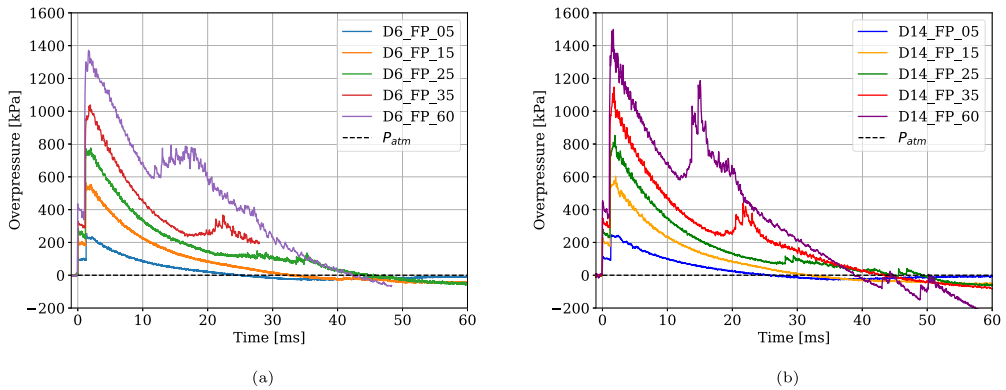


Fig. 5. Pressure histories for the tests on full plates (FP) without any defects: (a) the D6 material and (b) the D14 material.

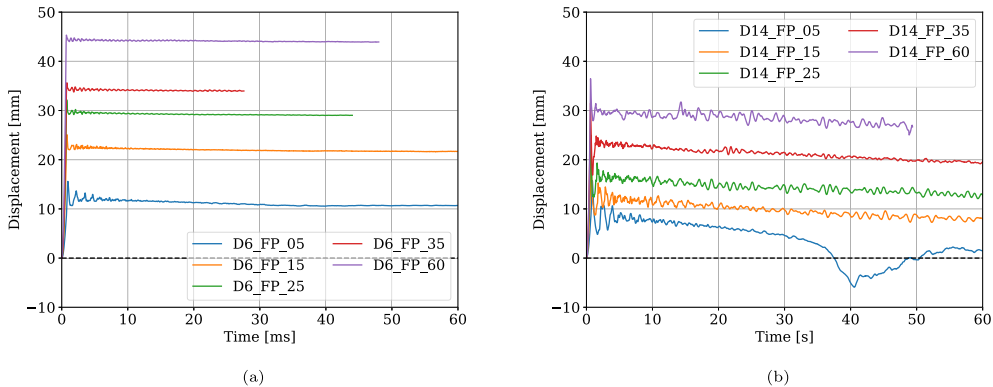


Fig. 6. Mid-point displacements versus time for the tests on full plates (FP) for both materials: (a) the D6 plates and (b) the D14 plates.

3.2. Experimental program

The aim of the experimental program was to assess the influence of material strength and ductility on the blast resistance of thin steel plates with various initial geometrical defects. Motivated by the ability

to trigger distinct fracture modes, the geometries used in the studies by Aune et al. [20] and Granum et al. [29] were adopted. In addition, two new plate geometries were used in this study. The geometries under consideration are presented in Fig. 4. While keeping the total

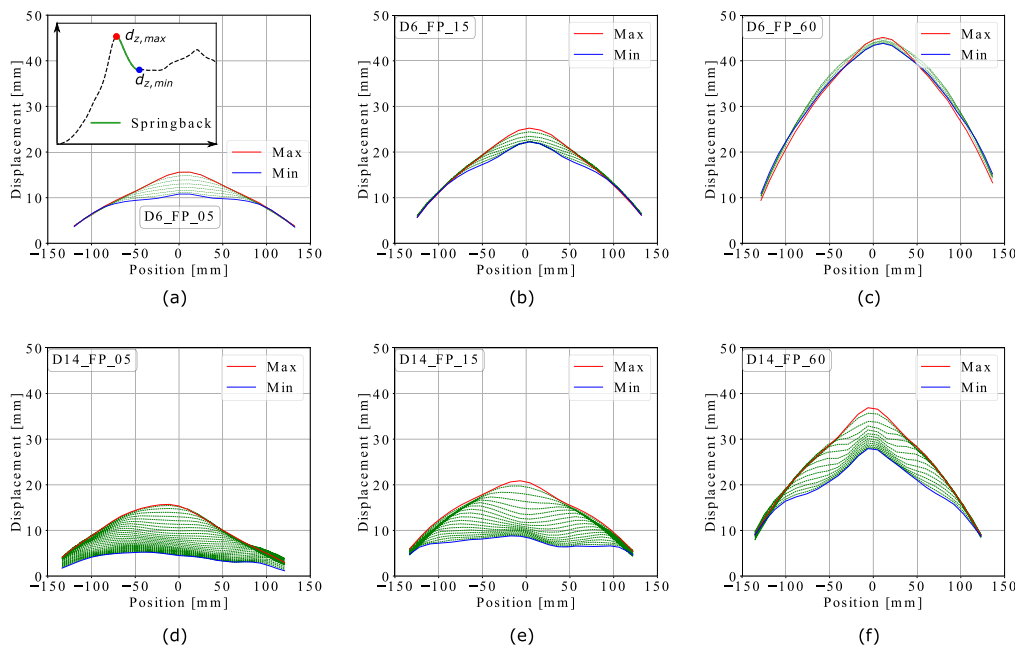


Fig. 7. Deformation profiles at maximum deflection ($d_{z,max}$) represented by red lines and at minimum deflection ($d_{z,min}$) indicated by blue lines: (a) D6_FP_05, (b) D6_FP_15, (c) D6_FP_60, (d) D14_FP_05, (e) D6_FP_15 and (f) D14_FP_60. The green lines show the development of the deformation profile from $d_{z,max}$ to $d_{z,min}$ at a constant sampling rate of $\Delta t = 0.027$ ms. The subplot in (a) indicates the elastic springback on a midpoint displacement curve. (For interpretation of the references to colour in this figure legend, the reader is referred to the web version of this article.)

hole area constant for all plate geometries, the two new pre-damaged configurations tested in this study had one single square perforation at the centre (P1 in Fig. 4a) and 16 square perforations (P3 in Fig. 4c). These perforations resulted in a 16% reduction of the blast-exposed area.

As ductility is assumed to influence the response of the target plate only in the presence of large plastic deformations, three distinctly different levels of deformations were investigated for each geometrical configuration. These responses were triggered using three distinct load levels, where the blast intensities were controlled by the firing pressures. The lowest blast intensity was intended to result in small plastic deformations, the intermediate pressures should result in large plastic deformations and possible crack initiation, and the highest pressure should result in large plastic deformations with considerable crack propagation and possible complete fracture. For both materials, all geometrical configurations were tested for the same blast intensity for a direct comparison with respect to the overall dynamic response and capacity in resisting the blast load.

The experimental programme is provided in Table 3. Each test is numbered DX_Y_Z, where D denotes deformable steel plate (D), X indicates either the medium-strength Docol 600DL (D6) or the high-strength Docol 1400M (D14). Y represents the plate geometry, i.e., full plate (FP), one hole in the centre (P1), four holes (P2), 16 holes (P3), four slits oriented horizontal and vertical (S1), four slits rotated 45° (S2) with respect to S1, or one rotated slit in the centre (S3). Z indicates the firing pressure in bar in the driver. The blast intensity in the various tests was varied by changing the firing pressure in the driver section of the SSTF. Note that the firing pressures presented in Table 3 are rounded to the lower multiple of 5.

Aune et al. [20] investigated the dynamic response of both full plates (FP) and plates with four pre-formed square holes for Docol

600DL (D6) and the results are adopted and labelled P2 in the present study.

4. Experimental results

The presentation of the experimental results is divided into three main parts. First, the global response of the target plates without holes are presented in Section 4.1. Then, the results from tests on plates with different pre-formed defects are presented in Section 4.2. The global response is evaluated based on the recorded pressure histories and deformations measured by 3D-DIC. Finally, fracture modes and the blast resistance are evaluated for the different geometries and materials in Section 4.3. It is important to emphasize that the presentation of results herein is limited to the representative findings of this study, whereas the complete set of experimental results is provided in Appendix A.

As the reflected pressure histories indicate the loading experienced by the target plates, they are presented in Section 4.1. It should be noted that a slightly different time axis is used for the presented pressure histories compared to the displacements, i.e., two different time axes are defined for the plotted results. For the pressure histories, $t = 0$ is set to the point in time where the incoming pressure passes Sensor 1 on its way towards the target plate. This is done to visualize both the incoming and reflected pressure as two separate peaks. For all deformation histories, $t = 0$ was set to the last measurement before any deformation occurred in the target plate. This allows for a better comparison of the dynamic response.

4.1. Plates without defects

Fig. 5 presents the pressure histories measured at Sensor 1 for the tests on D6 and D14 plates without any defects. Table 4 provides

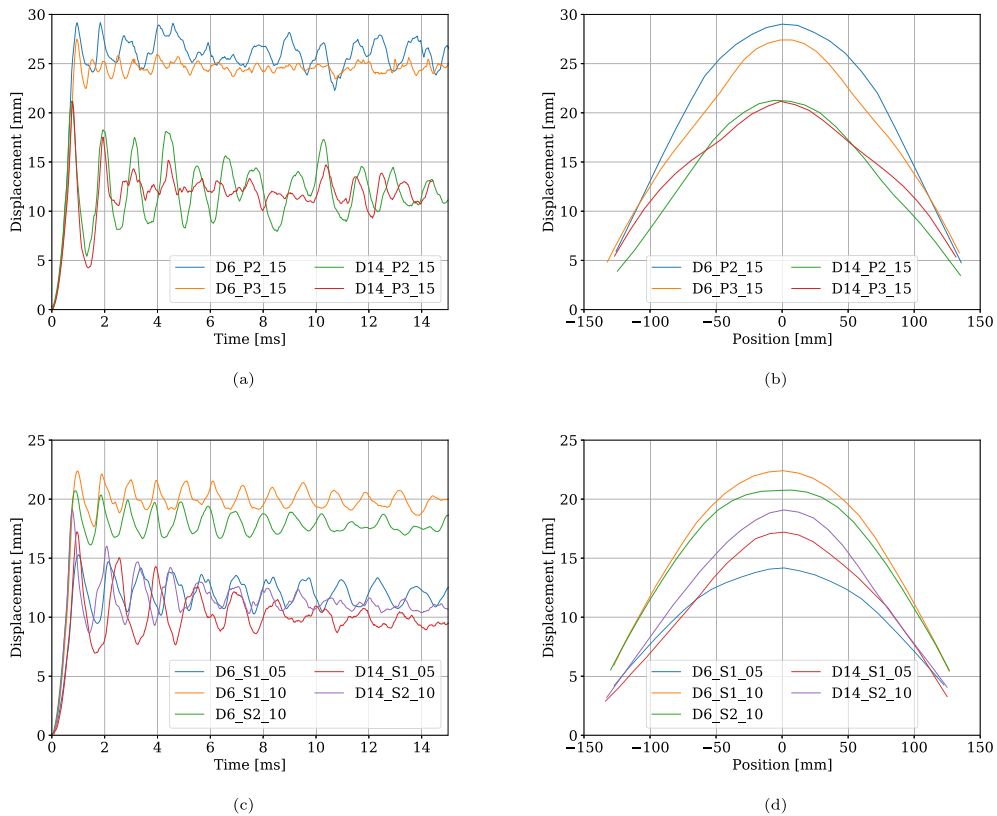


Fig. 8. Deflection measurements for tests on plates with pre-formed holes (P2 and P3), and pre-formed slits (S1 and S2) for both materials (D6 and D14): (a) and (c) show mid-point displacements histories, and (b) and (d) give the corresponding deformation profiles at $d_{z,max}$.

the nominal firing pressure, peak incoming pressure $P_{so,max}$ and peak reflected pressure $P_{r,max}$ for each test. It is emphasized that Sensor 1 is located 245 mm upstream the target plates (see Fig. 3) and that the initial rise in pressure corresponds to the incoming pressure wave, while the second peak is due to the reflected pressure wave on its way back towards the driver section after impacting the target plates. One important observation in Fig. 5 (a)–(b) is that similar firing pressures result in a similar pressure history for the incoming blast wave when varying the plate material. This confirms the repeatability of the tests and enables detailed studies on various geometries and materials exposed to the same blast intensity. The peak reflected pressure at Sensor 1 is influenced by the dynamic response of the plate. This is also observed in Fig. 5 where slightly lower magnitudes of reflected pressure are observed for the D6 plates when exposed to the same blast intensity as the D14 plates. A plausible explanation for the different magnitudes of the reflected pressure is fluid–structure interaction (FSI) effects during the initial response of the plates, i.e., before the plates have obtained their permanent deflection (see e.g., [36]). However, these FSI effects are considered as beyond the scope of this study and detailed studies on FSI effects are suggested as future work. Pressure histories for the remaining tests are given in Appendix A.1.

The effect of changing the steel material from D6 to D14 on the global response of the plates is presented in terms of mid-point displacements in Fig. 6 (see also Table 4). When the blast wave impacts

the target plate, an abrupt displacement is observed, followed by comparatively small oscillations. As expected, it is observed significantly larger displacements for the D6 plates when exposed to the same blast intensity as the D14 plates. It should be noted that similar colours in the figures represent the same blast intensity and that none of the plates without initial defects failed or ruptured during the tests.

Fig. 6 shows that the elastic oscillations are larger for the D14 plates than the D6 plates. For the D6 plates, the largest oscillations are found at the lowest blast intensity (D6_FP_05) and the magnitude of the elastic oscillations are reduced as the load intensity is increased.

The resistance against elastic oscillations is assumed to have two main contributors; first, the plastic dissipation of energy until the maximum displacement $d_{z,max}$ is reached, and second, the geometry of the permanent deformed configuration of the target plates at $d_{z,max}$. From Fig. 7, it is observed that the target plates deforms into a dome-shaped configuration, which adds a geometric stiffness against elastic springback. The magnitude and shape of the deformed configurations are further assumed to depend on both the strength and the work hardening of the plate material.

It is further noted that the D14 target plate exposed to the lowest blast intensity (D14_FP_05) undergoes negative displacements at about 40 ms in Fig. 6(b). Negative displacements are defined as displacements in the opposite direction as the incoming blast wave, commonly known as counter-intuitive behaviour. By considering the corresponding pressure history in Fig. 5, it is observed that the negative displacements

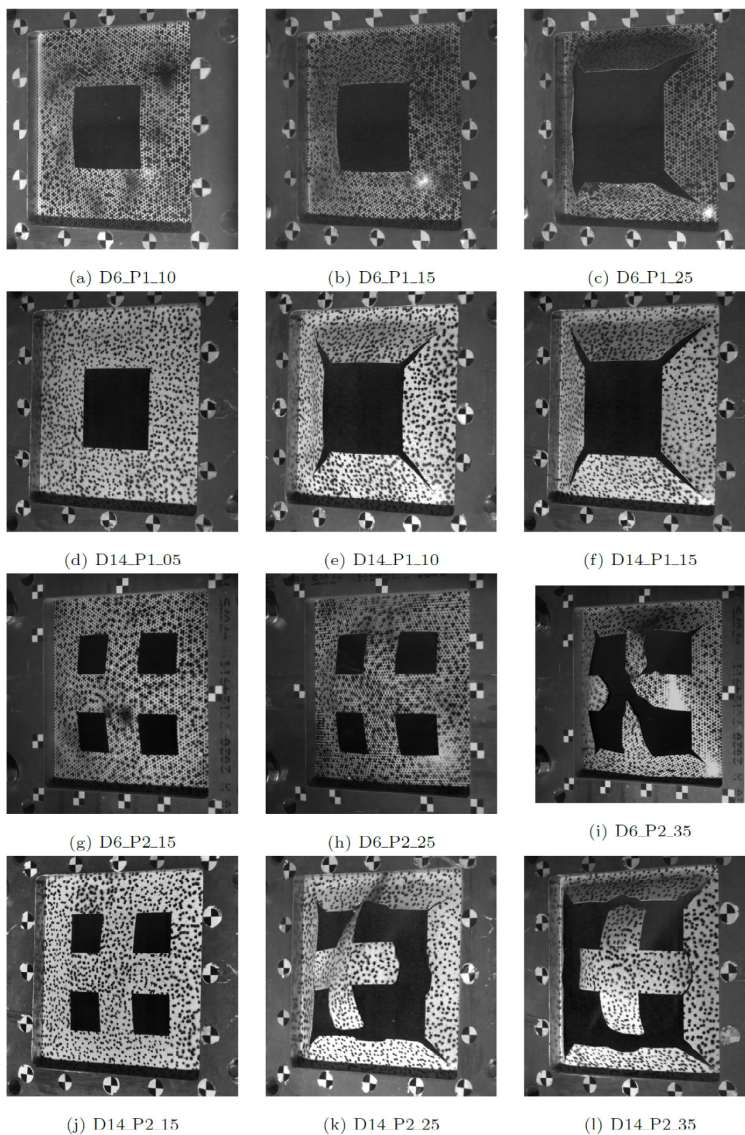


Fig. 9. Fracture modes for tests on plates with pre-formed holes (PX). The images are taken from one of the high-speed cameras and the test name is given in the sub-caption of each image.

occur during the negative duration of the reflected pressure. This phenomenon was also discussed by Aune et al. in [22]. However, negative displacements only occurred for the D14 material. All experiments experiencing negative displacements are given in Appendix A.3.

A more detailed insight on the response of the plates is gained by assessing the shape of the target plates during deformation. Fig. 7 provides the deformation profiles measured by 3D-DIC. Deformation profiles for the D6 plates are given in Fig. 7(a)–(c) and the D14 plates are given in Fig. 7(d)–(f). These profiles represent the out-of-plane

displacements along a horizontal line across the entire blast exposed area (see the blue line in Fig. 3). To gain insight into the deformation history of each plate, the deformed state at maximum deflection $d_{z,max}$ (red line) and the minimum deflection $d_{z,min}$ after the first elastic springback (blue line) are shown. The movement from $d_{z,max}$ to the first minimum $d_{z,min}$ is denoted the initial elastic springback, which is illustrated in the subplot in Fig. 7(a). The green curves illustrate the plate movement during the initial elastic springback for intervals of 0.027 ms. It should be noted that the blast wave travels back and forth

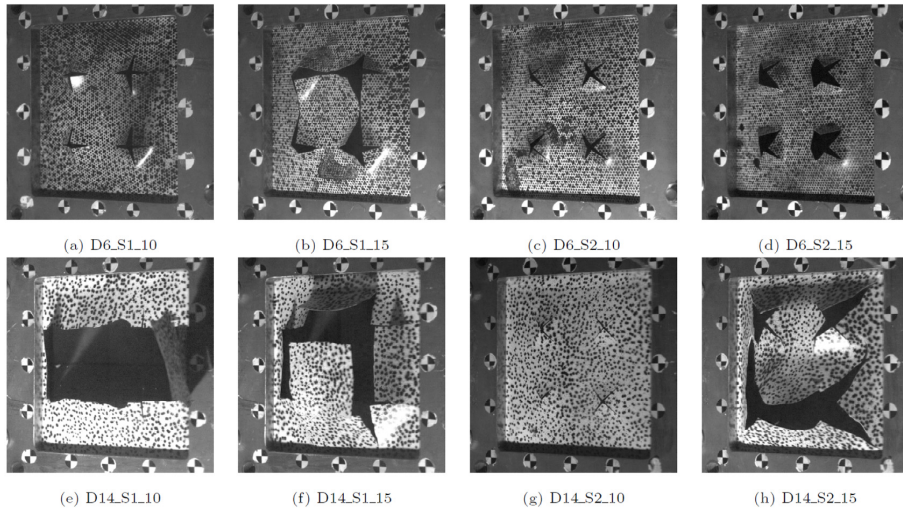


Fig. 10. Fracture modes for tests on plates with pre-formed slits (SX). The images are taken from one of the high-speed cameras and the test name is given in the sub-caption of each image.

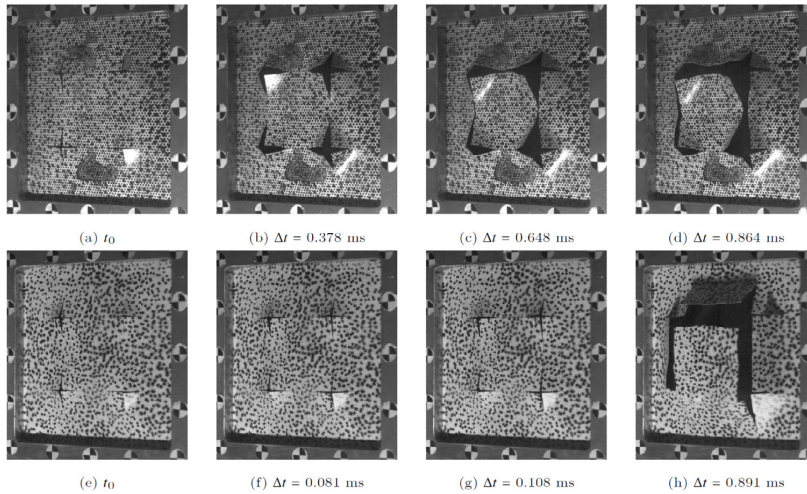


Fig. 11. Crack propagation for the S1 geometry at the highest blast intensity for test D6_S1_15 (top row) and test D14_S1_15 (bottom row). The images in the left column represent the instant before any visual cracks occurred, whereas the following images are presented for characteristic times during the fracture process.

inside the shock tube several times until a static overpressure is reached when the air comes to rest. This leads to multiple loading events on the plate such that the final configuration may not be representative for the primary loading event. It was therefore decided not to include the permanent deformation profile in Fig. 7.

Fig. 7 shows that the deformed shapes are different for the two plate materials, indicating different plastic strain distributions. As also observed by Aune et al. [20], the deformations initiate near the clamped

area and propagate towards the centre of the plate, resulting in a parabolic shape at $d_{z,max}$. For the D6 plates, springback is observed only on a local part of the plate near its centre. In contrast, springback is observed along most of the plate width for the D14 plates for the same blast intensities.

The experimental results are compiled in Table 4, giving the maximum ($d_{z,max}$) and the permanent ($d_{z,p}$) mid-point deflection for all tests on the full plates. Table 4 also contains information on the amount of

Table 4

Experimental results from the full plate (FP) tests measured with 3D-DIC. The firing pressure is the last measured pressure in the driver before the sudden pressure drop at diaphragm rupture, $P_{i0,max}$ and $P_{r,max}$ are the maximum incoming and maximum reflected pressure measured at Sensor 1, while Δd is calculated as $(d_{z,max} - d_{z,p})/d_{z,max}$.

Test	Firing pressure [bar]	$P_{i0,max}$ [kPa]	$P_{r,max}$ [kPa]	$d_{z,max}$ [mm]	$d_{z,p}$ [mm]	Δd [%]
D6_FP_05	5.16	111.5	254.4	15.62	10.71	31.4
D14_FP_05	5.18	115.5	246.6	15.72	3.42	78.2
D6_FP_15	15.83	219.6	563.3	25.25	21.84	13.5
D14_FP_15	15.07	227.0	604.2	20.90	7.60	63.6
D6_FP_25	26.15	288.1	776.5	31.73	28.57	9.9
D14_FP_25	23.61	282.0	852.7	25.00	12.05	51.8
D6_FP_35	36.92	328.4	1038.8	36.07	34.43	4.5
D14_FP_35	36.18	348.5	1147.5	32.22	19.24	40.3
D6_FP_60	61.18	435.8	1372.0	45.10	43.70	3.1
D14_FP_60	61.91	455.3	1499.0	36.15	26.49	26.7

elastic deformations in the plates (Δd) which is calculated based on the difference in $d_{z,max}$ and $d_{z,p}$. The maximum displacement ($d_{z,max}$) is taken as the maximum value during the test, while the permanent displacement ($d_{z,p}$) is estimated by finding the average value for the last 2.7 ms of the measured displacement history.

4.2. Plates with pre-formed defects

Due to the extensive number of experiments on plate geometries with pre-formed defects, displacement plots from only a representative selection of tests is provided in this section. Fig. 8 presents mid-point displacements and the corresponding deformation profiles at maximum deformation ($d_{z,max}$) for plates with pre-formed holes in (a)–(b), and slits in (c)–(d). The P1 and S3 geometries are not presented due to the absence of a midpoint (see Table 3). Similar as for the plates without defects, the pressure measurements and displacement data for the experiments are represented in Table 5. The results are organized in the same way as for those of the plates without defects in Table 4. The displacement histories not included in this section are given in Appendix A.2.

When introducing defects to the target plates, the clear trend was a shift from large plastic deformations (without any signs of crack initiation) to crack initiation and crack propagation. For target plates with defects, the effects of changing the steel material from D6 to D14 on the global response follow the same trends as for the full plates. As long as the plates do not fail, the D14 plates experience less deformation and more pronounced oscillations around the permanent deformed configuration (see Fig. 8). As for the plates without pre-formed defects, the peak reflected pressure was observed to be slightly reduced for the D6 plates relative to the D14 plates (see Table 5).

The effect of changing the plate geometry on the global response of the plates is represented using two geometries with pre-formed holes (P2 and P3) and two geometries with slits (S1 and S2), shown for the two lowest blast intensities in Fig. 8. The plates presented in Fig. 8 did not experience any visible fracture during the tests. From the overall global response in Fig. 8, it is seen that the plate material influence the response more than the plate geometry. That is, the D6 plates undergo the largest displacements for all geometries, and the D14 plates give the largest oscillations for all geometries. Moreover, the comparison of the deformation profiles in Fig. 8(d) indicates that the plate material also has an influence on the deformed shape of the plates. The D14 plates have a more pointed deformed shape than the D6 plates, which is interesting in view of the different work hardening characteristics (see Fig. 1).

4.3. Fracture modes and crack propagation

In short, the plates without fracture behaved according to the initial expectations of this study. That is, higher strength leads to increased blast resistance of the plates resulting in smaller magnitudes of deformation. However, in contrast to the plates without defects, most of the plates containing initial defects experienced crack initiation and crack propagation. Despite its higher material strength, the D14 plates consistently fractured at lower blast intensities than the D6 plates. Another observation was that the tests on D6 plates covered three distinct responses depending in the blast intensity. That is, the lowest blast intensity resulted in small plastic deformations without any crack initiation, while increasing blast intensities resulted in larger plastic deformations and arrested cracks at the intermediate intensities until complete fracture was observed for the highest load intensities. This was more or less as expected. However, it was interesting to note that these three different responses were not as evident for the D14 plates, where the plates mainly experienced either plastic deformations without any cracking or complete fracture. The only exception was test D14_P1_05 which resulted in arrested cracks.

As expected, the geometry of the pre-formed defects was also found to have a pronounced influence on the blast resistance of the plates. By comparing the damage characteristics of the plates with holes and slits presented in Table 5, it is evident that complete fracture is more frequently observed in geometries with slit defects than plates with holes. For plates with pre-formed holes (PX), 7 out of the 21 tests resulted in crack arrest while 9 of the tests resulted in complete fracture. Similarly, for plates with slits (SX), crack arrest was found in 6 out of the 16 tests while 8 tests resulted in complete fracture.

Figs. 9 and 10 present images of the target plates captured by one of the high-speed cameras during testing, showing the fracture modes for a representative selection of tests on plates with pre-formed holes (PX) and pre-formed slits (SX), respectively. The presentation is further limited to tests experiencing either partial or complete fracture. For completeness, the fracture modes of the remaining experiments are presented in Appendix B.1.

The P1 geometry showed the lowest capacity to fracture and resulted in the same fracture mode for both materials. For the P2 geometry, the effect of changing the plate material caused a shift in fracture mode. Two distinct fracture modes were observed, where the fracture mode seemed to be determined by the plate material. The D6 plates experienced cracks propagating along the diagonals until the plate reached complete fracture (see test D6_P2_35 in Fig. 9), whereas the D14 plates fractured along the horizontal and vertical extremities in-between the holes resulting in a cross-shaped fracture mode (see tests D14_P2_25 and D14_P2_35 in Fig. 9). It should be noted that only one of the tests resulted in complete fracture for the P2 geometry in the tests with D6 plates (D6_P2_35), which makes it challenging to draw any general conclusions for this particular geometry. However, assessing all the tests on plates with pre-formed holes, it is evident that the fracture mode and crack propagation are influenced by the material of the plates. It is interesting to note that the D6 plates seem to outperform the D14 plates under similar load intensities, given the fact that the D14 material has significantly higher strength than the D6 material (see Fig. 1).

Fig. 10 provides the same presentation of the fracture modes for tests on plates with pre-formed slits (SX). As for the geometries with pre-formed holes, a representative selection of the tests are presented (i.e., S1 and S2 geometries). The clear trend was that the plates with slit geometries (SX) fractured at lower load intensities than the plates with pre-formed holes (PX). The cracks always initiate at the extremities of the slits and started to propagate in the slit direction until the cracks reached the supports or reaches the path of other cracks. In contrast to the plates with pre-formed holes, the plate material were not observed to influence the fracture mode of the plates. This is clearly illustrated in Fig. 11, showing the fracture process of the S1 plates in tests D6_S1_15 and D14_S1_15.

Table 5

Displacement measurements obtained from 3D-DIC on the plates with pre-formed holes (PX) and slits (SX). Deformation measurements of tests experiencing complete fracture are given as (-), while geometries without a midpoint are denoted NA. The given firing pressure is the last measured pressure in the driver before the sudden pressure drop at diaphragm rupture.

Test	Firing pressure [bar]	$P_{i0,max}$ [kPa]	$P_{r,max}$ [kPa]	$d_{z,max}$ [mm]	$d_{z,p}$ [mm]	Δd [mm]	Damage
D6_P1_05	5.17	107.0	228.3	NA	NA	NA	No cracks
D14_P1_05	5.16	103.9	226.6	NA	NA	NA	Crack arrest
D6_P2_05	6.18	110.2	225.9	18.29	13.77	4.27	No cracks
D14_P2_05	5.17	112.1	214.7	14.45	2.58	11.87	No cracks
D6_S1_05	5.19	109.8	240.0	15.29	11.42	3.87	No cracks
D14_S1_05	5.15	111.2	254.6	17.23	0	17.23	No cracks
D6_P1_10	10.12	173.6	384.7	NA	NA	NA	Crack arrest
D14_P1_10	9.93	166.4	377.3	NA	NA	NA	Complete fracture
D6_S1_10	10.03	168.2	413.4	22.38	19.16	3.22	Crack arrest
D6_S2_10	9.98	164.6	383.2	20.71	17.49	3.22	Crack arrest
D14_S1_10	10.07	161.6	406.7	-	-	-	Complete fracture
D14_S2_10	10.03	165.5	414.7	19.10	7.16	11.94	Crack arrest
D14_S3_10	10.07	165.7	410.3	NA	NA	NA	Complete fracture
D6_P1_15	15.42	224.0	510.3	NA	NA	NA	Crack arrest
D14_P1_15	15.13	222.8	535.6	NA	NA	NA	Complete fracture
D6_P2_15	16.38	219.2	491.2	29.91	26.35	3.55	Crack arrest
D14_P2_15	15.06	230.9	490.4	21.17	11.81	9.36	No cracks
D6_P3_15	15.65	225.8	495.7	27.43	24.19	3.33	Crack arrest
D14_P3_15	15.08	222.8	481.2	21.18	11.77	9.41	No cracks
D6_S1_15	15.61	213.7	543.5	-	-	-	Complete fracture
D6_S2_15	15.34	227.9	571.1	26.36	23.22	3.14	Crack arrest
D14_S1_15	15.10	216.8	552.1	-	-	-	Complete fracture
D14_S2_15	15.10	229.4	568.0	-	-	-	Complete fracture
D14_S3_15	15.08	229.1	574.2	NA	NA	NA	Complete fracture
D6_P1_25	24.45	281.5	661.7	NA	NA	NA	Complete fracture
D6_P2_25	26.98	300.9	709.0	35.67	33.18	2.48	Crack arrest
D14_P2_25	24.73	276.5	688.7	-	-	-	Complete fracture
D6_P3_25	24.62	280.8	663.5	38.16	34.27	3.89	Crack arrest
D14_P3_25	24.64	294.8	708.8	-	-	-	Complete fracture
D6_S2_25	25.14	290.8	744.8	37.15	31.59	5.56	Crack arrest
D14_S2_25	24.61	290.5	790.8	-	-	-	Complete fracture
D6_S3_25	24.55	281.3	745.2	NA	NA	NA	Crack arrest
D14_S3_25	24.57	279.9	728.9	NA	NA	NA	Complete fracture
D6_P2_35	37.68	357.7	883.5	-	-	-	Complete fracture
D14_P2_35	36.63	339.7	875.5	-	-	-	Complete fracture
D6_P3_35	38.11	353.9	871.4	-	-	-	Complete fracture
D14_P3_35	37.68	-	-	-	-	-	Complete fracture
D6_S3_35	37.32	358.0	1033.6	NA	NA	NA	Complete fracture

By considering the time it takes a crack to propagate from the extremities of the defects towards the supports of the plate, a significant difference in crack propagation velocity was observed between the two materials. Since both materials experienced identical crack propagation paths to complete fracture for identical blast intensities for the S1 geometry presented in Fig. 11, it was decided to measure and compare the velocities of the propagating cracks from these tests. By visual evaluation of the high speed image recordings, the mean crack propagation velocity was found to be in the range 60–75 m/s and 220–280 m/s for D6 and D14, respectively. This builds confidence in that there is a strength–ductility trade-off in the blast performance of the plates, because the D6 plates outperform the D14 plates in both blast resistance and a larger ability to arrest cracks before the plates reach complete fracture.

5. Discussion

For target plates not experiencing fracture, the findings in this study are well aligned with previous studies on both full plates and plates with pre-formed defects, see e.g., [20,29]. That is, an increase in material strength resulted in smaller displacements and larger elastic

oscillations for a given blast intensity. Larger deformations for the low strength material are justified by the significantly lower yield stress, causing larger plastic deformations for a given load intensity [29]. As the strongest material (D14) has a significantly higher yield stress, this material will experience much higher internal stresses at maximum deformation. The increased internal stress state will in turn lead to higher internal forces for the elastic rebound, possibly causing larger oscillations. It is important to keep in mind that all blast tests on plates without any pre-formed defects resulted in global deformation without any signs of fracture. However, as pre-formed defects were introduced, the trend in global response remained unchanged, but fracture occurred for the highest load intensities.

The observations in this study indicate that the blast resistance is higher in the most ductile material despite its reduced strength. The strongest material (D14) was more prone to fracture and consistently fractured at lower blast intensities than the more ductile material (D6). High strength is typically accompanied by low ductility [27] and it is therefore not guaranteed that higher material strength leads to increased blast resistance of perforated steel plates. Ductile fracture is generally governed by local plastic deformation in a material [37], and the distribution of plastic strain tends to depend on the work hardening

of the plate material during blast loading (see e.g., Ref. [29]). That is, a material with limited work hardening will experience a more distinct localization of plastic deformation, and hence, a more rapid increase of plastic strains within the localized areas. It is emphasized that it is very challenging to quantify the effect of work hardening on the blast resistance of thin steel plates based on the experiments presented in this study, and further work involving numerical simulations is required for a more detailed investigation of the topic.

The D6 plates generally resulted in three distinct fracture modes. First, plastic deformations without any signs of fracture, then larger plastic deformations and arrested cracks, before significant cracks or complete fracture were observed for the highest blast intensities. The fracture mode involving crack arrest was not that evident in the tests with the high-strength plates, where the cracks were arrested in only a few tests for the D14 plates. That is, the D14 plates experienced either small plastic deformations without crack initiation or complete fracture as the blast intensity was increased. It is therefore reasonable to assume that the ability to arrest a propagating crack is strongly dependent upon the ductility, which in turn governs the amount of energy dissipated during crack propagation. This assumption is supported by the observation that the more ductile material (D6) showed larger plastic deformations around the propagating cracks than the high-strength material (see Fig. 11). Thus, the tests on the D14 plates clearly showed that cracks were allowed to propagate without any visual increase in global plastic deformations. In contrast to the findings in Ref. [29], the material did not only affect the capacity to fracture, but also the crack paths for experiments on the P2 geometry.

McDonald et al. [26] found that a high hardness armour steel with low ductility outperform a rolled homogeneous armour steel with higher ductility in terms of rupture threshold during blast loading. However, the target plates used in Ref. [26] were subjected to a different loading scenario, with a more localized and non-uniform loading on thicker target plates than those applied in the present study. In other words, the importance of the strength–ductility trade-off in the design of blast-resistant structures is expected to depend on both the loading conditions and the structural properties (i.e., the plate geometry and the material properties).

Finally, this study is motivated by more detailed studies into the influence of the strength–ductility trade-off on the performance of thin plates exposed to the combined effect of blast loading and fragment impacts. This topic was approached using a controlled laboratory environment and thin steel plates with pre-formed defects represented by square holes and cross-shaped slits. In realistic structures, pre-formed defects may also be present as e.g., bolt holes and window sections in facade elements, in addition to fragment or ballistic impact. Defects as a consequence of structural impact prior to the blast load would typically contain randomly distributed perforations with sharp notches and most likely accompanied with accumulated damage in front of the crack tip. Compared to the pre-formed defects investigated in this study, the additional ingredient of structural impact prior to the blast load is assumed to further reduce the capacity of the target plates. More realistic defects will also most probably result in less regularity in the observed fracture modes. Thus, the results in this study are not directly transferable to realistic design scenarios of combined fragment impact and blast loading. Similar studies should therefore be carried out on target plates with more complex initial defects and initial damage, aiding the design of future protective structures. However, such studies are considered beyond the scope of this study.

6. Concluding remarks

This work presents an experimental study on the influence of the strength–ductility trade-off on the blast resistance of thin steel plates with and without pre-formed defects. The dynamic response of the plates showed a strong dependence on both the material properties (strength, work hardening and ductility) and the plate geometry (shape, number and spatial distribution of the pre-formed defects). The main findings of this study can be summarized as follows:

- In the absence of initial defects, the strength of the material was the primary property influencing the response of the plates. As expected, the target plates with higher strength resulted in smaller global deformations and larger elastic oscillations during blast loading. None of the plates without pre-formed defects showed any signs of crack initiation under the blast intensities applied in this study.
- When defects were introduced in the form of pre-formed holes, the high-strength (D14) plates consistently fractured at lower blast intensities than the medium-strength (D6) plates for identical plate geometries. This finding clearly shows that plates with higher strength are more prone to cracking and fracture than the plates with lower strength. As a higher strength typically is accompanied with a lower ductility, the results indicate that work hardening and ductility are more important than the strength for the capacity of pre-damaged and blast-loaded thin steel plates. However, for very sharp defects represented by pre-formed slits, both the medium- and high-strength materials resulted in the same fracture mode at similar blast intensities. Still, even though less differences were observed in the fracture mode, the medium-strength (D6) plates outperformed the high-strength (D14) plates also for the tests on plates with pre-formed slits. This builds confidence in that there is a strength–ductility trade-off in the blast resistance of thin steel plates exposed to the combined effect of fragment impact and blast loading.
- The comprehensive experimental dataset presented in this study allows for validation and development of computational methods in future studies. This study also motivates further studies on the influence of the strength–ductility trade-off in protective design of combined fragment impact and blast loading scenarios.

CRedit authorship contribution statement

Benjamin S. Elveli: Conceptualization, Data curation, Formal analysis, Visualization, Writing – original draft. **Mads B. Iddberg:** Conceptualization, Data curation, Formal analysis, Writing – review & editing. **Tore Børvik:** Conceptualization, Writing – review & editing. **Vegard Aune:** Conceptualization, Formal analysis, Writing – original draft, Funding acquisition, Supervision.

Declaration of competing interest

The authors declare that they have no known competing financial interests or personal relationships that could have appeared to influence the work reported in this paper.

Acknowledgements

This work has been carried out with financial support from NTNU and the Research Council of Norway through the Centre for Advanced Structural Analysis (CASA), Centre for Research-based Innovation (Project No. 237885). The financial support by the Norwegian Ministry of Justice and Public Security is also greatly appreciated. Special thanks are given to Trond Auestad for his assistance during the laboratory work.

Appendix A

A.1. Global response - Pressure histories

Supplementary plots of the pressure histories measured at Sensor 1. In Fig. A.1, pressure curves are compared across the different geometries for a given material and pressure load in (a), (b) and (c). In (d) the pressure histories are compared for the two materials for the full plates (FP).

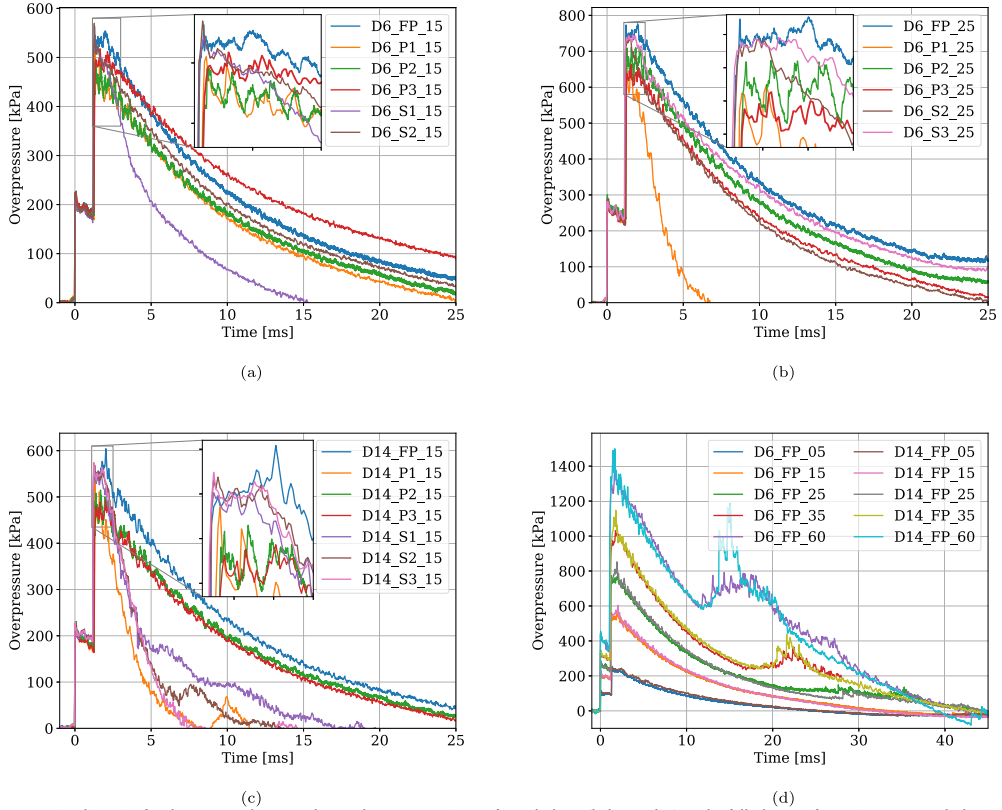


Fig. A.1. Pressure-time histories for the tests on the D6 and D14 plates, comparing perforated plates (holes vs slits) to the full plate configuration. A zoomed plot is also provided around the peak reflected pressure to enable a better comparison of the configurations.

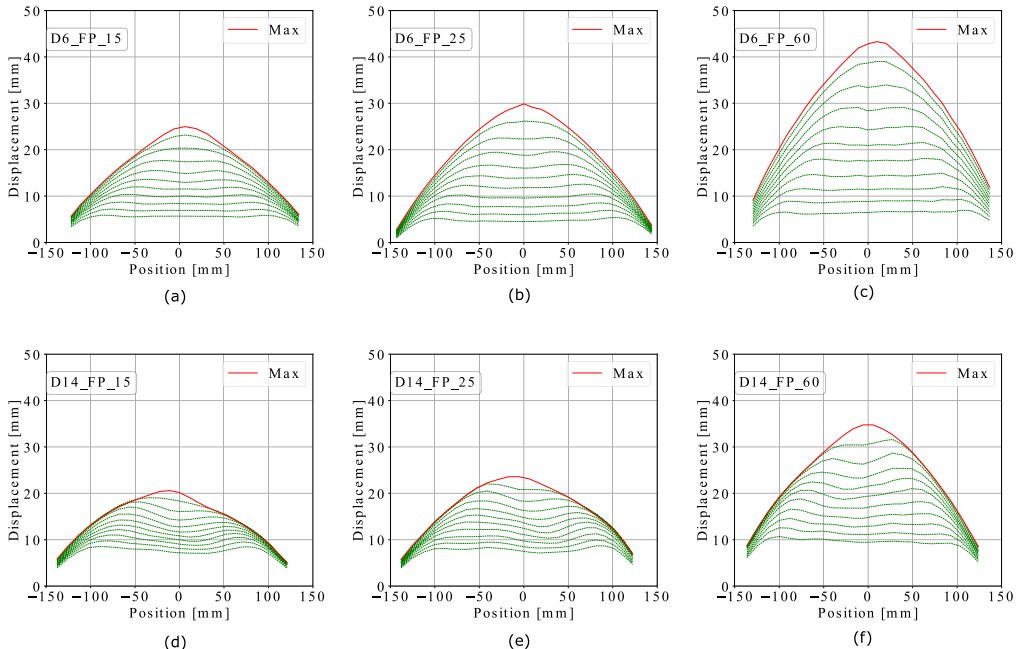
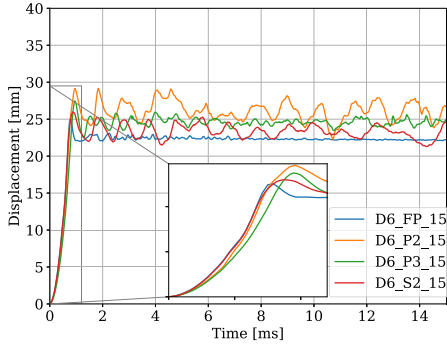
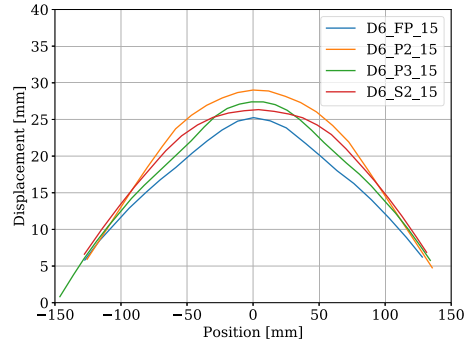


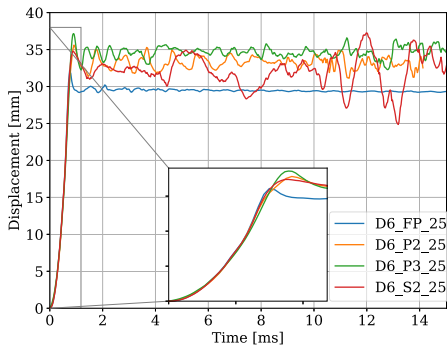
Fig. A.2. Development of deformation profiles until maximum deflection for the FP configuration, exposed to a blast intensities corresponding to firing pressures of 15, 25 and 60 bar. A selection of the D6 plates are shown in (a)–(c) and a similar selection of D14 plates in (d)–(e). The red line indicates the maximum displacement, whereas the green lines show the development in time. The time difference between each green line is constant and equal to the sampling rate ($\Delta t = 0.027$ ms) between each green profile. (For interpretation of the references to colour in this figure legend, the reader is referred to the web version of this article.)



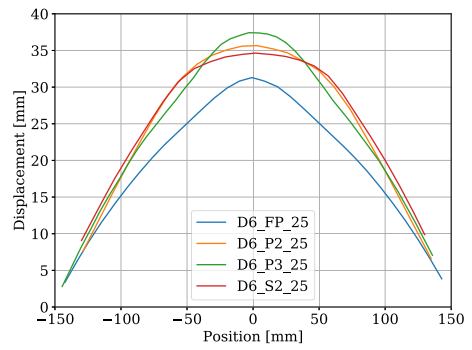
(a)



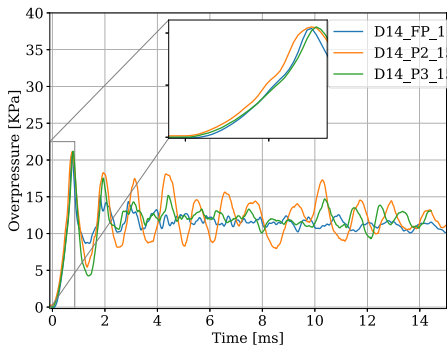
(b)



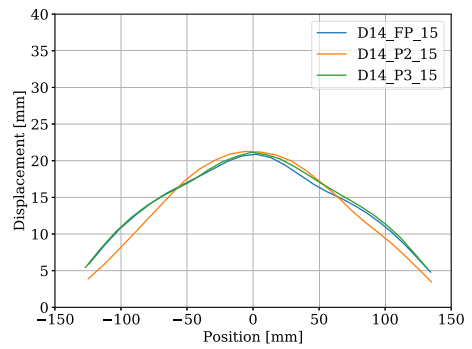
(c)



(d)



(e)



(f)

Fig. A.3. Mid-point displacements and deformation profiles at maximum displacement for tests on perforated plates (P2, P3, and S2) compared to the full-plate (FP) results at similar loading intensities (15 bar and 25 bar).

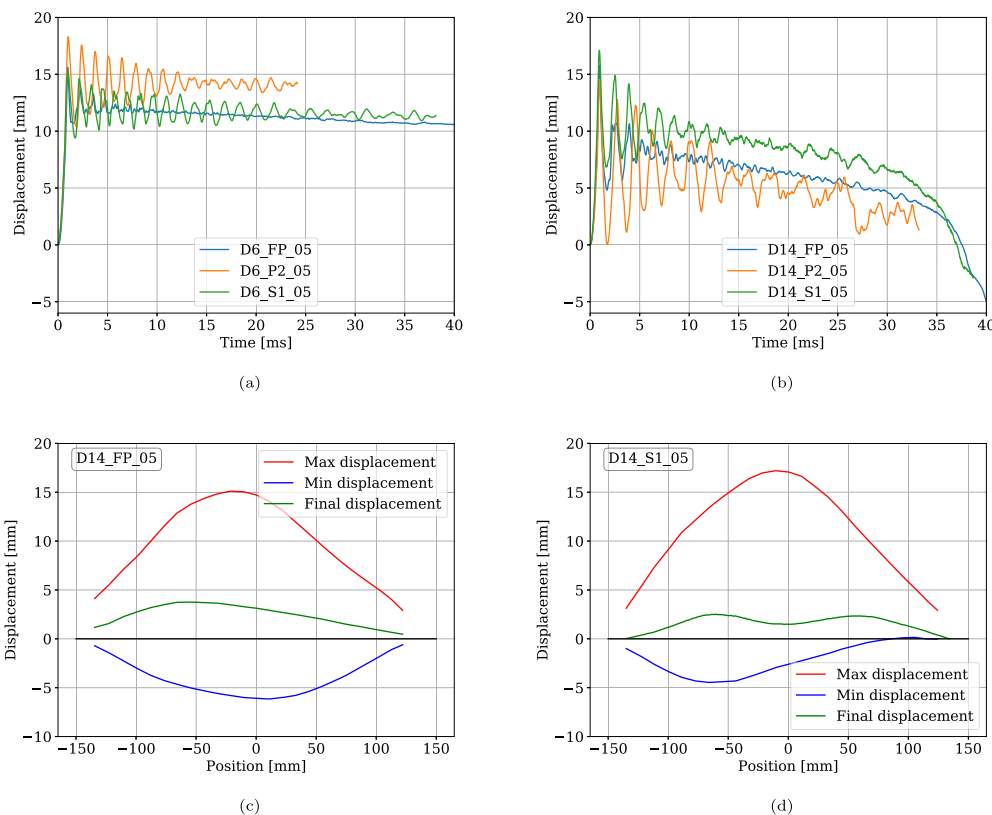


Fig. A.4. The mid-point displacements for all experiments exposed to blast intensities corresponding to a firing pressure of 5 bar are presented. The D6 target plates are presented in (a) and D14 plates in (b). The instants corresponding to the largest positive and negative displacement as well as the permanent displacement are shown for the D14_FP_05 and D14_S1_05 tests in (c) and (d), respectively.

A.2. Global response - deformation histories

Fig. A.2 provides the development of the deformation profiles up to the instant of maximum deflection for the FP configuration. The upper and lower row presents results for the tests on D6 and D14 plates, respectively, when exposed to a blast intensities corresponding to nominal firing pressures of 15, 25 and 60 bar. The deformation profiles marked with red lines indicate the maximum displacement, whereas the green lines indicate the development of the deformations. Each green line corresponds to an image pair taken with the high-speed cameras. The time difference between each green line is constant and equal to the sampling rate ($\Delta t = 0.027$ ms).

The mid-point displacement histories for the perforated geometries (holes vs slits) are compared to the full plates (FP) in Fig. A.3. Note that these plots are the same tests as for the pressure histories given in Fig. A.1. The displacement histories in Fig. A.3 are presented with mid-point displacements in (a), (c) and (e), while the corresponding deformation profiles at the instant of maximum displacement is provided in (b), (d) and (f).

A.3. Counter-intuitive behaviour

As mentioned in Section 4.1, the D14 target plates experienced negative displacements for the test involving the lowest blast intensities. Negative displacements are defined as displacements in the

opposite direction as the incoming blast wave, commonly known as counter-intuitive behaviour (CIB) (see e.g., Ref. [22]). Fig. A.4 shows a comparison of mid-point displacements for all experiments exposed to the lowest blast intensities for D6 plates in (a) and D14 plates in (b). In (c) and (d) the deformation profiles of two representative D14 tests are given for the maximum positive displacement, maximum negative displacement, and the permanent deflection.

Appendix B

B.1. Fracture modes

As only a selection of representative fracture modes were presented in Section 4.3, Figs. B.1 and B.2 show pictures of all tests experiencing either partial or complete fracture.

B.2. Crack initiation and crack arrest

The crack lengths for were used to investigate the influence of different materials and geometries on the resistance against localization and crack propagation. It was decided to measure the crack lengths for tests were this was possible from a practical point of view. The length of all visible cracks is for the tests under consideration is presented in

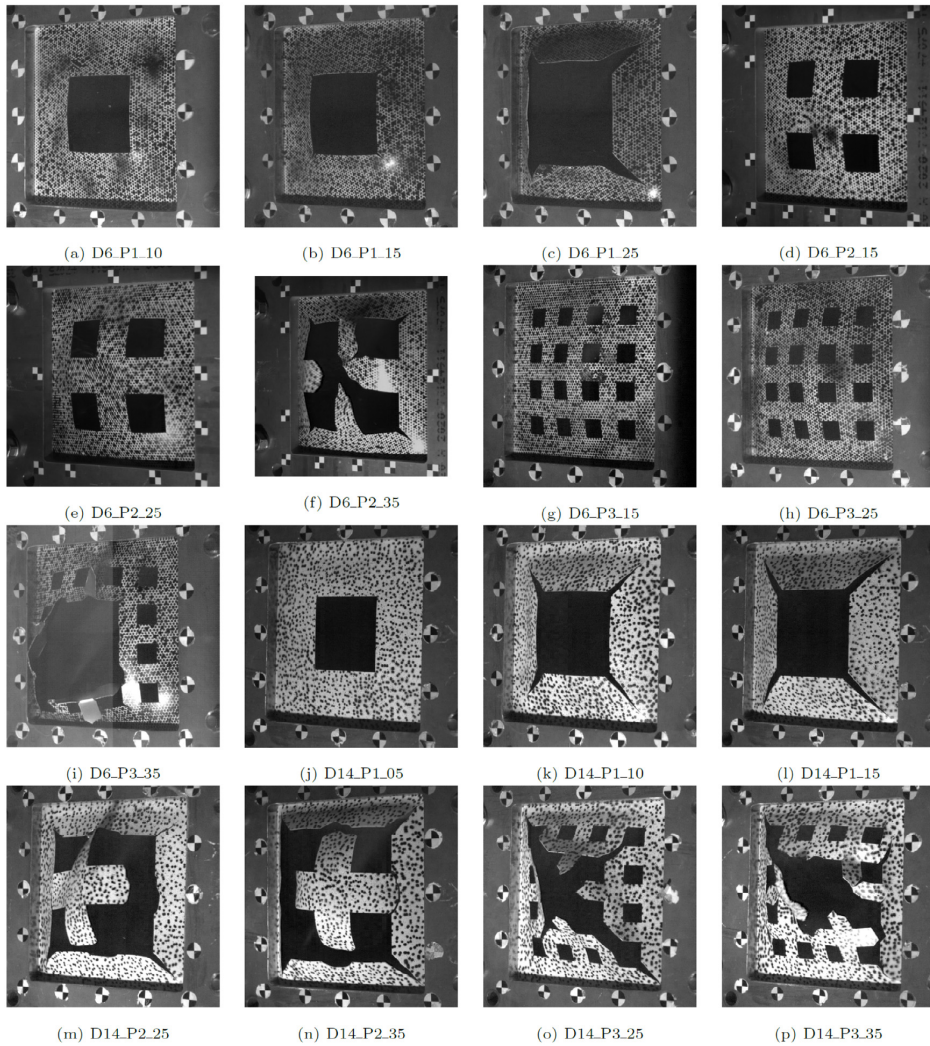


Fig. B.1. Fracture modes for tests on plates with pre-formed holes (PX). The images are taken from one of the high-speed cameras and the test name is given in the sub-caption for each image.

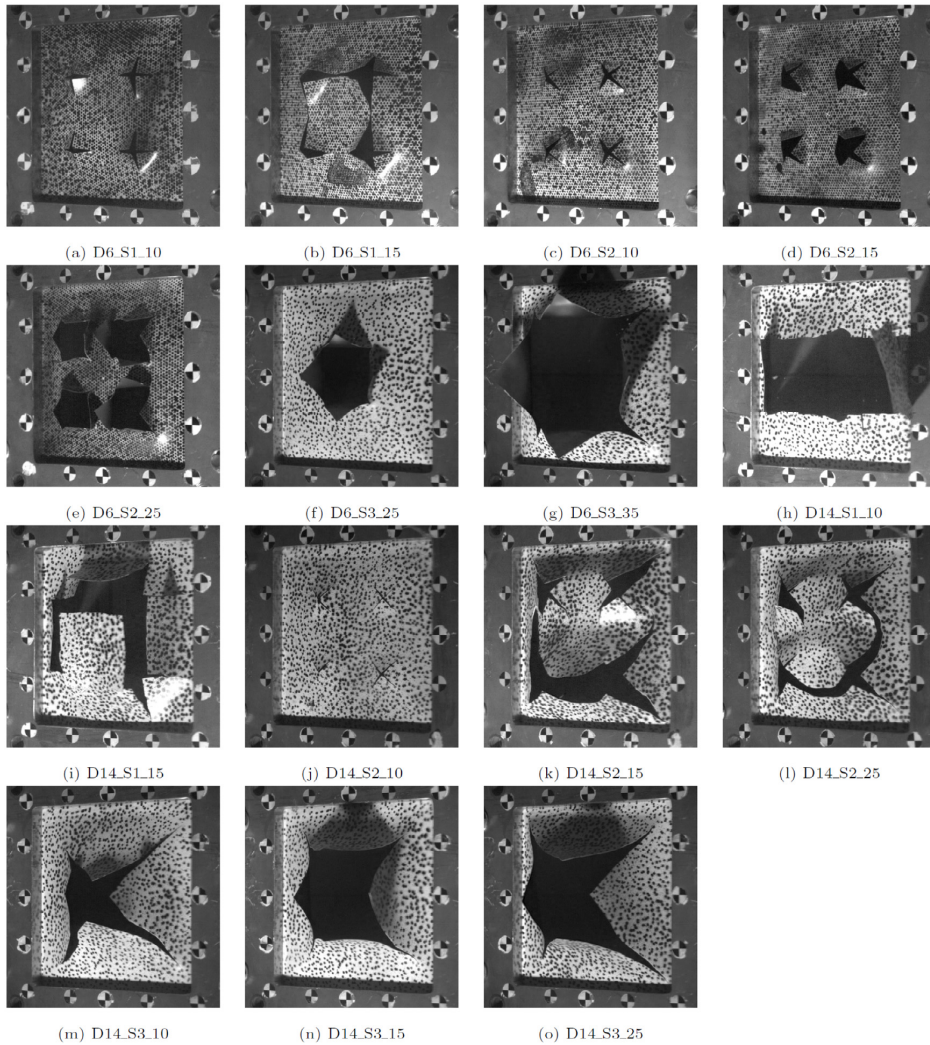


Fig. B.2. Fracture modes for tests on plates with pre-formed slits (SX). The images are taken from one of the high-speed cameras and the test name is given in the sub-caption for each image.

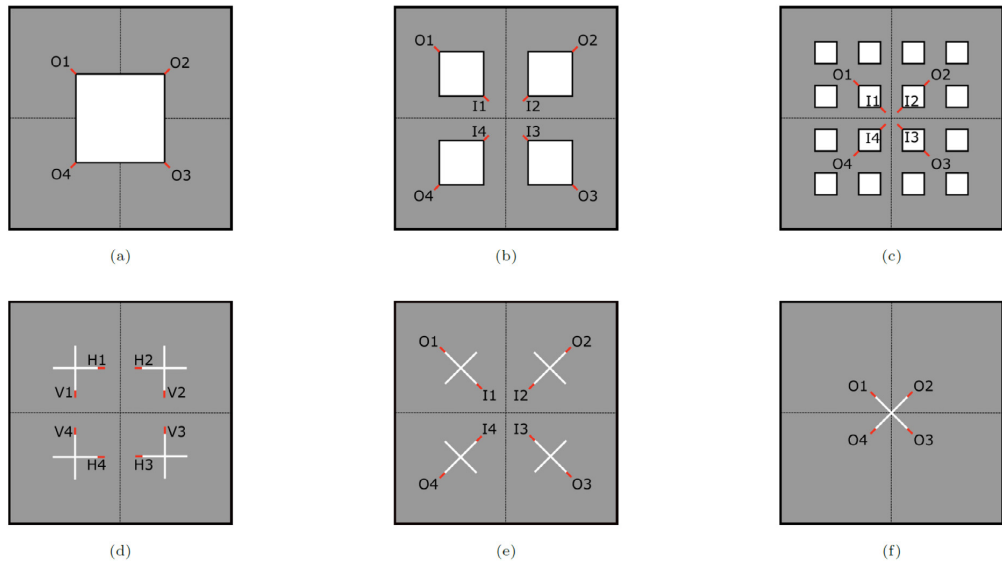


Fig. B.3. Location and naming conventions for measurements of arrested cracks for the selected tests. The cracks are indicated with red colour. (For interpretation of the references to colour in this figure legend, the reader is referred to the web version of this article.)

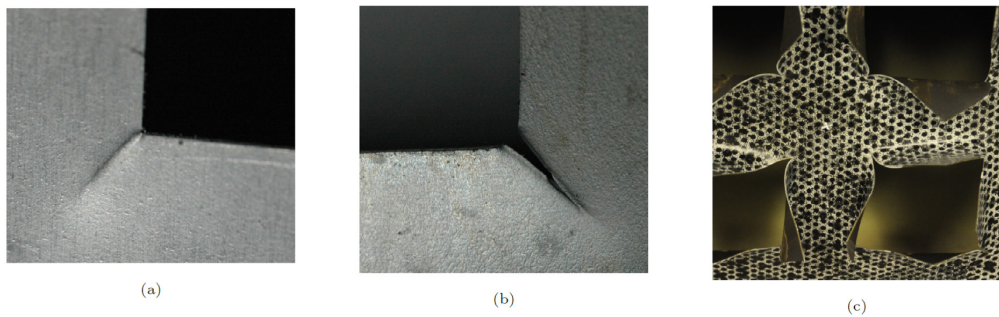


Fig. B.4. Images for some of the different fracture modes listed in Table B.1, where (a) shows a local necking (N) at the O3 location for the D14_P2_15 experiment, (b) shows a crack at the location O4 for D6_P2_25 and (c) illustrates cracks in areas with plastic deformations too large to practically measure for D6_S2_25.

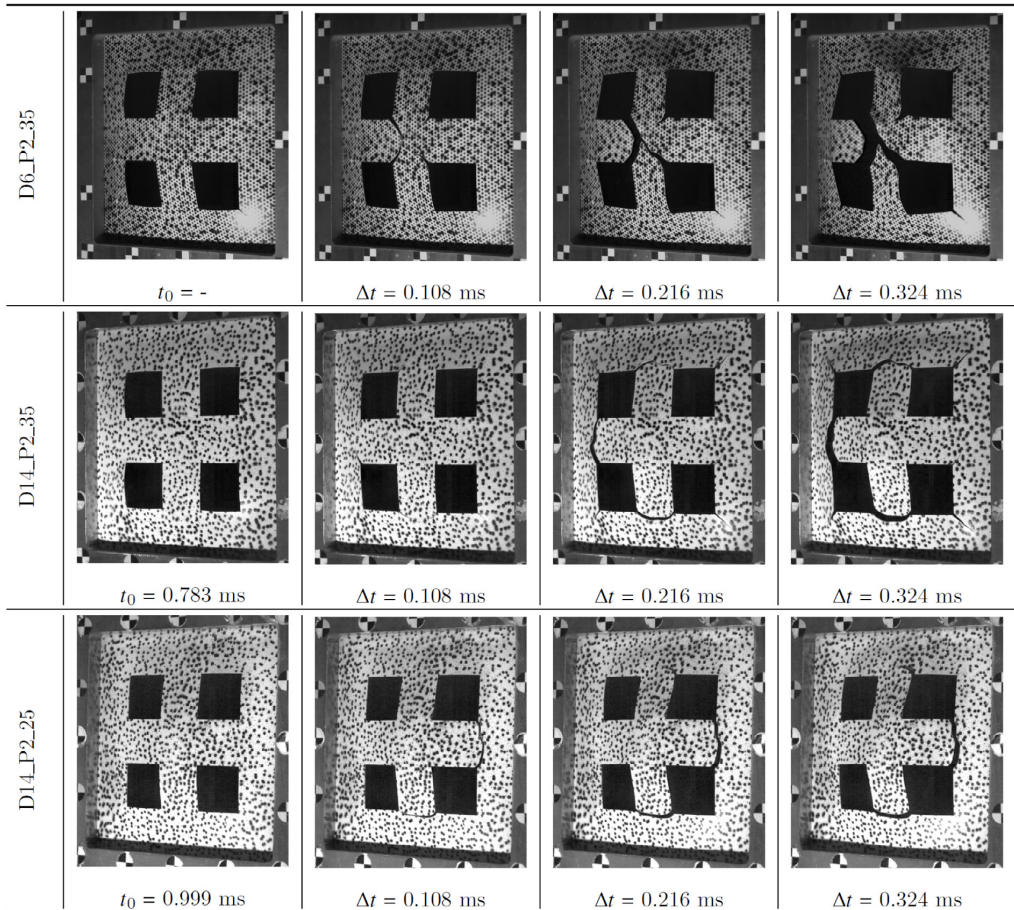


Fig. B.5. Images of the crack propagation for the P2 configuration exposed to blast intensities corresponding to firing pressures of 35 bar and 25 bar. Material, firing pressure and time for each image are given in the subcaptions. The given time for the images refers to the same time axis as the pressure plots, i.e., $t_0 = 0$ is defined as when the blast wave is passing the sensor closest to the target plate.

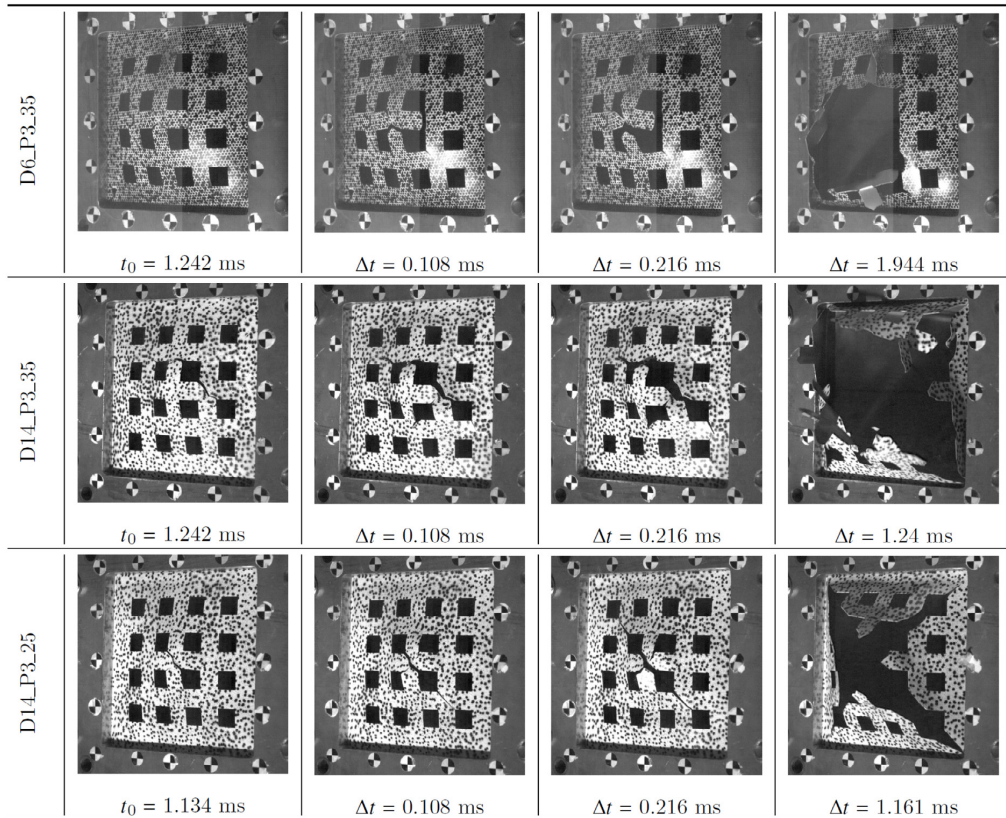


Fig. B.6. Images of the crack propagation for the P3 configuration exposed to blast intensities corresponding to firing pressures of 35 bar and 25 bar. Material, firing pressure and time for each image are given in the subcaptions. The given time for the images refers to the same time axis as the pressure plots, i.e., $t_0 = 0$ is defined as when the blast wave is passing the sensor closest to the target plate.

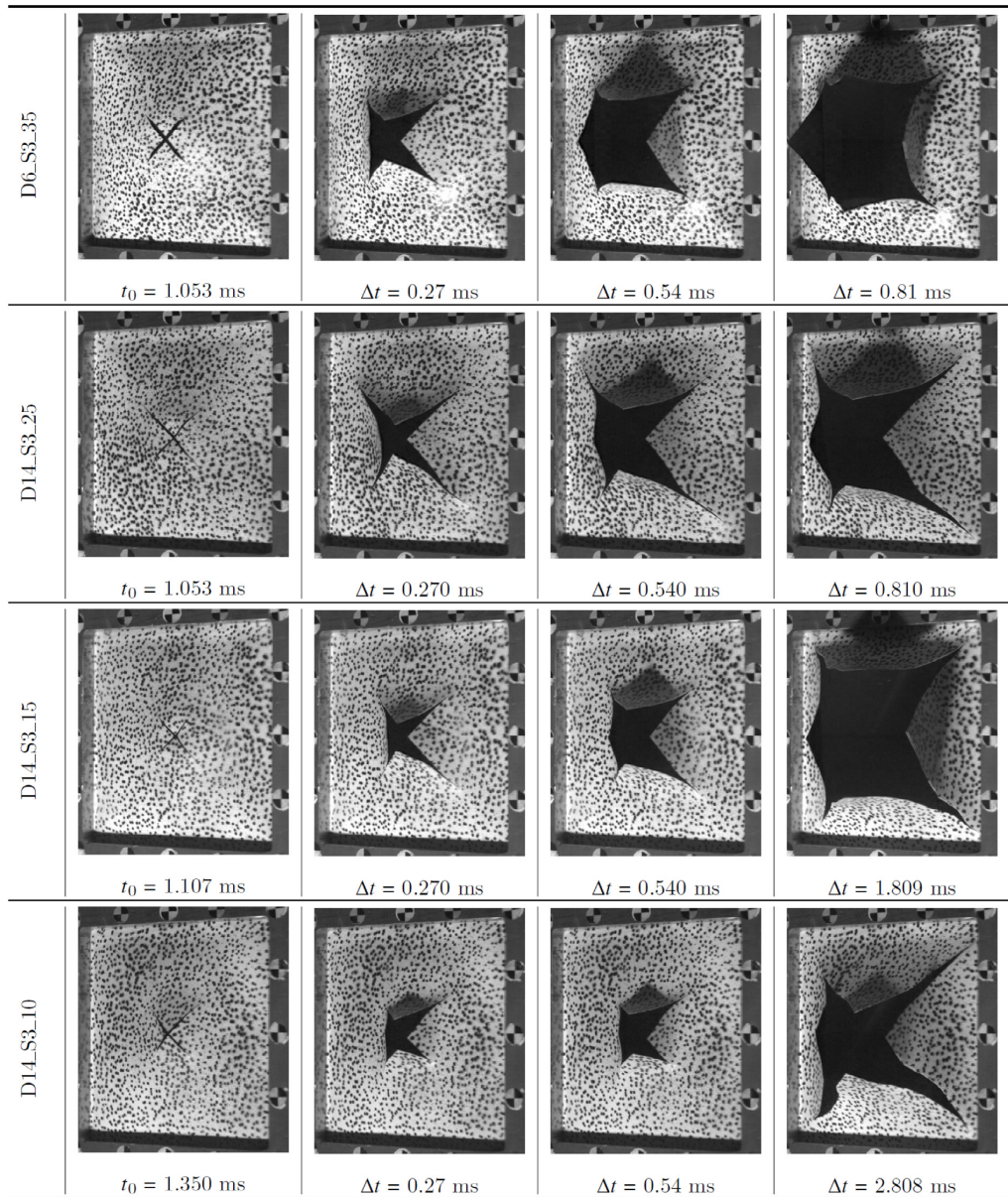


Fig. B.7. Image series of the crack propagation to complete fracture for the S3 configuration exposed to blast intensities corresponding to firing pressures of 35, 25, 15, and 10 bar, for both materials. The given time for the images refers to the same time axis as the pressure plots, i.e., $t_0 = 0$ is defined as when the blast wave is passing the sensor closest to the target plate.

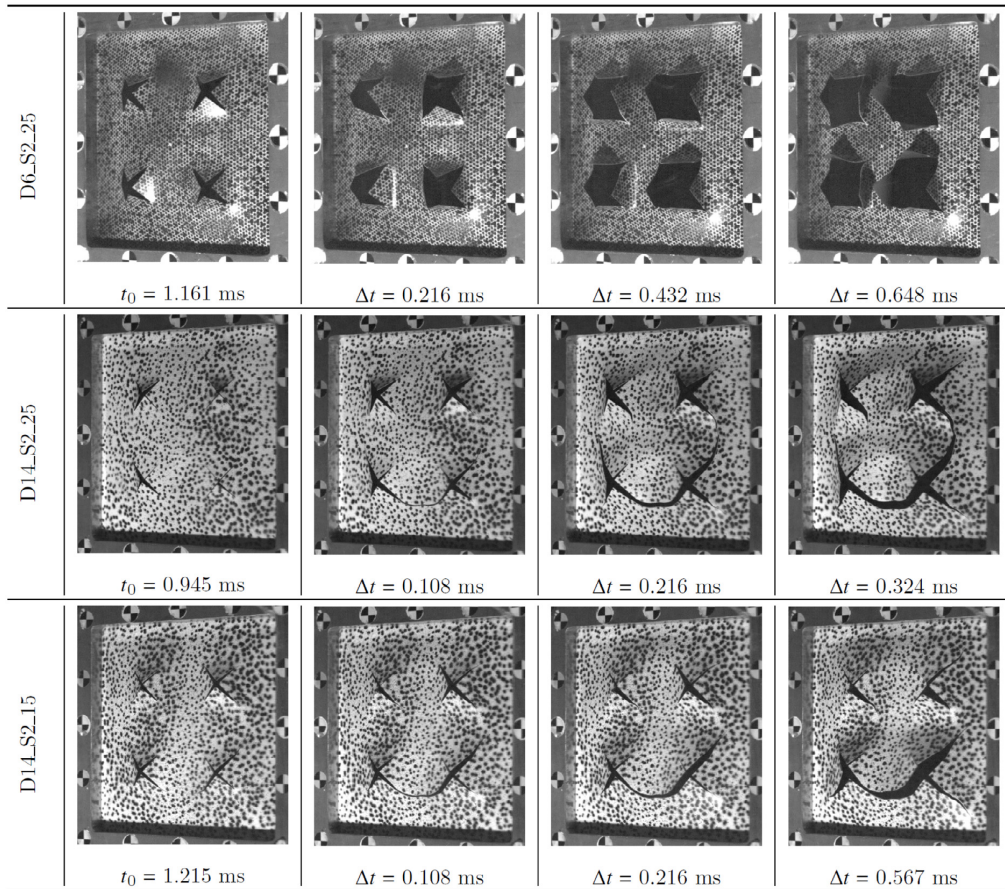


Fig. B.8. Image series of the crack propagation to fracture for the S2 configuration exposed to blast intensities corresponding to firing pressures of 15 bar and 25 bar, for both materials. The given time for the images refers to the same time axis as the pressure plots, i.e., $t_0 = 0$ is defined as when the blast wave is passing the sensor closest to the target plate.

Table B.1

Crack measurements for all tests that did not experience complete fracture. Measurements are made with reference to the crack identification introduced in Fig. B.3. Tests were only necking was observed is denoted with an N, while cracks that was too large to be practically measured have been identified by an X.

Test	O1	O2	O3	O4	I1	I2	I3	I4
D6_P2_05	–	–	–	–	–	–	–	–
D6_P2_15	N	N	N	N	N	N	N	N
D6_P2_25	7.41	8.35	8.68	7.83	11.76	13.56	15.67	12.62
D14_P2_05	–	–	–	–	–	–	–	–
D14_P2_15	N	N	N	N	N	N	N	N
D6_P3_15	N	N	N	N	N	N	N	N
D6_P3_25	N	N	N	N	2.0	2.4	1.6	2.2
D14_P3_15	N	N	N	N	N	N	N	N
D6_S2_10	N	N	N	N	4.4	4.7	4.3	4.2
D6_S2_15	5.1	4.4	4.7	4.8	11.4	10.8	10.9	10.3
D6_S2_25	22.8	22.2	21.2	22.5	X	X	X	X
D14_S2_10	N	N	N	N	N	1.6	N	2.0
	H1	H2	H3	H4	V1	V2	V3	V4
D6_S1_05	N	N	N	N	N	N	N	N
D6_S1_10	5.1	5.4	6.2	5.8	7.2	7.9	7.5	7.4
D14_S1_05	N	N	N	N	N	N	N	N
	O1	O2	O3	O4				
D6_P1_05	N	N	N	N				
D6_P1_10	6.1	6.2	6.4	6.1				
D6_P1_15	25.0	26.0	22.7	22.3				
D14_P1_05	5.99	9.96	17.14	4.24				

Table B.1, where the locations and naming conventions of the cracks are defined in Fig. B.3. Localized necking without any visual cracking was denoted (N), whereas large cracks in areas with deformations too large to practically measure the cracks were denoted (X). All cracks were measured manually using a digital calliper. Images of cases experiencing necking (N), cracks, or cracks too large to measure (X) are given in Fig. B.4.

B.3. Crack propagation

Figs. B.5–B.8 provide image sequences of additional crack propagation to what was presented in Section 4.3. Each test corresponds to one row in each figure, where the image series and time evolution for each test are given in the columns.

References

- [1] M. Ziya-Shamami, H. Babaei, T.M. Mostofi, H. Khodarahmi, Structural response of monolithic and multi-layered circular metallic plates under repeated uniformly distributed impulsive loading: An experimental study, *Thin-Walled Struct.* 157 (2020) 107024.
- [2] G. Langdon, A. Curry, A. Siddiqui, Improving the impulse transfer and response characteristics of explosion loaded compound angle V-plates, *Thin-Walled Struct.* 148 (2020) 106609.
- [3] R. Qi, G.S. Langdon, T.J. Cloete, C.K. Yuen, Behaviour of a blast-driven ball bearing embedded in rear detonated cylindrical explosive, *Int. J. Impact Eng.* 146 (2020) 103698.
- [4] S. Clarke, S. Rigby, S. Fay, A. Barr, A. Tyas, M. Gant, I. Elgy, Characterisation of buried blast loading, *Proc. R. Soc. A* 476 (2020) 20190791.
- [5] X. Jiang, W. Zhang, D. Li, T. Chen, Y. Tang, Z. Guo, Experimental analysis on dynamic response of pre-cracked aluminium plate subjected to underwater explosion shock loadings, *Thin-Walled Struct.* 159 (2021) 107256.
- [6] J. Zhu, Y. Zheng, W. Li, Y. Yang, X. Wang, X. Qiao, L. Xiangxin, R. Li, Axial distribution of fragments from the dynamic explosion fragmentation of metal shells, *Int. J. Impact Eng.* 123 (2019) 140–146.
- [7] K. Hu, G. Chen, C. Zhou, G. Reniers, S. Qi, Z. Zhou, Dynamic response of a large vehicle tank impacted by blast fragments from chemical equipment, *Saf. Sci.* 130 (2020) 104863.
- [8] H.Y. Grisaro, A.N. Dancygier, Characteristics of combined blast and fragments loading, *Int. J. Impact Eng.* 116 (2018) 51–64.

- [9] D. Hyde, U.A.E.W.E. Station, U.S.A.C. of Engineers, User's Guide for Microcomputer Programs ConWep and FunPro, Applications of TM 5-855-1, "Fundamentals of Protective Design for Conventional Weapons", Instruction Report, U.S. Army Engineer Waterways Experiment Station, 1988, URL <https://books.google.no/books?id=xhHxHAAACAAJ>.
- [10] U. Nyström, K. Gylltoft, Numerical studies of the combined effects of blast and fragment loading, *Int. J. Impact Eng.* 36 (2009) 995–1005.
- [11] W. Wilkinson, D. Cormie, M. Arkininstall, Calculation of blast loads for design against terrorism, *Proc. Inst. Civ. Eng. - Eng. Comput. Mech.* 166 (2013) 132–139.
- [12] J. Leppänen, Experiments and numerical analyses of blast and fragment impacts on concrete, *Int. J. Impact Eng.* 31 (7) (2005) 843–860.
- [13] H.Y. Grisaro, A.N. Dancygier, Dynamic response of RC elements subjected to combined loading of blast and fragments, *J. Struct. Eng.* 147 (2020) 04020315.
- [14] P.D. Linz, S.C. Fan, C.K. Lee, Modeling of combined impact and blast loading on reinforced concrete slabs, *Lat. Am. J. Solids Struct.* 13 (2016) 2266–2282.
- [15] P.D. Linz, T.C. Fung, C.K. Lee, W. Riedel, Response mechanisms of reinforced concrete panels to the combined effect of close-in blast and fragments: An integrated experimental and numerical analysis, *Int. J. Prot. Struct.* 12 (1) (2021) 49–72.
- [16] K. Rakvåg, N. Underwood, G. Schleyer, T. Børvik, O. Hopperstad, Transient pressure loading of clamped metallic plates with pre-formed holes, *Int. J. Impact Eng.* 53 (2012) 44–55.
- [17] L. Li, Q.-C. Zhang, R. Zhang, X. Wang, Z.-Y. Zhao, S.-Y. He, B. Han, T.J. Lu, A laboratory experimental technique for simulating combined blast and impact loading, *Int. J. Impact Eng.* 134 (2019) 103382.
- [18] W. Li, P. Wang, G.-P. Feng, Y.-G. Lu, J.-Z. Yue, H.-M. Li, The deformation and failure mechanism of cylindrical shell and square plate with pre-formed holes under blast loading, *Def. Technol.* 17 (2021) 1143–1159.
- [19] Y. Li, W. Wu, H. Zhu, ZhenWua, Z. Dub, The influence of different pre-formed holes on the dynamic response of square plates under air-blast loading, *Eng. Fail. Anal.* 78 (2017) 122–133.
- [20] V. Aune, G. Valsamos, F. Casadei, M. Langseth, T.B. rvik, On the dynamic response of blast-loaded steel plates with and without pre-formed holes, *Int. J. Impact Eng.* 108 (2017) 27–46.
- [21] V. Aune, E. Fagerholt, M. Langseth, T. Børvik, A shock tube facility to generate blast loading on structures, *Int. J. Prot. Struct.* 7 (2016) 340–366.
- [22] V. Aune, E. Fagerholt, K. Hauge, M. Langseth, T.B. rvik, Experimental study on the response of thin aluminium and steel plates subjected to airblast loading, *Int. J. Impact Eng.* 90 (2016) 106–121.
- [23] T. Fras, C.C. Roth, D. Mohr, Fracture of high-strength armour steel under impact loading, *Int. J. Impact Eng.* 111 (2018) 147–164.
- [24] T.B. rvik, S. Dey, A.H. Clausen, Perforation resistance of five different high-strength steel plates subjected to small-arms projectiles, *Int. J. Impact Eng.* 36 (2009) 948–964.
- [25] G.S. Langdon, W.C. Lee, L.A. Louca, The influence of material type on the response of plates to air-blast loading, *Int. J. Impact Eng.* 78 (2017) 150–160.
- [26] B. McDonald, H. Bornstein, G. Langdon, R. Curry, A. Daliri, A. Orifici, Experimental response of high strength steels to localised blast loading, *Int. J. Impact Eng.* 115 (2018) 106–119.
- [27] Y. Wei, Y. Li, L. Zhu, Y. Liu, X. Lei, G. Wang, Y. Wu, Z. Mi, J. Liu, H. Wang, H. Gao, Evading the strength–ductility trade-off dilemma in steel through gradient hierarchical nanotwins, *Nature Commun.* 5 (2014) 3580, <http://dx.doi.org/10.1038/ncomms4580>.
- [28] J.K. Holmen, J. Johnsen, O. Hopperstad, T. Børvik, Influence of fragmentation on the capacity of aluminum alloy plates subjected to ballistic impact, *Eur. J. Mech. A Solids* 55 (2016) 221–233, <http://dx.doi.org/10.1016/j.euromechsol.2015.09.009>.
- [29] H. Granum, V. Aune, T.B. rvik, O.S. Hopperstad, Effect of heat-treatment on the structural response of blast-loaded aluminium plates with pre-cut slits, *Int. J. Impact Eng.* 132 (2019) 103306.
- [30] C.O. Paulsen, Experimental Characterization of Two-Phase Steels, (Ph.D. thesis), Department of Materials Science and Engineering, NTNU, 2019.
- [31] Swedish Steel A.B. (SSAB), 2020, <https://www.ssab.com/products/brands/doccol> (Accessed 13 July 2021), Online.
- [32] G. Gruben, M. Langseth, E. Fagerholt, O. Hopperstad, Low-velocity impact on high-strength steel sheets: An experimental and numerical study, *Int. J. Impact Eng.* 88 (2016) 153–171.
- [33] E. Fagerholt, Field Measurements in Mechanical Testing Using Close-Range Photo-Grammetry and Digital Image Analysis, (Ph.D. thesis), NTNU, Norwegian University of Science and Technology, 2012.
- [34] J.K. Holmen, O.S. Hopperstad, T.B. rvik, Low-velocity impact on multi-layered dual-phase steel plates, *Int. J. Impact Eng.* 78 (2017) 161–177.
- [35] E. Fagerholt, Online, <https://www.ntnu.edu/kt/ecorr> (Accessed 13 July 2021).
- [36] V. Aune, G. Valsamos, F. Casadei, M. Langseth, T.B. rvik, Fluid-structure interaction effects during the dynamic response of clamped thin steel plates exposed to blast loading, *Int. J. Mech. Sci.* 195 (2021) 106263.
- [37] R. Ritchie, The conflicts between strength and toughness, *Nature Mater.* 10 (2011) 817–822, <http://dx.doi.org/10.1038/nmat3115>.

Benjamin Stavnar Elveli, Tore Børvik, Vegard Aune

Influence of material properties on the performance of blast-loaded steel plates with pre-cut defects

In: Proceedings of EPJ Web of Conferences 250, 02028 (2021)
DYMAT 2021

DOI: <https://doi.org/10.1051/epjconf/202125002028>

Influence of material properties on the performance of blast-loaded steel plates with pre-cut defects

Benjamin S. Elveli^{1,2*}, *Tore Børvik*^{1,2}, and *Vegard Aune*^{1,2}

¹Structural Impact Laboratory (SIMLab), Department of Structural Engineering, NTNU – Norwegian University of Science and Technology, Norway

²Centre for Advanced Structural Analysis (CASA), NTNU, Norway

Abstract. Experimental and numerical investigations are carried out to determine how thin steel plates with pre-cut defects behave under blast loading. The defects considered in this study are represented by four square holes, symmetrically distributed around the centre of the target plates. The target plates were manufactured from two types of steel, i.e., a dual-phase medium strength steel and a high-strength martensitic steel. A shock tube facility was used to expose the plates to blast-like loading conditions. The experiments showed that both the blast resistance and the corresponding fracture mode changed with material properties. Numerical simulations were performed using the finite element code LS-DYNA, where the numerical results were found to be in good agreement with the experimental data in predicting the ductile fracture during the blast-structure interaction. The numerical simulations confirmed that significant work hardening will distribute the plasticity throughout the plate material during deformation, while limited work hardening will tend to localize the plasticity that results in earlier fracture.

1 Introduction

Research on blast-resistant design has historically mostly been focusing on military installations with thick-walled massive constructions [1]. Civilian structures are often more lightweight and flexible than traditional fortified structures. As a result, it is seen an increased interest in studies on thin-walled structures [2,3]. These structures may also contain geometrical defects (e.g. for design purposes or by fragments accelerated by a blast wave that impacts the target plate prior to the blast pressure). This results in local areas of high stress concentrations and a more complex behaviour under blast loading.

Moreover, from a protective point of view, a common perception is that increased strength leads to increased protection against external loading. However, this is not always the case. A high strength generally comes at the price of a reduction in ductility. This strength-ductility trade-off has been a long-standing dilemma in materials science [4] and should be considered

* Corresponding author: benjamin.s.elveli@ntnu.no

in protective design. This motivates detailed studies on the influence of material properties on the blast performance of thin steel plates with pre-cut defects.

2 Materials

In this study, two different steel materials were investigated. Docol 600DL is a dual-phase, medium-strength steel that undergoes significant work hardening and plastic deformation before fracture, while Docol 1400M is a pure martensitic high-strength steel characterized by higher strength, less work hardening and lower ductility. Both materials are cold-rolled and produced by the Swedish manufacturer SSAB [5].

Dual-phase steels consist of a soft ferrite matrix with islands of hard martensite. This unique combination yields a material with a high ductility due to the ferrite, and a strength depending on the amount of martensite. Hence, an increased amount of martensite will lead to an increase in strength, but also to a decrease in ductility [6]. The chemical composition for both materials is given in Table 1.

Table 1. Chemical composition of Docol 600DL and Docol 1400M (in wt.%) [5].

Material	C (max %)	Si (max %)	Mn (max %)	P (max %)	S (max %)	Al (min %)	Nb+Ti (max %)
Docol 600DL	0.1	0.4	1.50	0.01	0.002	0.04	-
Docol 1400M	0.2	0.4	1.60	0.02	0.01	0.015	0.1

Quasi-static tension tests of the Docol 600DL material was conducted by Aune et al. [7]. Dog-bone test specimens were manufactured in 0°, 45° and 90° relative to the rolling direction of the target plates, and a slightly anisotropic behaviour was found both in flow stress and elongation to fracture. For the Docol 1400M material, a new set of quasi-static tension tests was performed in Ref. [8], using the same test setup as in Ref. [7]. The corresponding engineering stress-strain curves to fracture are given in Fig. 1. Here, the engineering fracture strain for the Docol 1400M material varied between 0.025 and 0.045, and for the Docol 600DL material between 0.22 and 0.28. Since an isotropic behaviour was assumed for both materials, the tension tests in the 0° direction were used for calibration of the constitutive model. Due to the large variations within the tension tests in the 0° direction for Docol 1400M, it was decided to calibrate material parameters for both the tension test giving the largest and the smallest engineering strain at failure within the 0° direction (see Fig. 1a and Table 2).

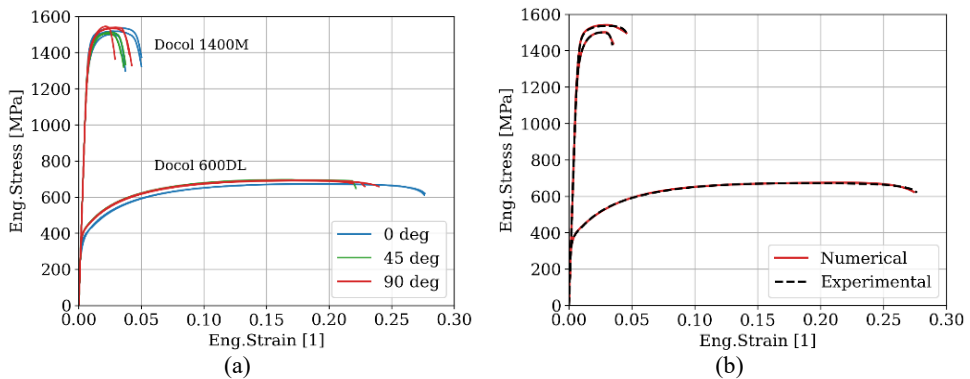


Fig. 1. Engineering stress-strain curves for Docol 600DL and Docol 1400M: (a) experimental curves and (b) numerical results applying the fitted material parameters in the simulations.

3 Experimental setup

All blast tests were carried out in the SIMLab Shock Tube Facility (SSTF) at NTNU. The performance of the SSTF in generating a blast-like environment is thoroughly described in Ref. [9]. The overall dimensions and features of the SSTF are given in Fig. 2a. The dynamic response of the target plates is recorded during the entire blast-loading event using two high-speed cameras (Phantom v2511) with a sampling rate of 37 kHz. Additionally, the pressure is recorded at the two pressure sensors indicated in Fig. 2a, both with a sampling rate synchronized with the high-speed camera recordings and at 500 kHz. The synchronization allows for a time axis related to the loading history of the target plates.

All target plates used in this study had a nominal thickness of 0.8 mm and a blast-exposed area of 300 mm × 300 mm, corresponding to the inner cross section of the SSTF. Four pre-formed 60 mm × 60 mm square holes were cut out of the target plates, as illustrated in Fig. 2b. Plates of both materials were exposed to blast intensities resulting from firing pressures of 15 bar, 25 bar and 35 bar. These three firing pressures correspond to a peak reflected pressure on the surface of the target plates of approximately 0.62 MPa, 0.83 MPa, and 1.19 MPa, followed by an exponential decay over a period of 45-75 ms.

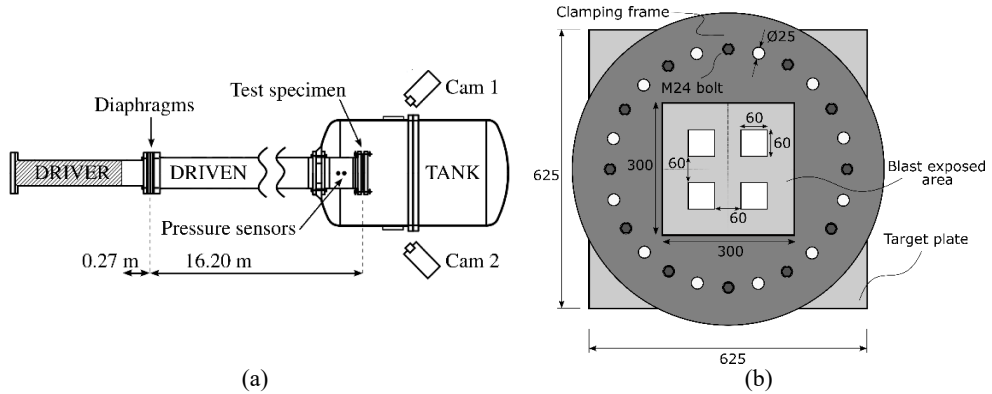


Fig. 2. The SIMLab Shock Tube Facility (SSTF) [9]: (a) a sketch of the entire facility and (b) the geometry of the clamping assembly and the blast-loaded target plates with pre-formed square holes.

4 Numerical model

All simulations in this study were performed in the explicit finite element code LS-DYNA. The material behaviour is described through a thermoviscoplastic constitutive model, which was implemented as a user-defined material model in LS-DYNA. The model is capable of describing large plastic strains, high strain rates and possible temperature softening, and is given by:

$$\sigma_{eq} = (\sigma_0 + R(p))(1 + \dot{p}^*)^c (1 - T^{*m}) \quad (1)$$

where σ_{eq} denotes the equivalent flow stress, given by a Hershey yield surface expressed in terms of the principal stresses σ_i as:

$$\sigma_{eq} = (|\sigma_1 - \sigma_2|^n + |\sigma_2 - \sigma_3|^n + |\sigma_3 - \sigma_1|^n)^{\frac{1}{n}} \quad (2)$$

where n determines the shape of the yield surface. The von Mises yield surface is obtained by setting $n = 2$, and Tresca by either $n = 1$ or $n = \infty$. $R(p)$ describes the work hardening

as a function of the equivalent plastic strain p , which is described by a three-term Voce hardening law on the form:

$$R(p) = \sum_{k=1}^3 Q_k (1 - e^{-c_k p}) \quad (3)$$

The initial yield stress is given by σ_0 , and (Q_k, c_k) are hardening parameters. The exponents c and m are constants governing the rate and temperature dependency of the material. The dimensionless plastic strain rate is given by $\dot{p}^* = \dot{p}/\dot{p}_0$, where \dot{p}_0 is the reference strain rate used in the quasi-static tension tests. In this study, $n = 6$ was applied for the yield surface and $m = 1$ for the temperature softening part for both materials.

Finally, ductile fracture is accounted for by the energy-based fracture criterion proposed by Cockcroft-Latham [10]

$$D = \frac{W}{W_c} = \frac{1}{W_c} \int_0^p \langle \sigma_1 \rangle dp \quad (4)$$

where σ_1 denotes the major principal stress, W is the accumulated damage, and W_c is the critical damage level leading to fracture in the model. D then represents the normalized damage parameter, and element erosion is used to delete the element when $D = 1$.

The critical damage W_c was determined for each material and mesh by inverse modelling of the quasi-static tension tests to fracture. The hardening parameters (Q_k, c_k) were found by an optimization of the numerical simulation of the tension tests. The strain rate sensitivity parameters were taken from Ref. [11]. All material parameters are given in Table 2.

Table 2. The material parameters applied for both materials in this study.

Material	σ_0 [MPa]	Q_1 [MPa]	C_1 [-]	Q_2 [MPa]	C_2 [-]	Q_3 [MPa]	C_3 [-]	c [-]	W_c [MPa]
Docol 600DL	303.3	68.3	849.1	272.4	30.2	825.9	1.2	0.01	865.0
Docol1400M-1	1072.9	211.7	1504.8	195.6	231.7	76.1	79.4	0.004	425.0
Docol1400M-2	1150.0	309.5	1061.0	113.0	131.7	9061.0	0.09	0.004	452.0

5 Results

The global response of thin steel plates exposed to blast loading has been evaluated thoroughly in Refs. [7,8,12], and the focus in this study is directed more towards fracture modes and crack propagation. Further, a detailed numerical study on the Docol 600DL material was performed in Ref. [7]. The numerical simulations were therefore limited to the tests on the Docol 1400M material in this study.

Experimentally, the behaviour of the six blast tests yielded three distinct responses of the target plates: plastic deformations without any signs of fracture, plastic deformations and crack initiation, and complete fracture. In Refs. [7,8], it was observed that the Docol 600DL material experienced plastic deformations and crack initiation at the extremities of the holes for the 15 bar and 25 bar firing pressures, while the highest firing pressure of 35 bar resulted in complete fracture of the target plate with cracks along the diagonals. In this study, the Docol 1400M plates resulted in small plastic deformations without any visual crack initiation for the 15 bar firing pressure, and complete fracture when the firing pressure was increased to 25 bar and 35 bar. The reduced ductility in Docol 1400M seems to reduce the plates capacity to arrest the crack propagation, while the Docol 600DL plates experienced only crack initiation at the lowest and intermediate firing pressures. Thus, an increase in the

material strength resulted in a reduced capacity against ductile fracture during blast loading. The final deformation or fracture mode of all six blast experiments are shown in Fig. 4.

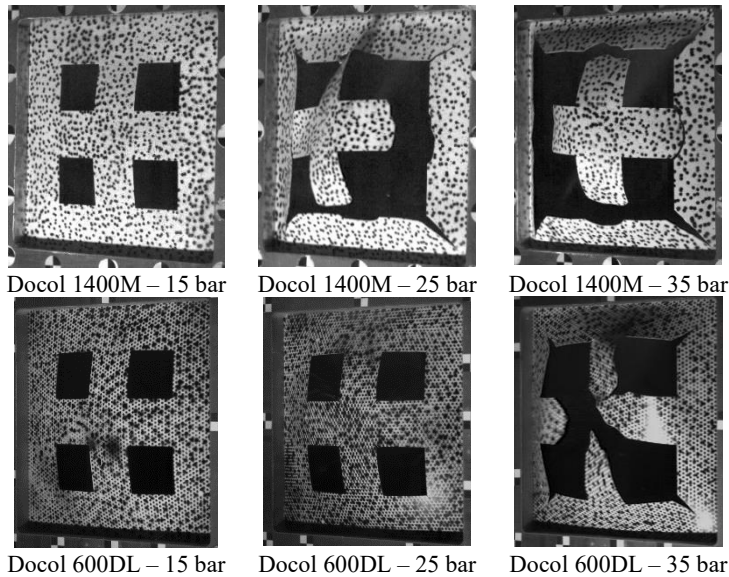


Fig. 4. Experimental results for all six experiments. Both the material and firing pressure are indicated in the sub-caption of each image.

All target plates were discretized using four solid elements across the thickness, corresponding to an element size of 0.2 mm. The full clamping assembly, shown in Fig. 2b was modelled, and quarter symmetry was utilized. The experimental results indicate that the 15 bar firing pressure for the Docol 1400M material is very close to the limit for crack initiation and ductile fracture. Therefore, it was further decided to run this simulation using material calibrations for two of the tension tests in the 0-direction, with different levels of flow stress and elongation to fracture (see Fig. 1 and Table 2).

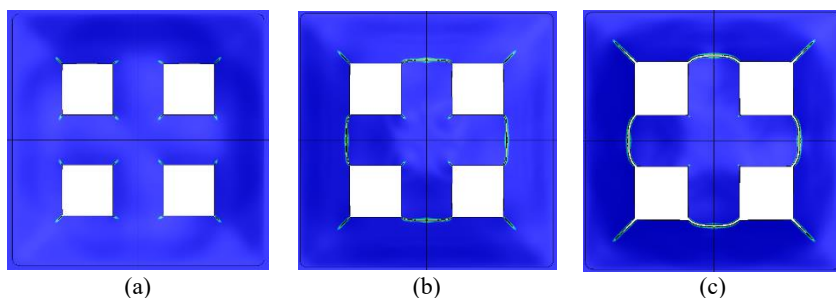


Fig. 5. Numerical results for the blast experiments on the Docol 1400M material for a firing pressure of 15 bar in (a) and (b), and 25 bar in (c). In (a) the fitted parameters for the Docol 1400M-2 was applied, while the material parameters for Docol 1400M-1 were used in (b).

As seen in Fig. 5c, the numerical model was capable of describing the fracture mode observed in the experiments for the 25 bar firing pressure. It is noted that an identical failure mode was also obtained for the simulation of the 35 bar firing pressure. For the lowest firing pressure of 15 bar, two different results were found based on the choice of stress-strain curves for the calibration of material parameters. As seen in Fig. 5 (a) and (b), the material parameters corresponding to the tension test in the 0-direction with the largest elongation to

fracture (Docol 1400M-2) resulted in small arrested cracks, while the material parameters corresponding to the test in the 0-direction with the smallest elongation to fracture (Docol 1400M-1) resulted in complete fracture at the same firing pressure. Hence, a strong sensitivity to the choice of experimental stress-strain curve for material calibration was found. This effect was however not investigated any further in this study and is suggested as further work.

6 Concluding remarks

The present study investigates the influence of material properties on the blast performance of thin steel plates with pre-cut defects. Such effects were studied by combining experimental and numerical results. The main conclusions from the study are as follows.

- The steel plates with the lowest strength and the highest ductility (Docol 600DL) showed an increased capacity against fracture during blast loading compared to the steel plates made of the stronger and less ductile Docol 1400M material.
- The steel materials under consideration resulted in distinct differences in fracture mode when exposed to the same blast intensity. This behaviour was also captured by the numerical simulations.
- The Docol 1400M material showed a stronger sensitivity to the choice of material curve used in the calibration of the material parameters than the Docol 600DL material.
- It is emphasized that this work is ongoing research and that the presented results should be used with caution. More detailed studies are planned as further work.

References

1. W. Wilkinson, D. Cormie, M. Arkininstall. Proc. Inst. Civ. Eng. Eng. Comput. Mech. **166** (2013) 132-139.
2. L. Li, Q.-C. Zhang, R. Zhang, X. Wang, Z.-Y. Zhao, S.-Y. He, B. Han, T. J. Lu. Int. J. Impact Eng. **134** (2019) 103382.
3. W. Li, P. Wang, G.-P. Feng, Y.-G. Lu, J.-Z. Yue, H.-M. Li. Def. Technol. In Press (2020).
4. Y. Wei, Y. Li, L. Zhu, Y. Liu, X. Lei, G. Wang, Y. Wu, Z. Mi, J. Liu, H. Wang, H. Gao. Nat. Commun. **5** (2014) 3580.
5. SSAB Swedish Steel Ltd. <https://www.ssab.com/products/brands/docol/docol-product-overview> [accessed 22.03.21].
6. C. O. Paulsen. Experimental characterization of two-phase steels. Ph.D. thesis, NTNU (2019).
7. V. Aune, G. Valsamos, F. Casadei, M. Langseth, T. Børvik. Int. J. Impact Eng. **108** (2017) 27-46.
8. B. S. Elveli, M. Iddberg, T. Børvik, V. Aune. To be submitted (2021).
9. V. Aune, E. Fagerholt, M. Langseth, T. Børvik. Int. J. Protective Struct. **7** (2016) 340-366.
10. M. G. Cockcroft, D. J. Latham. J. Inst. Met. **96** (1968) 33-39.
11. G. Gruben, M. Langseth, E. Fagerholt, O. Hopperstad. Int. J. Impact Eng. **88** (2016) 153-171.
12. H. Granum, V. Aune, T. Børvik, O.S. Hopperstad. Int. J. Impact Eng. **132** (2019) 103306.

PART 3

Benjamin Stavnar Elveli, Tore Børvik, Vegard Aune

Blast-load response of thin steel plates after ballistic impact from small-arms projectiles

In: proceedings of Light-Weight Armour Group for Defence and Security (2019)
166-175

This paper is not included due to copyright restrictions.

PART 4

Benjamin Stavnar Elveli, Torodd Berstad, Tore Børvik, Vegard Aune

Performance of thin blast-loaded steel plates after ballistic impact from small-arms projectiles

Submitted for possible peer review journal publication

Performance of thin blast-loaded steel plates after ballistic impact from small-arms projectiles

Benjamin Stavnar Elveli^{a,b,*}, Torodd Berstad^{a,b}, Tore Børvik^{a,b}, Vegard Aune^{a,b}

^a*Structural Impact Laboratory (SIMLab), Department of Structural Engineering, NTNU – Norwegian University of Science and Technology, NO-7491 Trondheim, Norway*

^b*Centre for Advanced Structural Analysis (CASA), NTNU, NO-7491 Trondheim, Norway*

Abstract

It is known from real blast-load events that the combined effect of fragment impact and blast loading is more severe than the effect of the blast loading alone. The present study investigates this effect by comparing the blast response of thin steel plates pre-damaged by either ballistic impacts or idealized pre-cut circular holes under similar blast loading conditions. The ballistic impacts were performed with a rifle, firing 7.62 mm APM2 projectiles, and the subsequent blast loading was applied in a shock tube facility. During the blast tests, pressure measurements and two high-speed cameras were used to record the dynamic response of the target plates and allowed for a reliable experimental procedure. To investigate the strength-ductility trade-off dilemma of the material during extreme loading, three different steels with different levels of strength and ductility were used in the tests. Numerical simulations were conducted in an attempt to obtain more insight into the fracture characteristics of the plates.

For similar loading conditions and material, the target plates exposed to ballistic impact showed a reduced resistance to fracture during blast loading compared with target plates containing pre-formed circular holes. As for the effect of material strength and ductility, the global deformation decreased, while the localization of plasticity increased, with an increased material strength. The fracture resistance was also observed to decrease with increased material strength. The numerical models were able to capture the main trends observed in the physical tests, i.e., a decrease in fracture resistance with initial ballistic impact, and a reduction in fracture resistance with increased material strength. The numerically predicted crack paths also showed a strong dependence upon the initial cracks caused by the petals from the ballistic impacts.

Keywords: Strength-ductility trade-off, Ballistic impact, Shock tube, Combined impact and blast loading

1. Introduction

Blast waves can be caused by industrial accidents, military actions or terrorist attacks, subjecting surrounding structures to extreme loading. In addition, the blast wave can accelerate objects in its proximity

*Corresponding author. Tel.: +47-73-59-47-05; fax: +47-73-59-47-01.

Email address: benjamin.s.elveli@ntnu.no (Benjamin Stavnar Elveli)

to high velocities. These objects are typically categorized as primary and secondary fragments. Primary fragments are defined as objects initially contained in the explosive device (e.g., ball bearings [1]) or parts from the fractured casing of the explosive (e.g., a shell or a vehicle). Fragments may impact the structure before, during or after the arrival of the blast wave, depending on the distance between the explosive charge and the structure [2]. These fragments may perforate the structure, introducing both geometrical defects and initial material damage. A fragment perforation prior to the arrival of the blast wave, may reduce the load-carrying capacity of the structure and the combined effects of blast and fragment impact can be more severe than the blast loading acting alone (see e.g. [3–7]). However, the literature is rather scarce when it comes to studies on the combined effects of blast and fragment loading, and most of the existing research on combined loading effects are on concrete structures [8–12]. Nevertheless, modern civilian structures tend to be more lightweight and flexible than the traditional fortified structures, and the responses of thin-walled metallic plates have received increased interest over the last few years [13–15].

Pre-cut defects may imitate the geometrical defects imposed by fragment impact. It was shown in [16] that idealized perforations reduce the plates resistance both against plastic deformations and fracture. Pre-cut defects typically introduce sharp corners and local areas of increased stress, which amplifies ductile crack initiation and growth. In [17–19], the blast response of target plates containing pre-formed circular holes and pre-formed square holes was compared. All three studies concluded that the fracture resistance during blast loading was dependent upon the pre-formed hole geometry, where the square perforations resulted in the lowest resistance. Further, Granum et al. [20] found that the effect of the number, distribution and orientation of pre-cut slits in thin blast-loaded aluminium plates strongly affects both the fracture resistance and the failure mode. However, during a fragment perforation, the corresponding fragment hole depends upon the size and shape of the fragment. Moreover, additional material damage can occur in the proximity of the hole. These effects are not covered by studies on plates with idealized preformed defects, which could lead to non-conservative estimates of the fracture resistance during blast loading.

Experimental studies on the combined effect of fragment and blast loading are ideal as they represent the actual physics of the problem, whereas theoretical and numerical methods need to be validated against experimental data to ensure that they provide reliable predictions. Testing on full-scale prototype structures is normally considered too expensive, time-consuming, and infeasible, and is seldom an option. Therefore, controlled small-scale experiments on simple structures have a significant potential in improving our understanding of the combined effect of blast loading and fragment impact. Cai et al. [21] performed an experimental study on multi-layered aluminum foam sandwich panels, exposed to a combined loading from TNT and 52 attached prefabricated square fragments. The experimental results gave three different responses for the backplate of the sandwich panel; petaling, cracking, or only deformation. Li et al. [22] applied a similar setup for an experimental and numerical study on composite laminates subjected to blast and fragment loading. It was concluded that the applied numerical model gave reliable results, and was in

good agreement with the experiments.

40 From a numerical point of view, fragment impact on a structure is similar to ballistic impact problems. A well known challenge in numerical modeling of ballistic impact is that a very fine discretization of the structure is required to obtain reliable predictions (see e.g., [23, 24]). Also, high-velocity impacts are commonly governed by local deformations in the material with a relatively short duration. In contrast, the deformation of blast loaded thin-walled structures is normally governed by global deformation, with a significantly longer
45 duration [16, 25, 26]. For a blast simulation to run within a reasonable computational (CPU) time, a much coarser discretization of the deforming structure is required. This is challenging when modelling the combined effect of fragment impact and blast loading of plated structures, especially if a realistic fracture mode from the fragment impact phase and a feasible CPU cost during the blast loading phase of the simulation are important.

50 In previous studies, fragment impact prior to blast loading has been represented by pre-cut defects with idealized geometries. This study aims to investigate the effect of more realistic perforations on the blast resistance of thin steel plates, assuming that the fragment impacts before the blast wave. First, the plates were perforated by 7.62 mm APM2 projectiles in a ballistic range. Then, the perforated plates were subjected to blast loading in a shock tube facility. Three different steel qualities were applied for the target plates
55 to also include the strength-ductility trade-off [27]. Finally, numerical simulations were conducted to gain more insight into the fracture characteristics of the blast-loaded plates. The main objectives of this study are: (1) to provide new insight into the effect of realistic fracture modes on the blast resistance of thin steel plates, comparing the performance of plates with ballistic perforations to that of plates with idealized pre-cut circular holes under similar blast loading conditions; (2) address challenges in the numerical modelling
60 and simulation of combined ballistic impact and blast loading; and (3) evaluate the capability of current computational methods in predicting the dynamic response and fracture resistance of the materials under consideration.

2. Materials

To study the effect of strength and ductility on the fracture resistance during testing, three different steel
65 qualities were used, i.e., Docol 600DL, Docol 1000DP and Docol 1400M. All target plates were produced by SSAB [28] and cold rolled to a thickness of 0.8 mm. Docol 600DL represents a dual-phase, medium strength, high-hardening steel with good formability compared to its strength. It has a reported yield strength in the range of 280 - 360 MPa and an ultimate tensile strength of 600 - 700 MPa. Docol 1000DP is also a dual-phase steel, but with a higher martensite fraction than Docol 600DL. Docol 1400M is a strong martensitic steel
70 with a reported minimum yield strength of 1150 MPa and an ultimate tensile strength in the range of 1400 - 1600 MPa. The high strength is obtained by a rapid water quenching of an austenitic steel so that the

carbon atoms are unable to diffuse and form cementite. The chemical compositions for all three materials are given in Table 1. For simplicity, the following abbreviations have been introduced for the material names; Docol 600DL is denoted D6, Docol 1000DP is denoted D10, and Docol 1400M is denoted D14.

Table 1: Chemical composition of the three materials (in wt.%) taken from the data sheet of the current batch.

Material	C	Si	Mn	P	S	Cr	Ni	V	Cu	Al	Nb+Ti	B	N
D6	0.095	0.30	1.45	0.012	0.003	0.02	0.03	0.01	0.01	0.052	0.0	0.0003	0.003
D10	0.137	0.20	1.51	0.008	0.003	0.02	0.04	0.01	0.01	0.04	0.015	0.0002	0.007
D14	0.173	0.19	1.32	0.011	0.003	0.03	0.04	0.02	0.15	0.042	0.03	0.0017	0.004

75 2.1. Material testing

Quasi-static uniaxial tension tests were carried out for all three materials in an Instron 5982 testing machine at a constant deformation rate of 2.1 mm/min. The specimen geometry is given in Figure 1(a). With a gauge length of 70 mm, the applied deformation rate corresponds to a global strain rate of $\dot{\epsilon}_0 = 5 \cdot 10^{-4} \text{s}^{-1}$. The specimens were cut from the 0.8 mm sheets with 0°, 45° and 90° relative to the rolling direction. Three repetitions were performed in each direction for each material to reveal possible anisotropy.

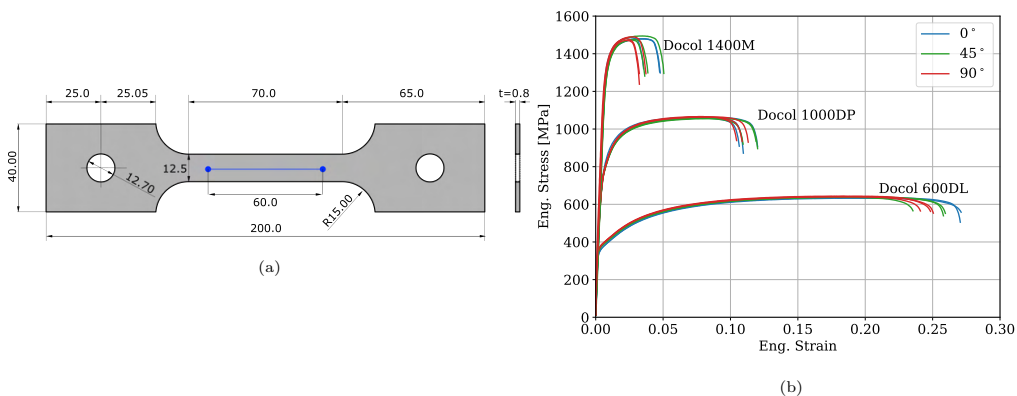


Figure 1: (a) Sketch of the uniaxial tension test specimen and the position of the virtual extensometer marked with a blue line, and (b) the corresponding engineering stress-strain curves for all three materials. All dimensions are in mm.

To determine the engineering stress-strain curves in Figure 1(b), the force was measured by the load cell in the testing machine and the displacement was obtained from 2D-DIC using a virtual extensometer. During each test, the force measurements were synchronized with images of the test specimen at a sampling rate of 4 Hz. Prior to the tests, each specimen was spray-painted with a black and white speckle pattern, allowing for two-dimensional (2D) digital image correlation (DIC). A virtual extensometer of 60 mm was

applied to calculate the engineering strain. The engineering stress was calculated by scaling the force with the initial gauge area of the test specimen, measured with a digital caliper.

Figure 1(b) confirms the step-wise change in yield stress, strength, and strain to fracture for the three materials under consideration. That is, the yield stress, strength and strain to fracture for Docol 1000DP lies between Docol 600DL and Docol 1400M. For all three materials, some variations are seen in the engineering failure strain. However, the variation between tests in the three different directions is of a similar magnitude as the variation between repeated tests within each direction. For both the flow and yield stress, no significant variation was observed. Gruben et al. [29] investigated both the D6 and D14 materials with similar results for the uniaxial tension tests, and concluded that the plastic anisotropy was negligible. This was later confirmed by Aune et al. [26].

3. Component tests

The main objective of the component tests was to study the effect of ballistic perforations on the subsequent blast response of thin steel plates, and to compare the performance of these plates to that of plates with idealized holes under similar blast loading conditions. Hence, plates with pre-cut circular holes with a diameter similar to the projectile were also tested against blast loading to establish a reference to the ballistic impact hole containing damage and petalling cracks. The target plates were first subjected to ballistic impact, before exposed to blast-like loading using two different load intensities for each plate configuration.

3.1. Ballistic impact tests - setup

The ballistic tests were done in the gas gun facility at SIMLab [30]. Instead of firing the projectiles from the gas gun itself, a smooth bore Mauser rifle was mounted inside the steel tank of the gas gun as illustrated in Figure 2(a). 7.62 mm APM2 projectiles were used as projectiles, with the dimensions and composition given in Figure 2(b). One shot was fired against the center of each target plate, with two repetitions for each of the three materials. This leaves a total of 6 ballistic impact tests.

The dimensions of the target plates and position of the pre-cut circular and ballistic impact holes are illustrated in Figure 3. The intention of the ballistic perforations at the same position and with similar hole diameters as the pre-cut circular holes, was to investigate the effect of damage and petalling cracks from ballistic impacts on the blast resistance of the plates. The initial velocities of the projectiles were chosen to be significantly higher than the ballistic limit velocity, facilitating localized fracture modes limited to the point of impact. Hence, the ballistic limit velocity for these plates was not of interest in this study.

The penetration and perforation process of the target plates were recorded by a Phantom v2511 high-speed camera, and the pitch both before and after impact was confirmed to be low. The image series also allowed for accurate measurements of both the initial and residual velocities of the projectile, as well as

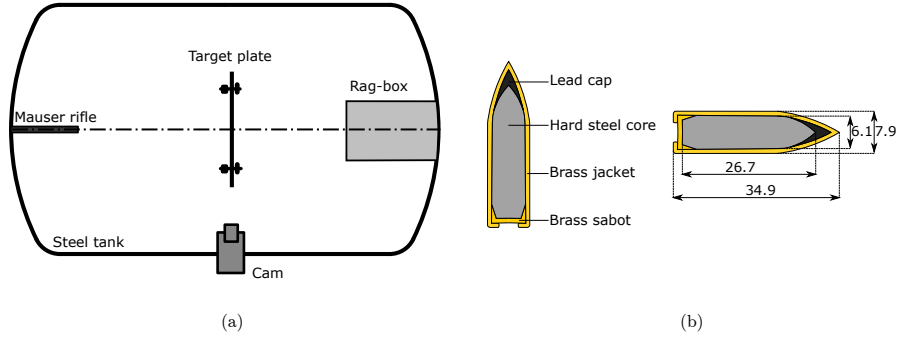


Figure 2: The experimental setup during the ballistic impact tests: (a) the target plate and smooth bore Mauser rifle inside the steel tank, and (b) the material composition and dimensions of the 7.62 APM2 bullet. All dimensions are in mm.

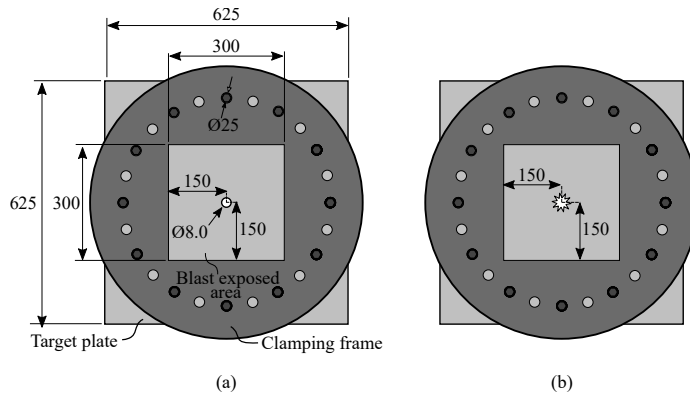


Figure 3: The two plate geometries under consideration in this study: (a) The plate with pre-cut circular hole (C) geometry, and (b) the plate with the ballistic hole (B) geometry. All dimensions are in mm and the plates had a thickness of 0.8 mm.

observing the dynamic response of the plates and possible deformations of the projectiles. The initial and residual velocities were obtained by using a point-tracking algorithm on the high-speed images using the in-house DIC software eCorr [31].

3.2. Ballistic impact tests - results

The ballistic impact tests were conducted with initial projectile velocities in the range of 910 m/s - 932 m/s, and the velocity reduction after perforation was less than 2% in all tests. Fig. 4(a) shows a representative image sequence of the ballistic impact event, where no visual damage or plastic deformation occurred in the projectiles. All target plates fractured by petalling, where three representative pictures of the exit holes are given in Fig. 4(b-d). Visual inspection of the target plates confirmed that the deformation was localized around the impact hole. The measured diameters of the bullet holes were in the range 8.1 mm

- 8.4 mm, comparable to the plate geometry with pre-cut circular holes as shown in Figure 3(a). It is noted that some of the petalling cracks extended slightly outside the periphery of the visual bullet hole (see e.g., Fig. 4(d)). However, no clear differences were observed in the petalling modes of the three materials, or between repeated tests. The important observation was that the ballistic impact tests succeeded in creating perforations containing local damage with good repeatability.

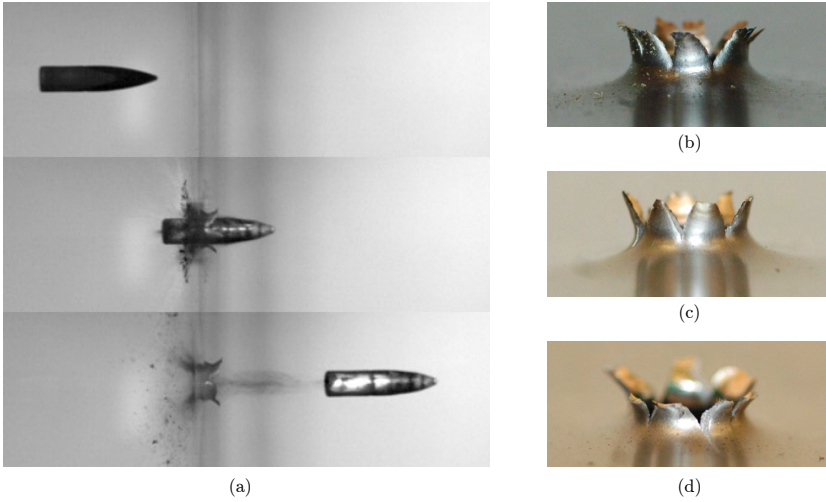


Figure 4: Representative image sequence of the projectile perforation: (a) High-speed photography of the ballistic impact, and representative images of the corresponding fracture modes for (b) D6 plates, (c) D10 plates and (d) D14 plates.

3.3. Blast load tests - setup

All blast load experiments were performed in the SIMLab Shock Tube Facility (SSTF). This test facility is thoroughly described and validated for blast-like loading by Aune et al. [16, 32], and is therefore only briefly presented in this section. The SSTF is designed to generate planar blast waves in air and allows for both the blast wave phenomena and the corresponding response of structures to be studied. A sketch of the SSTF is given in Fig. 5.

The propagation of the blast wave is initiated at the driver side of the shock tube and impacts the target plate just inside the steel tank at the right end of the tube. In this study, all experiments were performed with a driver length of 0.77 m and compressed air was used to pressurize the driver section. The target plates were mounted to the shock tube by using a clamping assembly. The dimensions of the clamping assembly are given in Fig. 3. All target plates had dimensions of 625 mm × 625 mm × 0.8 mm and a blast-exposed area of 300 mm × 300 mm.

To monitor the tests, the facility is equipped with two high-speed cameras (Phantom v2511) and several pressure sensors (Kistler type 603B) for a synchronized sampling of data. The high-speed cameras operated

at a frame rate of 37 kHz, while both the incoming and reflected overpressure were sampled with a frequency of 500 kHz at Sensor 1 in Fig. 5. Sensor 1 is located 245 mm upstream of the target plates and serves as the best available estimate for the pressure acting on the surface of the target plates. Hence, all pressure measurements presented in this study are measured at Sensor 1 and represent the overpressure relative to atmospheric conditions. After blast loading, the plates were measured in-situ with a portable Romer Absolute Arm 7525SI laser scanner that generates a point cloud of the deformed geometry of the tested plates.

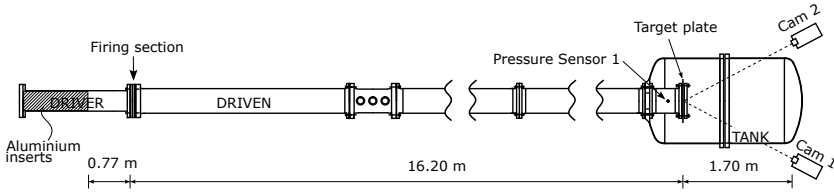


Figure 5: Illustration of the SIMLab Shock Tube Facility (SSTF), where the pressure sensor used in this study (Sensor 1) is located 245 mm upstream the target plate [27].

Plates with pre-cut circular holes (C) and plates with ballistic holes (B) were tested against two different blast intensities for each material. For a complete comparison of all three materials and the effect of pre-cut circular holes versus ballistic holes, it was decided to apply the same two blast intensities for both geometries and all three materials. This leaves a total of 12 blast-load experiments. The complete test matrix for all blast tests is given in Table 2, where each test is named according to the convention DX_Y_Z. DX refers to the materials, i.e., either D6, D10 or D14. Y specifies the geometry of the plate, i.e., pre-cut circular hole (C) or ballistic hole (B). Z indicates the blast intensity labeled by the firing pressure in the driver section in bar. The firing pressures listed in Table 2 are rounded to the lower multiple of 5, i.e., 25 or 35.

Table 2: Experimental program.

Firing pressure	C	B
25 bar	D6_C_25	D6_B_25
	D10_C_25	D10_B_25
	D14_C_25	D14_B_25
35 bar	D6_C_35	D6_B_35
	D10_C_35	D10_B_35
	D14_C_35	D14_B_35

3.4. Blast load tests - results

The presentation of the results focuses on the measured blast loading parameters from Sensor 1 (see Fig. 5), the global deformation fields of the target plates from the laser scans, and the crack initiation and propagation of cracks for a selection of representative tests. The firing pressure, the peak incoming pressure ($P_{\text{so,max}}$) and the peak reflected pressure ($P_{\text{r,max}}$), as well as the duration of the positive pressure phase (t_+) are all given in Table 3. The plate response under blast loading is also specified and divided into three response categories; no cracks, crack arrest, or total fracture.

Table 3: Blast parameters measured by Sensor 1 (Fig. 5). The firing pressure denotes the maximum pressure measured in the driver section right before rupture of the diaphragms. The peak incoming and peak reflected pressures at Sensor 1 are denoted $P_{\text{so,max}}$ and $P_{\text{r,max}}$, respectively. The duration of the positive phase of the reflected pressure at Sensor 1 is given by t_+ .

Test	Firing pressure [bar]	$P_{\text{so,max}}$ [kPa]	$P_{\text{r,max}}$ [kPa]	t_+ [ms]	Plate response
D6_C_25	24.9	270.1	772.5	46.1	No cracks
D6_B_25	23.9	260.9	726.4	44.5	No cracks
D10_C_25	24.2	276.5	775.8	42.4	No cracks
D10_B_25	24.3	280.6	791.2	42.3	Crack arrest
D14_C_25	24.1	266.7	796.6	44.3	No cracks
D14_B_25	24.3	277.7	809.9	42.4	Crack arrest
D6_C_35	35.0	327.4	958.2	49.9	No cracks
D6_B_35	36.9	344.6	1020.2	45.9	Crack arrest
D10_C_35	36.7	343.6	1069.0	43.0	No cracks
D10_B_35	36.9	338.1	1019.6	45.0	Crack arrest
D14_C_35	37.0	344.1	1106.6	46.3	Crack arrest
D14_B_35	37.8	340.1	1053.5	-	Total fracture

This study does not aim to present a detailed evaluation of possible fluid-structure interaction (FSI) effects. The blast parameters are mainly presented to verify that the applied blast loads are similar and repeatable for each of the load intensities. As the reflected pressure may depend upon the deformation history of the blast loaded plates, this is done by comparing $P_{\text{so,max}}$ between repeated tests. For tests at the same blast intensity, minor variations are observed in $P_{\text{so,max}}$. It is also noted that $P_{\text{r,max}}$ seems to increase with increased material strength, which indicates that FSI effects depend on the material under consideration. Aune et al. [33] investigated the FSI effects during the dynamic response of blast-loaded thin steel plates. The target plates in that study were manufactured from the D6 material with a thickness of 0.8 mm. It was found that the peak pressure experienced a reduction between 4% and 15% depending on

the blast intensity. However, FSI effects have not been investigated any further and are considered outside the scope of this study.

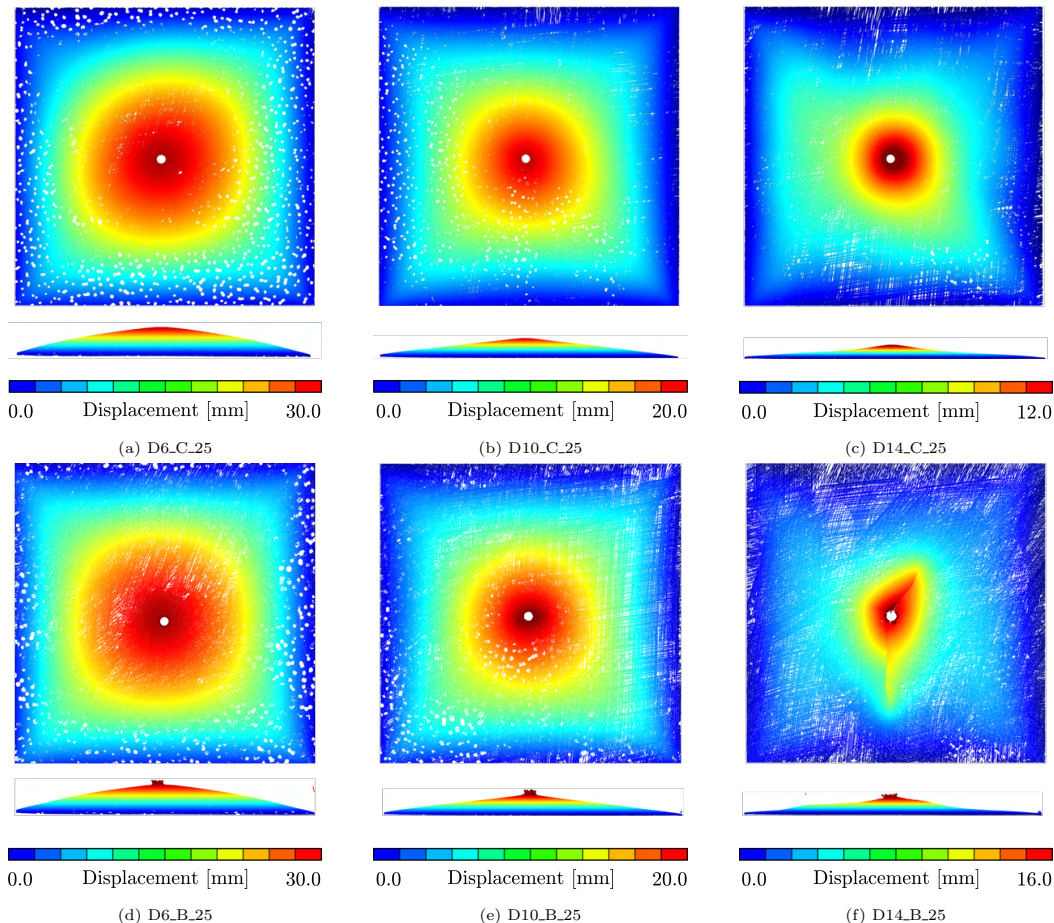


Figure 6: Point clouds from the laser scans of the target plates after blast loading. The colour map indicates the out of plane deformations. The limits for each colour map is given in the respective test, and the test names are given in the subcaptions. Test D14_B_25 in (f) experienced fracture, which is the reason for the discontinuities in the deformation field.

180 Fig. 6 presents the out-of-plane deformations of the plates as point clouds measured in-situ by the laser scanner after blast loading. The permanent deformations of the blast-exposed area are compared for all three plate materials when subjected to the lowest blast intensity. The colour map denotes the out-of-plane displacements with fringe levels given in the respective colour bars. For both geometries, the magnitude of the displacements decreases with an increase in material strength. As expected, the D6 plates

185 experience the largest displacements, the D14 plates undergo the smallest displacements, whereas the D10
plates are positioned in-between the other two plate materials. It is also observed that the distribution of
the deformations in the blast-exposed area changes with material. That is, the low strength material (D6)
experiences the largest deformations and distributes the deformations over the largest area. As the material
strength is increased, and the ductility decreased, the permanent deformations tend to localize in a smaller
190 region at the plate center. This is also in agreement with the findings of Refs. [20, 27, 34], because increased
work hardening tends to distribute plasticity on a larger area of the plate. The global response within each
plate material is however similar between the two hole geometries. It is noted that the D14_B.25 test (Fig.
6(f)) experienced significant cracking, and therefore increased displacements compared to the D14_C.25 test
(Fig. 6(c)). The cracks are seen as discontinuities in the displacement field. Hence, provided that the plates
195 do not fracture, the pre-damage does not seem to significantly affect the global deformations.

For the blast tests experiencing fracture, pictures showing the final state of the crack propagation are
given for tests on D6 and D10 plates in Fig. 7, and for tests on D14 plates in Fig. 8. The arrested cracks
in the D6 and D10 plates are rather short with crack lengths of about the same magnitude as the diameter
of the ballistic impact hole. It is noted that both the number and length of the cracks are increased from
200 D6_B.35 to D10_B.35, indicating that the D6 plate has greater resistance against both crack initiation and
crack propagation than the D10 plate. The D14 plates resulted in two tests with arrested cracks and one
test with total fracture (see Figure 8). The arrested cracks in the D14 plates are significantly larger than the
cracks for the D6 and D10 plates. Test D14_C.35 was the only test on the pre-cut circular hole (C) geometry
experiencing arrested cracks and test D14_B.35 was the only test resulting in total fracture. This shows
205 that the resistance against crack initiation and crack propagation is decreased when the material strength
is increased, i.e., D6 plates have the highest resistance, D14 plates have the lowest, whereas D10 ends up
in-between the other two. This confirms the results in Elveli et al. [27], where the strength-ductility trade-off
was studied for thin steel plates with idealized, pre-cut defects. That is, plates with low material strength
and high ductility resulted in better fracture resistance than stronger and less ductile plate materials.

210 Out of the 12 blast tests, 5 resulted in arrested cracks and one in total fracture. From Table 3, it is
concluded that the plates with the ballistic holes (B) are more prone to fracture. This shows that the
fracture resistance is reduced in the plates with ballistic holes, compared to the plates with idealized pre-cut
circular holes. This trend was observed for all three materials. Both the locations of crack initiation and the
directions of crack propagation during blast loading showed a strong dependence upon the petalling cracks
215 resulting from the ballistic impact prior to the blast loading. From Fig. 7 and 8, it is seen that all arrested
cracks in plates with the ballistic holes (B) were initiated at the initial petalling cracks. Thus, cracks started
to propagate in the directions of the petals formed during the ballistic impact. It was interesting to note that
the cracks propagated along other directions than the diagonals. The global response of thin, blast-loaded
plates are typically characterized by plastic hinges traveling from the supports toward the centre of the plate,

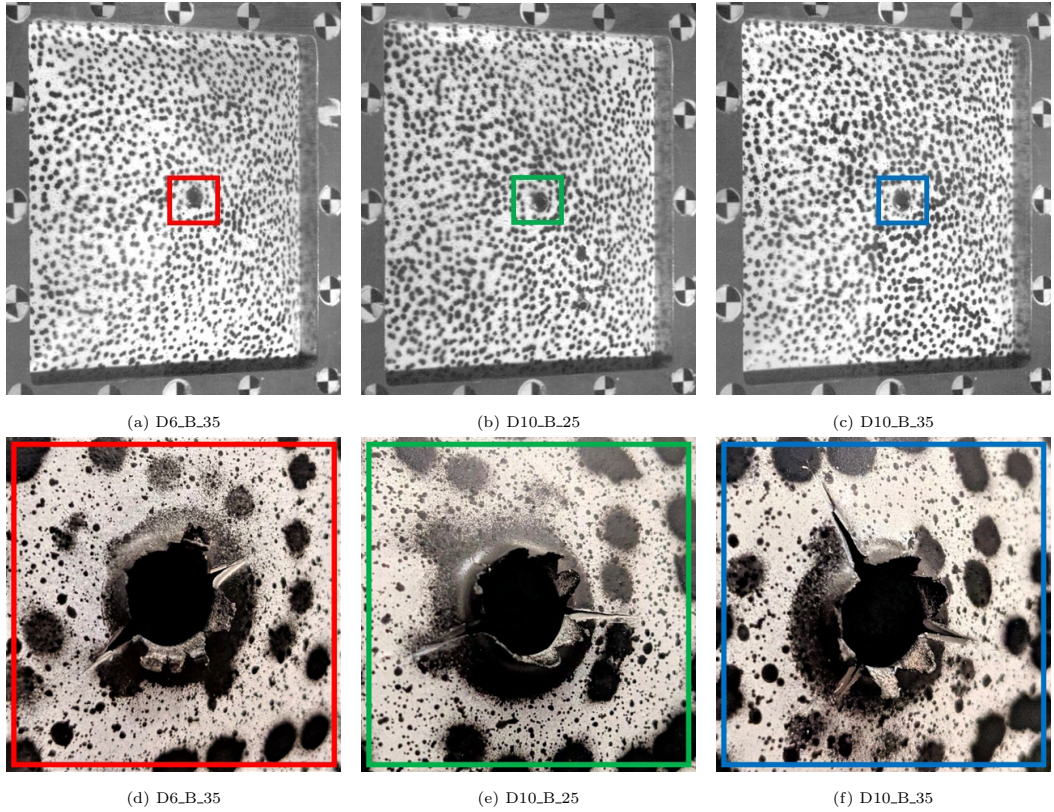


Figure 7: Pictures of the final state after blast loading for all tests on D6 and D10 plates experiencing cracking. The full blast exposed area is shown in (a)-(c), and zoomed-in views of the arrested cracks are presented in (d)-(f).

220 determining the deformed shape of the plate which is similar to a global dome. It is therefore often expected
that the cracks will turn towards the diagonals on their way towards the plate boundary [35]. However, this
was not the case in these tests. Test D14.B.35 showed that cracks propagated vertically and horizontally
from the center and all the way to the supports. It is also noted that, except for test D14.B.35, all crack
initiations and propagations were unsymmetrical. This is contrary to the findings in previous studies on
225 thin metallic plates with idealized pre-cut defects (see e.g., [16, 20, 27]), where cracks mainly initiated and
propagated along the plate diagonals in a symmetrical manner.

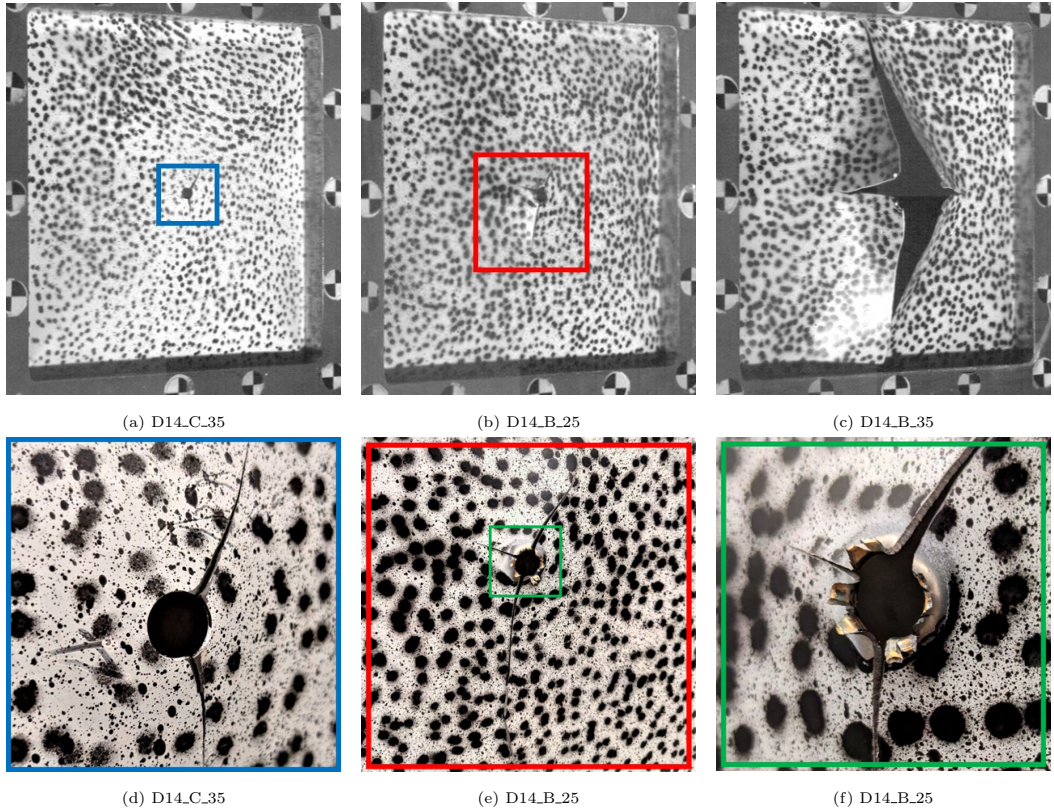


Figure 8: Pictures of the final state after blast loading for all D14 plates experiencing cracking. The full blast exposed area is given in (a)-(c), and zoomed-in views of the arrested cracks are given in (d)-(f). The test names are given in the subcaptions. Note that (f) gives a zoomed image of the green square in (e).

4. Material modelling

4.1. Constitutive relation and failure criterion

The thermoviscoplastic constitutive relation applied in this study is based on a modified version of the Johnson-Cook model, and has proven to give good results for metallic materials under extreme loading conditions [16, 20, 36, 37]. The flow stress accounts for plastic straining, elevated plastic strain rates, and temperature softening by

$$\sigma_{\text{eq}} = (A + R(p)) (1 + \dot{p}^*)^c (1 - T^{*m}) \quad (1)$$

where A is the yield stress, \dot{p}^* is the dimensionless plastic strain rate given by $\dot{p}^* = \dot{p}/\dot{p}_0$, where \dot{p} is the current equivalent plastic strain rate and $\dot{p}_0 = 5.0 \times 10^{-4} \text{ s}^{-1}$ is a reference strain rate. The strain rate sensit-

235 ivity of the material is governed by c , while the temperature softening term is governed by the homologous temperature $T^* = (T - T_0)/(T_m - T_0)$, where T_0 and T_m describes a reference temperature and the melting temperature, respectively. The temperature softening exponent is given by m .

The equivalent flow stress σ_{eq} was determined by a Hershey yield surface, expressed in terms of the principal stresses $\sigma_i, i = 1, 2, 3$, as

$$\sigma_{\text{eq}} = (|\sigma_1 - \sigma_2|^a + |\sigma_2 - \sigma_3|^a + |\sigma_3 - \sigma_1|^a)^{\frac{1}{a}} \quad (2)$$

240 where the exponent a determines the shape of the yield surface. If $a = 2$ or $a = 4$, Eq. (2) describes a von Mises yield surface, while $a = 1$ or $a = \infty$ results in the Tresca yield criterion. Hence, for $a > 4$, the shape of the yield surface will lie between the von Mises and Tresca criteria. The work hardening $R(p)$ was described through a three-term Voce hardening law

$$R(p) = \sum_{k=1}^3 Q_k (1 - e^{-c_k p}) \quad (3)$$

where Q_k and c_k are numerical parameters governing the saturation stress and hardening rate of the material, 245 and p is the equivalent plastic strain. Lastly, material fracture was governed by element erosion and the Cockcroft-Latham (CL) ductile failure criterion [38], given by

$$D = \frac{W}{W_c} = \frac{1}{W_c} \int_0^p \langle \sigma_1 \rangle dp, \quad \langle \sigma_1 \rangle = \max(\sigma_1, 0) \quad (4)$$

where D is the damage indicator defined in the range $[0,1]$, σ_1 is the major principal stress, and dp denotes the equivalent plastic strain increment. As W_c defines the critical damage for a given material, fracture emerges when the damage parameter D reaches unity. However, the major principal stress may be rewritten 250 in terms of the stress triaxiality, σ^* , the Lode parameter, μ_σ , and the flow stress. By substituting the alternative form of σ_1 into Eq.(4) and assuming a yield surface exponent of $a=2$, we get

$$D = \frac{1}{W_c} \int_0^p \left\langle \sigma^* + \frac{3 - \mu_\sigma}{3\sqrt{3 + \mu_\sigma^2}} \right\rangle \sigma_{\text{eq}} dp \quad (5)$$

where

$$\sigma^* = \frac{\sigma_1 + \sigma_2 + \sigma_3}{3\sigma_{\text{eq}}}, \quad \mu_\sigma = \frac{2\sigma_2 - \sigma_1 - \sigma_3}{\sigma_1 - \sigma_3} \quad (6)$$

From Eq.(5) it is observed that the CL damage accumulation represents the plastic work per unit volume, multiplied by a factor depending on the stress triaxiality and the Lode parameter. The damage evolution 255 rate decreases with a decrease in the stress triaxiality, and for sufficiently low values of σ^* , or if $\sigma_1 \leq 0$, no damage is accumulated.

4.2. Identification of material parameters

The constitutive relation described by Eqs. (1)-(4) was implemented as a user-defined subroutine in LS-DYNA. The work hardening parameters Q_i and C_i were obtained through inverse modeling of the uniaxial tension tests, where the measured engineering stress-strain curves were used as target curves in an optimization using LS-OPT. All numerical tension tests applied element type 1, which is the most time efficient and default solid element for explicit simulations in LS-DYNA. This element is formulated as a constant stress hexahedron utilizing a reduced integration [39]. The test specimen was discretized with an element size of 0.2 mm, corresponding to 4 elements over the thickness. An identical element size and element type were used for all simulations throughout this study.

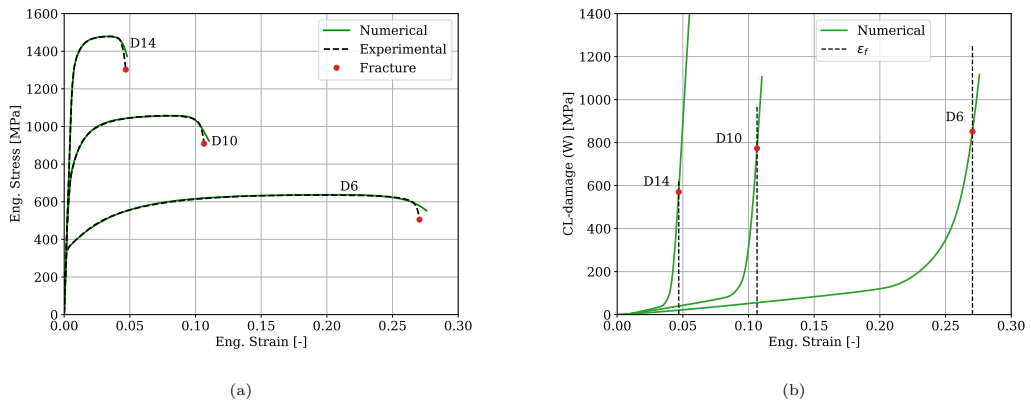


Figure 9: Comparison of numerically and experimentally obtained engineering stress-strain curves in (a), and the corresponding Cockcroft-Latham (CL) damage evolution in (b).

The CL fracture parameter W_c was extracted by following the critical element in the through-thickness centre of the tensile test simulations. This element is exposed to the largest equivalent plastic strain, and at the instant of fracture in the engineering stress-strain curves from the tests for all three materials, W_c was found by integration using Eq.(4). Numerically obtained engineering stress-strain curves are given in Figure 9(a), with the corresponding CL integrals in Figure 9(b). The estimated work hardening parameters are summarized in Table 4. Typical elastic and thermal material parameters from the literature were used for all three steels, i.e., $E=210$ GPa, $\nu=0.33$ and $\rho=7850$ kg/m³, while the specific heat capacity was set to $C_p=452$ J/kgK, the melting temperature to $T_m=1800$ K and the reference temperature to $T_r = 293$ K.

Table 4: Parameters for the constitutive relation described in Eqs.(1)-(4). All tension tests were performed with a nominal strain rate of $\dot{p}_0 = 5 \times 10^{-4} \text{s}^{-1}$. Both c and m are taken from [29].

Material	A [MPa]	Q_1 [MPa]	C_1 [-]	Q_2 [MPa]	C_2 [-]	Q_3 [MPa]	C_3 [-]	c [-]	m [-]	W_c [MPa]
D6	300.0	43.8	17642.7	275.0	28.5	942.4	0.9	0.01	1.0	851.4
D10	468.8	240.9	1340.5	289.8	118.1	245.0	11.7	0.008	1.0	773.6
D14	1114.8	180.0	1744.7	187.7	185.8	118.1	17.5	0.004	1.0	570.2

4.3. Numerical modelling of fracture

Ballistic impact and blast loading correspond to significantly different stress states during the plastic straining to fracture. By assuming proportional loading conditions, i.e., σ^* and μ_σ remains constant throughout the entire loading history to fracture, the fracture strain p_f may be determined as a function of σ^* , μ_σ , and the obtained material parameters, Q_k , C_k , and W_c by use of the CL failure criterion. The corresponding fracture loci are plotted for all three materials in Figure 10(a-c). The fracture strain is plotted as a function of σ^* for three given values of the Lode parameter. It is noted that $(\mu_\sigma, \sigma^*) = (-1, 1/3)$ corresponds to generalized tension ($\sigma_1 \geq \sigma_2 = \sigma_3$), $(\mu_\sigma, \sigma^*) = (0, 0)$ represents generalized shear ($2\sigma_2 = \sigma_1 + \sigma_3$), $(\mu_\sigma, \sigma^*) = (1, -1/3)$ represents generalized compression ($\sigma_1 = \sigma_2 \geq \sigma_3$), while $(\mu_\sigma, \sigma^*) = (1, 2/3)$ implies biaxial tension ($\sigma_1 = \sigma_2 \geq \sigma_3 = 0$). As the CL failure criterion is driven by positive values of σ_1 , the lowest fracture strain is found for generalized tension. Accordingly, the largest fracture strain occurs in generalized compression, and shear ends up in between. Independent of the Lode parameter, the fracture strain increased dramatically with a decrease in stress triaxiality. With sufficiently low stress triaxialities, the fracture strain approaches infinity, and the CL criterion will no longer result in fracture.

Ballistic impacts tend to give compression dominated loading paths for elements in direct contact with the projectile. In such loading cases, the CL failure criterion may result in a highly increased fracture strain for certain elements. To overcome this issue, an additional effective fracture strain ϵ_{eff} was introduced in the fracture model.

$$\epsilon_{\text{eff}} = \sqrt{\frac{2}{3} \epsilon_{ij}^{\text{dev}} \epsilon_{ij}^{\text{dev}}} \quad (7)$$

where $\epsilon_{ij}^{\text{dev}}$ represents the deviatoric strain tensor. Hence, the strain-based failure criterion in Eq. (7) will basically erode severely distorted elements. The additional fracture strain can be interpreted as a "capping" of the CL fracture loci and is visualized as the green dotted lines in Figure 10. Note that the y-axis of the fracture loci represents the equivalent plastic strain, and the applied fracture strain is an effective deviatoric strain. This means that the numerical values of the two strain measures do not have a one to one relationship.

In Figure 10(d), the loading paths for the most damaged element in the numerical tension tests are plotted for all three materials. During the numerical tension tests, both the stress triaxiality and the Lode parameter are changing, and these curves are hence not directly comparable to the fracture loci in Figure 10(a-c). For all three materials, the stress triaxiality lies between 0.32 and 0.62, and the corresponding Lode parameter is between -1 and -0.4, which places the fracture strain around the lower right portion of the loci.

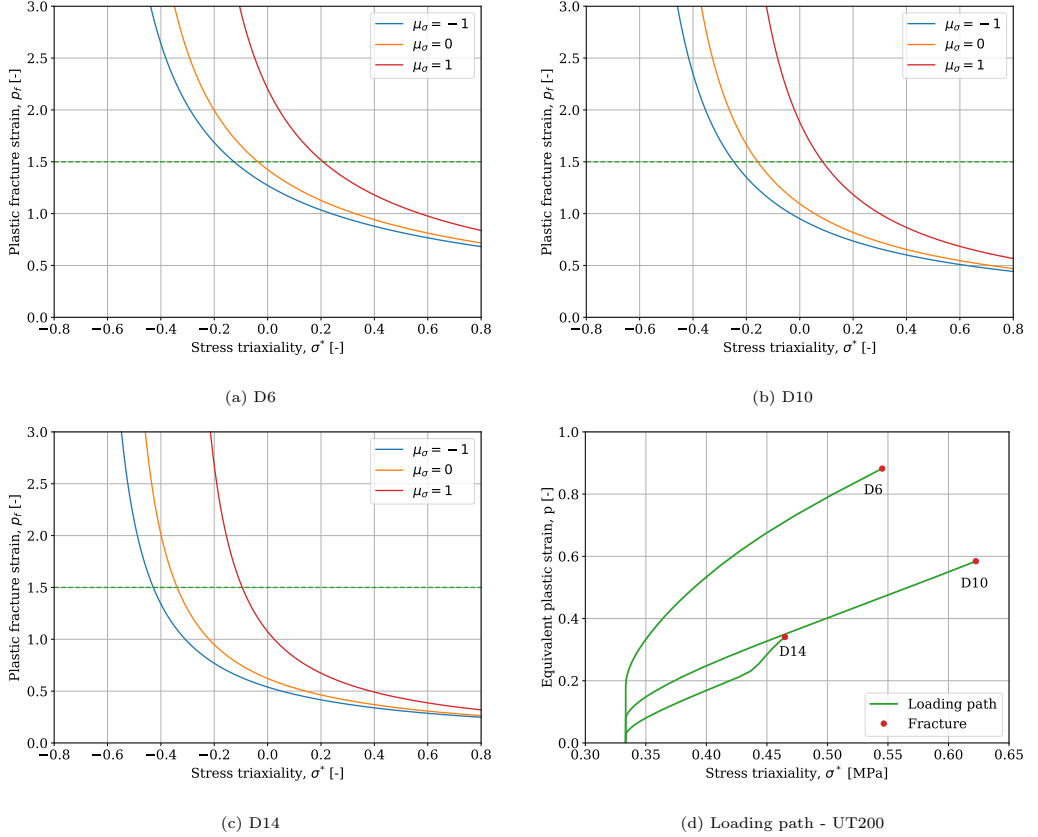


Figure 10: (a-c) Fracture loci based on the CL failure criterion for all materials at selected values of the Lode parameter, (d) the loading path to fracture for the most damaged element in the simulations of the tension tests are plotted for all materials.

Figure 11 presents results from numerical simulations using the specimen geometry in Figure 1(b) and the material parameters in Table 4. The results are presented as the damage field in Figure 11(a) at the instant of fracture initiation for the three materials under consideration, while the analytical expression of the work hardening $R(p)$ is plotted against the plastic strain p in Figure 11(b). It is evident that the three materials are experiencing distinct differences in the ability to distribute the damage over the gauge area of

the specimen geometry. While D14 experiences a strong localization of plastic deformation and damage, D6 and D10 are gradually distributing the damage across a larger area. It is interesting to note the correlation between localization of damage in Figure 11(a) and work hardening characteristics in Figure 11(b). That is, increased work hardening distributes the plastic deformations and the corresponding damage over a much larger area. In turn, this leads to a larger dissipation of plastic work and an increased resistance to fracture and crack propagation. The main trend is that the increased material strength leads to a reduction in work hardening, confirming the observations on the strength-ductility trade-off in Ref. [27].

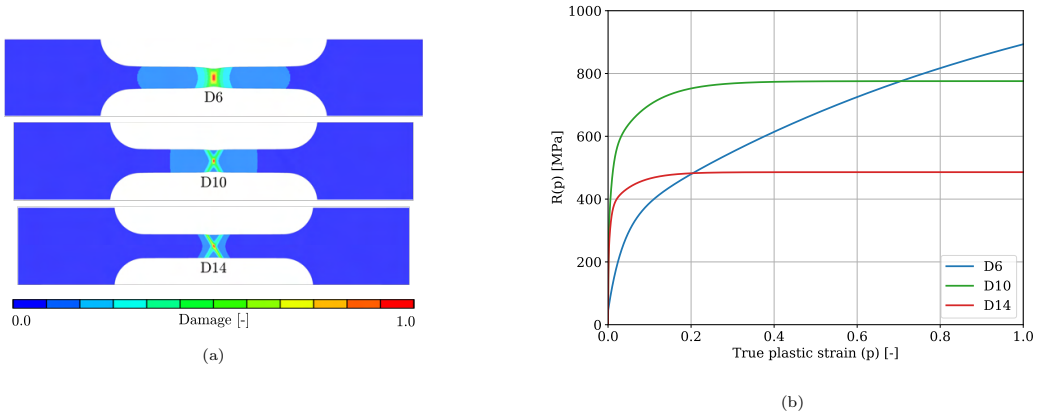


Figure 11: Numerical modelling of the three materials under consideration: (a) Damage fields extracted at the instant of fracture, and (b) the analytical expressions for the work hardening $R(p)$ when using the Voce parameters in Table 4. The damage fields is based on the CL criterion in Eq. (4).

5. Numerical simulations of combined ballistic impact and blast loading

Numerical simulations were used to gain more insight into the fracture characteristics of pre-damaged plates exposed to blast loading. However, before moving into the detailed simulations of the blast loaded plates, it is necessary to address some challenges in the numerical modelling and simulation of scenarios involving combined ballistic impact and blast loading.

5.1. Numerical model

To replicate the experimental tests, the ballistic impact and blast simulation were run in two separate analyses. This was formulated as a full deck restart analysis in LS-DYNA, using a **DAMPING_PART_MASS* numerical damping in between the two load cases to minimize elastic oscillations prior to the blast load.

The numerical model is shown in Fig. 12. The experimental setup allowed for the use of two symmetry planes. The clamping assembly consists of two steel plates which are coloured with green and brown in the

325 figure, and 3 bolts (2 full and 2 half). Both the bolts and the green clamping frame are fixed for translation
in all directions along the surface facing outwards in Fig. 12(c). The target plate and the brown clamping
frame are constrained by contact with the surrounding parts. As shown in Fig. 12(c), the blast-exposed
surface of the target plate is bounded by the inner square of the green clamping frame. The clamping
frame and bolts were modeled as elastic (*MAT_001), using standard material parameters for steel. The
330 constitutive relation and material parameters applied for the target plates are described in Section 4.1.

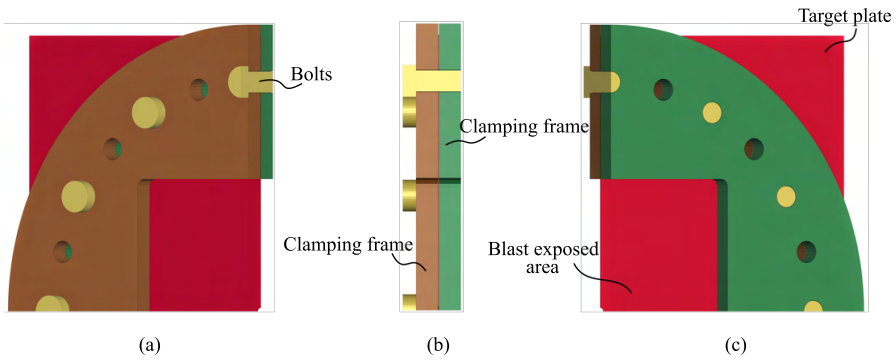


Figure 12: The numerical model of the clamping assembly and the target plate: (a) a view of the unloaded surface, (b) seen from the side, and (c) a view of the blast-exposed surface. It is noted that quarter symmetry has been utilized.

The overall aim of the ballistic simulations was to predict a realistic fracture mode in the target plates. That is, to obtain a realistic starting point for the blast simulations in terms of the number of petals and initial cracks from the ballistic impact. Hence, the ballistic resistance of the target plates was not considered in detail. As no visual deformation or damage was observed for the projectiles in the experiments, rigid
335 projectiles were applied in the numerical models. The projectiles were given an initial velocity of 900 m/s. The quarter symmetry of the target plate assembly was also adopted for the projectile.

During a ballistic impact, the localized area in which the material fails experiences high pressures, leading to low stress triaxialities. As a consequence, the CL failure criterion (Eq. 5) accumulates no damage in these elements under compressive stress states although there are significant plastic deformations. Numerically,
340 this allows for elements to exhibit excessive plastic deformation without failing [37]. If adiabatic heating is included, the localized areas of large plastic deformations and high plastic strain rates will experience significant heating and the element could therefore be eroded due to a temperature-based failure criterion. However, the local plastic deformation and corresponding adiabatic heating of each element within the impact zone is very mesh sensitive [23]. Simulations with a sufficiently fine mesh using 3D brick elements
345 is considered as unrealistic in the context of combined ballistic impact and blast loading. This presents a challenge on how to model such a loading event, because refining the mesh is not feasible within the scope

of this work.

Alternative modelling approaches to handle excessively distorted elements with low CL damage accumulation in ballistic impact simulations are typically to either erode elements if the critical time step drops below a given threshold or at a given strain limit. In this study it was decided to adopt an additional strain-based erosion criterion from Refs. [40, 41], where elements are eroded if the effective von Mises strain ε_{eff} from Eq. (7) reaches a given threshold. This is governed by the *EFFEPS* keyword in the **MAT_ADD_EROSION* module in LS-DYNA. To introduce an additional strain-based failure criterion is somewhat similar to capping the fracture locus, as illustrated in Figure 10. It is important to note that this was only applied during the ballistic impact simulations, and not in the subsequent blast simulations. Fracture in the blast simulation was governed solely by the CL failure criterion and the critical temperature.

Aune et al. [16] studied blast-loaded steel plates of similar dimensions as those used in this study. It was shown that a discretization consisting of 0.8 mm shell elements for the target plates gave an accurate description of both plastic deformations and fracture during blast loading. However, shell elements cannot be used in the ballistic impact simulations. As a compromise between numerical accuracy during ballistic impact and computational efficiency during blast loading, it was decided to apply a uniform mesh of 0.2 mm solid elements. This corresponds to 4 elements across the plate thickness. All blast simulations in this study used the idealized pressure histories from Aune et al. [32] shown in Figure 13. It is noted that the applied pressure histories are obtained in separate experiments obtaining pressure measurements on the blast-exposed surface of a massive, non-deformable steel plate. This gives a conservative estimate of the loading history, as FSI effects are expected to somewhat lower the blast pressure for thin steel plates [33].

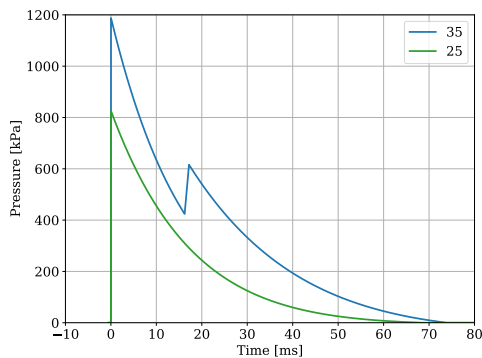


Figure 13: The pressure histories used in the blast simulations.

The two loading cases are evaluated separately with the ballistic impact simulations in Section 5.2, and the blast simulations in Section 5.3. More specific information regarding the modeling of the two loading

cases are given within the respective sections.

370 5.2. Numerical results for ballistic impact

The goal of this study is to investigate the influence of ballistic impact on the blast resistance of thin steel plates. Thus, the simulations of the ballistic impacts are conducted to generate similar petalling cracks as those seen in the physical tests as a starting point for the subsequent blast simulations. It was therefore considered necessary to carry out a parametric study on the influence of the threshold value of the effective fracture strain, ϵ_{eff} in Eq. (7), on the simulated petalling mode. This was done using three different thresholds of ϵ_{eff} for each material. It was decided to apply the same three thresholds for all three materials under consideration, i.e., 1.0, 1.5, and 2.0. As a reference, one simulation of each material excluding the strain-based failure criterion was also performed (i.e., $\epsilon_{\text{eff}} = 0.0$). The corresponding numerical results are given for plates of D6, D10 and D14 in Figure 14. It is noted that the quarter model was mirrored across the two symmetry planes in the ballistic holes for a better visualization. The applied level of ϵ_{eff} is given above each subfigure. The total number of eroded elements for each simulation is given at the bottom of each figure.

For all three materials, simulations where element erosion is based solely on the CL failure criterion and the critical temperature do not resemble the fracture mode observed in the physical tests, as seen in Figure 4. No distinct petals or cracks are formed around the bullet hole, and highly distorted elements with a low damage accumulation occur in the periphery of the holes. As ϵ_{eff} approaches a threshold of 1.0, the obtained fracture mode is more similar to the experimental observations, and the number of eroded elements are increasing for all three plate materials. The improved results and increased number of eroded elements with the additional strain-based failure criterion indicate that the CL failure criterion and critical temperature alone are not able to describe the physical mechanisms leading to fracture for the applied mesh.

Figure 14 shows that the D14 plate gave the largest number of eroded elements. This is reasonable as D14 is the material with the smallest amount of both ductility and hardening (see Figs. 9 and 11). It is also seen that the strain-based erosion criterion affects the interaction between the projectile and the target plate. As the elements in contact with the projectile are eroded early in the perforation process, the threshold for ϵ_{eff} will determine the ballistic hole geometry. Even though the D14 plates were the least sensitive to variations in the effective failure strain, the number of petals increased with almost a factor of 2 from $\epsilon_{\text{eff}}=1.0$ to $\epsilon_{\text{eff}}=1.5$. This effect was not found for the D6 and D10 simulations, where distinct petals mainly occurred for $\epsilon_{\text{eff}}=1.0$.

To better understand the need to include an additional strain-based failure criterion for the ballistic impact simulations, it was decided to study the stress state in selected elements in the simulations without the strain-based erosion criterion. The elements were selected based on their position across the plate thickness and with respect to the distance from the projectile nose. Figure 15 shows the selection of elements. Hence,

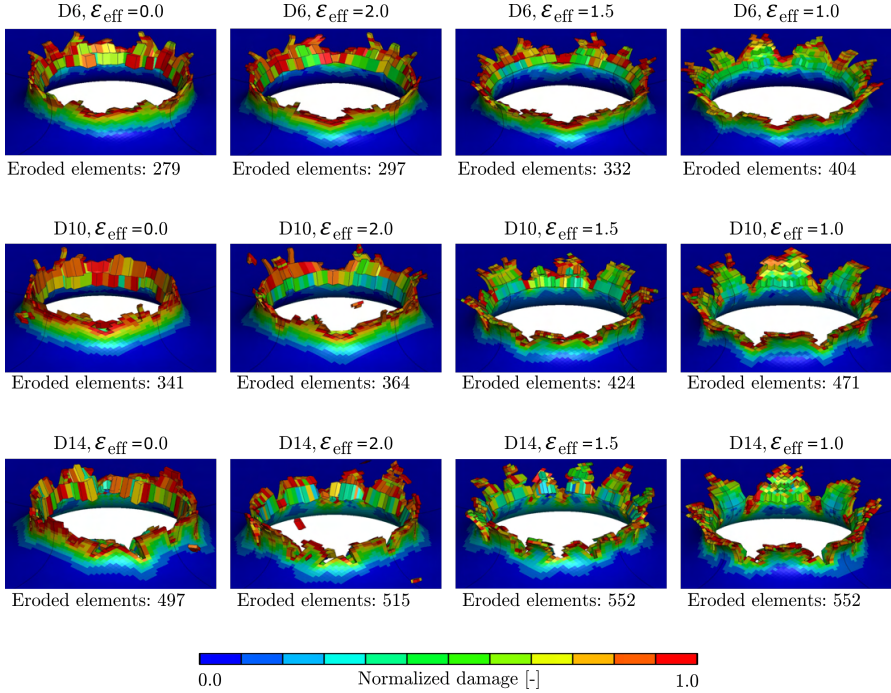


Figure 14: Numerical results for all ballistic impact simulations. The three different thresholds of the effective strain erosion criterion (ϵ_{eff} in Eq. (7)) are given at the top of each figure for each material. $\epsilon_{\text{eff}}=0.0$ denotes the simulation where only the CL failure criterion and critical temperature were applied. Note that the quarter model was mirrored across the two symmetry planes for a better visualization. The total number of eroded elements for each simulation is given at the bottom of each figure.

the elements across the thickness were evaluated at two separate distances from the plate center along one of the symmetry lines in the quarter model. The corresponding plots of the stress triaxiality and the damage (see Eq. (4)) shown in Figure 16 follow the same colour convention for each elements as indicated in Figure 15. As all three materials showed similar trends, it was decided to only present the stress triaxiality and damage for the D14 material.

From the plots of the stress triaxiality in Figure 16(a) and (b), it is observed that the stress state for the impacted elements is compression dominated. This is particularly the case for the elements in the upper half of the plate thickness (Elements 1 and 2). As Element 1 is in direct contact with the projectile and Element 4 lies on the opposite side of the plate thickness, it is reasonable that the stress triaxiality is increasing from Element 1 to Element 4. By considering the corresponding plots of the damage in Figure 16, the negative triaxialities translate to large plastic straining without any accumulation of damage. From Figure Figure 16(a) and (b) it is also seen that the stress triaxiality is decreasing, while Figure 16(c) and (d) indicates that the fracture strain is increasing as the distance to the plate center is decreased. Some elements

closer to the center than the evaluated elements experienced plastic strains above 3 without exceeding the CL criterion in Eq. (4).

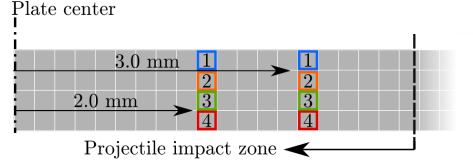


Figure 15: The selection of elements used for the evaluation of the stress state during ballistic impact. The cross section represents the plate thickness along one of the symmetry planes, where the left end represents the plate center. The projectile impacts the entire region called the "Projectile impact zone". The element IDs used in Figure 16 are indicated inside each element.

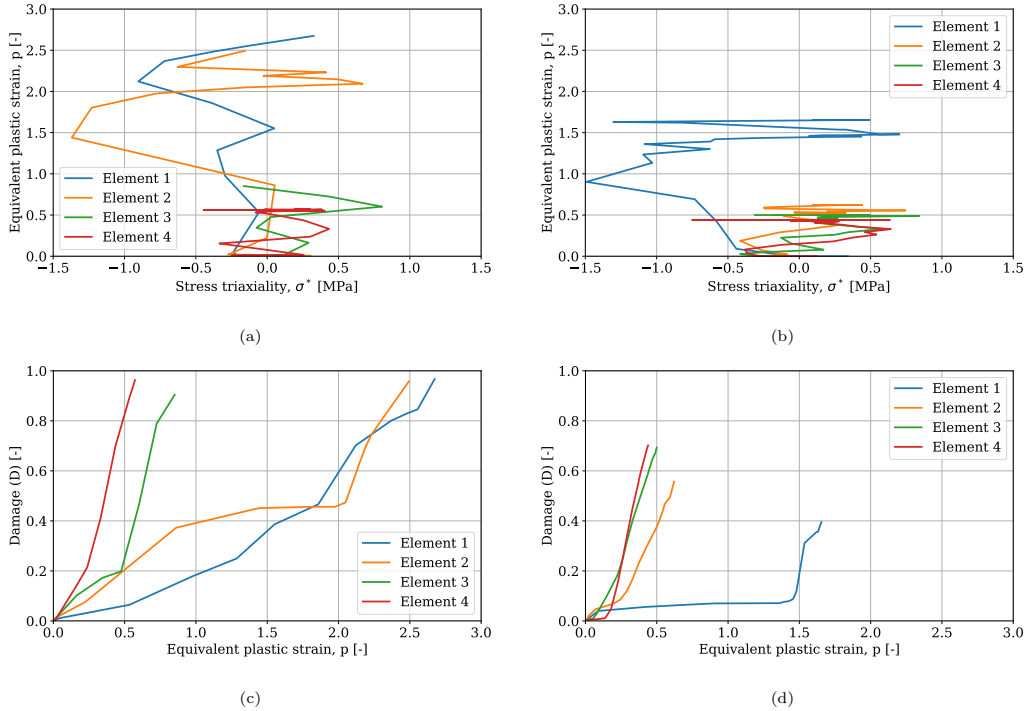


Figure 16: The stress triaxiality versus the equivalent plastic strain in the elements indicated in Figure 15: (a) the elements at a distance of 2.0 mm from the plate center, and (b) the elements at a distance of 3.0 mm from the plate center. The equivalent plastic strain versus the accumulated damage in the elements indicated in Figure 15: (c) the elements at a distance of 2.0 mm from the plate center, and (d) the elements at a distance of 3.0 mm from the plate center. As all three materials resulted in similar trends, only the results for the D14 material are presented.

It should also be noted that a mesh refinement corresponding to 8 elements across the thickness (element size of 0.1 mm) was also used in an attempt to improve the simulations of the fracture mode. However, even at this element size the fracture modes were poorly represented when using only the CL failure criterion and the critical temperature. Figure 16(a) and (b) show that the simulations of the ballistic impact resulted in stress triaxialities as low as -1.5 for a large portion of the critical elements. Even the major principal stress turned negative and no accumulation of damage occurred. Hence, it is found necessary to use an additional failure criterion to predict realistic fracture modes during ballistic impact on a course mesh, motivating the use of the strain-based criterion in Eq. (7). Another alternative would be to use a more advanced fracture criterion that better accounts for damage at lower stress triaxialities. However, this is beyond the scope of this study.

5.3. Numerical results for blast loading simulations

The numerical results of the blast simulations are divided into two main parts. First, the global response is evaluated for simulations that do not show any sign of fracture. Secondly, the fracture resistance in the different materials and plate geometries are considered.

5.3.1. Global response

The permanent out-of-plane displacement fields of plates with a pre-cut circular hole (C) are presented in Figure 17. It is noted that only results from the lowest blast intensity and the C geometry are presented in this section, as this is the only configuration where none of the materials experienced any fracture. As in the physical tests (see Figure 6(a-c)), the permanent deformations are decreasing with increasing material strength and the distribution of deformations gets more localized around the center for the D10 and D14 plates. However, increased magnitudes of permanent deformations are seen in the numerical simulations compared to the experimental observations. This was expected because the simulations are neglecting FSI effects, and the applied pressure histories are obtained in separate tests on rigid target plates. This will overestimate the deformations [16, 33].

Figure 18 provides the equivalent plastic strain p when the plates have reached the permanent deformed configuration. It is evident that the magnitude of the plastic strains are significantly larger for the D6 plate, compared to the D10 and D14 plates. The maximum plastic strain occurred at the periphery of the pre-cut hole for all tests, with a magnitude of 0.23 for D6_C_25 (Figure 18(a)), 0.13 for D10_C_25 (Figure 18(b)), and 0.12 for D14_C_25 (Figure 18(c)). However, the most dominant difference in the equivalent plastic strain fields is the difference in distribution. For the most ductile plate (i.e., D6_C_25), the plastic strains are distributed across a large area around the center of the target plate. As the ductility is reduced and the strength increased, D10_C_25 experiences a more localized distribution around the plate center. This effect is even more evident for test D14_C_25. Within the areas of localized plastic strain, some clear differences

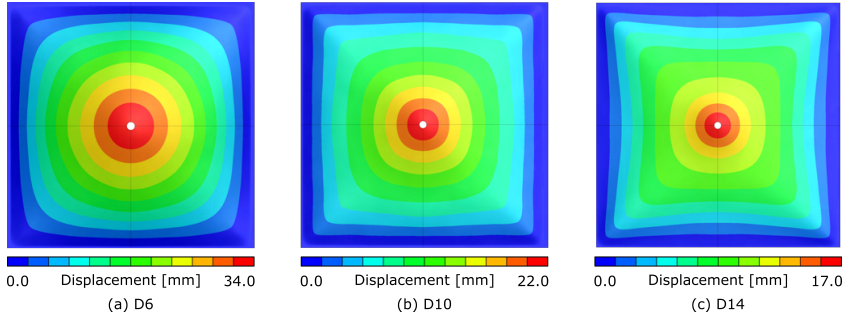


Figure 17: The permanent out-of-plane displacement fields from numerical simulations of plates with a pre-cut circular hole (C), exposed to the lowest blast intensity. The plate materials are indicated in the sub-caption of each image. Note that the quarter model was mirrored across the two symmetry planes for a better visualization.

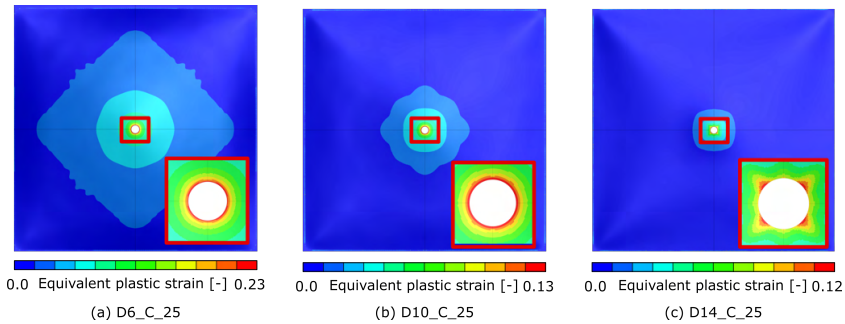


Figure 18: The equivalent plastic strain fields corresponding to the state of permanent deformation. Zoomed images of the plastic strain distribution around the pre-cut holes are given in the lower right corner of each figure, indicated with a red square. The test names are given in the sub-captions. Note that the quarter model was mirrored across the two symmetry planes for a better visualization.

are seen between the three materials when considering the zoomed images of the pre-cut holes in Figure 18. For D6_C_25, the strongest localization occurred as a circular area along the periphery of the pre-cut hole. A similar distribution is seen for D10_C_25. For D14_C_25, distinct localizations have formed along the diagonals. The comparison of the plastic strain distributions in Figure 18 resembles the same trends that were observed in the simulations of the uniaxial tension tests in Figure 11(a), where localization occurred at smaller strains for the D14 material compared to the D6 and D10 materials.

When the blast intensity was increased in the simulations, both D6_C_35 and D10_C_35 resulted in increased deformations, but no signs of fracture were found. As in the experiments, D14_C_35 experienced fracture in the numerical model. In the experiments, two large arrested cracks were observed, while the numerical model ended with complete tearing where the cracks initiated and propagated along the diagonals and all the way to the clamping frame.

5.3.2. Fracture resistance

As in the physical tests in Section 3.4, the numerical simulations showed that the blast resistance was strongly dependent on the fracture mode from the ballistic impact. The final state of crack propagation is given for tests D6_B_35 and D10_B_35 in Figure 19. Quarter symmetry was applied in all blast simulations, and all images have been mirrored across the two symmetry planes for a better visualization. It is emphasized that the strain-based failure criterion (ϵ_{eff}) in Eq. (7) was only applied during the ballistic impact simulations and was not used in the blast load simulations. Hence, the fracture during blast loading was only governed by the CL failure criterion in Eq. (4) and possible thermal effects.

As shown in Section 5.2, the fracture mode during the ballistic impact was sensitive to variations in the fracture strain. A successful result in predicting the petalling cracks for the D6 and D10 plates where obtained using $\epsilon_{\text{eff}}=1.0$. The absence of fully formed petals will influence the blast simulations such that the response is more similar to the target plates with pre-cut circular holes. The CL damage fields given for tests D6_B_35 and D10_B_35 in Figure 19 are therefore restarted from the ballistic simulations using $\epsilon_{\text{eff}}=1.0$. The lengths of the arrested cracks in the D6_B_35 and D10_B_35 simulations were measured to be of similar magnitude as what was found for the corresponding blast tests. However, the D6_B_35 and D10_B_35 tests resulted in only 2 and 3 arrested cracks, respectively. As the numerical models applied quarter symmetry, one crack in the quarter model corresponds to 4 cracks for the full geometry. This means that the numerical simulations predict a larger crack length than that observed in the physical tests.

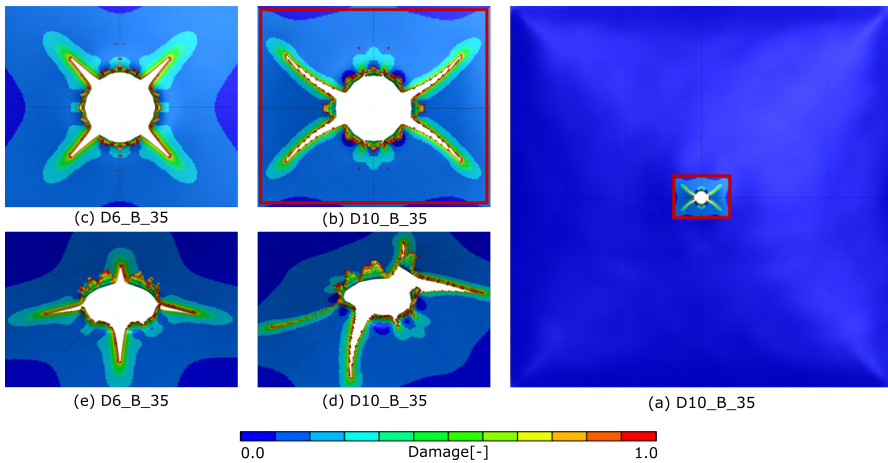


Figure 19: Final state of arrested cracks for D6_B_35 and D10_B_35. The full geometry of the blast exposed area is indicated in (e) to give a perspective of the lengths of the arrested cracks. Simulation identities are indicated in the subcaptions.

Figure 20 shows the final states of crack propagation for test D14_B_25. Two alternative results are given, due to the findings in Section 5.2 where both threshold values of $\epsilon_{\text{eff}}=1.0$ and $\epsilon_{\text{eff}}=1.5$ predicted

reasonable petalling cracks during the ballistic impact of the D14 plates. This allowed for a numerical study on the influence of the number of petalling cracks on the blast resistance of the D14 plates. The blast simulations starting from the ballistic simulations with $\epsilon_{\text{eff}}=1.0$ contained approximately half the number of petals compared to those starting from ballistic simulations using $\epsilon_{\text{eff}}=1.5$. It should also be noted that $\epsilon_{\text{eff}}=1.5$ have petalling cracks aligned with the plate diagonals, while $\epsilon_{\text{eff}}=1.0$ only have vertical and horizontal petalling cracks.

From Figure 20 it is clear that the two different petalling distributions ($\epsilon_{\text{eff}}=1.0$ and $\epsilon_{\text{eff}}=1.5$) for test D14_B_25 resulted in two different fracture patterns during blast loading. The blast simulation starting from the ballistic impact using $\epsilon_{\text{eff}}=1.0$ resulted in short arrested vertical cracks (Figure 20(a),(c)), while blast simulations starting from the ballistic results using $\epsilon_{\text{eff}}=1.5$ gave significantly longer cracks along the plate diagonal (Figure 20(b),(d)). All cracks are initiated at the petals resulting from the ballistic impact event. It is noted that both simulations resulted in smaller arrested cracks than in the physical tests. Both blast simulations of test D14_B_25 applied identical blast intensity and material parameters. The only difference between the two models in Figure 20 is the fracture mode from the ballistic impact. Hence, it is evident that the crack initiation and crack propagation during blast loading are sensitive to the petalling distribution and orientation from the ballistic impact.

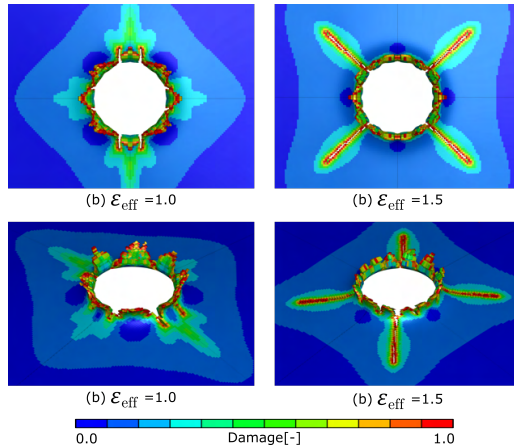


Figure 20: Final state of arrested cracks for D14_B_25 based on two different fracture strain thresholds from the ballistic impact. It is noted that the values of ϵ_{eff} are referring to the additional strain-based failure criterion during ballistic impact, as this strain criterion was not included in the blast simulations.

Figure 21 provides representative crack propagation paths for simulations of the D14 plate exposed to the highest blast intensity. The results for test D14_C_35 are given in Figure 21(a), while the results for the two petalling modes for test D14_B_35 are given in Figure 21(b) and Figure 21(c). As the pre-cut circular

hole (C) geometry in test D14_C_35 represents an ideal geometry, this simulation will also serve as a basis of comparison to evaluate the effect of the petalling mode in the crack initiation and propagation during the blast loading phase. Thin, square plates subjected to blast loading are expected to experience cracks propagating along the plate diagonals (see e.g., Refs. [16, 20, 27, 35]). Both D14_C_35 and D14_B_35 - $\epsilon_{\text{eff}}=1.5$ ended in total fracture, with cracks propagating along the diagonals. However, D14_B_35 - $\epsilon_{\text{eff}}=1.0$ corresponds to another petalling mode than $\epsilon_{\text{eff}}=1.5$, and resulted in significant arrested cracks along the horizontal direction. This means that the change in petalling mode from $\epsilon_{\text{eff}}=1.5$ to $\epsilon_{\text{eff}}=1.0$ changed the direction of crack propagation during blast loading, and hence increased the resistance to fracture of the target plate.

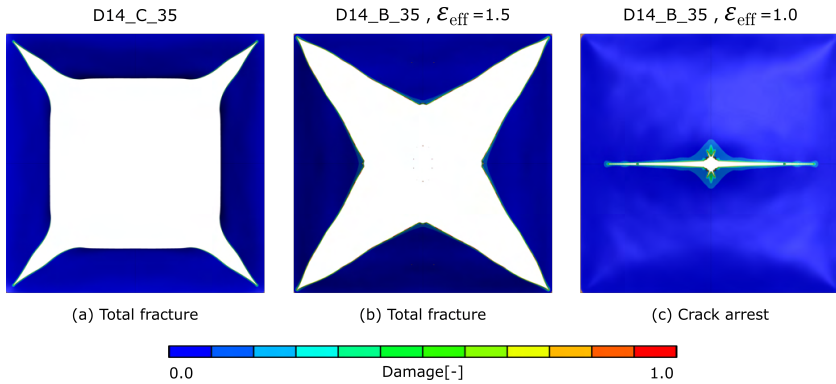


Figure 21: The final state of crack propagation from blast simulations for test D14_C_35 is shown in (a), while similar results from blast simulations with two different petalling modes from the ballistic simulations for test D14_B_35 are shown in (b) and (c). Note that ϵ_{eff} refers to the two different thresholds used for the strain-based failure criterion in the ballistic impact simulations. The strain-based failure criterion was not included in the blast simulations. It is stated in the subcaptions whether the simulation ended in crack arrest or total fracture.

Another interesting observation is the discrepancy in numerically predicted crack resistance between the different models. All blast simulations resulted in larger cracks than that in the physical tests, except for the blast simulations of the D14 plates with ballistic perforations (i.e., tests D14_B_25 and D14_B_35). Since FSI effects were neglected in this study, the applied loading curves could represent a slightly higher blast intensity than that in the actual tests (see Ref. [33]). However, this only explains the simulations giving conservative estimates of the fracture resistance. A plausible explanation for the non-conservative predictions of the fracture resistance in some of the blast simulations with ballistic perforations is the change in crack propagation path. All simulations leading to conservative estimates of the resistance to fracture experienced crack propagations along the plate diagonals. Simulations that overestimated the fracture resistance experienced crack propagation along the vertical and horizontal directions. Thus, the numerical

520 predictions are very sensitive to changes in the petalling modes resulting from the ballistic impact.

5.4. Stress states during blast loading

As the stress states and validity of the CL failure criterion were investigated for the ballistic impact simulations in Section 5.2, this section aims to perform a similar evaluation for the blast simulations. In Figure 22, the major principal stress σ_1 , the Lode parameter μ_σ , and the stress triaxiality σ^* , are presented for two representative blast simulations. The field plots show the unloaded surface of the target plates, and were captured right before crack initiation occurred. A zoomed image around the ballistic impact holes of the target plates is given at the lower right corner of each subfigure.

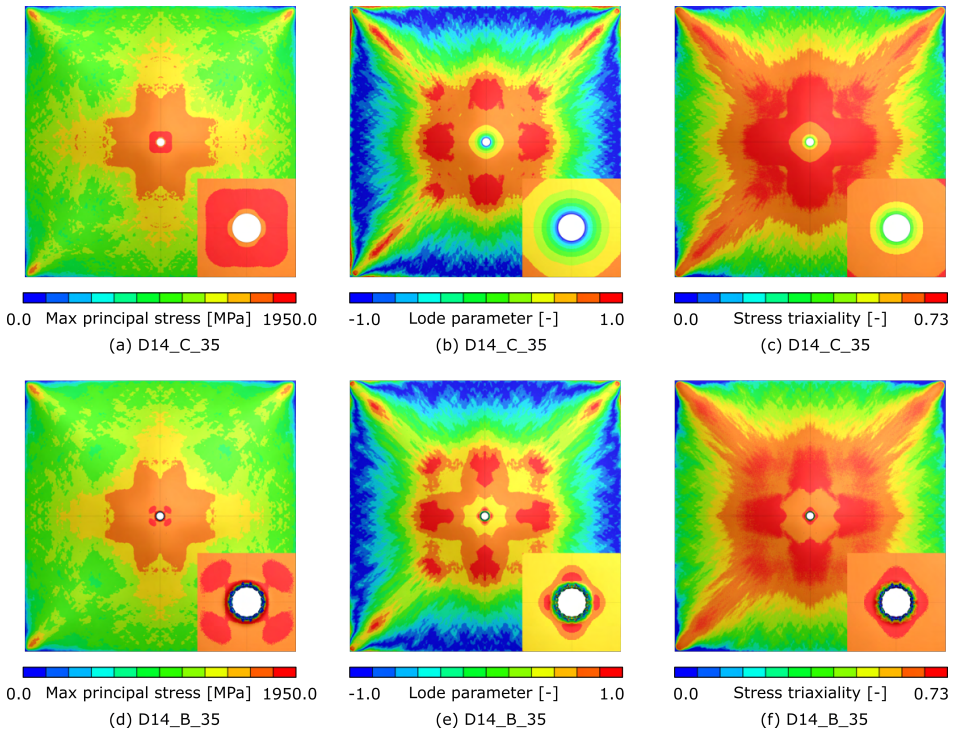


Figure 22: Field plots of the major principal stress σ_1 , the Lode parameter μ_σ , and the stress triaxiality σ^* right before the crack initiation occurred. The D14_C_35 simulation is presented in (a)-(c) and the D14_B_35 simulation in (d)-(f). All field plots are taken from the unloaded surface of the target plates.

Overall, it is seen that both σ_1 , μ_σ , and σ^* gives similar distributions for the two simulations in Figure 22. However, some differences are observed around the bullet hole in D14_B_35 compared to the pre-cut circular hole in D14_C_35. For σ_1 , which is the driving force in the CL-fracture criteria, a stronger localization along the diagonals is observed for D14_B_35 than for D14_C_35. This is reasonable, as the bullet hole contains

small petalling cracks, which generally leads to increased stress concentrations. From the definitions of μ_σ and σ^* in Section 4.3, it is seen in Figure 22 (b) and (c) that the D14_C35 simulation is experiencing a stress state close to uniaxial tension at the periphery of the pre-cut hole right before crack initiation. The D14_B35 simulation on the other hand undergoes larger values for both μ_σ and σ^* , yielding a stress state closer to biaxial tension. However, both target plate geometries correspond to stress states within the same range as the uniaxial tension tests applied to determine the CL failure parameter W_c , shown in Figure 10.

6. Concluding remarks

Experimental and numerical studies were conducted to investigate the effect of ballistic impact prior to blast loading of thin steel plates. This was done by comparing the response of plates with pre-cut circular holes to that of plates with ballistic perforations when exposed to the same blast intensity. Three steel qualities with distinct differences in strength, ductility and work hardening characteristics were tested to get a better understanding of the strength-ductility trade-off. Numerical models were evaluated based on the experimental observations, where special focus was placed on the compromise between computational accuracy during ballistic impact and computational efficiency during blast loading. The numerical simulations were also used to address challenges related to the distinct differences in the loading paths to fracture for both the ballistic impact and the blast loading. The main conclusions from the study are as follows.

- As expected, the ballistic impact resulted in reduced blast resistance compared to the target plates with pre-cut holes. This trend was found for all plate materials, both in the physical tests and in the numerical simulations. Even though the pre-cut circular holes (C) and ballistic holes (B) both were circular with a diameter of about 8 mm, the ballistic impact introduced small petalling cracks and additional damage to the material around the perforation. It was evident that the crack propagation during blast loading was initiated at these petalling cracks. Hence, pre-cut holes containing initial material damage gives a lower fracture resistance than pre-cut circular holes in thin blast-loaded steel plates.
- The three materials evaluated in this study showed a step-wise increase in material strength and a corresponding decrease in ductility. The fracture resistance during blast loading decreased with an increase in material strength. Furthermore, the reduced fracture resistance as a result of the ballistic impact increased with increased material strength. This confirms previous findings on the influence of the strength-ductility trade-off on the fracture resistance of perforated plates, where plates with higher strength are more prone to cracking and fracture than plates with lower strength. Higher material strength typically comes with lower ductility. Thus, this study shows that work hardening and ductility may be more important than the strength for the fracture resistance of pre-damaged and blast-loaded thin steel plates.

- 565 • The numerical models were able to capture the main trends observed in the physical tests, i.e., a decrease in blast resistance after ballistic impact and reduced fracture resistance with increased material strength. The most challenging aspect of a successful result in the numerical simulations of combined ballistic impact and blast loading was the representation of the fracture mode during the ballistic impact using a rather coarse finite element model. Provided a good description of the petalling cracks from the ballistic impact, the numerical simulations of the blast loaded plates predicted the same trends as those observed in the physical tests. The numerical simulations did not succeed in obtaining a good description of the fracture mode in the ballistic impact using the CL failure criterion in combination with a temperature criterion using a coarse mesh. To capture the experimentally observed petalling cracks during ballistic impact in this study, a strain-based failure criterion was included in addition to the CL failure criterion to erode elements at low triaxialities. The blast simulations only used the CL failure criterion and critical temperature.
- 570
- 575
- The numerical models of the target plates can be used to gain more insight into the combined effect of ballistic impact and blast loading. It is emphasized that this study is limited to load intensities generated within the capability of a shock tube facility. This motivates further studies on the influence of other load intensities, e.g., those generated by close-in detonations.
- 580

Acknowledgements

This work has been carried out with financial support from NTNU and the Research Council of Norway through the Centre for Advanced Structural Analysis (CASA), Centre for Research-based Innovation (Project No. 237885). The financial support by the Norwegian Ministry of Justice and Public Security is also greatly appreciated. The authors would also like to express their gratitude to Mr. Trond Auestad for his contributions during the experimental work.

585

References

- [1] R. Qi, G. S. Langdon, T. J. Cloete, C. K. Yuen, Behaviour of a blast-driven ball bearing embedded in rear detonated cylindrical explosive, *International Journal of Impact Engineering* 146 (2020) 103698.
- 590 [2] J. Leppanen, Concrete structures subjected to fragment impacts, dynamic behaviour and material modelling, Ph.D. thesis, Department of Structural Engineering and Mechanics, Concrete Structures, Chalmers University of Technology (2004).
- [3] U. Nyström, K. Gylltoft, Numerical studies of the combined effects of blast and fragment loading, *International Journal of Impact Engineering* 36 (2009) 995—1005.
- [4] H. Y. Grisaro, A. N. Dancygier, Characteristics of combined blast and fragments loading, *International Journal of Impact Engineering* 116 (2018) 51—64.
- 595 [5] K. A. Marchand, M. M. Vargas, J. D. Nixon, The synergistic effects of combined blast and fragment loadings, Tech. rep., San Antonio Texas (1992).
- [6] D. W. Hyde, U. A. E. W. E. Station, U. S. A. C. of Engineers, User's Guide for Microcomputer Programs ConWep and FunPro, Applications of TM 5-855-1, "Fundamentals of Protective Design for Conventional Weapons", Instruction report, U.S. Army Engineer Waterways Experiment Station, 1988.
- 600 URL <https://books.google.no/books?id=xhHxHAAACAAJ>
- [7] X. Kong, W. Wu, J. Li, P. Chen, F. Liu, Experimental and numerical investigations on a multi-layer protective structure under the synergic effect of blast and fragment loadings, *International Journal of Impact Engineering* 65 (2014) 146–62.
- [8] J. Leppänen, Experiments and numerical analyses of blast and fragment impacts on concrete, *International Journal of Impact Engineering* 31 (7) (2005) 843 – 860.
- 605 [9] H. Y. Grisaro, A. N. Dancygier, Dynamic response of rc elements subjected to combined loading of blast and fragments., *Journal of Structural Engineering* 147 (2020) 04020315.
- [10] H. Y. Grisaro, Effect of combined blast and fragmentation load on the dynamic response of reinforced concrete structures, *Engineering Structures* 248 (09 2021).
- 610 [11] P. D. Linz, S. C. Fan, C. K. Lee, Modeling of combined impact and blast loading on reinforced concrete slabs, *Latin American Journal of Solids and Structures* 13 (2016) 2266–2282.
- [12] P. D. Linz, T. C. Fung, C. K. Lee, W. Riedel, Response mechanisms of reinforced concrete panels to the combined effect of close-in blast and fragments: An integrated experimental and numerical analysis, *International Journal of Protective Structures* 0 (0) (2020).
- 615 [13] Y. Yuan, P. Tan, Deformation and failure of rectangular plates subjected to impulsive loadings, *International Journal of Impact Engineering* 59 (2013) 46–59.
- [14] L. Li, Q.-C. Zhang, R. Zhang, X. Wang, Z.-Y. Zhao, S.-Y. He, B. Han, T. J. Lu, A laboratory experimental technique for simulating combined blast and impact loading., *International Journal of Impact Engineering* 134 (2019) 103382.
- [15] W. Li, P. Wang, G.-P. Feng, Y.-G. Lu, J.-Z. Yue, H.-M. Li, The deformation and failure mechanism of cylindrical shell and square plate with pre-formed holes under blast loading., *Defence Technology In Press* (2020).
- 620 [16] V. Aune, G. Valsamos, F. Casadei, M. Langseth, T. Børvik, On the dynamic response of blast-loaded steel plates with and without pre-formed holes, *International Journal of Impact Engineering* 108 (2017) 27—46.
- [17] Y. Li, W. Wu, H. Zhu, Z. Wua, Z. Dub, The influence of different pre-formed holes on the dynamic response of square plates under air-blast loading, *Engineering Failure Analysis* 78 (2017) 122—133.
- 625 [18] K. Rakvåg, N. Underwood, G. Schleyer, T. Børvik, O. Hopperstad, Transient pressure loading of clamped metallic plates with pre-formed holes, *International Journal of Impact Engineering* 53 (2012) 44—55.
- [19] C. Zhang, P. Tan, Y. Yuan, Confined blast loading of steel plates with and without pre-formed holes, *International Journal of Impact Engineering* 163 (2022) 104183.

- [20] H. Granum, V. Aune, T. Børvik, O. S. Hopperstad, Effect of heat-treatment on the structural response of blast-loaded aluminium plates with pre-cut slits, *International Journal of Impact Engineering* 132 (2019) 103306.
- [21] S. Cai, J. Liu, P. Zhang, C. Li, Y. Cheng, C. Chen, Experimental study on failure mechanisms of sandwich panels with multi-layered aluminum foam/uhmwpe laminate core under combined blast and fragments loading, *Thin-Walled Structures* 159 (2021) 107227. doi:<https://doi.org/10.1016/j.tws.2020.107227>.
- [22] J. Li, C. Huang, T. Ma, H. Xiancong, W. Li, M. Liu, Numerical investigation of composite laminate subjected to combined loadings with blast and fragments, *Composite Structures* 214 (02 2019). doi:10.1016/j.compstruct.2019.02.019.
- [23] J. K. Holmen, O. S. Hopperstad, T. Børvik, Influence of yield-surface shape in simulation of ballistic impact, *International Journal of Impact Engineering* 108 (2017) 136–146.
- [24] S. Dey, T. Børvik, O. S. Hopperstad, J. R. Leinum, M. Langseth, The effect of target strength on the perforation of steel plates using three different projectile nose shapes, *International Journal of Impact Engineering* 30 (2004) 1005–1038.
- [25] K. Spranghers, I. Vasilakos, D. Lecompte, H. Sol, J. Vantomme, Full-field deformation measurements of aluminum plates under free air blast loading, *Experimental Mechanics* 52 (2012) 1371–1384.
- [26] V. Aune, E. Fagerholt, K. Hauge, M. Langseth, T. Børvik, Experimental study on the response of thin aluminium and steel plates subjected to airblast loading, *International Journal of Impact Engineering* 90 (2012) 106–121.
- [27] B. S. Elveli, M. B. Iddberg, T. Børvik, V. Aune, On the strength-ductility trade-off in thin blast-loaded steel plates with and without initial defects - an experimental study, *Thin-Walled Structures* 171 (2022) 108787.
- [28] SSAB, Docol automotive steels, <https://www.ssab.com/products/brands/docol>, [Online; accessed 23-May-2022] (2020).
- [29] G. Gruben, M. Langseth, E. Fagerholt, O. Hopperstad, Low-velocity impact on high-strength steel sheets: An experimental and numerical study, *International Journal of Impact Engineering* 88 (2016) 153–171.
- [30] T. Børvik, M. Langseth, O. Hopperstad, K. Malo, Ballistic penetration of steel plates, *International Journal of Impact Engineering* 22 (9) (1999) 855–886.
- [31] E. Fagerholt, , <https://www.ntnu.edu/kt/ecorr>, [Online; accessed 23-May-2022] (2008).
- [32] V. Aune, E. Fagerholt, M. Langseth, T. Børvik, A shock tube facility to generate blast loading on structures, *International Journal of Protective Structures* 7 (2016) 340–366.
- [33] V. Aune, G. Valsamos, F. Casadei, M. Langseth, T. Børvik, Fluid-structure interaction effects during the dynamic response of clamped thin steel plates exposed to blast loading, *International Journal of Mechanical Sciences* 195 (2021) 106263. doi:<https://doi.org/10.1016/j.ijmecsci.2020.106263>.
- [34] B. Abrahamsen, H. Alsos, V. Aune, E. Fagerholt, O. Faltinsen, O. Hellan, Hydroplastic response of a square plate due to impact on calm water, *Physics of Fluids* 32 (08 2020). doi:10.1063/5.0013858.1.
- [35] US Army Corps of Engineers (USACE), Structures to resist the effects of accidental explosions, UFC 3-340-02. Supersedes TM5-1300, dated November 1990. US Department of Defense, Washington DC, 2008.
- [36] T. Børvik, O. S. Hopperstad, T. Berstad, M. Langseth, A computational model of viscoplasticity and ductile damage for impact and penetration, *The European Journal of Mechanics A/Solids* 20 (2001) 685–712.
- [37] T. Børvik, O. Hopperstad, T. Berstad, M. Langseth, Perforation of 12mm thick steel plates by 20mm diameter projectiles with flat, hemispherical and conical noses - part ii: Numerical simulations, *International Journal of Impact Engineering* 27 (2002) 37–64.
- [38] M. G. Cockcroft, D. J. Latham, Ductility and workability of metals, *Journal of the Institute Metals* 96 (1968) 33–39.
- [39] T. Erhart, Review of solid element formulations in LS-DYNA, <https://www.dynamore.de/en/downloads/papers/forum11/entwicklerforum-2011/erhart.pdf/view>, [Online; accessed 23-May-2022] (2011).
- [40] J. K. Holmen, J. Johnsen, O. Hopperstad, T. Børvik, Influence of fragmentation on the capacity of aluminum alloy plates subjected to ballistic impact, *European Journal of Mechanics - A/Solids* 55 (2016) 221–233.
- [41] J. K. Holmen, T. Børvik, O. Hopperstad, Experiments and simulations of empty and sand-filled aluminum alloy panels

subjected to ballistic impact, *Engineering Structures* 130 (2017) 216–228.

PART 5

Benjamin Stavnar Elveli, Ole Vestrum, Knut Ove Hauge, Torodd Berstad, Tore Børvik,
Vegard Aune

Thin steel plates exposed to combined ballistic impact and partially confined airblast loading

Submitted for possible peer review journal publication.

Thin steel plates exposed to combined ballistic impact and partially confined airblast loading

Benjamin Stavnar Elveli^{a,b,*}, Ole Vestrum^c, Knut Ove Hauge^c, Torodd Berstad^{a,b}, Tore Børvik^{a,b}, Vegard Aune^{a,b}

^a*Structural Impact Laboratory (SIMLab), Department of Structural Engineering, NTNU – Norwegian University of Science and Technology, NO-7491 Trondheim, Norway*

^b*Centre for Advanced Structural Analysis (CASA), NTNU, NO-7491 Trondheim, Norway*

^c*Research and Development Department, Norwegian Defence Estates Agency, 0103 Oslo, Norway*

Abstract

Pre-formed defects created by high-velocity impact have the potential to reduce the structural integrity of lightweight, flexible structures. This study evaluates the effect of realistic pre-formed defects in thin steel plates exposed to partially confined detonations. Target plates containing pre-cut circular holes with a diameter of 8.0 mm are compared to target plates exposed to an initial ballistic impact from 7.62 mm APM2 projectiles. The target plates were exposed to blast loading generated from detonating C-4 inside a steel tube. The stand-off distance was fixed and set equal to the tube radius, where the rear end of the tube was kept open. All blast tests were recorded with several pressure sensors, synchronized with two high-speed cameras monitoring the dynamic response of the target plates. This allowed for a reliable experimental procedure, serving as a benchmark for different numerical methods. For similar loading conditions, the target plates containing initial ballistic impact showed a reduced fracture resistance during blast loading compared to the target plates with pre-cut circular holes. Two different numerical approaches were tested and compared, i.e., a purely Lagrangian particle-based approach and a fully coupled simulation using an ALE description of the blast domain. The ALE simulations were found to underestimate the structural response, while the particle-based approach overestimated the structural response.

Keywords: Ballistic impact, Blast loading, Particle blast method, ALE, LS-DYNA

1. Introduction

Blast waves can occur in various environments and typically originates from accidental, industrial or intended explosions [1–3]. Hazardous fragments are often accelerated by and move together with the blast wave. Such objects may be parts originating from an explosive’s container or debris from surrounding structures, i.e., primary and secondary fragments. Several studies indicate that the combined effects of blast

*Corresponding author. Tel.: +47-73-59-47-05; fax: +47-73-59-47-01.

Email address: benjamin.s.elveli@ntnu.no (Benjamin Stavnar Elveli)

and fragment impact can be more severe than the blast loading acting alone (see e.g., [4–8]). Considering a cased explosive, the initial fragment velocity is normally much smaller than the initial velocity of the blast wave. As the blast wave expands, its velocity is reduced at a higher rate than the fragments. This means that the high velocity fragments may strike before, during, or after the arrival of the blast wave, depending on distance [8].

Several studies exist on blast-loaded plates with pre-cut idealized defects, which represent fragment impact prior to blast loading [9–15]. The pre-cut defects significantly reduce the blast resistance of the target plates. That is, fracture tends to occur around the defects rather than at the supports, which is a common fracture mode for target plates without any pre-cut defects [16–18]. Granum et al. [12] found that the shape, orientation and number of pre-cut defects affected both the fracture resistance and the crack path in the target plates. Elveli et al. [19] further investigated the effect of pre-formed ballistic impact holes compared to pre-cut circular holes for thin steel plates exposed to blast-like loading conditions in a shock tube facility. As expected, the target plates with pre-formed ballistic impact holes showed a reduced fracture resistance compared to the plates with pre-cut circular holes. All crack propagations were initiated from the initial petalling cracks around the ballistic impact hole. The pre-formed ballistic impact holes and pre-cut circular holes were located at the plate center, and the loading characteristics showed similarities to that of a far-field detonation. That is, a uniformly distributed pressure field with a relatively low peak pressure and a large duration of the positive phase. A novel experimental technique was recently suggested by Atoui et al. [20], where a solid explosive with an embedded steel sphere was detonated at the entrance of an explosive-driven shock tube. The objective of the study was to control the time interval between the arrival of the steel sphere and the shock wave at the target. The experimental setup succeeded in creating repeatable loading conditions, where the spatiotemporal evolution of both the shock and the sphere were recorded using optical diagnostics.

Compared to blast loads generated in a shock tube or by detonations in free air, the number of studies on confined explosions are more limited. Confined blast loads are also more complex than those in free air. Previous studies [21, 22] have shown that the common design manual UFC-3-340-02 [23] is unable to predict a satisfactory loading history and pressure distribution from confined detonations. Because of the interactions between the propagating shock and the confinement, the loading history typically consists of several pressure peaks [21, 24, 25] with amplified magnitudes [26–28], and hence, significantly increased damage potentials [29]. The multiple pressure peaks tend to decrease towards a static overpressure, or back to atmospheric conditions depending on the venting of the confinement. Although each pressure peak evaluated alone may represent a relatively short duration, the duration of the full loading event is typically much longer than what is found for free air detonations.

However, the pressure history, pressure distribution and deformation mode are all significantly affected by the degree of confinement and the position of the explosive charge. For circular mild steel plates exposed

to confined blast loading, changes in stand-off distance affect the global deformation response. At stand-off distances smaller than the confinement radius, the plates deform as a global dome with a superimposed local dome around the plate center. As the stand-off is set to a larger distance than the distance to the confinement, the plates deform in a global dome (see e.g., [30]).

45 A similar study was performed by Yuan et al. [31], where the dynamic response of thin square steel plates were investigated for several stand-off distances for fully confined detonations. By placing one deformable steel plate in each end of a squared confinement tank, two different stand-off distances were studied for each detonation. The plate with the largest stand-off distance consistently experienced the largest maximum displacements, through a global dome deformation mode. The closest plate resulted in smaller deformations,
50 but with a superimposed local dome on the global dome, similarly as the observations in Ref. [30]. The larger stand-off led to lower peak pressures and longer durations for the transferred impulse. The total impulse was the largest for the closest plate, but the saturated impulse was seemingly larger for the plate with the largest stand-off. Generally, for confined detonations, it is observed that if the explosive charge is positioned at a distance larger than the distance to the confinement, the incoming pressure takes a more uniform
55 distribution. For stand-off distances smaller than the distance to the confinement, the pressure distribution of the initial pressure peak takes a distribution similar to that observed for unconfined detonations.

Zhang et al. [15] studied thin square steel plates with different pre-cut defects exposed to fully confined blast loads. The response of the plates without any defects were compared to the plates containing circular and square holes. It was found that the target plates with pre-cut holes experienced smaller deformations
60 than the plates without any defects. This was explained by the venting effect of the holes and is contrary to previous findings in studies on similar plate geometries exposed to blast loads from a shock tube facility (see e.g., [11, 32]). It is also noted that only the target plates with square holes experienced fracture during blast loading. Hence, the circular holes showed a larger resistance to fracture.

As confined blast loading is dependent upon interactions with the confinement on its way towards the
65 blast-loaded structure, simple pressure time histories from free-field detonations (e.g., ConWep) are seldom an option. To capture the pressure build-up during the propagation phase, a more realistic coupled description is normally required for the explosive in numerical simulations. A common choice is the Arbitrary Lagrangian-Eulerian (ALE) description. Here, the structural domain follows the traditional Lagrangian description and solved using the Finite Element Method (FEM). The fluid domain is also described using
70 FEM, but through a framework which is neither Eulerian nor Lagrangian [33–38]. The ALE description of multi-material models describing the detonation of high explosives follows the so-called operator split method, where the calculations within each time step is divided into two phases [39]. First, the mesh moves with the fluid materials according to a Lagrangian description. In the following phase, the distorted mesh is remapped back to its original configuration through an advection step. The fluid-structure coupling is
75 described through a penalty contact formulation based on the penetration of the fluid through the structural

domain.

This approach was successfully applied in Refs. [15, 31, 40–42]. The ALE approach with fully coupled FSI simulations is often very computationally expensive, and the description of the blast loading tend to be slightly underestimated. In Ref. [15], the target plate displacement was underestimated with approximately 10%, whereas Ref. [31] found that the agreement between numerical and experimental observations varied with the stand-off distance. As a too coarse discretization of the fluid domain smears out the shock discontinuity, and gives too low pressure peaks, convergence studies should be performed. Another issue with the ALE approach is related to the fluid-structure coupling, where material leakage is commonly encountered. Langdon et al. [41] suggested that the discretization of the structure must be significantly finer than the discretization of the fluid domain to overcome this issue. An element size ratio of 1/4 between the structural and fluid domains resulted in no leakage.

A simpler and computationally more efficient approach is formulated through the particle blast method (PBM). This blast modelling approach is based on the corpuscular method for airbag deployment in LSDYNA [43]. Later it was modified and successfully validated to also represent blast loads by Børvik et al. [44, 45].

The study presented herein evaluates the effect of more realistic pre-formed defects in thin steel plates exposed to partially confined detonations. That is, target plates containing pre-cut circular holes with a diameter of 8.0 mm are compared to target plates exposed to an initial ballistic impact from 7.62 mm APM2 projectiles. This study therefore follows the previous work of Elveli et al. [19]. However, in Ref. [19], the blast-like loading was generated using a shock tube facility, resulting in uniform pressure distributions with relatively low peak pressures and longer durations. In this study, the target plates are exposed to blast loading generated from detonating C-4 in a vented tube. The stand-off distance was fixed and set equal to the tube radius, where the rear end of the tube was kept open. This was done in an attempt to create a loading history with focusing effects from interaction with the tube wall, but also to reduce the sequential loading that is expected from a fully confined detonation.

The main objectives of this study are: (1) establish a repeatable and controlled experimental setup to study the dynamic response of structures subjected to loading caused by partially confined detonations; (2) investigate the effect of more realistic fragment impact defects in thin steel plates exposed to a complex blast environment; (3) to validate and compare different numerical approaches for the modeling of the partially confined blast environment against experimental observations.

2. Experimental study

In this study, the dynamic response of thin steel plates exposed to partially confined airblast loading has been investigated. Full plates, plates containing pre-cut circular holes, and plates with pre-formed

ballistic impact holes were evaluated. All blast tests were performed at an indoor testing facility operated
110 by the Norwegian Defence Estate Agency (NDEA). The experimental setup and all corresponding measuring
equipment are described in Section 2.1, while the results are given in Section 3.

2.1. Experimental setup

All blast tests were carried out by detonating an explosive charge of Composition C-4 inside a steel tube
with a length of 1 m and an inner diameter of 0.4 m, as illustrated in Figure 2 (a). The C-4 charges were
115 suspended vertically from the highest point of the tube's hull at a horizontal distance of 0.2 m from the target
plates and as close to the center as possible in the radial direction. As the position of the explosives was
kept fixed in all tests, two different charge masses of 10 g and 20 g were used to vary the blast intensity. The
target plates were clamped to the flange of the tube at the right end in Figure 2 (a). The inner diameter of
120 the clamping frame was equal to the inner diameter of the tube. A more detailed illustration of the clamping
frame is given in Figure 2 (b). For fully confined detonations, the loading history on the target plates would
consist of several pressure peaks as the shock travels back and forth inside the tube [21, 24, 25]. In turn,
this would also increase the duration of the total loading history. To obtain a controlled loading on the
target plates with a shorter duration, it was decided to keep the rear end open in all blast tests [46]. The
full assembly with the steel pipe, target plate and clamping frame were put on a stack of wooden pallets,
125 and strapped to the floor as shown in Figure 1.

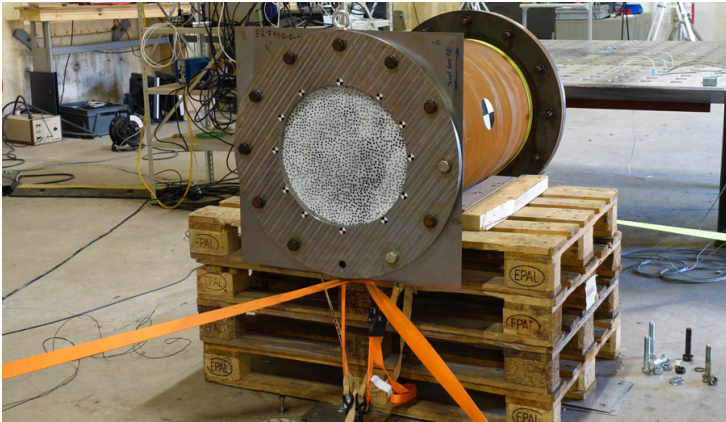


Figure 1: The testing rig used for partially confined detonations with a mounted target plate prepared for blast testing.

To study the effect of pre-formed defects in thin steel plates exposed to the partially confined airblast
loading, three different plate configurations were studied. One configuration without any pre-formed defects,
denoted FP, one configuration containing pre-cut circular holes, denoted C, and one configuration containing

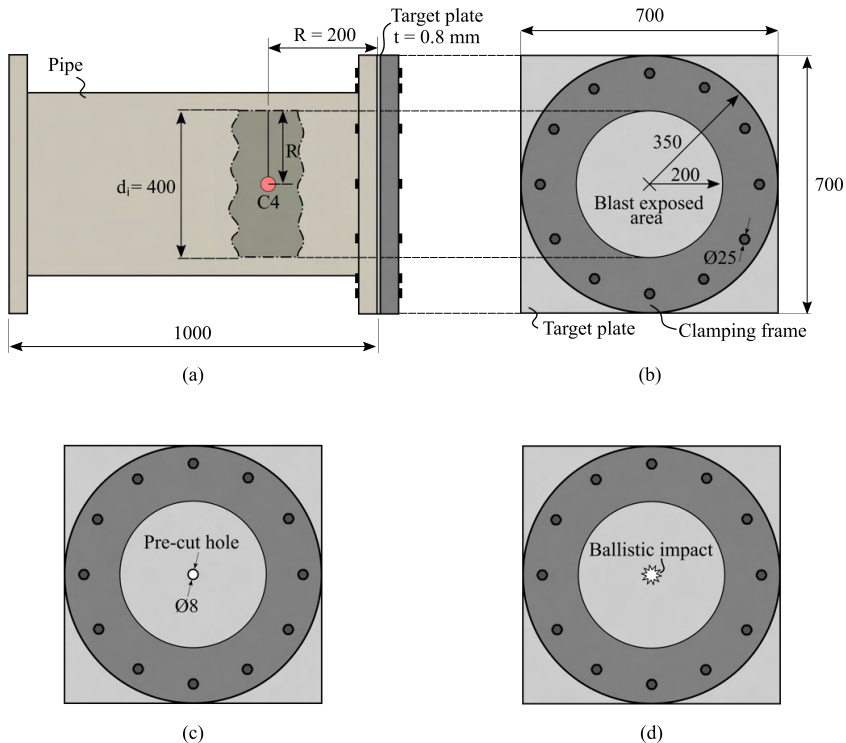


Figure 2: Schematic of the experimental setup: (a) The dimensions of the test rig and the position of the explosive charge, (b) the dimensions of the clamping frame and target plates, and the plate geometries containing (c) pre-cut circular holes and (d) pre-formed ballistic holes. All dimensions are in mm.

an initial ballistic impact hole, denoted B. All target plates had a thickness of 0.8 mm and the geometries of the plates are illustrated in Figure 2 (b-d). The two hole geometries are adopted from Ref. [19].

The blast response of the steel plates were recorded with two synchronized Phantom v2012 high-speed cameras with a sampling rate of 22626 frames per second at a resolution of 1200 x 800 pixels. The two cameras were positioned in a stereoscopic setup as shown in Figure 3. Prior to each test, the target plates were spray painted with a black and white speckle pattern. This enables measurements of the displacement fields of the target plates during blast loading by using the in-house three-dimensional digital image correlation (3D-DIC) software eCorr [47]. The movement of the testing rig was also tracked in eCorr by applying checkerboard stickers to the clamping frame around the target plates.

To measure the repeatability of each detonation, two Kistler 603B pressure sensors with a sampling rate of 500 kHz measured the pressure history at two separate locations during each blast experiment of the deformable steel plates. The location of both pressure sensors, P11 and PR02, are indicated in Figure 3.

Pressure sensor P11 was mounted on the inner tube wall, 600 mm away from the explosive charge. PR02 was placed on a fixed table outside the open end of the tube, with a height aligned with the center of the tube. A breakwire was placed inside each explosive charge, which recorded the current in the wire at the same sampling rate as the pressure sensors. The time of the detonation is established as the wire is cut by the detonation of the charge. All pressure and deformation histories are plotted with the time of detonation defined as $t=0$ ms.

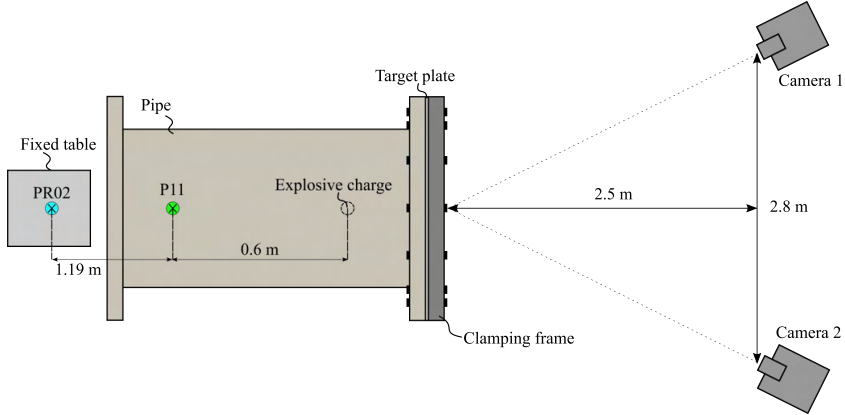


Figure 3: The setup for high-speed camera recordings and the positioning of the pressure sensors for all experiments on thin steel plates.

As an attempt to estimate the pressure on the blast-exposed surface of the deformable plates, additional blast tests using a 199 kg pendulum were performed. The schematic presentation of the pendulum is shown in Figure 4. Two additional pressure sensors were mounted on the blast-exposed surface of the pendulum, denoted P01 and P02 with positions given in Figure 4 (a). As the confinement tube is fixed and exposed to extreme loads, significant structural vibrations are expected. The pendulum was attached to the 4 m high roof of the testing facility using four steel wires. That is, two pairs of wires at each end of the pendulum, as shown in Figure 4 (b). In turn, these vibrations tend to affect the measurements from the pressure sensors. This means that the pendulum is free to move after the detonation and that movement is restricted only by the wires. It is assumed that this leads to less high-frequency oscillations and hence to cleaner pressure measurements. The total blast-exposed area of the pendulum has a diameter of 700 mm, identical to the outer diameter of the flanges of the tube. As the pendulum rests at the end of the tube before detonation, the initial blast-exposed area coincides with the inner diameter, $d_i=400$ mm, of the tube. The sensors P01 and P02 are located within the initial blast-exposed area.

The three plate geometries and the pendulum were all tested against the two different charge masses of 10 g and 20 g of C-4. For the target plates containing pre-cut circular holes (C) and the target plates

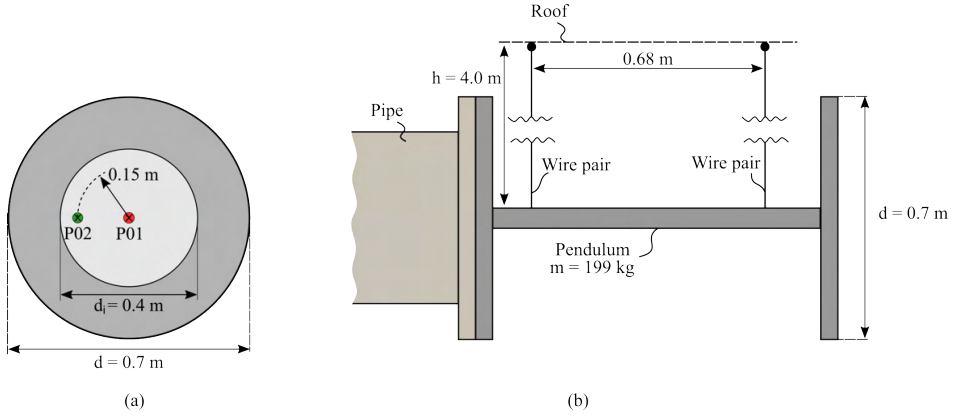
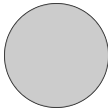
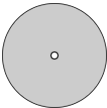
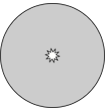
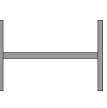


Figure 4: Schematic illustration of the ballistic pendulum tests: (a) The blast exposed area of the pendulum with indicated locations for the two pressure sensors, P01 and P02, and (b) the dimensions of the pendulum assembly. In (b) it is noted that each wire pair represents two wires with an out-of-plane distance of 100 mm.

exposed to initial ballistic impact (B), three repetitions were performed for each unique configuration. Two repetitions were also conducted for the pendulum tests. Lastly, for the full plate geometry (FP) only one test was performed. This gives a total of 18 partially confined airblast experiments. The corresponding test matrix is given in Table 1, where each test is labeled according to the naming convention XX_YY_ZZ. Here, XX denotes the geometry of the test sample, i.e., FP for the full plate, C for the pre-cut circular hole, B for the initial ballistic impact hole, or P for the pendulum. YY refers to the mass of the C-4 charge in grams. Lastly, ZZ denotes the repetition number of the same configuration.

Table 1: Experimental program.

Charge mass				
	FP	C	B	P
10 g	FP_10_1	C_10_1	B_10_1	P_10_1
	-	C_10_2	B_10_2	P_10_2
	-	C_10_3	B_10_3	-
20 g	FP_20_1	C_20_1	B_20_1	P_20_1
	-	C_20_2	B_20_2	P_20_2
	-	C_20_3	B_20_3	-

2.2. Target plate material

170 All target plates applied in this study were manufactured from a medium-strength and high-hardening dual phase steel called Docol 600DP. The steel plates were cold rolled to the desired thickness of 0.8 mm and produced by Swedish Steel Ltd. (SSAB). During the production process, the plates are heat treated after cold rolling to obtain the desired properties of the material and microstructure [48]. The manufacturer reported a yield strength in the range 350-450 MPa and an ultimate tensile strength in the range 600-700 MPa. Docol 600DP is a material developed mainly for the automotive industry due to its good formability.

180 Quasi-static tension tests of the plate material were performed using an Instron 5566 universal testing machine to document the mechanical properties of the steel material. The tension test specimens were cut in three different directions, 0° , 45° , and 90° relative to the rolling direction of the target plates. Three repetitions were performed in each direction. The dimensions of the tensile test specimen are given in Figure 5 (a). With a gauge length of 70 mm, the applied deformation rate 2.1 mm/min corresponds to an initial strain rate of $\dot{\epsilon}_0 = 5 \cdot 10^{-4} \text{s}^{-1}$.

The force F was measured by the load cell of the testing machine and the elongation ΔL was obtained from 2D-DIC using a virtual extensometer with an initial length of $L_0=60$ mm. The force measurements were synchronized with images sampled at a rate of 4 Hz. The engineering stress and strain was then calculated by Eq. (1), where A_0 denotes the measured gauge area of each test specimen.

$$s = \frac{F}{A_0} \quad \epsilon = \frac{\Delta L}{L_0} \quad (1)$$

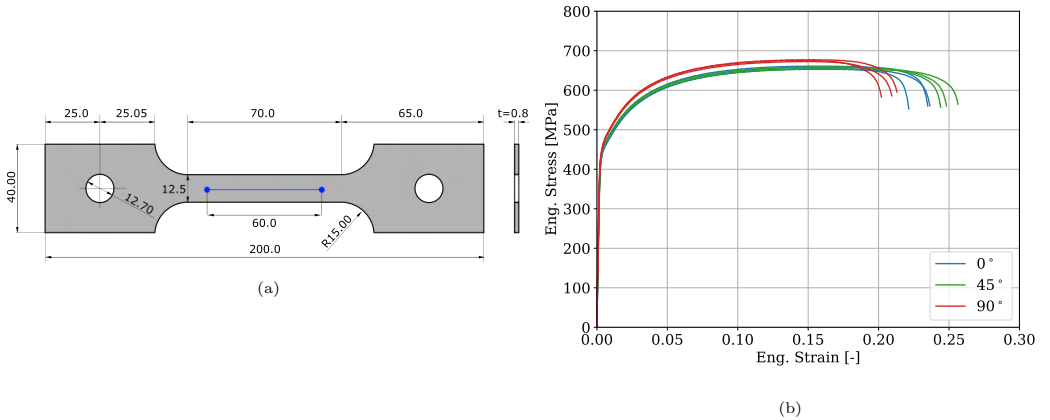


Figure 5: Uniaxial tension tests: (a) Sketch of the dog-bone specimen and the position of the virtual extensometer marked with a blue line, and (b) the corresponding engineering stress-strain curves for the Docol 600DP material. All dimensions are in mm.

The engineering stress-strain curves in Figure 5 confirm the yield and ultimate tensile stress reported by the manufacturer. However, there are minor deviations in engineering stress between the three directions. The 90° experienced higher engineering stress and a smaller elongation to fracture than the 0° and 45° tests. Similar trends were found for the uniaxial tension tests in Refs. [11, 49] for the comparable material
190 Docol 600DL, also produced by SSAB. Here, in both cases, it was concluded that the plastic anisotropy was negligible.

2.3. Ballistic impact tests

The ballistic impact holes were created by firing a 7.62 mm APM2 projectile from a smooth-bore Mauser rifle mounted in a firing-rig with an initial velocity of around 900 m/s. One single shot was fired against the
195 center of the target plates, perpendicular to the surface of the sheet. The procedure for the ballistic testing was done under identical conditions as in Elveli et al. [19] and is therefore only briefly described herein. The intention of the ballistic impact event was to introduce a more realistic fracture mode to the target plates prior to the blast load. For a better comparability to the target plates containing 8.0 mm pre-cut circular holes, it was desired to produce bullet holes with as little global deformation as possible.

200 The initial projectile velocity of 900 m/s was significantly higher than the ballistic limit velocity of the 0.8 mm target plates. The resulting velocity reduction after impact with the target plates was in the range of 1-2%. Further, all target plates failed by petalling and experienced only local plastic deformations and fracture around the impact hole. Three representative images of the obtained fracture mode from the ballistic impact event are given in Figure 6. It should be noted that an evaluation of the ballistic capacity
205 of the target plates was not performed, as it was considered beyond the scope of this study.

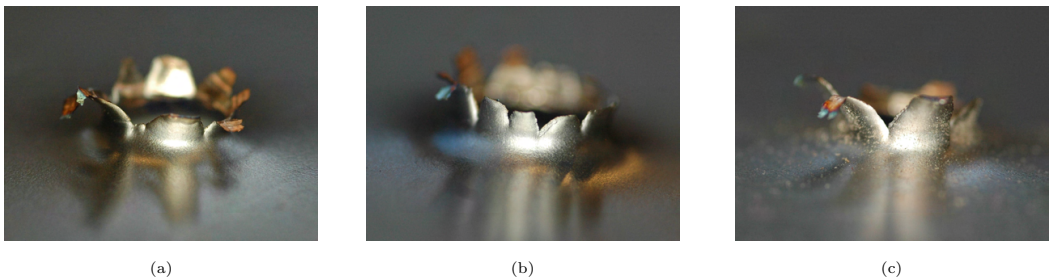


Figure 6: Three representative images of the obtained petalling fracture mode from the ballistic impact tests.

3. Partially confined detonations

The results of all airblast experiments are presented in this section and are divided into three main parts. First, the measured pressure histories are presented with the main objective of understanding the

characteristics of the loading history and its repeatability between tests. Secondly, the global deformations of
210 the target plates are considered through deformation histories obtained by 3D-DIC analyses of the high-speed
camera recordings. Lastly, the fracture resistance of the different plate geometries are evaluated.

3.1. Pressure measurements

To date, there are no experimental techniques capable of measuring full-field surface pressures acting
on thin plates undergoing large deformations [50]. This motivated the blast tests on the 199 kg pendulum
215 exposed to identical loading conditions. As shown in Figure 4 (a), the reflected pressure was measured at
two locations (P01 and P02) on the blast-exposed surface of the pendulum. The corresponding pressure
histories are compared for the two repetitions in Figure 4 (a) and (b), for the 10 g and 20 g detonations,
respectively. All pressure histories have been adjusted according to the breakwire, so that the detonation
occurs at $t=0$ ms.

220 As the explosive charge was placed one tube radius away from the pendulum, the first pressure peak
represents the incoming shock impacting the pendulum without any interaction with the tube wall. As P01
has the shortest distance to the explosive charge, the first pressure peak arrives at P01 before P02. The
second pressure peak occur as the shock is reflected at the tube wall, and then redirected towards the center
of the pendulum. P02 is positioned closer to the tube wall, and therefore, the delay between the first and
225 second peak is much shorter for P02 than for P01. It is also observed that the secondary pressure peak at
P02 is significantly smaller than the first. For P01, the secondary pressure peak is similar, or even slightly
larger than the first reflection. This could be explained by the axisymmetry in the confinement tube. As
the pressure reflects at the tube wall, all reflections will eventually meet at the tube center and amplify the
secondary pressure peak measured at P01.

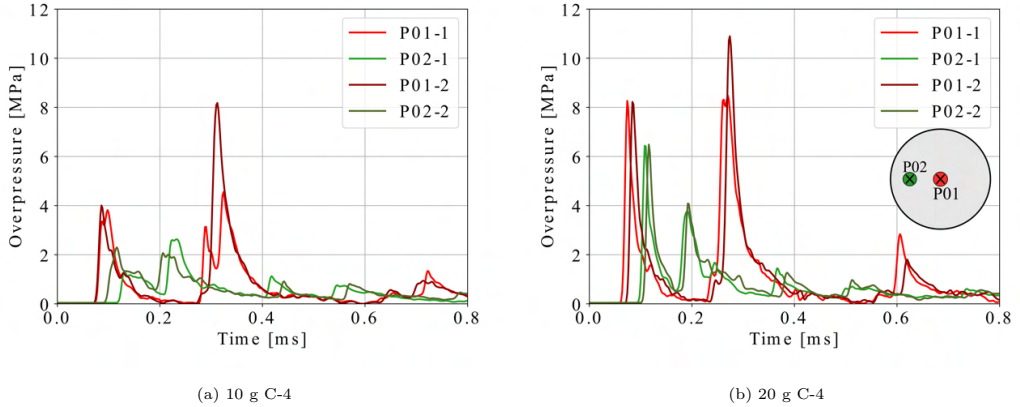


Figure 7: The reflected pressure histories on the blast-exposed surface of the pendulum, measured at sensors P01 and P02 (see Figure 4). The recorded pressure is compared for both of the two repetitions of the 10 g detonation in (a) and the 20 g detonation in (b). The position of the two sensors is also indicated in (b).

230 Between the repeated tests the magnitude of the pressure peaks, the duration, and the overall behavior were comparable within each of the two charge masses. However, small deviations were observed in the time of arrival between the two 20 g charge tests (see Figure 7 (b)). Both P01-2 and P02-2 experienced an identical offset relative to P01-1 and P02-1. All measurements were time-shifted similarly by the breakwire, and the reason for the slight offset is unknown. Another difference between the two repetitions, observed
 235 for both charge masses, is the magnitude of the second pressure peak for sensor P01. P01-2 experienced a larger magnitude of the second pressure peak than P01-1. It is unclear whether this is caused by actual differences in the loading history, or if it is caused by disturbances of the sensor.

From the measurements of P01 and P02 in Figure 7 it is evident that the loading history on the blast-exposed surface of the pendulum is non-uniform and has a relatively short duration for both charge masses.
 240 The majority of the loading history experienced a duration of around 0.35 ms, with only minor pressure peaks from this point and out. Between the two different charge masses, the initial pressure peak at P01 is halved from 8 MPa for the 20 g charge, to 4 MPa for the 10 g charge. It should be noted that the measured peak pressures are limited by the sampling rate of the pressure sensors, and that higher pressures could occur between measurements.

245 For the deformable steel plates, the only available pressure measurements are from sensor P11 and PR02. As illustrated in Figure 3, P11 was mounted along the inner wall of the tube, while PR02 was positioned on a fixed table right outside the free end of the tube. The corresponding pressure measurements from pressure sensors P11 and PR02 are presented in Figure 8 for all 10 g detonations on deformable steel plates with and without pre-cut defects.

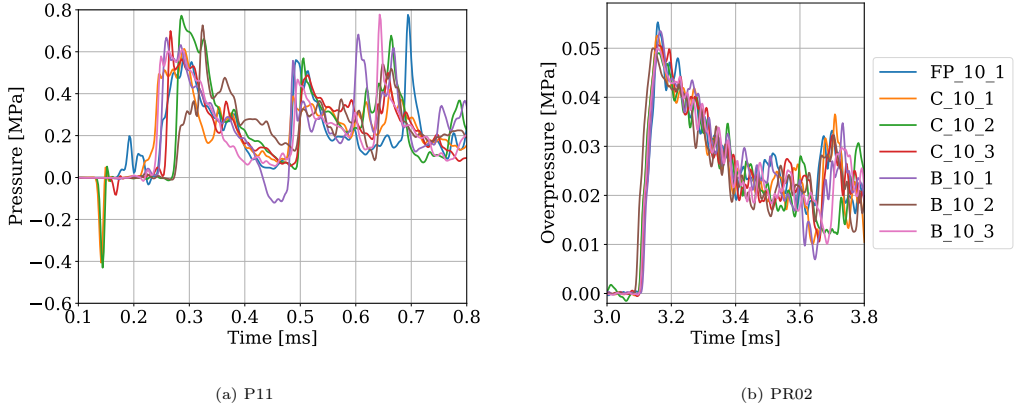


Figure 8: Pressure measurements from the 10 g detonations for pressure sensors P11 and PR02 with positions indicated in Figure 3. The applied sensor corresponding to each plot is given in the sub-caption

250 The pressure histories obtained from both P11 and PR02 are more noisy than those measured for P01 and P02 in Figure 7. For the measurements at P11, large variations in both the initial peak pressure and the overall pressure history was found. Some of the measurements even experienced oscillations before the arrival of the shock wave, as seen in Figure 8 (a). A more clean rise in pressure up to the initial peak was found for the measurements from PR02, as seen in Figure 8 (b). Also here, some oscillations were observed
 255 after the initial pressure peak. These oscillations or noise in the pressure measurements for P11 and PR02 are assumed to be caused by vibrations in the structures that are instrumented with the pressure sensors. However, if we consider the measurements from PR02 and further only the initial pressure peak, the loading history seems to be quite consistent across all tests within a similar charge mass. As the 20 g detonation showed similar trends for P11 and PR02, the pressure histories are not plotted. All measured peak pressures
 260 at P11 and PG02 are listed in Table 2.

To summarize, it was challenging to obtain clean pressure measurements for all blast tests, especially for tests on thin, deformable steel plates where the sensors had to be mounted to the test rig. The reflected pressure measurements from the blast-exposed surface of the pendulum showed clean pressure peaks, with minor fluctuations, and good repeatability of the loading histories. The repeatability of the loading
 265 history seems to be quite consistent also for the deformable steel plates, if the measurements from PR02 are considered.

3.2. Deformation response

To obtain reliable deformation fields from the 3D-DIC analysis, the spray-painted speckle pattern must remain intact throughout the dynamic response of the target plates. Unfortunately, the spray paint was

270 detached from the thin steel plates around the plate center for some of the tests. Another 3D-DIC issue
occurred for the target plates containing pre-formed holes, as the fireball from the detonation saturated the
high-speed camera recordings for some of the images during the deformation process. That is, the visibility
of the recorded images was poor due to the strong light resulting from the detonation process. This issue
was overcome by simply skipping the images with poor quality from the DIC analysis. Figures 9 and 10
275 show representative deformation profiles from the successful 3D-DIC analyses. The deformation profiles
correspond to the out-of-plane displacements at a given time along a vector starting at the plate boundary
and moving through the plate center.

Figure 9 shows the deformation profiles for tests FP_10_1 and FP_20_1 for all recorded deformation states
from zero displacement and up to the maximum displacement. The total time-span from the detonation up
280 to maximum deformation is given in the upper right corner of each plot. For each plot, four main states
of deformation are labeled according to factors relative to the maximum displacement, i.e., factors of 0.25,
0.50, 0.75 and 1.0. The green dotted lines indicate the plate movement in-between the labeled states of
deformation. It should be noted that the spray paint detached around the center of the FP_10_1 test right
before maximum displacement was reached, and therefore the center portion of the "1.0" deformation profile
285 was not obtained.

It is observed that the deformation process is characterized by three main phases (see Figure 9). During
the first phase, the blast-exposed area of the target plate is activated and moves as a rigid body. A plastic
hinge starts to propagate from the outer boundary of the target plate towards the center. Between the
plastic hinge and the boundary, the plate takes a triangular shape, with limited visual curvature. This takes
290 place mainly up to the 0.5 deformation profile, marked with blue in Figure 9 (c).

In the second phase, the plastic hinges gradually started to move faster than the center portion of the
plate in the out-of-plane direction. From the mid-point displacement plot in Figure 9 (d), the deformation
rate is decreasing slightly between the orange and the blue dots. Between the blue and purple deformation
profiles in Figure 9 (c), a local dent starts to form around the center, as the mid-point moves to slow to keep
295 up with the rest of the plate. This continues until approximately 0.75 ms after the detonation.

In the third and last phase, the local dent at the center of the plate rapidly starts to accelerate outwards.
At this point, the plastic hinges has moved almost all the way to the plate center, and the deformation
profile takes a triangular shape. With respect to the mid-point, this is also the phase with the largest
deformation rate, seen as a rapid increase of displacements in Figure 9 (d). The deformation profile at
300 maximum displacement takes the shape of a global dome with a superimposed local dome around the plate
center, similar to the findings in Refs. [18, 30].

The entire deformation process up to the time of maximum deformation takes about 1 ms from the time
of detonation. Compared to the loading rate presented in Figure 7, it is observed that the entire loading
history ends after about 0.4 ms. According to the pressure measurements, the movements from the blue

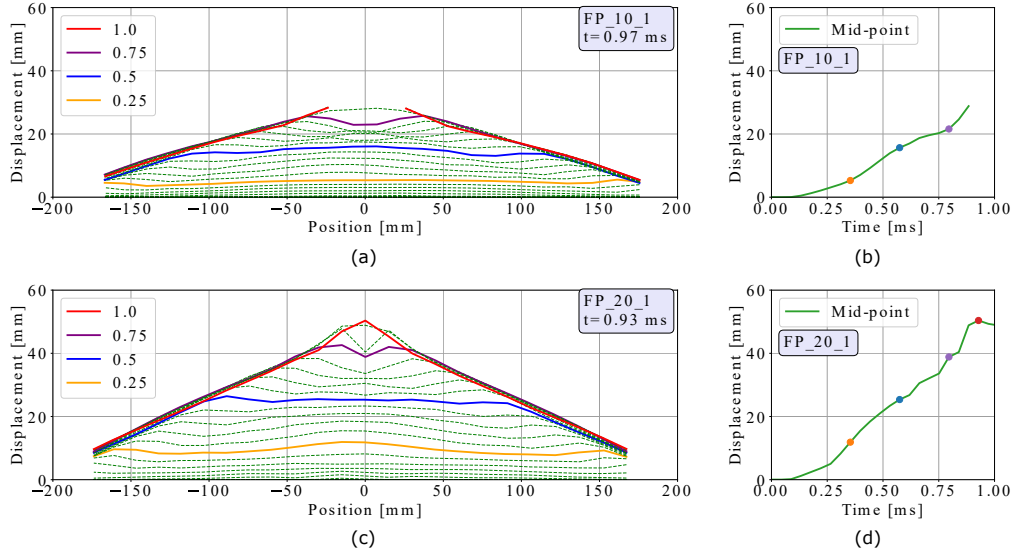


Figure 9: Deformation profiles for tests FP_10_1 in (a) and FP_20_1 in (c). For each plot, four main states of deformation are labeled relative to the maximum displacement, i.e., factors of 0.25, 0.50, 0.75 and 1.0. The green dotted lines indicate the plate movement in-between the labeled states of deformation, with a time difference of $\Delta t = 0.044$ ms between each sampling. The total time between the detonation and the occurrence of the maximum displacement t is given in the upper left corner of each plot. The corresponding mid-point displacements versus time are plotted for both tests in (b) and (d). It is noted that the spray paint detached around the plate center for the FP_10_1 test, and hence, the center portion of the deformation profile as well as the last part of the mid-point displacement response was excluded from the plots in (a) and (b).

305 deformation profile in 9 (c) and up to maximum deformation occur without any applied loading from the detonation.

As expected, the reduction in the charge mass from 20 g in test FP_20_1 to 10 g in test FP_10_1 reduced both the maximum deformations and the deformation rates. This is seen by comparing the deformation histories from the 20 g detonation in Figure 9 (c) and (d), to the 10 g detonations in Figure 9 (a) and (b).

310 Even though the deformations and deformation rate are observed to decrease in test FP_10_1, the main trends in the deformation response are similar, but less pronounced.

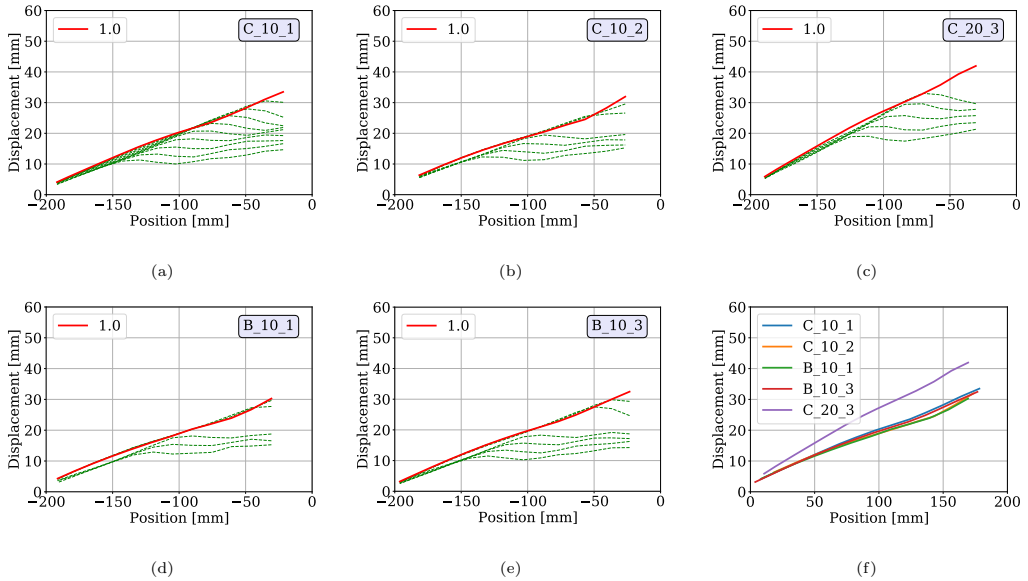


Figure 10: All available deformation profiles for the airblast experiments on target plates with pre-cut defects in (a-e). The test identity is indicated in the upper right corner of each sub-figure. In (f), the deformation profile at maximum displacement are plotted together for all tests in (a-e) for comparison. It is noted that the deformation profiles of the C and B geometry consists of only one side of the plate center, due to issues with the fireball coming through the center.

Before studying the fracture resistance of the target plates with pre-formed defects, the global response was evaluated briefly. Figure 10 compares the deformation profiles for the pre-cut hole (C) and ballistic hole (B) geometries, in an attempt to validate the repeatability in the loading conditions. Because of the fireball coming through the pre-formed defects, the deformation profiles are only obtained at one side of the plate center. Some images were also discarded, which is seen as fewer green lines indicating the plate movement.

Out of the 12 airblast tests on target plates with pre-formed holes, only 5 are presented in Figure 10. For the remaining 7 experiments, the high-speed images were either too affected by the light from the fireball, or suffering from detachment of spray paint. All available deformation profiles are given in Figure 10 (a-e), while Figure 10 (f) gives a comparison of all deformation profiles at maximum displacement. It is observed that the deformation response for the C and B geometries follows trends similar to those for the FP geometry in Figure 9. For the comparison of all deformation profiles at maximum displacement, only minor variations are seen. Thus, the results indicate that the loading conditions from the detonations are comparable for the repetitions within each of the two charge masses, and that the repeatability between tests with the same charge mass was good.

3.3. Fracture resistance

Figures 11 and 12 show the permanent deformed configuration of the C and B geometries, respectively. The charge mass and repetition of each test are given in the sub-captions. No image sequences were made from these tests due to the challenges with the fireball dominating the high-speed images in the area of interest. From the images in Figure 11 (a-c), it is clear that none of the three repetitions of the C₁₀

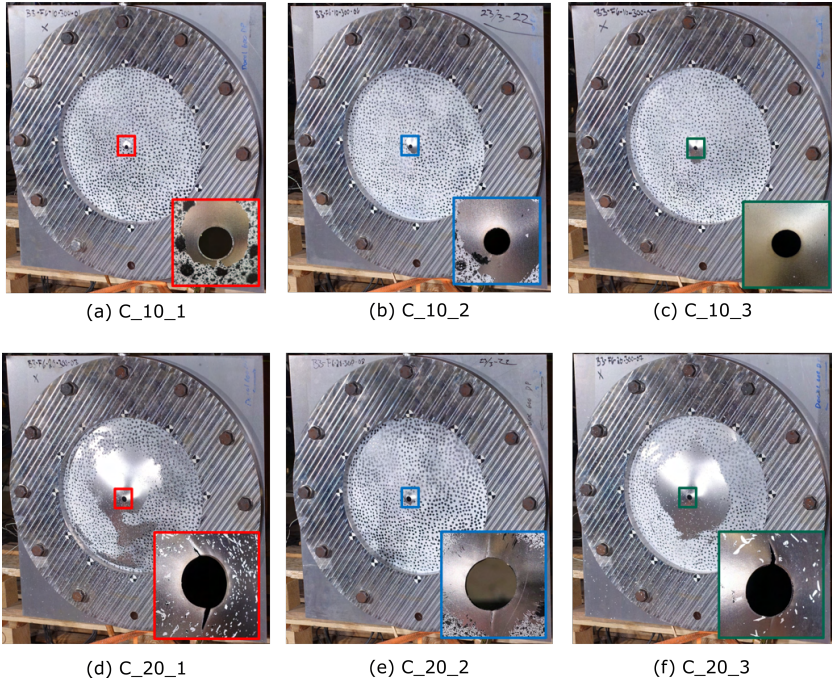


Figure 11: Post images of all airblast tests on target plates with the C geometry. The test identity indicating the charge mass and repetition is given in the sub-captions. An additional zoomed image around the pre-formed hole is given at the lower right corner of each sub-figure.

330 configuration experienced any signs of fracture or localized necking around the pre-cut circular hole. As the charge mass was increased to 20 g in Figure 11 (d)-(f), all three repetitions resulted in small arrested cracks from the periphery of the circular holes. The crack lengths were measured to be 5.6 mm and 7.3 mm for C_{20_1}, 7.3 mm for C_{20_2}, and 6.1 mm and 4.9 mm for C_{20_3}. It is also noted that all cracks for the C₂₀
 335 configuration propagated in the vertical direction only. As all target plates are mounted with the rolling direction vertically, the results indicate that the crack resistance is the lowest 90° to the rolling direction. This corresponds to the 90° material curves in Figure 5.

The findings in the tests with the B geometry confirm the observations in previous studies [19], where the B geometry showed a reduced fracture resistance during blast loading compared to the C geometry (Figure

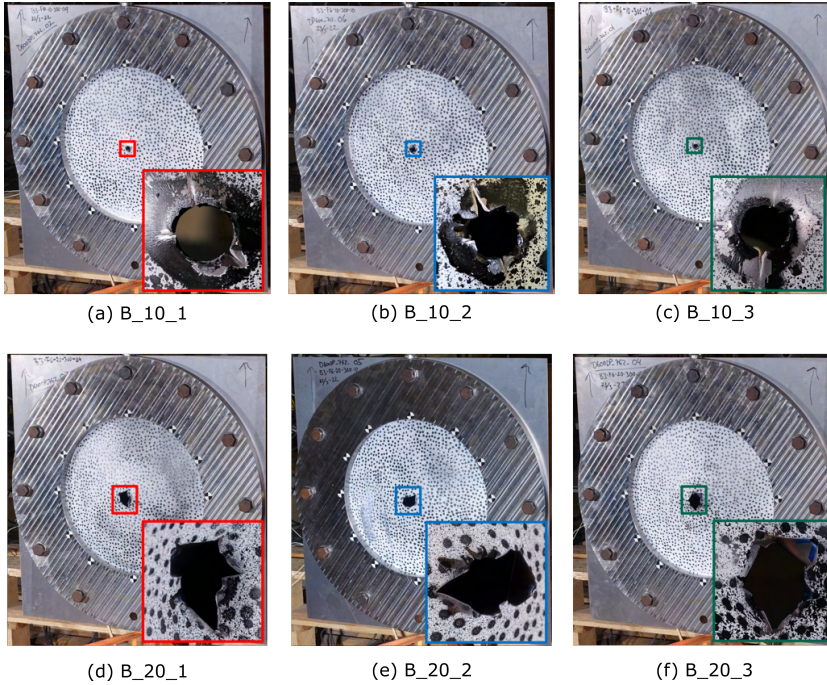


Figure 12: Post images of all airblast tests on target plates with the B geometry. The test identity indicating the charge mass and repetition is given in the sub-captions. An additional zoomed image around the pre-formed hole is given at the lower right corner of each sub-figure.

12). In fact, it is seen that even at the 10 g charge mass, all three repetitions experienced crack initiation in some of the initial petalling cracks (see Figure 12 (a-c)). For the 20 g charge mass, all three B₂₀ tests resulted in large arrested cracks (see Figure 12 (d-f)). The material around the arrested cracks experienced large plastic deformations, where the petals around the pre-formed holes were bent outward. This final state of plastic deformation made it difficult to measure the arrested crack lengths. Instead, the largest measured distance between two crack tips was measured across the ballistic hole. For comparison, this was also done for the C geometry, and all measurements are given together with the pressure measurements in Table 2. By comparing the C and B geometries for the 20 g charge, it is seen that the B₂₀ tests experienced approximately twice as large cracks as the C₂₀ tests. For the change in charge mass from 20 g to 10 g for the B geometry, the crack lengths were reduced by almost a factor of 4. It should however be noted that non of the arrested cracks extended outside the local dome of plastic deformation at the center of the blast-loaded target plates. The largest measured distance between crack tips was 47.2 mm for the B_{20_1} test, and this only covers 12% of the 400 mm diameter blast-exposed area of the target plates.

Table 2: Summarizing the peak values of the pressure measurements at the sensors P11 and PR2 for the blast tests on deformable steel plates. The given crack lengths represent the largest distance between two crack tips across the pre-formed hole.

Test	Repetition #	P11 [MPa]	PR02 [MPa]	Crack length [mm]
FP_10	1	0.594	0.054	No cracks
C_10	1	0.667	0.052	No cracks
	2	0.726	0.048	No cracks
	3	0.603	0.050	No cracks
B_10	1	0.615	0.052	12.7
	2	0.770	0.049	13.3
	3	0.699	0.049	20.6
FP_20	1	1.494	0.084	No cracks
C_20	1	-	-	25.8
	2	1.278	0.075	21.1
	3	1.095	0.075	23.9
B_20	1	1.701	0.076	47.2
	2	1.242	0.075	45.1
	3	1.085	0.075	44.5

4. Numerical work

All numerical simulations in this study were performed using the explicit finite element code LS-DYNA. More specifically, the F14.0 development version of the solver was used. Two different approaches for the modelling of explosives and air were tested and compared. That is, the Particle Blast Method (PBM) [42] and an Arbitrary Eulerian Lagrangian (ALE) approach [15, 31, 40–42]. The two different modelling techniques are briefly described in Sections 4.3 and 4.4.

4.1. Material modelling of the target plates

The Docol 600DP material used in the blast-loaded steel plates was modeled using *MAT_107, which is an elastic-thermoviscoplastic constitutive relation formulated through the modified Johnson-Cook relation as described in Ref. [51], and given in Eq. (2).

$$\sigma_{\text{eq}} = (A + R(p)) (1 + \dot{p}^*)^c (1 - T^{*m}) \quad (2)$$

where σ_{eq} denotes the equivalent stress, A the initial yield stress, and $R(p)$ the plastic strain hardening given in Eq. (3). The dimensionless plastic strain rate is given by $\dot{p}^* = \dot{p}/\dot{p}_0$, where the reference strain rate is given by $\dot{p}_0 = 5.0 \cdot 10^{-4} \text{s}^{-1}$. The strain rate sensitivity of the material is accounted for by c , and the last term in Eq. (2) determines the temperature softening of the material. Here, $T^* = (T - T_0)/(T_m - T_0)$, where T_0 is a reference temperature and T_m is the melting temperature of the material.

$$R(p) = \sum_{k=1}^2 Q_k (1 - e^{-c_k p}) \quad (3)$$

In Eq. (3), Q_k and c_k are the material parameters of the Voce hardening law, and p denotes the equivalent plastic strain. The modelling of fracture was done through the Cockcroft-Latham (CL) fracture criterion [52], given in Eq. (4) as

$$D = \frac{W}{W_c} = \frac{1}{W_c} \int_0^p \langle \sigma_1 \rangle dp, \quad \langle \sigma_1 \rangle = \max(\sigma_1, 0) \quad (4)$$

Here, D denotes the damage indicator and W_c is the critical fracture parameter. Fracture initiates when W reaches W_c , i.e., when $D=1.0$. Both the plastic strain hardening parameters Q_k and c_k , and the fracture parameter, W_c were calibrated through an inverse modelling approach of the uniaxial tension tests to fracture. The tension test specimen was discretized using 0.8 mm shell elements, equal to the thickness of the specimen. The calibrated material parameters are summarized in Table 3, and the corresponding numerical engineering stress-strain curve is given and compared to the experimental curve in Figure 13.

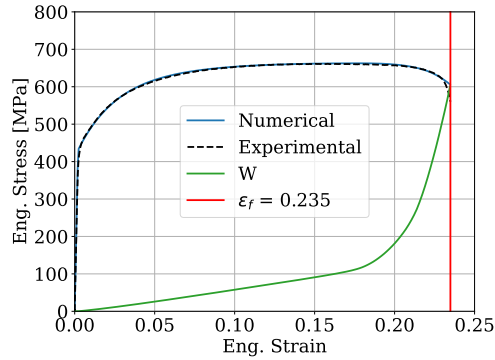


Figure 13: Comparison of numerical and experimental stress-strain curves to fracture. The fracture parameter W_c was determined at the engineering fracture strain observed in the experiments, and is indicated with ϵ_f .

Table 3: Parameters for the constitutive relation described in Eqs.(2)-(4). The strain rate sensitivity parameter, c , and the thermal exponent, m , are both taken from [11].

A	Q_1	C_1	Q_2	C_2	c	m	W_c
[MPa]	[MPa]	[-]	[MPa]	[-]	[-]	[-]	[MPa]
431.2	195.434	42.137	455.018	2.558	0.01	1.0	606.6

4.2. Discretization and boundary conditions - solids

The target plates for all three geometries were discretized using shell elements with an in-plane element size of 0.8 mm, equivalent to the plate thickness. The clamping frame, the bolts, and the confinement tube were modeled using solid elements. For simplicity, all structural parts applied the material model as described in Section 4.1. The boundary conditions for the bolts were applied similarly as in Ref. [11]. That is, the bolt tightening force was represented as a constant pressure applied to the clamping frame in the area covered by the bolt head. The free ends of the bolts were fixed on the opposite side of the bolt head for translation in all directions. Lastly, quarter symmetry was applied, and the corresponding numerical model of the clamping frame and target plate is shown in Figure 14. Since a restart analysis with the particle blast

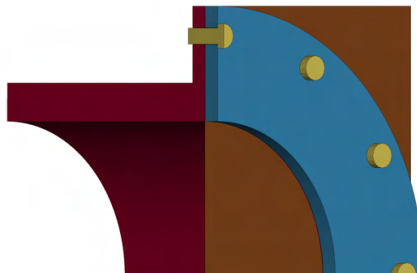


Figure 14: The numerical model of the target plate, the confinement tube, and the clamping assembly, utilizing quarter symmetry for all parts.

method (PBM) was not possible, the ballistic impact and the blast loading were applied in the same analysis for all simulations. The projectile was modeled with solid elements, a rigid material model, and an initial velocity of 900 m/s. A parametric study of the fluid domain indicated that the length of the confinement tube and the fluid domain could be shortened significantly without affecting the blast load. For numerical efficiency, the current models used a confinement tube length of two pipe radii (i.e., 400 mm).

4.3. Particle Blast Method (PBM)

The particle blast method (PBM) is governed by the *DEFINE_PARTICLE_BLAST keyword in LS-DYNA, and represents a pure Lagrangian description of the detonation product and the resulting blast

load on the surrounding structure. The air particles are initialized with a total amount of kinetic energy corresponding to the internal energy of the air at atmospheric conditions. For the high explosive (HE), the full chemical energy release from the detonation is transferred to the HE particles as kinetic energy. At time $t = 0$ ms, all HE particles are frozen and tightly packed. At a given detonation time, the HE particles are activated based on the distance to the given detonation point and the given detonation velocity for the explosive material [44].

Each particle typically represents $10^{15} - 10^{20}$ molecules. To model each molecule as its own particle would result in unrealistic computational costs, and memory requirements for a full scale model. The relationship between the number of HE particles (NPHE) and the number of air particles (NPAIR) was determined so it reflects the ratios of the molar mass between the HE and air. This was done using the formula in Eq. (5)

$$NPAIR = \left(\frac{MAIR}{MHE} \right) NPHE \quad (5)$$

where $MAIR$ denotes the mass of air within the modelled domain, and MHE is the mass of the explosive charge. The reference model applied for the PBM approach in this study used 80k particles for the HE and 2174k particles for the air domain. Due to interaction issues between the solid elements and the air particles, the confinement tube was modeled using shell elements. As no contact definition is required between the clamping frame and the particles, this was modeled in the same way as given in Section 4.2. As the inclusion of air particles impose a pressure of 1 atm, the air filled domain has to extend across both sides of the target plates to avoid an artificial overpressure inside the confinement tube. Ambient boundary conditions were applied to the boundaries of the air domain, which means that only particles representing a pressure higher than 1 atm are allowed to translate across the boundary.

4.4. Arbitrary Eulerian-Lagrangian (ALE) method

The ALE description of the partially confined detonation is based on a finite element formulation for both the structural and fluid domains. All fluids are formulated through an ALE description, while the structural domain is represented by a Lagrangian formulation.

It should be noted that LS-DYNA offers two different ALE solvers, the traditional Multi-Material ALE (MMALE), and a more recent formulation called Structured ALE (SALE). The main difference between the two alternative ALE approaches is the discretization of the fluid domain. In MMALE, the fluid mesh is designed by the user in a similar way as for structural parts, without any restrictions on the shape of the mesh. In SALE, the meshing of the fluid domain is simply defined in the keyword-file, and the mesh is generated during the initialization of the model. Here, the mesh has to be structured, i.e., it has to take the shape of a rectangular box, containing only rectangular elements. As both the shape and varying element sizes within the fluid domain tend to affect the corresponding solution, the new meshing restrictions remove some of these uncertainties away from the user. Another difference between MMALE and SALE is the

FSI algorithm used to enforce the interactions between the structural and fluid domains. For the MMALE models, several keywords need to be defined for the contact handling and leakage issues. In SALE, these options are removed, and the majority of contact options are determined automatically by the solver and defined by the keyword *STRUCTURED_FSI. In this study, it was decided to only consider the more recent SALE solver.

The fluid domain consists of two separate materials, i.e., the air and the detonation products. Both materials flow through the same fluid mesh, but they are not allowed to mix. The expansion of the detonation product leads to compression of the surrounding air and hence to an increase in pressure. The air was represented with the *LINEAR_POLYNOMIAL equation of state (EOS) expressed in terms of a perfect gas given by Eq. (6)

$$P = (\gamma - 1) \frac{\rho}{\rho_0} E, \quad \gamma = \frac{C_p}{C_v} \quad (6)$$

where C_p and C_v are defined as the specific heat capacities under constant pressure and volume, respectively. As γ , E , and ρ_0 are all considered material constants, volumetric changes is the only contributor to the pressure change in this EOS. The pressure-volume relation for the expansion of the detonation product is governed by the Jones-Wilkins-Lee (JWL) EOS. Here, the relationship between pressure, P , volume V , and energy E is given by Eq. (7) as

$$P_{jwl} = A \left(1 - \frac{\omega}{R_1 V} \right) e^{-R_1 V} + B \left(1 - \frac{\omega}{R_2 V} \right) e^{-R_2 V} + \frac{\omega E}{V} \quad (7)$$

where A, B, R_1, R_2 , and $\omega = \gamma - 1$ are material parameters linked to the type of explosive material. The first two terms in Eq. (7) represent the rapid pressure drop in the detonation products from the expansion of the initially hot gases. The third and last term describes the behavior of an expanding ideal gas.

The detonation of the explosive material was initiated at the specified detonation point given by *INITIAL_DETONATION. During the initialization of the model, the air was governed by the EOS in Eq. (6) at atmospheric conditions. The explosive material is initially filled into the fluid domain as a un-detonated sphere with zero pressure and its solid state density (ρ_{C-4}). The detonation of the explosive material is dealt with by *MAT_HIGH_EXPLOSIVE_BURN. Two alternative burn fractions are calculated based on the initial density of the un-detonated explosive, ρ_{C-4} , the detonation pressure (Chapman-Jouguet pressure), P_{CJ} , and the detonation velocity, D . F_1 corresponds to a programmed burn and F_2 to a beta burn. The effective burn fraction for each element is always taken as the maximum of F_1 and F_2 , i.e.,

$$F_1 = \begin{cases} \frac{2}{3} \left(\frac{A_{max}}{v_e} \right) (t - t_1) D, & t > t_1 \\ 0, & t \leq t_1 \end{cases} \quad (8)$$

$$F_2 = \frac{1 - V}{1 - V_{CJ}}, \quad V_{CJ} = 1 - \frac{P_{CJ}}{\rho_{C-4} D^2} \quad (9)$$

$$F = \max(F_1, F_2) \quad (10)$$

The pressure at any time is given by the EOS for the detonation products, P_{jwl} , scaled by the burn fraction, F , as given in Eq. (11). Thus,

$$P = P_{jwl}F \quad (11)$$

The lightning time for an element, t_1 , is based on its distance to the defined detonation point and the detonation velocity. v_e is the volume of an element and A_{max} the maximum projected area of the element. As an element approaches $F = 1.0$, F is fixed and the pressure is determined solely by the EOS. If F exceeds 1.0, it is reset to 1.0. In principle, this means that the detonation of the explosive is based on either the passing of the detonation wave (F_1), or by volumetric compression (F_2), where the first criterion to reach unity decides. The material parameters applied for the air and the explosive are taken from Ref. [44], and are given in Table 4.

Table 4: Material parameters applied for C-4 and air. All parameters are taken from [44]. It is noted that $E_0 = P_0/(\gamma - 1)$.

High explosive - C-4							Air				
ρ_{C-4}	D	P_{CJ}	A	B	R_1	R_2	ω	ρ_0	γ	P_0	E_0
[kg/m ³]	[m/s]	[MPa]	[MPa]	[MPa]	[-]	[-]	[-]	[kg/m ³]	[-]	[MPa]	[MPa]
1601	8190	28000	597400	13900	4.5	1.5	0.32	1.225	0.4	0.1	0.25

4.4.1. Advection method

The re-mapping in the ALE methods involves transfer of state variables from the deformed Lagrangian configuration back to the undeformed mesh. The particular advection algorithm is chosen by the user. Several methods are available and governed by the "METH" keyword in *CONTROL_ALE. LS-DYNA recommends METH=-2 in combination with *MAT_HIGH_EXPLOSIVE_BURN. This choice represents a Van Leer advection scheme where the state variables are assumed to vary with a higher order interpolation function internally in each element for the advection calculations. This gives an advection scheme with second-order accuracy, which is also stated to better preserve the interface of materials described by *MAT_HIGH_EXPLOSIVE_BURN in certain conditions [53].

In this study, it was decided to apply the recommended advection method, "METH=-2" for the reference model, and all ALE elements are formulated with element formulation 11. This represents a one-point ALE multi-material element. However, an alternative advection method was tested, and the corresponding results are given in Appendix A.

4.5. Numerical results

As a benchmark for the SALE model, the reflected pressure histories were compared at the same locations as P01 and P02 in the ballistic pendulum tests (see Figures 4 and 7). Additionally, the force acting from the fluid onto the pendulum was evaluated, and denoted "FSI force". This force is governed by the keyword

480 *DATABASE_FSI, and is defined as the averaged total estimated coupling force along the global coordinate directions between a given Lagrangian surface entity and the fluids. Both the pressure and force histories are presented in Figure 15. For the PBM simulations, some difficulties were encountered with respect to the modelling of surrounding air particles, and the interaction with structural parts when modelled with solid elements. That is, air particles were filled both around and inside all structural parts, resulting in artifacts
485 and non-physical behavior. This problem was most evident in the modelling and simulation of the ballistic pendulum tests. As a consequence, the PBM simulations were only evaluated based on the experimental findings in tests involving the deformable steel plates.

Figure 15 shows that the main trends from the experimental observations are captured in the SALE simulations. For P02, the initial and the second pressure peaks are occurring at similar times and are of
490 a comparable magnitude numerically and experimentally. The numerical measurements at pressure sensor P01 experienced significant oscillations and amplified magnitudes compared to the experiments, especially for the second pressure peak. Due to the symmetry in the model, this sensor lies at the border of the two symmetry planes, and at the blast-exposed surface of the pendulum. A possible explanation for the unstable measurements at this point could be that the air element at this position represents the most
495 constrained element in the entire model. As the reflected pressure builds up, the two fluids are trapped between three reflective planes. It should also be noted that the fluid domain consists of two materials, the HE and the surrounding air. Each finite element may then contain both materials, which are described by two separate EOS. The numerically sampled pressure represents the volume weighted pressure of the two fluids at the given location. Rapid changes in volume fractions and pressure could also possibly affect the
500 pressure histories. However, the corresponding total force seems to remain stable through the entire event, despite the oscillating pressure histories at the P01 location. The corresponding pressure fields and log files from the simulations do not indicate any instabilities either.

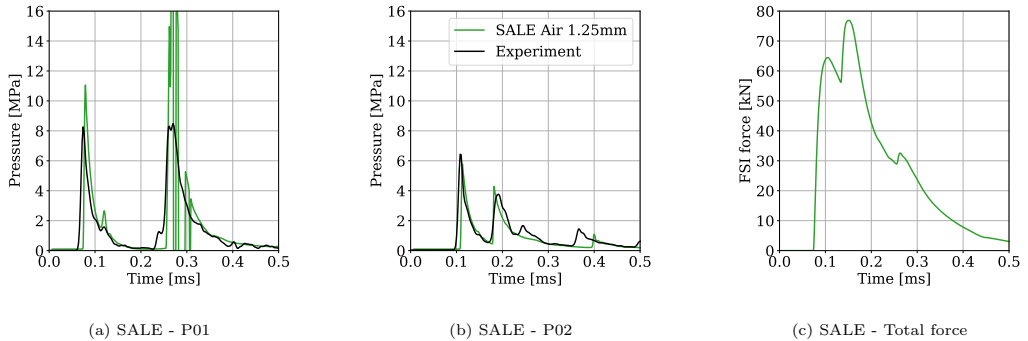


Figure 15: The recorded pressure histories from pressure sensors P01 and P02 compared to the experimental observations for the SALE simulations in (a) and (b) for the pendulum test detonating 20 g of C-4. The corresponding total force history is given in (c). The applied element size for the fluid domain is indicated in the legend.

As the effect of the fluid element size was investigated, an element size of 1.25 mm was found to give a sufficiently converged predictions. Only minor improvements were observed for a further refinement to 1.0 mm air elements. However, the computational time increase rapidly with a decreased element size, and the 1.25 mm mesh was applied in the simulations of the deformable steel plates in Section 4.5.1.

4.5.1. Deformable steel plates

As the pendulum was replaced by deformable steel plates, discretized by 0.8 mm shell elements, pressure and material leakage became an issue. By increasing the penalty factor in the FSI contact the simulations showed a strong trade-off between leakage and stability. Different contact and penalty factor definitions were tested, but ultimately it was decided to accept some leakage in the models.

Since there are no real alternative for experimental techniques capable of measuring surface pressures acting on thin plates undergoing large deformations, the numerical results were used in an attempt to better understand the loading conditions. That is, three additional pressure sensors were defined in the simulations together with the previously evaluated sensors P01 and P02. The three additional sensors are named P50, P100, and P200, and placed 50 mm, 100 mm and 200 mm away from the plate center at the blast-exposed area. This means that the initial blast-exposed area is now covered with five pressure sensors between the center and the confinement wall, with a distance of 50 mm between each sensor. The position of the numerical sensors is indicated in Figure 16 (a). The corresponding pressure histories for the simulation of test FP_20 are given in Figure 16 (b).

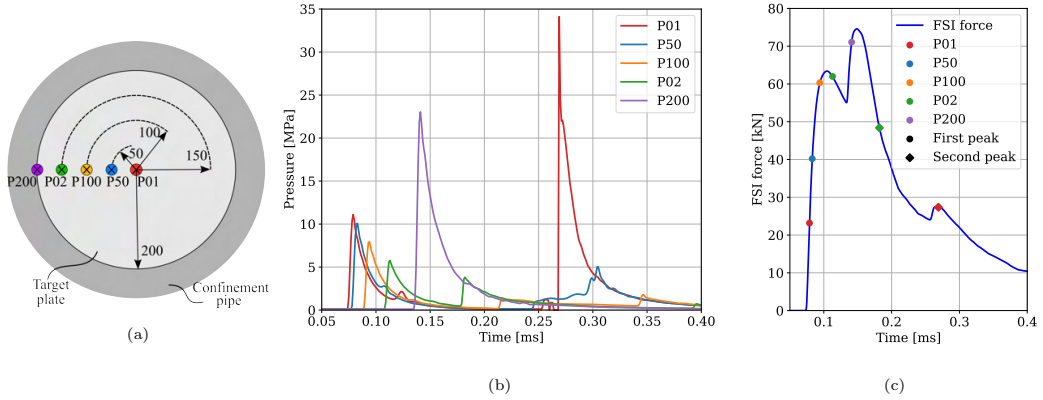


Figure 16: Positioning and naming conventions of numerical pressure sensors are shown in (a). The corresponding pressure histories for the FP_20 simulation and the total force are given in (b) and (c). For the total force plot in (c), the times for the pressure peaks of each sensor in (b) are indicated with the dots on the graph. The colour of the dots follow the same colour convention as in the pressure plots in (a), as indicated in the legend box.

Based on the pressure histories at the five sensors in Figure 16(b), it is observed that all five sensors have its own distinct pressure history. That is, an initial peak pressure followed by an exponential decay. P01 was located at the target plate center and experienced the lowest arrival time and the highest initial peak pressure. As expected, an increasing distance from the sensor to the plate center results in an increase in the time of arrival increased and a decrease in the magnitude of the initial pressure peak. This trend was however with one exception. The pressure sensor placed in the corner between the target plate and the confinement tube experienced an initial pressure peak significantly higher than the other four.

To better understand the spatial and temporal pressure distributions, the numerically obtained pressure fields at six selected times are shown in Figure 17. As the explosive charge is placed exactly one tube radius away from the target plate, the reflections from the tube wall reaches the corner simultaneously as the reflections from the target plate, which causes an amplification of the reflected pressure. This is shown in Figure 17 (b) and (c). The reflected pressure at the corner then starts to travel along the target plate back towards the center of the target plate, as indicated with the secondary peaks recorded at P02, P100, and also at P50 (see Figure 16(b)). The secondary peaks are decreasing rapidly with respect to the distance from the corner, and it is observed that they coincide with the decay in the pressure history of P200 in Figure 16 (b). The largest peak pressure throughout the entire blast loading event occurred for the secondary peak at the plate center, i.e., at P01. A strong focusing effect of the pressure develops as the reflections from the tube wall propagating towards the center line of the confinement tube and starts to interact with the reflections from the target plate, as seen in Figure 17 (c-e).

The pressure measurements in Figure 16 (b) only describes the pressure histories at discrete points across

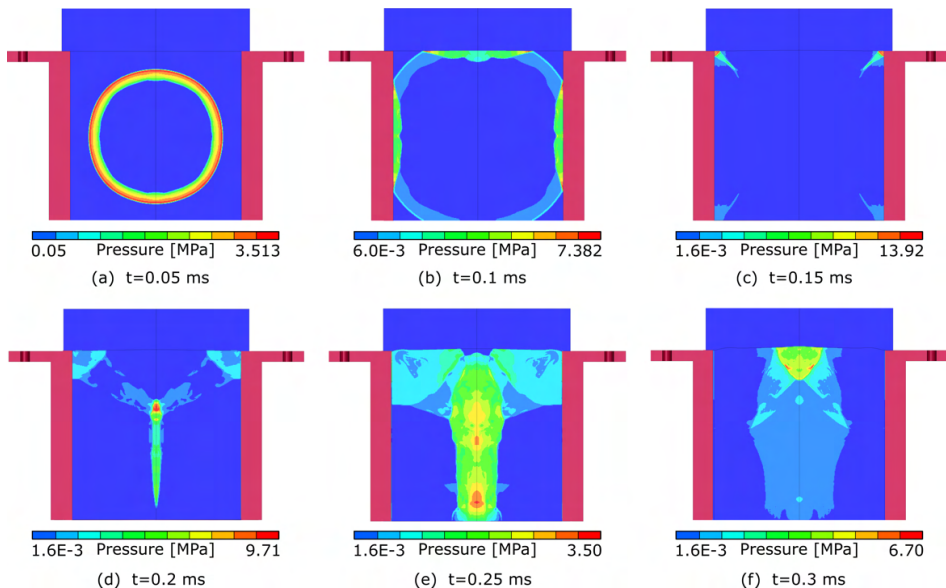


Figure 17: Numerically obtained pressure fields at six selected times for the simulation of test FP_20. The time for each pressure field is given in the sub-caption. The deformable steel plate is seen as the thin horizontal line at the upper end of the tube.

the blast-exposed area of the target plates. To relate the pressure histories to the corresponding total force on the target plates, the total force is plotted in Figure 16 (c), where the pressure peaks of all numerical pressure sensors are indicated. Here, it is seen that the force history contain three force peaks, two major peaks, and one minor.

545 The initial rise in force was obviously caused by the first pressure wave impacting the target plate, which occurred about 0.075 ms after the detonation. The maximum force during the first peak was reached at 0.105 ms, which is in-between the first pressure peak at sensors P100 and P02 in Figure 16. This is also very close to the pressure field given in Figure 17 (b).

The second and largest force peak started to increase at 0.135 ms, which coincides perfectly with the initial rise in pressure at sensor P200 in Figure 16. The local maximum for the second force peak occurred at 0.15 ms, placing it between the the initial pressure peak at P200 and the secondary pressure peak at P02. With respect to the pressure fields in Figure 17, the second peak occur between (b) and (d). The magnitude of the second force peak suggests that the largest force transfer between the fluid and the structure takes place closer to the confinement wall than the plate center.

555 The third and smallest force peak was initiated at 0.26 ms, i.e., during the local focusing effect of pressure around the plate center. This is when the major pressure peak for P01 occurred in Figure 16. It is however

interesting that the lowest peak force corresponds to the highest measured pressure during the entire blast loading event. This indicate that the focusing effect of pressure only covers a small area, as it induces a small force.

560 For the evaluation of the corresponding global deformations in the steel plates without pre-formed defects (FP), both the midpoint displacements and deformation profiles are presented in Figures 18 and 19. The midpoint displacements are presented for both FP_10 and FP_20, while the corresponding deformation profiles are only given for FP_20. As no pressure fields were available for the PBM simulations, the structural response was the best available comparison between the experiments and the SALE and PBM simulations.

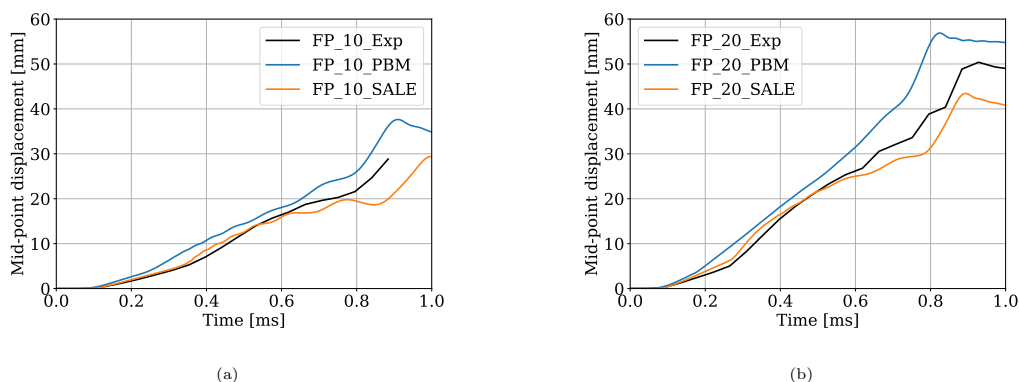


Figure 18: Midpoint displacement histories for FP_10 in (a) and FP_20 in (b). In both plots, the simulation results from PBM are compared to SALE and the experimental observations. As previously mentioned in Section 3, midpoint displacement from the FP_10 experiment was not recorded all the way up to the maximum displacement due to detachment of the spray paint.

565 The midpoint displacements in Figure 18 showed similar trends for both FP_10 in (a) and FP_20 in (b) for the comparison between PBM, SALE and the experimental results. The predictions from the PBM simulations resulted in larger displacements than the experiments, while the SALE simulations resulted in smaller displacements than the experiments. Moreover, the SALE simulations resulted in varying deformation rates up to maximum displacement, similarly to what was found in the experiments. The PBM 570 simulations resulted in almost linearly increasing deformations with a slightly increased deformation rate closer to the maximum displacement.

The observed differences in midpoint displacement rates between the PBM and SALE approaches could be explained by the corresponding deformation profiles in Figure 19. For the SALE simulations in (a), the center portion of the plate is deforming the fastest for the first 0.45 ms. After this point, the plastic hinge 575 starts to move faster than the mid-section, and at 0.75 ms the mid section experienced smaller out-of-plane deformations than the plastic hinge. From this point and up to maximum displacement, the deformations mainly take place at the mid-section of the plate, resulting in the increased midpoint displacement rate seen

in Figure 18 (b). The deformation profiles from the PBM simulation experienced a much more distinct plastic hinge with a relatively flat mid-section (Figure 19 (b)). This is also closer to what one would expect from a thin plate exposed to a uniform and impulsive loading (see e.g., Ref. [54]). This could also indicate that the loading conditions from the PBM simulations give a more uniform distribution across the blast-exposed area of the target plates than the more advanced SALE simulations. This assumption is however hard to justify, as the total force histories between the plate and the particles experienced significant oscillations.

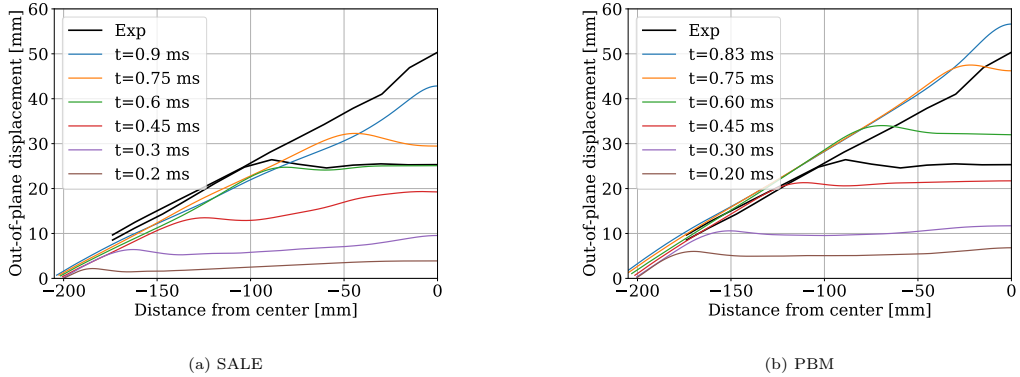


Figure 19: Deformation profiles for FP_20 obtained from the SALE simulation in (a) and the PBM approach in (b). The deformation profiles are plotted at selected times which are given in the legends for each sub-figure. The experimentally obtained deformation profiles at maximum deformation and 0.5 of maximum from Figure 9 are included in both plots with black and labeled "Exp".

To sum up the comparison of the structural response, the PBM simulations ended with approximately 10% larger displacements than the experiments, and the SALE simulations with approximately 10% lower displacements than the experimental findings. The leakage observed in the SALE simulations is assumed to be part of the reason for the underestimation of the deformation response. At about 0.3 ms after the detonation, right after the second pressure peak at the center of the plate, some of the HE material started to flow through the center of the target plate in the SALE simulations. Leakage occurred only for the shell elements and the tube did not experience leakage in any of the simulations. It is also noted that no leakage occurred in the pendulum simulations, even though the contact formulation was identical to the one for the target plates. This motivated one simulation of test FP_20 using solid elements for the target plate, to investigate whether the leakage issue was related to the element formulation. This did not solve the leakage problem, which seems to be related to the small thickness of the target plate. This is however not confirmed, and require further numerical investigation. Such investigations are considered beyond the scope of this work.

4.5.2. Fracture resistance

The numerically predicted fracture resistance in the different models reflects the findings of the global deformation response in Section 4.5.1. Hence, the SALE approach underpredicts the dynamic response for the FP geometry. Interestingly, the SALE simulations failed to predict fracture for the C and B geometries. The PBM approach overpredicted the dynamic response to such an extent that it was able to predict fracture for both the C_20 and B_20 tests. The numerically obtained damage fields from C_20_PBM, B_20_PBM and B_20_SALE are given in Figure 20. The field plot is represented as the CL-damage parameter from Eq. (4), and the images were sampled at the instant of maximum displacement.

The C_20_PBM simulation in Figure 20 (a) ended in several small cracks arrested around the pre-formed circular hole. The largest cracks were found in the B_20_PBM simulation, where four significant cracks occurred pointing towards the plate diagonals. The material between the arrested cracks was also deformed outward as in the experiments after the crack propagation was arrested. This is however not illustrated in Figure 20, as the images were sampled at the initial maximum displacement. Even though the PBM approach overestimated the dynamic response, and most likely the impulse transfer from the detonation, the length of the arrested cracks in the C and B geometries were underestimated compared to the experiments. This could indicate that the discretization of the target plates with 0.8 mm shell elements is too coarse to represent the experimentally observed fracture patterns. Based on the findings by Elveli et al. [19], this was however as expected for the B geometry. The B_20_SALE model, shown in Figure 20 (c), applied a discretization too coarse to describe the fracture response, combined with an FSI algorithm leading to an underestimation of the impulse transfer between from the explosive. This resulted in an evolution of damage of approximately half of the critical value to initiate fracture around the ballistic hole after blast loading. As the charge mass was reduced to 10 g, none of the numerical simulations resulted in crack initiation. For the PBM

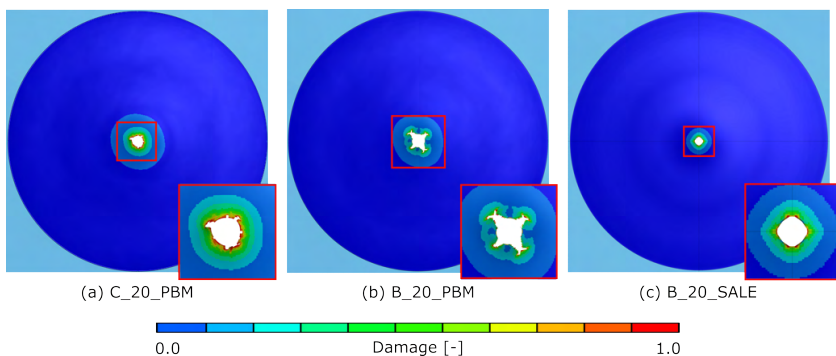


Figure 20: Numerically obtained damage fields and arrested cracks for (a) C_20_PBM, (b) B_20_PBM and (c) B_20_SALE. The identity of each simulation is given in the sub-caption. All three field maps were sampled right after the instant of maximum displacement.

simulations, the reduced fracture resistance in the B geometry compared to the C geometry was captured.

620 Although the discretization of the target plate was too coarse to give a satisfactory representation of the ballistic impact event, cracks were initiated at the most damaged locations from the ballistic impact holes. The numerical models generally resulted in an overestimation of the fracture resistance compared to the experimental findings.

The findings in this work confirm the trade-off between computational (CPU) time and accuracy in the 625 numerical modelling of combined ballistic impact and blast loading. That is, simulations of ballistic impact require a very fine discretization of the target plate to obtain reliable predictions, while blast simulations need to use a much coarser mesh to run within a reasonable computational time. This is challenging when modelling the combined effect of fragment impact and blast loading on plated structures, especially if a realistic fracture mode from the ballistic impact and a feasible CPU cost during the blast loading phase of 630 the simulation are important.

4.6. Discussion on the performance of the SALE and PBM approaches in blast simulations

Based on the predictive capabilities of the PBM and SALE approaches, some important differences need to be discussed. Both the PBM and SALE models resulted in structural deformations with an approximate deviation of 10% relative to the experimental findings, meaning that the predictive capabilities are in the 635 same order of magnitude. However, the PBM models overestimated the structural response, leading to conservative estimates of the fracture resistance during blast loading. On the contrary, the SALE simulations underestimated the experimental observations in terms of deformation response, resulting in non-conservative estimates of the fracture resistance.

Concerning the CPU cost, the two numerical approaches performed similar when running on the same 640 amount of CPUs. It was however possible to run the PBM simulations on more CPUs than the SALE simulations without causing numerical issues during the massively parallel processing (MPP) domain decomposition in the initialization of the models. Hence, the PBM simulations may further reduce the total simulation time by increasing the number of CPUs. All PBM simulations presented in this study included both the modeling of the explosive charge and the surrounding air. The number of particles representing the 645 explosive charge was responsible for less than 4% of the total amount of particles in the model. This means that most of the CPU efforts were occupied to describe the surrounding air particles. The importance in the modelling of the surrounding air is very case dependent, and the comparison of CPU costs between SALE and PBM may vary significantly for other applications.

Compared to the SALE approach, the PBM approach involves a more user-friendly procedure in the 650 establishing the numerical model. The PBM in LS-DYNA requires less input, with only a few keywords governing the blast loading domain. There are no need for any additional EOS for the particle domain. However, a too coarse description in the number of particles, or a too large time-step definition generally

leads to an overestimation of the blast load and more conservative estimates of the structural response. On the contrary, a coarse mesh of the fluid domain in a SALE simulation distributes the shock across a larger area, leading to an underestimation of both the propagation of the shock and the pressure amplifications during interaction with its surroundings. The great advantage of a well-defined SALE model is the detailed description of the entire loading event, including both the pressure build-up and the effects of interactions with surrounding structures. The SALE models are superior compared to the simpler PBM approach for a more detailed understanding of the different mechanisms governing the fluid-structure interaction (FSI) during a confined detonation.

As both approaches have their strengths and weaknesses, it is challenging to generalize and favor one approach above the other. The advantages of the two modelling approaches come down to the problem at hand, and the desired output and requirements from the numerical simulations.

5. Concluding remarks

This work presents an experimental and numerical investigation on the effect of more realistic pre-formed defects on the blast resistance of thin steel plates subjected to partially confined detonations, assuming that the fragment impacts before the blast wave. First, the plates were perforated by 7.62 mm APM2 projectiles in a ballistic impact. Then, the perforated plates were subjected to blast loading resulting from partially confined detonations. The blast resistance of the plates with perforations from the ballistic impact (B) was compared to that of target plates containing idealized pre-cut circular (C) holes. The confined airblast loading was generated by detonating spherical charges of C-4 inside a 200-mm-radius and 1-m-long circular steel tube. The explosive charges were positioned at a distance of one tube radius from the target plates, while the opposite end of the tube was kept open. The loading was evaluated experimentally by a set of additional blast tests on a 199 kg pendulum with pressure sensors mounted on its blast-exposed surface. Numerical simulations were used to gain more insight into the pressure build-up and FSI inside the partially confined tube. Different numerical approaches were compared with respect to the representation of the loading resulting from the partially confined detonations. The main conclusions from the study are as follows.

- The experimental setup succeeded in creating reliable measurements for both the pressure histories and the resulting dynamic response. For pressure sensors mounted to the confined tube, excessive oscillations were observed. However, the measurements from the pressure sensors mounted on the blast-exposed surface of the pendulum resulted in very good measurements. Deformation fields of the thin steel plates were successfully obtained using 3D-DIC for almost all blast tests. Some challenges were however encountered for experiments where the visual fireball saturated some of the images from the high-speed camera recordings.

- 690 • The proposed setup with the explosive charge located one tube radius away from the target plates gave a loading history consisting of three main phases. First, the incoming shock front impacted the target plate and the confined tube simultaneously. Here, the pressure histories on the blast-exposed surface of the target plate followed a similar behavior as for unconfined detonations. Second, the shock propagation along the blast-exposed area of the target plate reached the confinement wall. The reflected pressure at the boundary was amplified to more than twice the magnitude of the initial peak reflected pressure at the center of the plate during the first phase. The third and last phase of the blast loading event occurred as the reflections along the circular confinement wall reached the center axis of the confined tube. This resulted in a strong focusing effect of pressure with a significant pressure peak located in a small area around the center of the plate. The SALE simulations showed that the highest interaction forces between the blast load and the target plate occurred during the second phase of the loading event.
- 700 • The deformation distribution across the blast-exposed area of the target plates took the shape of a global dome with a superimposed local dome around the center of the plate. If no significant fracture occurred, all three plate geometries showed similar deformation fields. Hence, the global deformations seems to be unaffected by the plate geometry.
- 705 • The three plate geometries showed distinct differences in terms of fracture resistance during blast loading. The target plates without any pre-formed defects resulted in large plastic deformations without any signs of fracture for both charge masses. The target plates with pre-cut circular holes (C) experienced vertical arrested cracks for the largest charge mass, whereas the target plates containing initial ballistic impact holes (B) experienced multiple arrested cracks for both charge masses. The B geometry experienced both larger and more arrested cracks than the C geometry. For the largest charge mass, the largest measured crack lengths were almost twice as large in the tests with the B geometry compared to those with the C geometry. For the B geometry, all arrested cracks were initiated at the initial petalling cracks from the ballistic impact holes. Lastly, it was noted that none of the arrested cracks extended outside the superimposed local dome in the center of the plate.
- 710 • Compared to the previous studies using a shock tube environment (see Ref. [19]), the trends in global deformation and fracture resistance were the same when evaluating the target plates with idealized pre-cut circular holes, ballistic impact holes, and plates without defects. The change in loading environment did not change the overall conclusions from the shock tube tests in terms of plate response. That is, the target plates with ballistic impact holes failed at lower blast intensities than the plates with idealized pre-cut circular holes. Moreover, the petalling cracks initiated the crack propagation during blast loading.

- 720 • The SALE simulations showed good agreement with the experimental findings for the measured reflected pressure histories in the pendulum experiments. Numerical simulations were used in an attempt to obtain a better understanding of the partially confined blast loading event. These models enabled the use of several pressure sensors to monitor pressure histories at given points on the target plates, as well as the corresponding visualization of the spatial distribution of the pressure fields. However, some difficulties were encountered for the simulations of the thin deformable steel plates, where leakage occurred during the third phase of the blast loading event. This was also assumed to be one of the contributors to the slight underprediction of the dynamic response for the SALE simulations. Compared to the experimental findings, the PBM simulations overestimated the dynamic response by approximately 10%, while the SALE simulations underestimated the deformations with a similar magnitude.
- 730 • The numerical models of the target plates can be used to gain more insight into the combined effect of ballistic impact and blast loading in partially confined detonations. Compared to previous studies in Ref. [19], this study therefore extends the validity of the models to also include load environments of localised, non-uniform pressure distributions and confined detonations.

Acknowledgements

735 This work has been carried out with financial support from the Research Council of Norway (RCN) through the Centre for Advanced Structural Analysis (CASA), Centre for Research-based Innovation (RCN Project No. 237885); the Norwegian Defence Estates Agency; and the Norwegian Ministry of Justice and Public Security.

References

- 740 [1] J. Wei, M. S. Shetty, L. R. Dharani, Failure analysis of architectural glazing subjected to blast loading, *Engineering Failure Analysis* 13 (7) (2006) 1029–1043.
- [2] M. Kristoffersen, A. Minoretti, T. Børvik, On the internal blast loading of submerged floating tunnels in concrete with circular and rectangular cross-sections, *Engineering Failure Analysis* 103 (2019) 462–480.
- 745 [3] S. Yao, D. Zhang, F. Lu, N. Zhao, Y. Li, Fast prediction method of failure modes for steel box structures under internal blast loading, *Engineering Failure Analysis* 120 (2021) 104919.
- [4] K. A. Marchand, M. M. Vargas, J. D. Nixon, The synergistic effects of combined blast and fragment loadings, Tech. rep., San Antonio Texas (1992).
- [5] D. W. Hyde, U. A. E. W. E. Station, U. S. A. C. of Engineers, User's Guide for Microcomputer Programs ConWep and FunPro, Applications of TM 5-855-1, "Fundamentals of Protective Design for Conventional Weapons", Instruction report, U.S. Army Engineer Waterways Experiment Station, 1988.
- 750 [6] U. Nystrøm, K. Gylltoft, Numerical studies of the combined effects of blast and fragment loading, *International Journal of Impact Engineering* 36 (2009) 995–1005.
- [7] X. Kong, W. Wu, J. Li, P. Chen, F. Liu, Experimental and numerical investigations on a multi-layer protective structure under the synergic effect of blast and fragment loadings, *International Journal of Impact Engineering* 65 (2014) 146–62.
- 755 [8] H. Y. Grisaro, A. N. Dancygier, Characteristics of combined blast and fragments loading, *International Journal of Impact Engineering* 116 (2018) 51–64.
- [9] K. Rakvåg, N. Underwood, G. Schleyer, T. Børvik, O. Hopperstad, Transient pressure loading of clamped metallic plates with pre-formed holes, *International Journal of Impact Engineering* 53 (2012) 44–55.
- [10] Y. Li, W. Wu, H. Zhu, Z. Wua, Z. Dub, The influence of different pre-formed holes on the dynamic response of square plates under air-blast loading, *Engineering Failure Analysis* 78 (2017) 122–133.
- 760 [11] V. Aune, G. Valsamos, F. Casadei, M. Langseth, T. Børvik, On the dynamic response of blast-loaded steel plates with and without pre-formed holes, *International Journal of Impact Engineering* 108 (2017) 27–46.
- [12] H. Granum, V. Aune, T. Børvik, O. S. Hopperstad, Effect of heat-treatment on the structural response of blast-loaded aluminium plates with pre-cut slits, *International Journal of Impact Engineering* 132 (2019) 103306.
- 765 [13] V. Aune, G. Valsamos, F. Casadei, M. Langseth, T. Børvik, Influence of fluid-structure interaction effects on the ductile fracture of blast-loaded steel plates, *EPJ Web of Conferences* 250 (2021) 02019.
- [14] W. Li, P. Wang, G. peng Feng, Y. gang Lu, J. zheng Yue, H. min Li, The deformation and failure mechanism of cylindrical shell and square plate with pre-formed holes under blast loading, *Defence Technology* 17 (4) (2021) 1143–1159.
- [15] C. Zhang, P. Tan, Y. Yuan, Confined blast loading of steel plates with and without pre-formed holes, *International Journal of Impact Engineering* 163 (2022) 104183.
- 770 [16] N. Gupta, Nagesh, Deformation and tearing of circular plates with varying support conditions under uniform impulsive loads, *International Journal of Impact Engineering* 34 (1) (2007) 42–59.
- [17] Y. Yuan, P. Tan, Deformation and failure of rectangular plates subjected to impulsive loadings, *International Journal of Impact Engineering* 59 (2013) 46–59.
- 775 [18] V. Aune, E. Fagerholt, K. Hauge, M. Langseth, T. Børvik, Experimental study on the response of thin aluminium and steel plates subjected to airblast loading, *International Journal of Impact Engineering* 90 (2012) 106–121.
- [19] B. S. Elveli, T. Berstad, T. Børvik, V. Aune, Performance of thin blast-loaded steel plates after ballistic impact from small-arms projectiles, Submitted for possible publication.
- [20] O. Atoui, G. Kechagiadakis, A. Moumen, A. Maazoun, B. Belkassam, L. Pyl, D. Lecompte, An explosive driven shock tube-based laboratory scale test for combined blast and fragment impact loading, *Applied Sciences* 12 (14) (2022).
- 780

- [21] Y. Hu, C. Wu, M. Lukaszewicz, J. Dragos, J. Ren, M. Haskett, Characteristics of confined blast loading in unvented structures, *International Journal of Protective Structures* 2 (2011) 21–44.
- [22] I. Edri, Z. Savir, V. Feldgun, Y. Karinski, D. Yankelevsky, On blast pressure analysis due to a partially confined explosion: I. experimental studies, *International Journal of Protective Structures* 2 (1) (2011) 1–20.
- 785 [23] US Army Corps of Engineers (USACE), Structures to resist the effects of accidental explosions, UFC 3-340-02. Supersedes TM5-1300, dated November 1990. US Department of Defense, Washington DC, 2008.
- [24] Q. Dong, Q. Li, J. Zheng, Interactive mechanisms between the internal blast loading and the dynamic elastic response of spherical containment vessels, *International Journal of Impact Engineering* 37 (4) (2010) 349–358.
- [25] V. Feldgun, Y. Karinski, I. Edri, D. Yankelevsky, Prediction of the quasi-static pressure in confined and partially confined explosions and its application to blast response simulation of flexible structures, *International Journal of Impact*
790 *Engineering* 90 (2016) 46–60.
- [26] M. Silvestrini, B. Genova, F. Leon Trujillo, Energy concentration factor. a simple concept for the prediction of blast propagation in partially confined geometries, *Journal of Loss Prevention in the Process Industries* 22 (4) (2009) 449–454.
- [27] S. Yao, D. Zhang, Z. Lu, Y. Lin, F. Lu, Experimental and numerical investigation on the dynamic response of steel chamber under internal blast, *Engineering Structures* 168 (2018) 877–888.
- 795 [28] G. Langdon, S. Kriek, G. Nurick, Influence of venting on the response of scaled aircraft luggage containers subjected to internal blast loading, *International Journal of Impact Engineering* 141 (2020) 103567.
- [29] C. Geretto, S. Yuen, G. Nurick, An experimental study of the effects of degrees of confinement on the response of square mild steel plates subjected to blast loading, *International Journal of Impact Engineering* 79 (2015) 32–44, recent development of experimental techniques under impact loading- IUTAM Symposium, Xian, 2013.
- 800 [30] N. Jacob, G. Nurick, G. Langdon, The effect of stand-off distance on the failure of fully clamped circular mild steel plates subjected to blast loads, *Engineering Structures* 29 (10) (2007) 2723–2736.
- [31] Y. Yuan, C. Zhang, Y. Xu, Influence of standoff distance on the deformation of square steel plates subjected to internal blast loadings, *Thin-Walled Structures* 164 (2021) 107914.
- 805 [32] B. S. Elveli, M. B. Iddberg, T. Børvik, V. Aune, On the strength-ductility trade-off in thin blast-loaded steel plates with and without initial defects - an experimental study, *Thin-Walled Structures* 171 (2022) 108787.
- [33] W. Noh, CEL: A time-dependent two-space-dimensional coupled Eulerian-Lagrangian code, In Alder, B., Fernbach, S., Rotenberg, M., eds.: *Methods in Computational Physics*. Volume 3., Academic Press: New York (1964) 117–179.
- [34] C. Hirth, A. Amsden, J. Cook, An Arbitrary Lagrangian-Eulerian computing method for all flow speeds, *Journal of*
810 *Computational Physics* 14 (1974) 227–253.
- [35] J. Donea, P. Fasoli-Stella, P. Giuliani, Lagrangian and eulerian finite element techniques for transient fluid-structure interaction problems, In: *Transactions of the 4th International Conference on Structural Mechanics in Reactor Technology* (1977).
- [36] T. Belytschko, J. Kennedy, Computer models for subassembly simulation, *Nuclear Engineering and Design* 49 (1978)
815 17–38.
- [37] T. Belytschko, J. Kennedy, D. Schoeberle, Quasi-Eulerian finite element formulation for fluid structure interaction, *Journal of Pressure Vessel Technology* 102 (1980) 62–69.
- [38] T. Hughes, W. Liu, T. Zimmermann, Lagrangian-Eulerian finite element formulation for incompressible viscous flows, *Computer Methods in Applied Mechanics and Engineering* 29 (1981) 329–349.
- 820 [39] M. Souli, A. Ouahsine, L. Lewin, Ale formulation for fluid–structure interaction problems, *Computer Methods in Applied Mechanics and Engineering* 190 (5) (2000) 659–675.
- [40] C. Zheng, X. shao Kong, W. guo Wu, S. xi Xu, Z. wei Guan, Experimental and numerical studies on the dynamic response of steel plates subjected to confined blast loading, *International Journal of Impact Engineering* 113 (2018) 144–160.

- 825 [41] G. Langdon, A. Ozinsky, S. Chung Kim Yuen, The response of partially confined right circular stainless steel cylinders to internal air-blast loading, *International Journal of Impact Engineering* 73 (2014) 1–14.
- [42] T. Børvik, A. Hanssen, M. Langseth, L. Olovsson, Response of structures to planar blast loads – a finite element engineering approach, *Computers & Structures* 87 (9) (2009) 507–520.
- [43] L. Olovsson, Corpuscular method for airbag deployment simulations in ls-dyna, Tech. rep., ISBN 978-82-997587-0-3 (2007).
- 830 [44] L. Olovsson, A. Hanssen, T. Børvik, M. Langseth, A particle-based approach to close-range blast loading, *European Journal of Mechanics - A/Solids* 29 (1) (2010) 1–6.
- [45] T. Børvik, L. Olovsson, A. Hanssen, K. Dharmasena, H. Hansson, H. Wadley, A discrete particle approach to simulate the combined effect of blast and sand impact loading of steel plates, *Journal of the Mechanics and Physics of Solids* 59 (5) (2011) 940–958.
- [46] M. Kristoffersen, K. O. Hauge, A. Minoretti, T. Børvik, Experimental and numerical studies of tubular concrete structures subjected to blast loading, *Engineering Structures* 233 (2021) 111543.
- 835 [47] E. Fagerholt, , <https://www.ntnu.edu/kt/ecorr>, [Online; accessed 23-May-2022] (2008).
- [48] S. S. A. (SSAB), , <https://www.ssab.com/en-us/brands-and-products/doco1/automotive-steel-grades/dual-phase-steel/doco1-600dp>, [Online; accessed 23-June-2022] (2022).
- [49] G. Gruben, M. Langseth, E. Fagerholt, O. Hopperstad, Low-velocity impact on high-strength steel sheets: An experimental and numerical study, *International Journal of Impact Engineering* 88 (2016) 153–171.
- 840 [50] R. Kaufmann, S. Olufsen, E. Fagerholt, V. Aune, Reconstruction of surface pressures on flat plates impacted by blast waves using the virtual fields method, *International Journal of Impact Engineering* 171 (2023) 104369.
- [51] T. Børvik, O. S. Hopperstad, T. Berstad, M. Langseth, A computational model of viscoplasticity and ductile damage for impact and penetration, *The European Journal of Mechanics A/Solids* 20 (2001) 685–712.
- 845 [52] M. G. Cockcroft, D. J. Latham, Ductility and workability of metals, *Journal of the Institute Metals* 96 (1968) 33–39.
- [53] LS-DYNA Keyword User’s Manual Volume I, version 13, Livermore Software Technology Corporation, Livermore, California, 2021.
URL https://www.dynasupport.com/manuals/ls-dyna-manuals/ls-dyna{_}manual{_}volume{_}i{_}r13.pdf
- [54] N. Jones, *Structural impact*, Cambridge university press, 2011.

850 **Appendix A. Advection method**

The advection method represented by METH=3 has also been applied in studies on confined blast loading [20]. This method replaces the higher-order variations of state variables within each element in METH=2, to a constant value. This leads to a first order accuracy. Generally, it is not possible to conserve both the kinetic energy and the momentum during advection. METH=3 is formulated through the donor cell method, which is expected to be more dissipative than the Van Leer method. To improve the conservation of energy, METH=3 additionally stores the loss of kinetic energy as increased internal energy during the advection step [53]. However, both methods apply the same algorithm for the re-mapping of node-specific variables.

The numerical pressure measurements at a selection of pressure sensors are plotted together with the corresponding FSI force and mid-point displacements for the comparison of the two alternative advection methods described in Section 4.4.1 are presented in Figure A.1. Only the 20 g detonation was considered. From the pressure measurements in Figure A.1 (a), it is seen that the incoming pressure is fairly similar for the two methods. The initial pressure peaks are somewhat smaller for METH=3, while the second pressure peaks after the interaction effects are slightly larger. A slight time-shift is also observed between the two methods, where the pressure peak from the interactions with the confinement occur earlier for METH=3 than for METH=-2. The corresponding FSI force and midpoint displacements are increased from METH=-2 to METH=3.

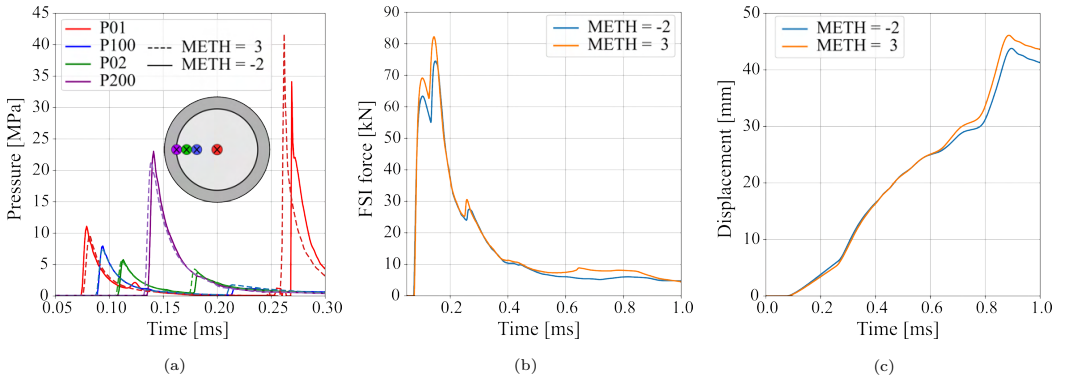


Figure A.1: Comparison of two alternative advection methods, METH=-2, and METH=3, for the ALE domain. The pressure histories at a selection of pressure sensors are given in (a), the corresponding FSI force in (b), and the resulting midpoint displacements in (c). It is noted that the reference model for the numerical work in this study applied METH=-2. The two simulations represents the 20 g detonation.

The obtained pressure fields for the two advection methods are compared in Figure A.2. Here, the two models are aligned next to each other at six selected times during the blast simulations. For the initial shock

870 propagation, it is seen that METH=3 gives a thicker shock front than METH=-2, while a slightly higher pressure is seen for METH=-2. Generally, it seems that METH=3 gives a slightly larger volume with high pressures than METH=-2. However, the effects of changing the advection method was not studied in any further detail than what presented in Figures A.1 and A.2.

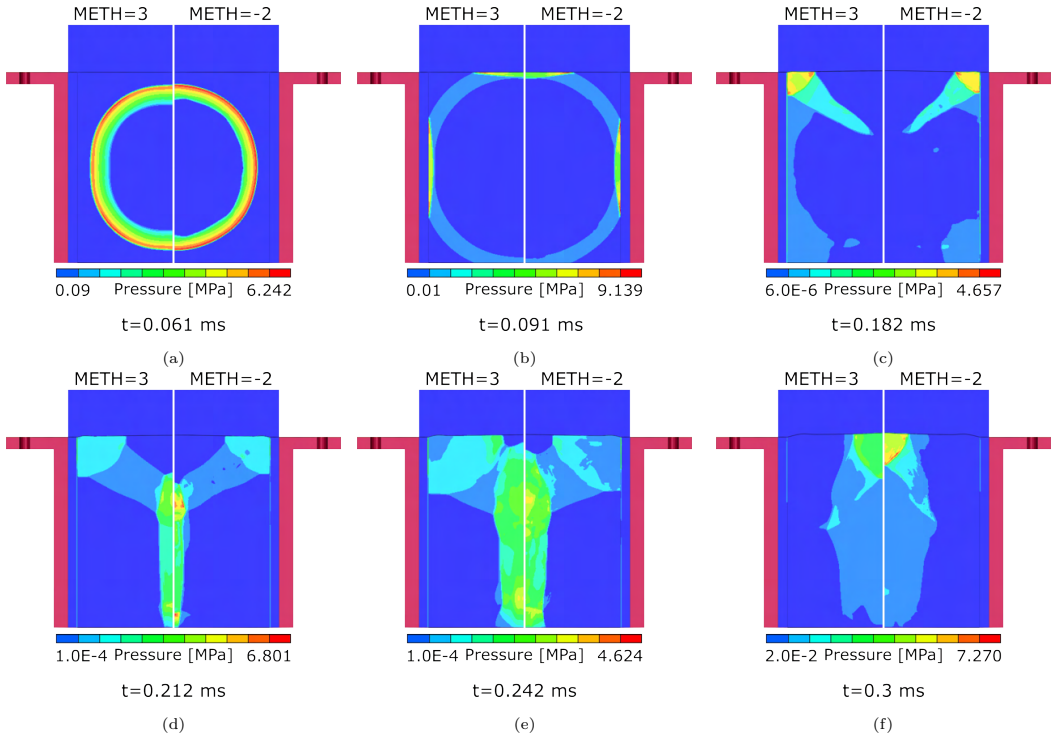


Figure A.2: Comparison of the pressure field for the two advection methods. The two models are compared at six given times which are labeled for each subfigure. The two simulations represents the 20 g detonation.

**DEPARTMENT OF STRUCTURAL ENGINEERING
NORWEGIAN UNIVERSITY OF SCIENCE AND TECHNOLOGY**

N-7491 TRONDHEIM, NORWAY
Telephone: +47 73 59 47 00

"Reliability Analysis of Structural Systems using Nonlinear Finite Element Methods",
C. A. Holm, 1990:23, ISBN 82-7119-178-0.

"Uniform Stratified Flow Interaction with a Submerged Horizontal Cylinder",
Ø. Arntsen, 1990:32, ISBN 82-7119-188-8.

"Large Displacement Analysis of Flexible and Rigid Systems Considering
Displacement-Dependent Loads and Nonlinear Constraints",
K. M. Mathisen, 1990:33, ISBN 82-7119-189-6.

"Solid Mechanics and Material Models including Large Deformations",
E. Levold, 1990:56, ISBN 82-7119-214-0, ISSN 0802-3271.

"Inelastic Deformation Capacity of Flexurally-Loaded Aluminium Alloy Structures",
T. Welo, 1990:62, ISBN 82-7119-220-5, ISSN 0802-3271.

"Visualization of Results from Mechanical Engineering Analysis",
K. Aamnes, 1990:63, ISBN 82-7119-221-3, ISSN 0802-3271.

"Object-Oriented Product Modeling for Structural Design",
S. I. Dale, 1991:6, ISBN 82-7119-258-2, ISSN 0802-3271.

"Parallel Techniques for Solving Finite Element Problems on Transputer Networks",
T. H. Hansen, 1991:19, ISBN 82-7119-273-6, ISSN 0802-3271.

"Statistical Description and Estimation of Ocean Drift Ice Environments",
R. Korsnes, 1991:24, ISBN 82-7119-278-7, ISSN 0802-3271.

"Properties of concrete related to fatigue damage: with emphasis on high strength
concrete",
G. Petkovic, 1991:35, ISBN 82-7119-290-6, ISSN 0802-3271.

"Turbidity Current Modelling",
B. Brørs, 1991:38, ISBN 82-7119-293-0, ISSN 0802-3271.

"Zero-Slump Concrete: Rheology, Degree of Compaction and Strength. Effects of
Fillers as Part Cement-Replacement",
C. Sørensen, 1992:8, ISBN 82-7119-357-0, ISSN 0802-3271.

"Nonlinear Analysis of Reinforced Concrete Structures Exposed to Transient Loading",
K. V. Høiseeth, 1992:15, ISBN 82-7119-364-3, ISSN 0802-3271.

"Finite Element Formulations and Solution Algorithms for Buckling and Collapse
Analysis of Thin Shells",
R. O. Bjærum, 1992:30, ISBN 82-7119-380-5, ISSN 0802-3271.

"Response Statistics of Nonlinear Dynamic Systems",
J. M. Johnsen, 1992:42, ISBN 82-7119-393-7, ISSN 0802-3271.

"Digital Models in Engineering. A Study on why and how engineers build and operate
digital models for decision support",
J. Høyte, 1992:75, ISBN 82-7119-429-1, ISSN 0802-3271.

"Sparse Solution of Finite Element Equations",
A. C. Damhaug, 1992:76, ISBN 82-7119-430-5, ISSN 0802-3271.

"Some Aspects of Floating Ice Related to Sea Surface Operations in the Barents Sea",
S. Løset, 1992:95, ISBN 82-7119-452-6, ISSN 0802-3271.

"Modelling of Cyclic Plasticity with Application to Steel and Aluminium Structures",
O. S. Hopperstad, 1993:7, ISBN 82-7119-461-5, ISSN 0802-3271.

"The Free Formulation: Linear Theory and Extensions with Applications to Tetrahedral
Elements
with Rotational Freedoms",
G. Skeie, 1993:17, ISBN 82-7119-472-0, ISSN 0802-3271.

"Høyfast betongs motstand mot piggdekkslitasje. Analyse av resultater fra prøving i
Veisliter'n",
T. Tveter, 1993:62, ISBN 82-7119-522-0, ISSN 0802-3271.

"A Nonlinear Finite Element Based on Free Formulation Theory for Analysis of
Sandwich Structures",
O. Aamlid, 1993:72, ISBN 82-7119-534-4, ISSN 0802-3271.

"The Effect of Curing Temperature and Silica Fume on Chloride Migration and Pore
Structure of High Strength Concrete",
C. J. Hauck, 1993:90, ISBN 82-7119-553-0, ISSN 0802-3271.

"Failure of Concrete under Compressive Strain Gradients",
G. Markeset, 1993:110, ISBN 82-7119-575-1, ISSN 0802-3271.

"An experimental study of internal tidal amphidromes in Vestfjorden",
J. H. Nilsen, 1994:39, ISBN 82-7119-640-5, ISSN 0802-3271.

- "Structural analysis of oil wells with emphasis on conductor design",
H. Larsen, 1994:46, ISBN 82-7119-648-0, ISSN 0802-3271.
- "Adaptive methods for non-linear finite element analysis of shell structures",
K. M. Okstad, 1994:66, ISBN 82-7119-670-7, ISSN 0802-3271.
- "On constitutive modelling in nonlinear analysis of concrete structures",
O. Fyrileiv, 1994:115, ISBN 82-7119-725-8, ISSN 0802-3271.
- "Fluctuating wind load and response of a line-like engineering structure with emphasis on motion-induced wind forces",
J. Bogunovic Jakobsen, 1995:62, ISBN 82-7119-809-2, ISSN 0802-3271.
- "An experimental study of beam-columns subjected to combined torsion, bending and axial actions",
A. Aalberg, 1995:66, ISBN 82-7119-813-0, ISSN 0802-3271.
- "Scaling and cracking in unsealed freeze/thaw testing of Portland cement and silica fume concretes",
S. Jacobsen, 1995:101, ISBN 82-7119-851-3, ISSN 0802-3271.
- "Damping of water waves by submerged vegetation. A case study of laminaria hyperborea",
A. M. Dubi, 1995:108, ISBN 82-7119-859-9, ISSN 0802-3271.
- "The dynamics of a slope current in the Barents Sea",
Sheng Li, 1995:109, ISBN 82-7119-860-2, ISSN 0802-3271.
- "Modellering av delmaterialenes betydning for betongens konsistens",
Ernst Mørtzell, 1996:12, ISBN 82-7119-894-7, ISSN 0802-3271.
- "Bending of thin-walled aluminium extrusions",
Birgit Søvik Opheim, 1996:60, ISBN 82-7119-947-1, ISSN 0802-3271.
- "Material modelling of aluminium for crashworthiness analysis",
Torodd Berstad, 1996:89, ISBN 82-7119-980-3, ISSN 0802-3271.
- "Estimation of structural parameters from response measurements on submerged floating tunnels",
Rolf Magne Larssen, 1996:119, ISBN 82-471-0014-2, ISSN 0802-3271.
- "Numerical modelling of plain and reinforced concrete by damage mechanics",
Mario A. Polanco-Loria, 1997:20, ISBN 82-471-0049-5, ISSN 0802-3271.
- "Nonlinear random vibrations - numerical analysis by path integration methods",
Vibeke Moe, 1997:26, ISBN 82-471-0056-8, ISSN 0802-3271.

- “Numerical prediction of vortex-induced vibration by the finite element method”,
Joar Martin Dalheim, 1997:63, ISBN 82-471-0096-7, ISSN 0802-3271.
- “Time domain calculations of buffeting response for wind sensitive structures”,
Ketil Aas-Jakobsen, 1997:148, ISBN 82-471-0189-0, ISSN 0802-3271.
- "A numerical study of flow about fixed and flexibly mounted circular cylinders",
Trond Stokka Meling, 1998:48, ISBN 82-471-0244-7, ISSN 0802-3271.
- “Estimation of chloride penetration into concrete bridges in coastal areas”,
Per Egil Steen, 1998:89, ISBN 82-471-0290-0, ISSN 0802-3271.
- “Stress-resultant material models for reinforced concrete plates and shells”,
Jan Arve Øverli, 1998:95, ISBN 82-471-0297-8, ISSN 0802-3271.
- “Chloride binding in concrete. Effect of surrounding environment and concrete composition”,
Claus Kenneth Larsen, 1998:101, ISBN 82-471-0337-0, ISSN 0802-3271.
- “Rotational capacity of aluminium alloy beams”,
Lars A. Moen, 1999:1, ISBN 82-471-0365-6, ISSN 0802-3271.
- “Stretch Bending of Aluminium Extrusions”,
Arild H. Clausen, 1999:29, ISBN 82-471-0396-6, ISSN 0802-3271.
- “Aluminium and Steel Beams under Concentrated Loading”,
Tore Tryland, 1999:30, ISBN 82-471-0397-4, ISSN 0802-3271.
- "Engineering Models of Elastoplasticity and Fracture for Aluminium Alloys",
Odd-Geir Lademo, 1999:39, ISBN 82-471-0406-7, ISSN 0802-3271.
- "Kapazität og duktilitet av dybelforbindelser i trekonstruksjoner",
Jan Siem, 1999:46, ISBN 82-471-0414-8, ISSN 0802-3271.
- “Etablering av distribuert ingeniørarbeid; Teknologiske og organisatoriske erfaringer fra en norsk ingeniørbedrift”,
Lars Line, 1999:52, ISBN 82-471-0420-2, ISSN 0802-3271.
- “Estimation of Earthquake-Induced Response”,
Simon Ólafsson, 1999:73, ISBN 82-471-0443-1, ISSN 0802-3271.
- “Coastal Concrete Bridges: Moisture State, Chloride Permeability and Aging Effects”
Ragnhild Holen Relling, 1999:74, ISBN 82-471-0445-8, ISSN 0802-3271.
- ”Capacity Assessment of Titanium Pipes Subjected to Bending and External Pressure”,
Arve Bjørset, 1999:100, ISBN 82-471-0473-3, ISSN 0802-3271.

“Validation of Numerical Collapse Behaviour of Thin-Walled Corrugated Panels”,
Håvar Ilstad, 1999:101, ISBN 82-471-0474-1, ISSN 0802-3271.

“Strength and Ductility of Welded Structures in Aluminium Alloys”,
Mirosław Matusiak, 1999:113, ISBN 82-471-0487-3, ISSN 0802-3271.

“Thermal Dilation and Autogenous Deformation as Driving Forces to Self-Induced Stresses in High Performance Concrete”,
Øyvind Bjøntegaard, 1999:121, ISBN 82-7984-002-8, ISSN 0802-3271.

“Some Aspects of Ski Base Sliding Friction and Ski Base Structure”,
Dag Anders Moldestad, 1999:137, ISBN 82-7984-019-2, ISSN 0802-3271.

"Electrode reactions and corrosion resistance for steel in mortar and concrete",
Roy Antonsen, 2000:10, ISBN 82-7984-030-3, ISSN 0802-3271.

"Hydro-Physical Conditions in Kelp Forests and the Effect on Wave Damping and Dune Erosion. A case study on Laminaria Hyperborea",
Stig Magnar Løvås, 2000:28, ISBN 82-7984-050-8, ISSN 0802-3271.

"Random Vibration and the Path Integral Method",
Christian Skaug, 2000:39, ISBN 82-7984-061-3, ISSN 0802-3271.

"Buckling and geometrical nonlinear beam-type analyses of timber structures",
Trond Even Eggen, 2000:56, ISBN 82-7984-081-8, ISSN 0802-3271.

”Structural Crashworthiness of Aluminium Foam-Based Components”,
Arve Grønsund Hanssen, 2000:76, ISBN 82-7984-102-4, ISSN 0809-103X.

“Measurements and simulations of the consolidation in first-year sea ice ridges, and some aspects of mechanical behaviour”,
Knut V. Høyland, 2000:94, ISBN 82-7984-121-0, ISSN 0809-103X.

”Kinematics in Regular and Irregular Waves based on a Lagrangian Formulation”,
Svein Helge Gjørund, 2000-86, ISBN 82-7984-112-1, ISSN 0809-103X.

”Self-Induced Cracking Problems in Hardening Concrete Structures”,
Daniela Bosnjak, 2000-121, ISBN 82-7984-151-2, ISSN 0809-103X.

"Ballistic Penetration and Perforation of Steel Plates",
Tore Børvik, 2000:124, ISBN 82-7984-154-7, ISSN 0809-103X.

"Freeze-Thaw resistance of Concrete. Effect of: Curing Conditions, Moisture Exchange and Materials",
Terje Finnerup Rønning, 2001:14, ISBN 82-7984-165-2, ISSN 0809-103X

"Structural behaviour of post tensioned concrete structures. Flat slab. Slabs on ground",
Steinar Trygstad, 2001:52, ISBN 82-471-5314-9, ISSN 0809-103X.

"Slipforming of Vertical Concrete Structures. Friction between concrete and slipform panel",
Kjell Tore Fosså, 2001:61, ISBN 82-471-5325-4, ISSN 0809-103X.

"Some numerical methods for the simulation of laminar and turbulent incompressible flows",
Jens Holmen, 2002:6, ISBN 82-471-5396-3, ISSN 0809-103X.

"Improved Fatigue Performance of Threaded Drillstring Connections by Cold Rolling",
Steinar Kristoffersen, 2002:11, ISBN: 82-421-5402-1, ISSN 0809-103X.

"Deformations in Concrete Cantilever Bridges: Observations and Theoretical Modelling",
Peter F. Takács, 2002:23, ISBN 82-471-5415-3, ISSN 0809-103X.

"Stiffened aluminium plates subjected to impact loading",
Hilde Giæver Hildrum, 2002:69, ISBN 82-471-5467-6, ISSN 0809-103X.

"Full- and model scale study of wind effects on a medium-rise building in a built up area",
Jónas Thór Snæbjørnsson, 2002:95, ISBN82-471-5495-1, ISSN 0809-103X.

"Evaluation of Concepts for Loading of Hydrocarbons in Ice-infested water",
Arnor Jensen, 2002:114, ISBN 82-417-5506-0, ISSN 0809-103X.

"Numerical and Physical Modelling of Oil Spreading in Broken Ice",
Janne K. Økland Gjosteen, 2002:130, ISBN 82-471-5523-0, ISSN 0809-103X.

"Diagnosis and protection of corroding steel in concrete",
Franz Pruckner, 20002:140, ISBN 82-471-5555-4, ISSN 0809-103X.

"Tensile and Compressive Creep of Young Concrete: Testing and Modelling",
Dawood Atrushi, 2003:17, ISBN 82-471-5565-6, ISSN 0809-103X.

"Rheology of Particle Suspensions. Fresh Concrete, Mortar and Cement Paste with Various Types of Lignosulfonates",
Jon Elvar Wallevik, 2003:18, ISBN 82-471-5566-4, ISSN 0809-103X.

"Oblique Loading of Aluminium Crash Components",
Aase Reyes, 2003:15, ISBN 82-471-5562-1, ISSN 0809-103X.

"Utilization of Ethiopian Natural Pozzolans",
Surafel Ketema Desta, 2003:26, ISSN 82-471-5574-5, ISSN:0809-103X.

“Behaviour and strength prediction of reinforced concrete structures with discontinuity regions”, Helge Brå, 2004:11, ISBN 82-471-6222-9, ISSN 1503-8181.

“High-strength steel plates subjected to projectile impact. An experimental and numerical study”, Sumita Dey, 2004:38, ISBN 82-471-6282-2 (printed version), ISBN 82-471-6281-4 (electronic version), ISSN 1503-8181.

“Alkali-reactive and inert fillers in concrete. Rheology of fresh mixtures and expansive reactions.”

Bård M. Pedersen, 2004:92, ISBN 82-471-6401-9 (printed version), ISBN 82-471-6400-0 (electronic version), ISSN 1503-8181.

“On the Shear Capacity of Steel Girders with Large Web Openings”.

Nils Christian Hagen, 2005:9 ISBN 82-471-6878-2 (printed version), ISBN 82-471-6877-4 (electronic version), ISSN 1503-8181.

”Behaviour of aluminium extrusions subjected to axial loading”.

Østen Jensen, 2005:7, ISBN 82-471-6873-1 (printed version), ISBN 82-471-6872-3 (electronic version), ISSN 1503-8181.

”Thermal Aspects of corrosion of Steel in Concrete”.

Jan-Magnus Østvik, 2005:5, ISBN 82-471-6869-3 (printed version), ISBN 82-471-6868 (electronic version), ISSN 1503-8181.

”Mechanical and adaptive behaviour of bone in relation to hip replacement.” A study of bone remodelling and bone grafting.

Sébastien Muller, 2005:34, ISBN 82-471-6933-9 (printed version), ISBN 82-471-6932-0 (electronic version), ISSN 1503-8181.

“Analysis of geometrical nonlinearities with applications to timber structures”.

Lars Wollebæk, 2005:74, ISBN 82-471-7050-5 (printed version), ISBN 82-471-7019-1 (electronic version), ISSN 1503-8181.

“Pedestrian induced lateral vibrations of slender footbridges”,

Anders Rönnquist, 2005:102, ISBN 82-471-7082-5 (printed version), ISBN 82-471-7081-7 (electronic version), ISSN 1503-8181.

“Initial Strength Development of Fly Ash and Limestone Blended Cements at Various Temperatures Predicted by Ultrasonic Pulse Velocity”,

Tom Ivar Fredvik, 2005:112, ISBN 82-471-7105-8 (printed version), ISBN 82-471-7103-1 (electronic version), ISSN 1503-8181.

“Behaviour and modelling of thin-walled cast components”,

Cato Dørum, 2005:128, ISBN 82-471-7140-6 (printed version), ISBN 82-471-7139-2 (electronic version), ISSN 1503-8181.

- “Behaviour and modelling of selfpiercing riveted connections”,
Raffaele Porcaro, 2005:165, ISBN 82-471-7219-4 (printed version), ISBN 82-471-7218-6 (electronic version), ISSN 1503-8181.
- ”Behaviour and Modelling of Aluminium Plates subjected to Compressive Load”,
Lars Rønning, 2005:154, ISBN 82-471-7169-1 (printed version), ISBN 82-471-7195-3 (electronic version), ISSN 1503-8181.
- ”Bumper beam-longitudinal system subjected to offset impact loading”,
Satyanarayana Kokkula, 2005:193, ISBN 82-471-7280-1 (printed version), ISBN 82-471-7279-8 (electronic version), ISSN 1503-8181.
- “Control of Chloride Penetration into Concrete Structures at Early Age”,
Guofei Liu, 2006:46, ISBN 82-471-7838-9 (printed version), ISBN 82-471-7837-0 (electronic version), ISSN 1503-8181.
- “Modelling of Welded Thin-Walled Aluminium Structures”,
Ting Wang, 2006:78, ISBN 82-471-7907-5 (printed version), ISBN 82-471-7906-7 (electronic version), ISSN 1503-8181.
- ”Time-variant reliability of dynamic systems by importance sampling and probabilistic analysis of ice loads”,
Anna Ivanova Olsen, 2006:139, ISBN 82-471-8041-3 (printed version), ISBN 82-471-8040-5 (electronic version), ISSN 1503-8181.
- “Fatigue life prediction of an aluminium alloy automotive component using finite element analysis of surface topography”,
Sigmund Kyrre Ås, 2006:25, ISBN 82-471-7791-9 (printed version), ISBN 82-471-7791-9 (electronic version), ISSN 1503-8181.
- ”Constitutive models of elastoplasticity and fracture for aluminium alloys under strain path change”,
Dasharatha Achani, 2006:76, ISBN 82-471-7903-2 (printed version), ISBN 82-471-7902-4 (electronic version), ISSN 1503-8181.
- “Simulations of 2D dynamic brittle fracture by the Element-free Galerkin method and linear fracture mechanics”,
Tommy Karlsson, 2006:125, ISBN 82-471-8011-1 (printed version), ISBN 82-471-8010-3 (electronic version), ISSN 1503-8181.
- “Penetration and Perforation of Granite Targets by Hard Projectiles”,
Chong Chiang Seah, 2006:188, ISBN 82-471-8150-9 (printed version), ISBN 82-471-8149-5 (electronic version), ISSN 1503-8181.

“Deformations, strain capacity and cracking of concrete in plastic and early hardening phases”,

Tor Arne Hammer, 2007:234, ISBN 978-82-471-5191-4 (printed version), ISBN 978-82-471-5207-2 (electronic version), ISSN 1503-8181.

“Crashworthiness of dual-phase high-strength steel: Material and Component behaviour”, Venkatapathi Tarigopula, 2007:230, ISBN 82-471-5076-4 (printed version), ISBN 82-471-5093-1 (electronic version), ISSN 1503-8181.

“Fibre reinforcement in load carrying concrete structures”,

Åse Lyslo Døssland, 2008:50, ISBN 978-82-471-6910-0 (printed version), ISBN 978-82-471-6924-7 (electronic version), ISSN 1503-8181.

“Low-velocity penetration of aluminium plates”,

Frode Grytten, 2008:46, ISBN 978-82-471-6826-4 (printed version), ISBN 978-82-471-6843-1 (electronic version), ISSN 1503-8181.

“Robustness studies of structures subjected to large deformations”,

Ørjan Fyllingen, 2008:24, ISBN 978-82-471-6339-9 (printed version), ISBN 978-82-471-6342-9 (electronic version), ISSN 1503-8181.

“Constitutive modelling of morsellised bone”,

Knut Birger Lunde, 2008:92, ISBN 978-82-471-7829-4 (printed version), ISBN 978-82-471-7832-4 (electronic version), ISSN 1503-8181.

“Experimental Investigations of Wind Loading on a Suspension Bridge Girder”,

Bjørn Isaksen, 2008:131, ISBN 978-82-471-8656-5 (printed version), ISBN 978-82-471-8673-2 (electronic version), ISSN 1503-8181.

“Cracking Risk of Concrete Structures in The Hardening Phase”,

Guomin Ji, 2008:198, ISBN 978-82-471-1079-9 (printed version), ISBN 978-82-471-1080-5 (electronic version), ISSN 1503-8181.

“Modelling and numerical analysis of the porcine and human mitral apparatus”,

Victorien Emile Prot, 2008:249, ISBN 978-82-471-1192-5 (printed version), ISBN 978-82-471-1193-2 (electronic version), ISSN 1503-8181.

“Strength analysis of net structures”,

Heidi Moe, 2009:48, ISBN 978-82-471-1468-1 (printed version), ISBN 978-82-471-1469-8 (electronic version), ISSN 1503-8181.

“Numerical analysis of ductile fracture in surface cracked shells”,

Espen Berg, 2009:80, ISBN 978-82-471-1537-4 (printed version), ISBN 978-82-471-1538-1 (electronic version), ISSN 1503-8181.

“Subject specific finite element analysis of bone – for evaluation of the healing of a leg lengthening and evaluation of femoral stem design”,
Sune Hansborg Pettersen, 2009:99, ISBN 978-82-471-1579-4 (printed version), ISBN 978-82-471-1580-0 (electronic version), ISSN 1503-8181.

“Evaluation of fracture parameters for notched multi-layered structures”,
Lingyun Shang, 2009:137, ISBN 978-82-471-1662-3 (printed version), ISBN 978-82-471-1663-0 (electronic version), ISSN 1503-8181.

“Modelling of Dynamic Material Behaviour and Fracture of Aluminium Alloys for Structural Applications”
Yan Chen, 2009:69, ISBN 978-82-471-1515-2 (printed version), ISBN 978-82-471-1516-9 (electronic version), ISSN 1503-8181.

“Nanomechanics of polymer and composite particles”
Jianying He 2009:213, ISBN 978-82-471-1828-3 (printed version), ISBN 978-82-471-1829-0 (electronic version), ISSN 1503-8181.

“Mechanical properties of clear wood from Norway spruce”
Kristian Berbohm Dahl 2009:250, ISBN 978-82-471-1911-2 (printed version) ISBN 978-82-471-1912-9 (electronic version), ISSN 1503-8181.

“Modeling of the degradation of TiB₂ mechanical properties by residual stresses and liquid Al penetration along grain boundaries”
Micol Pezzotta 2009:254, ISBN 978-82-471-1923-5 (printed version) ISBN 978-82-471-1924-2 (electronic version) ISSN 1503-8181.

“Effect of welding residual stress on fracture”
Xiabo Ren 2010:77, ISBN 978-82-471-2115-3 (printed version) ISBN 978-82-471-2116-0 (electronic version), ISSN 1503-8181.

“Pan-based carbon fiber as anode material in cathodic protection system for concrete structures”
Mahdi Chini 2010:122, ISBN 978-82-471-2210-5 (printed version) ISBN 978-82-471-2213-6 (electronic version), ISSN 1503-8181.

“Structural Behaviour of deteriorated and retrofitted concrete structures”
Irina Vasililjeva Sæther 2010:171, ISBN 978-82-471-2315-7 (printed version) ISBN 978-82-471-2316-4 (electronic version) ISSN 1503-8181.

“Prediction of local snow loads on roofs”
Vivian Meløysund 2010:247, ISBN 978-82-471-2490-1 (printed version) ISBN 978-82-471-2491-8 (electronic version) ISSN 1503-8181.

“Behaviour and modelling of polymers for crash applications”
Virgile Delhaye 2010:251, ISBN 978-82-471-2501-4 (printed version) ISBN 978-82-471-2502-1 (electronic version) ISSN 1503-8181.

“Blended cement with reduced CO₂ emission – Utilizing the Fly Ash-Limestone Synergy”,
Klaartje De Weerd 2011:32, ISBN 978-82-471-2584-7 (printed version) ISBN 978-82-471-2584-4 (electronic version) ISSN 1503-8181.

“Chloride induced reinforcement corrosion in concrete” Concept of critical chloride content – methods and mechanisms.
Ueli Angst 2011:113, ISBN 978-82-471-2769-9 (printed version) ISBN 978-82-471-2763-6 (electronic version) ISSN 1503-8181.

“A thermo-electric-Mechanical study of the carbon anode and contact interface for Energy savings in the production of aluminium”.
Dag Herman Andersen 2011:157, ISBN 978-82-471-2859-6 (printed version) ISBN 978-82-471-2860-2 (electronic version) ISSN 1503-8181.

“Structural Capacity of Anchorage Ties in Masonry Veneer Walls Subjected to Earthquake”. The implications of Eurocode 8 and Eurocode 6 on a typical Norwegian veneer wall.
Ahmed Mohamed Yousry Hamed 2011:181, ISBN 978-82-471-2911-1 (printed version) ISBN 978-82-471-2912-8 (electronic ver.) ISSN 1503-8181.

“Work-hardening behaviour in age-hardenable Al-Zn-Mg(-Cu) alloys”.
Ida Westermann , 2011:247, ISBN 978-82-471-3056-8 (printed ver.) ISBN 978-82-471-3057-5 (electronic ver.) ISSN 1503-8181.

“Behaviour and modelling of selfpiercing riveted connections using aluminium rivets”.
Nguyen-Hieu Hoang, 2011:266, ISBN 978-82-471-3097-1 (printed ver.) ISBN 978-82-471-3099-5 (electronic ver.) ISSN 1503-8181.

“Fibre reinforced concrete”.
Sindre Sandbakk, 2011:297, ISBN 978-82-471-3167-1 (printed ver.) ISBN 978-82-471-3168-8 (electronic ver) ISSN 1503:8181.

“Dynamic behaviour of cablesupported bridges subjected to strong natural wind”.
Ole Andre Øiseth, 2011:315, ISBN 978-82-471-3209-8 (printed ver.) ISBN 978-82-471-3210-4 (electronic ver.) ISSN 1503-8181.

“Constitutive modeling of solargrade silicon materials”
Julien Cochard, 2011:307, ISBN 978-82-471-3189-3 (printed ver). ISBN 978-82-471-3190-9 (electronic ver.) ISSN 1503-8181.

“Constitutive behavior and fracture of shape memory alloys”
Jim Stian Olsen, 2012:57, ISBN 978-82-471-3382-8 (printed ver.) ISBN 978-82-471-3383-5 (electronic ver.) ISSN 1503-8181.

“Field measurements in mechanical testing using close-range photogrammetry and digital image analysis”

Egil Fagerholt, 2012:95, ISBN 978-82-471-3466-5 (printed ver.) ISBN 978-82-471-3467-2 (electronic ver.) ISSN 1503-8181.

“Towards a better understanding of the ultimate behaviour of lightweight aggregate concrete in compression and bending”

Håvard Nedrelid, 2012:123, ISBN 978-82-471-3527-3 (printed ver.) ISBN 978-82-471-3528-0 (electronic ver.) ISSN 1503-8181.

“Numerical simulations of blood flow in the left side of the heart”

Sigrid Kaarstad Dahl, 2012:135, ISBN 978-82-471-3553-2 (printed ver.) ISBN 978-82-471-3555-6 (electronic ver.) ISSN 1503-8181.

“Moisture induced stresses in glulam”

Vanessa Angst-Nicollier, 2012:139, ISBN 978-82-471-3562-4 (printed ver.) ISBN 978-82-471-3563-1 (electronic ver.) ISSN 1503-8181.

“Biomechanical aspects of distraction osteogenesis”

Valentina La Russa, 2012:250, ISBN 978-82-471-3807-6 (printed ver.) ISBN 978-82-471-3808-3 (electronic ver.) ISSN 1503-8181.

“Ductile fracture in dual-phase steel. Theoretical, experimental and numerical study”

Gaute Gruben, 2012:257, ISBN 978-82-471-3822-9 (printed ver.) ISBN 978-82-471-3823-6 (electronic ver.) ISSN 1503-8181.

“Damping in Timber Structures”

Nathalie Labonnote, 2012:263, ISBN 978-82-471-3836-6 (printed ver.) ISBN 978-82-471-3837-3 (electronic ver.) ISSN 1503-8181.

“Biomechanical modeling of fetal veins: The umbilical vein and ductus venosus bifurcation”

Paul Roger Leinan, 2012:299, ISBN 978-82-471-3915-8 (printed ver.) ISBN 978-82-471-3916-5 (electronic ver.) ISSN 1503-8181.

“Large-Deformation behaviour of thermoplastics at various stress states”

Anne Serine Ognedal, 2012:298, ISBN 978-82-471-3913-4 (printed ver.) ISBN 978-82-471-3914-1 (electronic ver.) ISSN 1503-8181.

“Hardening accelerator for fly ash blended cement”

Kien Dinh Hoang, 2012:366, ISBN 978-82-471-4063-5 (printed ver.) ISBN 978-82-471-4064-2 (electronic ver.) ISSN 1503-8181.

“From molecular structure to mechanical properties”

Jianyang Wu, 2013:186, ISBN 978-82-471-4485-5 (printed ver.) ISBN 978-82-471-4486-2 (electronic ver.) ISSN 1503-8181.

“Experimental and numerical study of hybrid concrete structures”

Linn Grepstad Nes, 2013:259, ISBN 978-82-471-4644-6 (printed ver.) ISBN 978-82-471-4645-3 (electronic ver.) ISSN 1503-8181.

“Mechanics of ultra-thin multi crystalline silicon wafers”

Saber Saffar, 2013:199, ISBN 978-82-471-4511-1 (printed ver.) ISBN 978-82-471-4513-5 (electronic ver.) ISSN 1503-8181.

“Through process modelling of welded aluminium structures”

Anizahyati Alisibramulisi, 2013:325, ISBN 978-82-471-4788-7 (printed ver.) ISBN 978-82-471-4789-4 (electronic ver.) ISSN 1503-8181.

“Combined blast and fragment loading on steel plates”

Knut Gaarder Rakvåg, 2013:361, ISBN 978-82-471-4872-3 (printed ver.) ISBN 978-82-4873-0 (electronic ver.) ISSN 1503-8181.

“Characterization and modelling of the anisotropic behaviour of high-strength aluminium alloy”

Marion Fourmeau, 2014:37, ISBN 978-82-326-0008-3 (printed ver.) ISBN 978-82-326-0009-0 (electronic ver.) ISSN 1503-8181.

“Behaviour of threaded steel fasteners at elevated deformation rates”

Henning Fransplass, 2014:65, ISBN 978-82-326-0054-0 (printed ver.) ISBN 978-82-326-0055-7 (electronic ver.) ISSN 1503-8181.

“Sedimentation and Bleeding”

Ya Peng, 2014:89, ISBN 978-82-326-0102-8 (printed ver.) ISBN 978-82-326-0103-5 (electronic ver.) ISSN 1503-8181.

“Impact against X65 offshore pipelines”

Martin Kristoffersen, 2014:362, ISBN 978-82-326-0636-8 (printed ver.) ISBN 978-82-326-0637-5 (electronic ver.) ISSN 1503-8181.

“Formability of aluminium alloy subjected to prestrain by rolling”

Dmitry Vysochinskiy, 2014:363, ISBN 978-82-326-0638-2 (printed ver.) ISBN 978-82-326-0639-9 (electronic ver.) ISSN 1503-8181.

“Experimental and numerical study of Yielding, Work-Hardening and anisotropy in textured AA6xxx alloys using crystal plasticity models”

Mikhail Khadyko, 2015:28, ISBN 978-82-326-0724-2 (printed ver.) ISBN 978-82-326-0725-9 (electronic ver.) ISSN 1503-8181.

“Behaviour and Modelling of AA6xxx Aluminium Alloys Under a Wide Range of Temperatures and Strain Rates”

Vincent Vilamosa, 2015:63, ISBN 978-82-326-0786-0 (printed ver.) ISBN 978-82-326-0787-7 (electronic ver.) ISSN 1503-8181.

“A Probabilistic Approach in Failure Modelling of Aluminium High Pressure Die-Castings”

Octavian Knoll, 2015:137, ISBN 978-82-326-0930-7 (printed ver.) ISBN 978-82-326-0931-4 (electronic ver.) ISSN 1503-8181.

“Ice Abrasion on Marine Concrete Structures”

Egil Møen, 2015:189, ISBN 978-82-326-1034-1 (printed ver.) ISBN 978-82-326-1035-8 (electronic ver.) ISSN 1503-8181.

“Fibre Orientation in Steel-Fibre-Reinforced Concrete”

Giedrius Zirgulis, 2015:229, ISBN 978-82-326-1114-0 (printed ver.) ISBN 978-82-326-1115-7 (electronic ver.) ISSN 1503-8181.

“Effect of spatial variation and possible interference of localised corrosion on the residual capacity of a reinforced concrete beam”

Mohammad Mahdi Kioumarsi, 2015:282, ISBN 978-82-326-1220-8 (printed ver.) ISBN 978-82-1221-5 (electronic ver.) ISSN 1503-8181.

“The role of concrete resistivity in chloride-induced macro-cell corrosion”

Karla Horbostel, 2015:324, ISBN 978-82-326-1304-5 (printed ver.) ISBN 978-82-326-1305-2 (electronic ver.) ISSN 1503-8181.

“Flowable fibre-reinforced concrete for structural applications”

Elena Vidal Sarmiento, 2015:335, ISBN 978-82-326-1324-3 (printed ver.) ISBN 978-82-326-1325-0 (electronic ver.) ISSN 1503-8181.

“Development of chushed sand for concrete production with microproportioning”

Rolands Cepuritis, 2016:19, ISBN 978-82-326-1382-3 (printed ver.) ISBN 978-82-326-1383-0 (electronic ver.) ISSN 1503-8181.

“Withdrawal properties of threaded rods embedded in glued-laminated timber elements”

Haris Stamatopoulos, 2016:48, ISBN 978-82-326-1436-3 (printed ver.) ISBN 978-82-326-1437-0 (electronic ver.) ISSN 1503-8181.

“An Experimental and numerical study of thermoplastics at large deformation”

Marius Andersen, 2016:191, ISBN 978-82-326-1720-3 (printed ver.) ISBN 978-82-326-1721-0 (electronic ver.) ISSN 1503-8181.

“Modeling and Simulation of Ballistic Impact”

Jens Kristian Holmen, 2016:240, ISBN 978-82-326-1818-7 (printed ver.) ISBN 978-82-326-1819-4 (electronic ver.) ISSN 1503-8181.

“Early age crack assessment of concrete structures”

Anja B. Estensen Klausen, 2016:256, ISBN 978-82-326-1850-7 (printed ver.) ISBN 978-82-326-1851-4 (electronic ver.) ISSN 1503-8181.

- “Uncertainty quantification and sensitivity analysis for cardiovascular models”
Vinzenc Gregor Eck, 2016:234, ISBN 978-82-326-1806-4 (printed ver.) ISBN 978-82-326-1807-1 (electronic ver.) ISSN 1503-8181.
- “Dynamic behaviour of existing and new railway catenary systems under Norwegian conditions”
Petter Røe Nåvik, 2016:298, ISBN 978-82-326-1935-1 (printed ver.) ISBN 978-82-326-1934-4 (electronic ver.) ISSN 1503-8181.
- “Mechanical behaviour of particle-filled elastomers at various temperatures”
Arne Ilseeng, 2016:295, ISBN 978-82-326-1928-3 (printed ver.) ISBN 978-82-326-1929-0 (electronic ver.) ISSN 1503-8181.
- “Nanotechnology for Anti-Icing Application”
Zhiwei He, 2016:348, ISBN 978-82-326-2038-8 (printed ver.) ISBN 978-82-326-2019-5 (electronic ver.) ISSN 1503-8181.
- “Conduction Mechanisms in Conductive Adhesives with Metal-Coated Polymer Spheres”
Sigurd Rolland Pettersen, 2016:349, ISBN 978-82-326-2040-1 (printed ver.) ISBN 978-82-326-2041-8 (electronic ver.) ISSN 1503-8181.
- “The interaction between calcium lignosulfonate and cement”
Alessia Colombo, 2017:20, ISBN 978-82-326-2122-4 (printed ver.) ISBN 978-82-326-2123-1 (electronic ver.) ISSN 1503-8181.
- “Behaviour and Modelling of Flexible Structures Subjected to Blast Loading”
Vegard Aune, 2017:101, ISBN 978-82-326-2274-0 (printed ver.) ISBN 978-82-326-2275-7 (electronic ver.) ISSN 1503-8181.
- “Behaviour of steel connections under quasi-static and impact loading”
Erik Løhre Grimsmo, 2017:159, ISBN 978-82-326-2390-7 (printed ver.) ISBN 978-82-326-2391-4 (electronic ver.) ISSN 1503-8181.
- “An experimental and numerical study of cortical bone at the macro and Nano-scale”
Masoud Ramenzanzadehkoldeh, 2017:208, ISBN 978-82-326-2488-1 (printed ver.) ISBN 978-82-326-2489-8 (electronic ver.) ISSN 1503-8181.
- “Optoelectrical Properties of a Novel Organic Semiconductor: 6,13-Dichloropentacene”
Mao Wang, 2017:130, ISBN 978-82-326-2332-7 (printed ver.) ISBN 978-82-326-2333-4 (electronic ver.) ISSN 1503-8181.
- “Core-shell structured microgels and their behavior at oil and water interface”
Yi Gong, 2017:182, ISBN 978-82-326-2436-2 (printed ver.) ISBN 978-82-326-2437-9 (electronic ver.) ISSN 1503-8181.

“Aspects of design of reinforced concrete structures using nonlinear finite element analyses”

Morten Engen, 2017:149, ISBN 978-82-326-2370-9 (printed ver.) ISBN 978-82-326-2371-6 (electronic ver.) ISSN 1503-8181.

“Numerical studies on ductile failure of aluminium alloys”

Lars Edvard Dæhli, 2017:284, ISBN 978-82-326-2636-6 (printed ver.) ISBN 978-82-326-2637-3 (electronic ver.) ISSN 1503-8181.

“Modelling and Assessment of Hydrogen Embrittlement in Steels and Nickel Alloys”

Haiyang Yu, 2017:278, ISBN 978-82-326-2624-3 (printed. ver.) ISBN 978-82-326-2625-0 (electronic ver.) ISSN 1503-8181.

“Network arch timber bridges with light timber deck on transverse crossbeams”

Anna Weronika Ostrycharczyk, 2017:318, ISBN 978-82-326-2704-2 (printed ver.) ISBN 978-82-326-2705-9 (electronic ver.) ISSN 1503-8181.

“Splicing of Large Glued Laminated Timber Elements by Use of Long Threaded Rods”

Martin Cepelka, 2017:320, ISBN 978-82-326-2708-0 (printed ver.) ISBN 978-82-326-2709-7 (electronic ver.) ISSN 1503-8181.

“Thermomechanical behaviour of semi-crystalline polymers: experiments, modelling and simulation”

Joakim Johnsen, 2017:317, ISBN 978-82-326-2702-8 (printed ver.) ISBN 978-82-326-2703-5 (electronic ver.) ISSN 1503-8181.

“Small-Scale Plasticity under Hydrogen Environment”

Kai Zhao, 2017:356, ISBN 978-82-326-2782-0 (printed ver.) ISBN 978-82-326-2783-7 (electronic er.) ISSN 1503-8181.

“Risk and Reliability Based Calibration of Structural Design Codes”

Michele Baravalle, 2017:342, ISBN 978-82-326-2752-3 (printed ver.) ISBN 978-82-326-2753-0 (electronic ver.) ISSN 1503-8181.

“Dynamic behaviour of floating bridges exposed to wave excitation”

Knut Andreas Kvåle, 2017:365, ISBN 978-82-326-2800-1 (printed ver.) ISBN 978-82-326-2801-8 (electronic ver.) ISSN 1503-8181.

“Dolomite calcined clay composite cement – hydration and durability”

Alisa Lydia Machner, 2018:39, ISBN 978-82-326-2872-8 (printed ver.). ISBN 978-82-326-2873-5 (electronic ver.) ISSN 1503-8181.

“Modelling of the self-excited forces for bridge decks subjected to random motions: an experimental study”

Bartosz Siedziako, 2018:52, ISBN 978-82-326-2896-4 (printed ver.). ISBN 978-82-326-2897-1 (electronic ver.) ISSN 1503-8181.

“A probabilistic-based methodology for evaluation of timber facade constructions”
Klodian Gradeci, 2018:69, ISBN 978-82-326-2928-2 (printed ver.) ISBN 978-82-326-2929-9 (electronic ver.) ISSN 1503-8181.

“Behaviour and modelling of flow-drill screw connections”
Johan Kolstø Sønstabø, 2018:73, ISBN 978-82-326-2936-7 (printed ver.) ISBN 978-82-326-2937-4 (electronic ver.) ISSN 1503-8181.

“Full-scale investigation of the effects of wind turbulence characteristics on dynamic behavior of long-span cable-supported bridges in complex terrain”
Aksel Fenerci, 2018 100, ISBN 978-82-326-2990-9 (printed ver.) ISBN 978-82-326-2991-6 (electronic ver.) ISSN 1503-8181.

“Modeling and simulation of the soft palate for improved understanding of the obstructive sleep apnea syndrome”
Hongliang Liu, 2018:101, ISBN 978-82-326-2992-3 (printed ver.) ISBN 978-82-326-2993-0 (electronic ver.) ISSN 1503-8181.

“Long-term extreme response analysis of cable-supported bridges with floating pylons subjected to wind and wave loads”
Yuwang Xu, 2018:229, ISBN 978-82-326-3248-0 (printed ver.) ISBN 978-82-326-3249-7 (electronic ver.) ISSN 1503-8181.

“Reinforcement corrosion in carbonated fly ash concrete”
Andres Belda Revert, 2018:230, ISBN 978-82-326-3250-3 (printed ver.) ISBN 978-82-326-3251-0 (electronic ver.) ISSN 1503-8181.

“Direct finite element method for nonlinear earthquake analysis of concrete dams including dam-water-foundation rock interaction”
Arnkjell Løkke, 2018:252, ISBN 978-82-326-3294-7 (printed ver.) ISBN 978-82-326-3295-4 (electronic ver.) ISSN 1503-8181.

“Electromechanical characterization of metal-coated polymer spheres for conductive adhesives”
Molly Strimbeck Bazilchuk, 2018:295, ISBN 978-82-326-3380-7 (printed. ver.) ISBN 978-82-326-3381-4 (electrical ver.) ISSN 1503-8181.

“Determining the tensile properties of Arctic materials and modelling their effects on fracture”
Shengwen Tu, 2018:269, ISBN 978-82-326-3328-9 (printed ver.) ISBN 978-82-326-3329-6 (electronic ver.) ISSN 1503-8181.

“Atomistic Insight into Transportation of Nanofluid in Ultra-confined Channel”
Xiao Wang, 2018:334, ISBN 978-82-326-3456-9 (printed ver.) ISBN 978-82-326-3457-6 (electronic ver.) ISSN 1503-8181.

“An experimental and numerical study of the mechanical behaviour of short glass-fibre reinforced thermoplastics”

Jens Petter Henrik Holmstrøm, 2019:79, ISBN 978-82-326-3760-7 (printed ver.) ISBN 978-82-326-3761-4 (electronic ver.) ISSN 1503-8181.

“Uncertainty quantification and sensitivity analysis informed modeling of physical systems”

Jacob Sturdy, 2019:115, ISBN 978-82-326-3828-4 (printed ver.) ISBN 978-82-326-3829-1 (electric ver.) ISSN 1503-8181.

“Load model of historic traffic for fatigue life estimation of Norwegian railway bridges”

Gunnstein T. Frøseth, 2019:73, ISBN 978-82-326-3748-5 (printed ver.) ISBN 978-82-326-3749-2 (electronic ver.) ISSN 1503-8181.

“Force identification and response estimation in floating and suspension bridges using measured dynamic response”

Øyvind Wiig Petersen, 2019:88, ISBN 978-82-326-3778-2 (printed ver.) ISBN 978-82-326-377-9 (electronic ver.) ISSN 1503-8181.

“Consistent crack width calculation methods for reinforced concrete elements subjected to 1D and 2D stress states”

Reignard Tan, 2019:147, ISBN 978-82-326-3892-5 (printed ver.) ISBN 978-82-326-3893-2 (electronic ver.) ISSN 1503-8181.

“Nonlinear static and dynamic isogeometric analysis of slender spatial and beam type structures”

Siv Bente Raknes, 2019:181, ISBN 978-82-326-3958-8 (printed ver.) ISBN 978-82-326-3959-5 (electronic ver.) ISSN 1503-8181.

“Experimental study of concrete-ice abrasion and concrete surface topography modification”

Guzel Shamsutdinova, 2019:182, ISBN 978-82-326-3960-1 (printed ver.) ISBN 978-82-326-3961-8 (electronic ver.) ISSN 1503-8181.

“Wind forces on bridge decks using state-of-the art FSI methods”

Tore Andreas Helgedagsrud, 2019:180, ISBN 978-82-326-3956-4 (printed ver.) ISBN 978-82-326-3957-1 (electronic ver.) ISSN 1503-8181.

“Numerical Study on Ductile-to-Brittle Transition of Steel and its Behavior under Residual Stresses”

Yang Li, 2019:227, ISBN 978-82-326-4050-8 (printed ver.) ISBN 978-82-326-4015-5 (electronic ver.) ISSN 1503-8181.

“Micromechanical modelling of ductile fracture in aluminium alloys”

Bjørn Håkon Frodal, 2019:253, ISBN 978-82-326-4102-4 (printed ver.) ISBN 978-82-326-4103-1 (electronic ver.) ISSN 1503-8181.

“Monolithic and laminated glass under extreme loading: Experiments, modelling and simulations”

Karoline Osnes, 2019:304, ISBN 978-82-326-4204-5 (printed ver.) ISBN 978-82-326-4205-2 (electronic ver.) ISSN 1503-8181.

“Plastic flow and fracture of isotropic and anisotropic 6000-series aluminium alloys: Experiments and numerical simulations “

Susanne Thomesen, 2019:312, ISBN 978-82-326-4220-5 (printed ver.), ISBN 978-82-326-4221-2 (electronic ver.) ISSN 1503-8181

“Stress-laminated timber decks in bridges”

Francesco Mirko Massaro, 2019:346, ISBN 978-82-326-4288-5 (printed ver.), ISBN 978-82-326-4289-2 (electronic ver.) ISSN 1503-8181

“Connections between steel and aluminium using adhesive bonding combined with self-piercing riveting: Testing, modelling and analysis”

Matthias Reil, 2019:319, ISBN 978-82-326-4234-2 (printed ver.), ISBN 978-82-326-4235-9 (electronic ver.) ISSN 1503-8181

“Designing Polymeric Icephobic Materials”

Yizhi Zhuo, 2019:345, ISBN 978-82-326-4286-1 (printed ver.), ISBN 978-82-326-4287-8 (electronic ver.) ISSN 1503-8181

“Fundamental Mechanisms of Ice Adhesion”

Rønneberg, Sigrid 2020:87, ISBN 978-82-326-4527-8 (printed version) ISBN 978-82-326-4524-5 (electronic version) ISSN 1503-8181

“Mechanical modeling of the polymeric coating on a subsea pipeline” Vestrum, Ole

2020:105, ISBN 978-82-326-4562-6 (printed version) ISBN 978-82-326-4563-3 (electronic version) ISSN 1503-8181

“Conceptual form-finding in structural engineering” Marcin Luczkowski 2020: “Self-assembled superstructures of magnetic nanoparticles: advanced nanofabrication and enhanced mechanical properties”

“Self-assembled superstructures of magnetic nanoparticles: advanced nanofabrication and enhanced mechanical properties” Verner Håkonsen 2020:271, ISBN 978-82-326-4890-0

(printed version) ISBN 978-82-326-4891-7 (electronic version) ISSN 1503-8181

“Micromechanical modelling of fracture in ductile alloys with applications to high-strength steel”

Sondre Bergo 2020:313, ISBN 978-82-326-4974-7 (printed version) ISBN 978-82-326-4975-4 (electronic version) ISSN 1503-8181

“Fracture in wood of Norway spruce - Experimental and numerical study”
Katarzyna Ostapska 2020:314, ISBN 978-82-326-4976-1 (printed version) ISBN 978-82-326-4977-8 (electronic version) ISSN 1503-8181

“Dynamic anti-icing surfaces (DAIS)” Feng Wang 2020:330 ISBN 978-82-326-5006-4 (printed version) ISBN 978-82-326-5007-1 (electronic version) ISSN 1503-8181

“«Multiaxial Fatigue analysis of offshore mooring chains, considering the effects of residual stresses and corrosion pits» Ershad P. Zarandi 2020:337 ISBN 978-82-326-5020-0 (printed version) ISBN 978-82-326-5021-7 (electronic version) ISSN 1503-8181

“Production and documentation of frost durable high-volume fly ash concrete: air entrainment, cracking and scaling in performance testing” Andrei Shpak 2020:366 ISBN 978-82-326-5078-1 (printed version) ISBN 978-82-326-5079-8 (electronic version) ISSN 1503-8181

“Physics-based and data-driven reduced-order blood flow models: Applications to coronary artery disease diagnostics” Fredrik Eikeland Fossan 2020:362 ISBN 978-82-326-5070-5 (printed version) ISBN 978-82-326-5071-2 (electronic version) ISSN 1503-8181

“Multi-scale modelling and simulation of ductile failure in aluminium structures” Henrik Granum 2020:374 ISBN 978-82-326-5094-1 (printed version) ISBN 978-82-326-5095-8 (electronic version) ISSN 1503-8181

“Testing and modelling of multi-material joints” Jon Fredrick Berntsen 2020:368 ISBN 978-82-326-5082-8 (printed version) ISBN 978-82-326-5083-5 ISSN 1503-8181

“Heuristic models for wear prediction and dynamic-based condition monitoring techniques in pantograph-catenary interaction” Stefano Derosa 2020:381 ISBN 978-82-326-5108-5 (printed version) ISBN 978-82-326-5109-2 (electronic version) ISSN 1503-8181

“Experimental and numerical study of dilation in mineral filled PVC” Sindre Nordmark Olufsen 2020:388 ISBN 978-82-326-5122-1 (printed version) ISBN 978-82-326-5123-8 (electronic version) ISSN 1503-8181

“Residual stresses and dimensional deviation in metal additive manufacturing: prediction and mitigation methods” Li Sun 2020:411 ISBN 978-82-471-9600-7 (printed version) ISBN 978-82-471-9581-9 (electronic version) ISSN 1503-8181 (printed version) ISSN 2703-8084 (online version)

“Moment-resisting timber frames with semi-rigid connections” Aivars Vilguts 2021:88 ISBN 978-82-326-6987 (printed version) ISBN 978-82-326-5737-7 (electronic version) ISSN 2703-8084 (online version)

“Thermal transport in metal-polymer systems” Susanne Sandell 2021:63 ISBN 978-82-326-5304-1 (printed version) ISBN 978-82-326-6278-4 (electronic version) ISSN 2703-8084 (online version)

“Competitive timber floors” Sveinung Ørjan Nesheim 2021:134 ISBN 978-82-326-6481-8 (printed version) ISBN 978-82-326-5399-7 (electronic version) ISSN 2703-8084

“Thermodynamics of Nanoscale Films and Fluid Volumes” Bjørn Andre Strøm 2021:166 ISBN 978-82-326-6778-9 (printed version) ISBN 978-82-326-5900-5 (electronic version) ISSN 2703-8084 (online version)

“Characterization and modeling of the mechanical behavior of polymer foam” Daniel Thor Morton 2021:173 ISBN 978-82-326-6245-6 (printed version) ISBN 978-82-326-5699-8 (electronic version) ISSN 2703-8084 (online version)

“Atomistic Insights to Interfacial Dynamics” Yuequn Fu 2021:233 ISBN 978-82-326-5530-4 (printed version) ISBN 978-82-326-6894-6 (electronic version) ISSN 2703-8084 (online version)

“Mechanisms and enhancement of CO₂ condensation heat transfer” Ingrid Snustad 2021:236 ISBN 978-82-326-5606-6 ISBN 978-82-236-6715-4 (electronic version) ISSN 2703-8084

“Experimental study of reinforced concrete slabs subjected to fire exposure and blast loading” Assis Arano Barenys 2021:239 ISBN 978-82-326-5289-1 ISBN 978-82-326-5876-3 (electronic version) ISSN 2703-8084 (online version)

“Long-term extreme buffeting response investigations for long-span bridges considering uncertain turbulence parameters based on field measurements” Tor Martin Lystad 2021:216 ISBN 978-82-326-5797-1 (printed version) ISBN 978-82-326-6154-1 (electronic version) ISSN 2703-8084 (online version)

“Development and Application of a Vision-Based System for Structural Monitoring of Railway Catenary System” Tengjiao Jiang 2021:280 ISBN 978-82-326-6866-3 (printed ver.) ISBN 978-82-326-5778-0 (electronic ver.) ISSN 1503-8181 (online ver.)

“Integrated design and maintenance of deteriorating structural systems” Jorge Mendoza Espinosa 2021:351 ISBN 978-82-326-6608-9 (printed ver.) ISBN 978-82-326-6954-7 (electronic ver.) ISSN 2703-8084 (online ver.)

“Numerical and experimental studies for damage detection and structural health monitoring of steel bridges” Bjørn T. Svendsen 2021:382 ISBN 978-82-326-6327-9 (printed ver.) ISBN 978-82-326-5895-4 (electronic ver.) ISSN 2703-8084 (online ver.)

“Uncertainty quantification for multiphase flow” Andreas Strand 2021:410 ISBN 978-82-326-6519-8 (printed ver.) ISBN 978-82-326-6928-8 (electronic ver.) ISSN 2703-8084 (online ver.)

“Prediction of rheological properties of filler modified cement paste from constituent properties, flow measurements and modelling” Elisabeth Leite Skare 2022:38 ISBN

978-82-326-5753-7 (printed ver.) ISBN 978-82-326-6958-5 (electronic ver.) ISSN 2703-8084 (online ver.)

“Nanomechanical characterization of additively manufactured metallic alloys” Siqi Liu 2022:96 ISBN 978-82-326-5457-4 (printed ver.) ISBN 978-82-326-5481-9 (electronic ver.) ISSN 2703-8084 (online ver.)

“Modeling and experiments in transient potential drop measurements for nondestructive evaluation” Øyvind Othar Aunet Persvik 2022:146 ISBN 978-82-326-5682-0 (printed ver.) ISBN 978-82-326-5365-2 (electronic ver.) ISSN 2703-8084 (online ver.)

“Ductile fracture of aluminium alloys in the low to moderate stress triaxiality range” Asle Joachim Tomstad 2022:150 ISBN 978-82-326-6681-2 (printed ver.) ISBN 978-82-326-5506-9 (electronic ver.) ISSN 2703-8084 (online ver.)

“Application of marine field data for prediction of chloride ingress in concrete” Simon Fjendbo 2022:173 ISBN 978-82-326-6071-1 (printed ver.) ISBN 978-82-326-6659-1 (electronic ver.) ISSN 1503-8181 (online ver.)

“On the use of a virtual laboratory for aluminum alloys: application to large-scale analyses of extruded profiles” Marcos Fernandez Garcia 2022:199 ISBN 978-82-326-5527-4 (printed ver.) ISBN 978-82-326-6036-0 (electronic ver.) ISSN 2703-8084 (online ver.)

“Energy absorption and failure in aluminum alloys: An experimental and numerical study” Kristin Qvale 2022:213 ISBN 978-82-326-5172-6 (printed ver.) ISBN 978-82-326-5208-2 (electronic ver.) ISSN 2703-8084 (online ver.)

“Probabilistic modelling of wind induced load effects for suspension bridges with emphasis on long-term extreme value analysis” Dario Rafael Fernandez Castellon 2022:218 ISBN 978-82-326-5343-0 (printed ver.) ISBN 978-82-326-5401-7 (electronic ver.) ISSN 2703-8084 (online ver.)